Measurement of the elastic electron-proton cross section and separation of the electric and magnetic form factor in the Q^2 range from 0.004 to 1 $(\mathrm{GeV/c})^2$

Dissertation
zur Erlangung des Grades
„Doktor der Naturwissenschaften“
am Fachbereich Physik, Mathematik und Informatik
der Johannes Gutenberg-Universität
in Mainz

Jan C. Bernauer
geb. in Mainz

Institut für Kernphysik
Johannes Gutenberg-Universität Mainz
April 2010

Tag der mündlichen Prüfung: 24.09.2010

D77 (Dissertation Universität Mainz)

Abstract

The electromagnetic form factors of the proton are fundamental quantities sensitive to the distribution of charge and magnetization inside the proton. Precise knowledge of the form factors, in particular of the charge and magnetization radii provide strong tests for theory in the non-perturbative regime of QCD. However, the existing data at Q^2 below 1 $(\mathrm{GeV}/c)^2$ are not precise enough for a hard test of theoretical predictions.

For a more precise determination of the form factors, within this work more than 1400 cross sections of the reaction $H(e,e')p$ were measured at the Mainz Microtron MAMI using the 3-spectrometer-facility of the A1-collaboration. The data were taken in three periods in the years 2006 and 2007 using beam energies of 180, 315, 450, 585, 720 and 855 MeV. They cover the Q^2 region from 0.004 to 1 $(\mathrm{GeV}/c)^2$ with counting rate uncertainties below 0.2% for most of the data points. The relative luminosity of the measurements was determined using one of the spectrometers as a luminosity monitor. The overlapping acceptances of the measurements maximize the internal redundancy of the data and allow, together with several additions to the standard experimental setup, for tight control of systematic uncertainties.
To account for the radiative processes, an event generator was developed and implemented in the simulation package of the analysis software which works without peaking approximation by explicitly calculating the Bethe-Heitler and Born Feynman diagrams for each event.

To separate the form factors and to determine the radii, the data were analyzed by fitting a wide selection of form factor models directly to the measured cross sections. These fits also determined the absolute normalization of the different data subsets. The validity of this method was tested with extensive simulations. The results were compared to an extraction via the standard Rosenbluth technique.

The dip structure in G_E that was seen in the analysis of the previous world data shows up in a modified form. When compared to the standard-dipole form factor as a smooth curve, the extracted G_E exhibits a strong change of the slope around $0.1(\mathrm{GeV}/c)^2$, and in the magnetic form factor a dip around 0.2 $(\mathrm{GeV}/c)^2$ is found. This may be taken as indications for a pion cloud. For higher Q^2, the fits yield larger values for G_M than previous measurements, in agreement with form factor ratios from recent precise polarized measurements in the Q^2 region up to 0.6 $(\mathrm{GeV}/c)^2$.

The charge and magnetic rms radii are determined as

$$\begin{aligned} \langle r_e \rangle &= 0.879 \pm 0.005_{\mathrm{stat.}} \pm 0.004_{\mathrm{syst.}} \pm 0.002_{\mathrm{model}} \pm 0.004_{\mathrm{group}}\ \mathrm{fm}, \\ \langle r_m \rangle &= 0.777 \pm 0.013_{\mathrm{stat.}} \pm 0.009_{\mathrm{syst.}} \pm 0.005_{\mathrm{model}} \pm 0.002_{\mathrm{group}}\ \mathrm{fm}. \end{aligned}$$

This charge radius is significantly larger than theoretical predictions and than the radius of the standard dipole. However, it is in agreement with earlier results measured at the Mainz linear accelerator and with determinations from Hydrogen Lamb shift measurements. The extracted magnetic radius is smaller than previous determinations and than the standard-dipole value.

Zusammenfassung

Die elektromagnetischen Formfaktoren des Protons sind fundamentale Messgrößen, sensitiv auf die Verteilung der Ladung und der Magnetisierung innerhalb des Protons. Die genaue Kenntnis der Formfaktoren, d.h. insbesondere auch des Ladungs- und des magnetischen Radius, sind wichtige Tests für die Theorie im nicht-perturbativen Gebiet der QCD. Die existierenden Daten sind jedoch nicht genau genug für einen belastbaren Test von Theorie-Vorhersagen.

Um die Formfaktoren genauer zu bestimmen, wurden im Rahmen dieser Arbeit mehr als 1400 Wirkungsquerschnitte der Reaktion $H(e,e')p$ am Mainzer Microtron MAMI mit der 3-Spektrometer-Anlage der A1-Kollaboration gemessen. Die Daten wurden in drei Messperioden in den Jahren 2006 und 2007 bei den Strahlenergien 180, 315, 450, 585, 720 und 855 MeV aufgenommen. Sie bedecken den Q^2-Bereich zwischen 0.004 und 1 $(\mathrm{GeV}/c)^2$ mit Zählstatistik-Unsicherheiten unter 0.2% für die Mehrzahl der Datenpunkte. Die relative Luminosität wurde mit einem der Spektrometer als Luminositätsmonitor bestimmt. Der Überlapp der Akzeptanzen der Messungen maximiert die interne Redundanz der Daten und erlaubt zusammen mit einer Reihe von Zusätzen zu dem Standard-Messaufbau eine genaue Kontrolle der systematischen Fehler.
Um die Strahlungsprozesse zu berücksichtigen, wurde ein Ereignisgenerator entwickelt und im Rahmen des Simulationspakets der Analysesoftware implementiert, der ohne Peaking-Näherung die Bethe-Heitler und Born Feynman-Diagramme ereignisweise berechnet.

Um die Formfaktoren zu separieren und um die Radien zu bestimmen, wurden die Daten mit Anpassungen einer breiten Auswahl an Formfaktor-Modellen analysiert. Diese Anpassungen dienten auch zur Bestimmung der absoluten Normierung der verschiedenen Daten-Untergruppen. Die Anwendbarkeit dieser Methode wurde mit ausgiebigen Simulationen getestet. Die Ergebnisse wurden mit einer Extraktion über die Standard-Rosenbluth-Separations-Methode verglichen.

Die in Analysen früherer Daten identifizierte Dellen-Struktur in G_E zeigt sich in diesem neuen Datensatz in anderer Form. Verglichen mit dem Standard-Dipol-Formfaktor zeigt das extrahierte G_E ein starke Änderung der Steigung bei $0.1(\mathrm{GeV}/c)^2$, und in G_M zeigt sich eine Delle bei 0.2 $(\mathrm{GeV}/c)^2$. Dies kann als Anzeichen für eine Pionen-Wolke gesehen werden. Die Daten ergeben im höheren Q^2-Bereich größere Werte für G_M als frühere Messungen, in Übereinstimmung mit Formfaktor-Verhältnissen aus jüngeren präzisen polarisierten Messungen im Q^2-Bereich bis 0.6 $(\mathrm{GeV}/c)^2$.

Der Ladungs- und der magnetische Radius ergeben sich zu

$$\begin{aligned} \langle r_e \rangle &= 0.879 \pm 0.005_{\mathrm{stat.}} \pm 0.004_{\mathrm{syst.}} \pm 0.002_{\mathrm{model}} \pm 0.004_{\mathrm{group}}\ \mathrm{fm}, \\ \langle r_m \rangle &= 0.777 \pm 0.013_{\mathrm{stat.}} \pm 0.009_{\mathrm{syst.}} \pm 0.005_{\mathrm{model}} \pm 0.002_{\mathrm{group}}\ \mathrm{fm}. \end{aligned}$$

Der Ladungsradius, der im Rahmen dieser Arbeit ermittelt wurde, ist deutlich größer als theoretische Vorhersagen und als der Radius des Standard-Dipols, ist aber in Übereinstimmung mit Ergebnissen früherer Messungen am Mainzer Linearbeschleuniger und mit H-Lamb-Shift-Messungen. Der extrahierte magnetische Radius ist kleiner als frühere Bestimmungen und als der des Standard-Dipols.

Contents

1 Introduction

Physics is often driven by the search for fundamental limits. For a long time, the atom was such a limit, perceived as indivisible, an opaque object with no internal structure. The first experimental indications for internal structure inside atoms were found by Rutherford, Geiger and Marsden in 1911 [GM09; Rut11]. Stimulated by the surprising results found in scattering α particles off gold foils, Rutherford developed his model of the atom and shaped the modern view of the atom as a system comprised of an electron hull and a very small nucleus with almost all of the mass.
He also discovered the unique role of the hydrogen nucleus, the proton, when he transmuted nitrogen into oxygen in 1919 [Rut19]. Together with the discovery of the electron by Thomson [Tho97] in 1897 and of the neutron by Chadwick [Cha32] in 1932, three fundamental building blocks were believed to be found.

Dirac developed a formalism to describe pointlike spin-$\frac{1}{2}$-particles in relativistic quantum mechanics. From his equations, it follows that a particle with charge Ze and mass M has a magnetic moment

$$\mu = \frac{g}{2} \cdot \frac{Ze}{M} \cdot \frac{\hbar}{2}. \tag{1.1}$$

$\hbar$ is Plancks constant divided by 2π. The gyromagnetic ratio g has a value of 2. Experiments have shown a deviation of g from 2, this is explained precisely by quantum electrodynamics[1]. For a proton, one defines

$$\tilde{\mu_p} = \mu_p \cdot \mu_K = \frac{g_p}{2} \cdot \mu_K \tag{1.2}$$

where μ_K is the nuclear magnetic moment, i.e. μ calculated from eq. (1.1) for the mass and charge of the proton. Hence, from the Dirac equation, one expects $\mu_p = 1$. However, μ_p was found by Stern et al. [FS33; ES33] to differ significantly from the Dirac prediction, namely (with updated values from [MTN08]) $\mu_p = +2.792847356(23)$. This deviation of μ_p from unity can not be explained by higher order calculations in quantum electrodynamics, but is a direct proof for internal structure of the proton.

Direct access to the internal structure of a system is provided by the measurement of form factors. In unpolarized elastic electron-proton scattering, the electric and magnetic form factors, G_E and G_M, are accessible. In a non-relativistic picture, the form factors are the Fourier transform of the charge

[1] These higher order corrections depend on the fine structure constant α. The experimental value and calculations [KN06] are in such good agreement that, reversing the chain of thought, the measurement of g gives the best value for the fine structure constant α [OHDG06; GHK$^+$07]

and magnetic distribution inside the proton. This strict correspondence is lost in the relativistic case, however, the mathematical identity can be recovered in the Breit frame, where no energy is transferred to the nucleon in the scattering process.

The first measurements were performed by Hofstadter in the 1950s at the High Energy Physics Laboratory (HEPL) at Stanford [HM55; CH56; Hof56]. A dipole form could describe the results for both form factors of the proton and also for the magnetic form factor of the neutron. The choice of this parametrization, which relates to an exponential distribution of the charge, was purely empirical. Nevertheless, it is used until today as a simple approximation to the data, though, since the measurements by Simon et al. in Mainz [SSBW80], it is known that a simple dipole is not sufficient.

From the time of the experiment of Hofstadter up to now, the form factors of the proton and neutron were continuously in the focus of experiments, leading to a wealth of data points, which roughly agreed with the smooth dipole parametrization. In recent years, the interest in the form factors below 1 $(\mathrm{GeV}/c)^2$ was kindled by two findings: a) A possible bump/dip structure in the proton and neutron form factors at low Q^2 as a signature of a pion cloud, and b) the electric radius extracted from Lamb shift measurements which is significantly higher than the radius given by the standard dipole.

a) In 2003, Friedrich and Walcher performed a reanalysis of the world form factor data for the proton and neutron [FW03]. One of their models, which was constructed to describe the data phenomenologically, consisted of two dipole terms and a bump term, which was needed to achieve a good fit. This bump term was found in all four form factors, with very similar positions (see fig. 1.1). While the exact position and shape of this bump or dip depends on the choice of the smooth part of the fit, the existence of such a structure was taken as an indication for a pion cloud, which arises from the picture of the proton as a superposition of a bare proton and a combination of neutron and π^+ (respectively, of a neutron as a superposition of a bare neutron and a combination of proton and π^-).

b) Further interest in the form factors is driven by the atomic physics community. The proton electric radius plays an important role in the interpretation of high precision atomic transition measurements, linking the fields of nuclear and atomic physics. These measurements were pushed to extreme precision (e.g. the 2p-1s energy difference and hyperfine splitting in hydrogen [N^+00; EGS01]), in order to measure fundamental constants and to test QED. Assuming QED to be correct, the difference between measurement and theory was used to determine a radius. The current particle data book [Ams09] quotes $r_E = 0.8768 \pm 0.0069$, the result of the CODATA analysis [MTN08], which essentially determines the radius as a free parameter of a fit of the measured energy levels of hydrogen. This analysis uses the result of the reanalysis of the electron scattering data by Sick [Sic03], $r_E = 0.895\,\mathrm{fm}$, as additional input. Several other determinations of the radius are summarized in table 1.1 and displayed graphically in fig. 1.2.

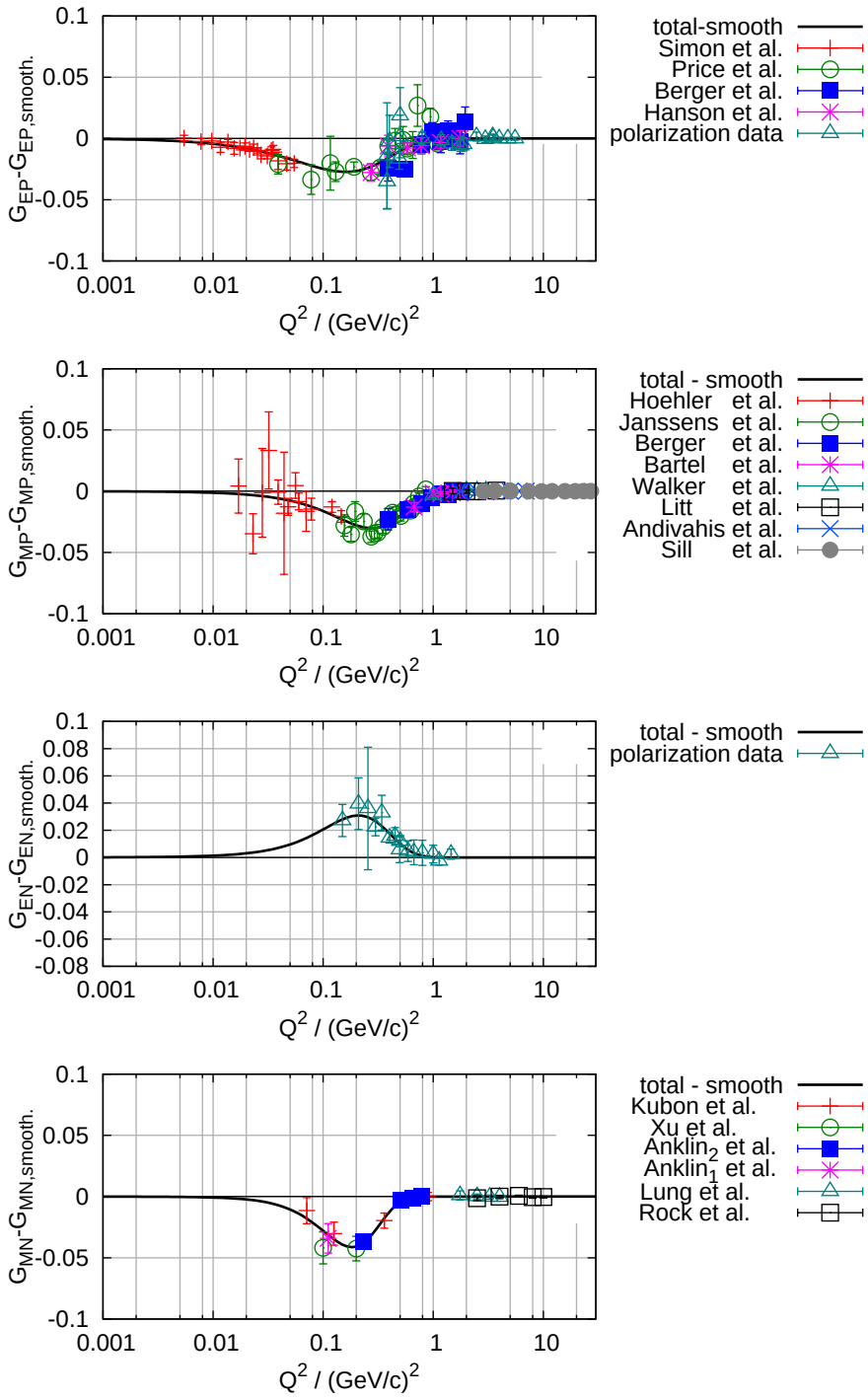

Figure 1.1: The difference of the measured data for the form factors G_E^P, G_M^P, G_E^N, and G_M^N to the smooth part of the phenomenological fit of Friedrich and Walcher. All form factors exhibit a bump/dip structure around 0.2 $(\mathrm{GeV}/c)^2$ (source: [FW03]).

r_E [fm]	Reference	Comment
0.8768±0.0069	Mohr et al. [MTN08]	2006 CODATA value
0.8750±0.0068	Mohr et al. [MT05]	2002 CODATA value
0.883±0.014	Melnikov et al. [Mv00]	1S Lamb Shift in H
0.890±0.014	Udem et al. [U$^+$97; Kar99]	1S Lamb Shift in H
0.897±0.018	Blunden et al. [BS05]	[Sic03] + 2γ corrections
0.895±0.010±0.013	Sick [Sic03]	ep world data reanalysis
0.880±0.015	Rosenfelder et al. [Ros00]	$ep \rightarrow ep$ + Coulomb corr.
0.847±0.008	Mergell et al. [MMD96]	$ep \rightarrow ep$ + disp. relations
0.877±0.024	Wong et al. [Won94]	Mainz data reanalysis
0.830±0.040±0.040	Eschrich et al. [GE$^+$01]	$ep \rightarrow ep$
0.865±0.020	McCord et al. [M$^+$91]	$ep \rightarrow ep$
0.862±0.012	Simon et al. [SSBW80]	$ep \rightarrow ep$
0.880±0.030	Borkowski et al. [BPS$^+$75]	$ep \rightarrow ep$
0.810±0.020	Akimov et al. [A$^+$72]	$ep \rightarrow ep$
0.800±0.025	Frerejacque et al. [FBD66]	$ep \rightarrow ep$ (CH_2 target)
0.805±0.011	Hand et al. [HMW63]	$ep \rightarrow ep$

Table 1.1: Overview of different proton charge-radius results.

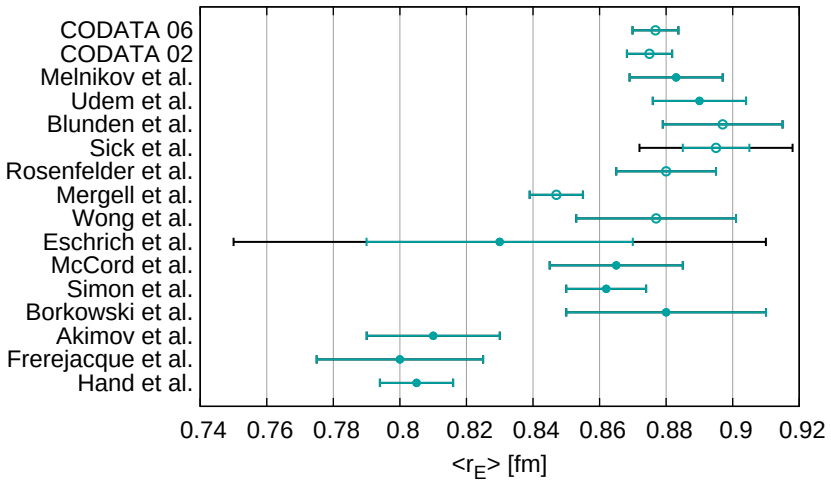

Figure 1.2: Overview of different proton charge-radius results. Filled dots: Results from new measurements. Hollow dots: Reanalyses of existing data.

It has to be noted that a large fraction of the quoted results are reanalyses of either the Mainz data by Simon et al. [SSBW80] or of the world data set. However, the low Q^2/small error data by Simon dominate the fit also in the latter case.
Newer analyses with better theoretical corrections [Ros00; Sic03; BS05] seem to reconcile the Lamb shift results with the result of Simon et al. [SSBW80].

The shortcomings of the existing world data for electron-proton scattering is illustrated in figure 1.3, which displays the ratio of G_E to the standard dipole for the data, the Friedrich-Walcher fit [FW03] and a dispersion theoretical calculation by Belushkin et al. [BHM07]. As can be seen, in the lowest Q^2 region the data by Simon et al. [SSBW80] dominate. The negative slope (which leads to the large radius) can not be reproduced by the theoretical calculation, the same is true for the "jump" or "shoulder" around 0.4 $(\mathrm{GeV}/c)^2$. However, the existence of the "dip" around 0.3 $(\mathrm{GeV}/c)^2$ and the "shoulder" is in fact questionable in the light of the precision of the data. Therefore, a high precision data set is highly desirable which starts at a Q^2 as small as possible (to extract a precise radius) and which covers the complete region of the bump/dip.

The excellent beam of the Mainz accelerator facility and the detector setup available at the A1-collaboration allow such a high precision measurement of the elastic electron-proton cross section in the Q^2 region below 1 $(\mathrm{GeV}/c)^2$. In order to achieve high accuracy, this experiment does not only aim at a statistical accuracy of the order of 0.2% on the single data point, but also at a high redundancy within the total data set. Hence, this program consists of the measurement of more than 1400 cross sections, making use of all three spectrometers of the MAMI facility.
The main method to decompose the cross sections into G_E and G_M will be a kind of super-Rosenbluth-separation by fitting sufficiently flexible model functions for G_E and G_M to the measured cross sections. This procedure makes obsolete the requirement to measure the cross sections with different energies at precisely the same Q^2 values. It also allows for the determination of the normalization directly from the data. The method is similar to to the technique used by Arrington for a reanalysis of the world data [AMT07].
In addition, the standard Rosenbluth technique will be used as a cross check of the super-Rosenbluth result. It also allows us to look for possible non-linearities in the Rosenbluth plots.

In chapter 2, the theoretical foundation of the elastic electron-proton cross section is reviewed and the required theoretical corrections are discussed. These include the radiative corrections, Coulomb distortion corrections and two photon exchange effects.
Chapter 3 describes the facilities available in Mainz. This includes the accelerator MAMI, the 3-spectrometer-facility of the A1-collaboration, the detector system of the spectrometers and the target system. Also, the additions to the standard setup required for this experiment will be discussed.
Details about the extensive measurement program are given in chapter 4.
In chapter 5, the main features of the simulation software for the data analysis are presented. Here, the event generator used for the analysis is explained in

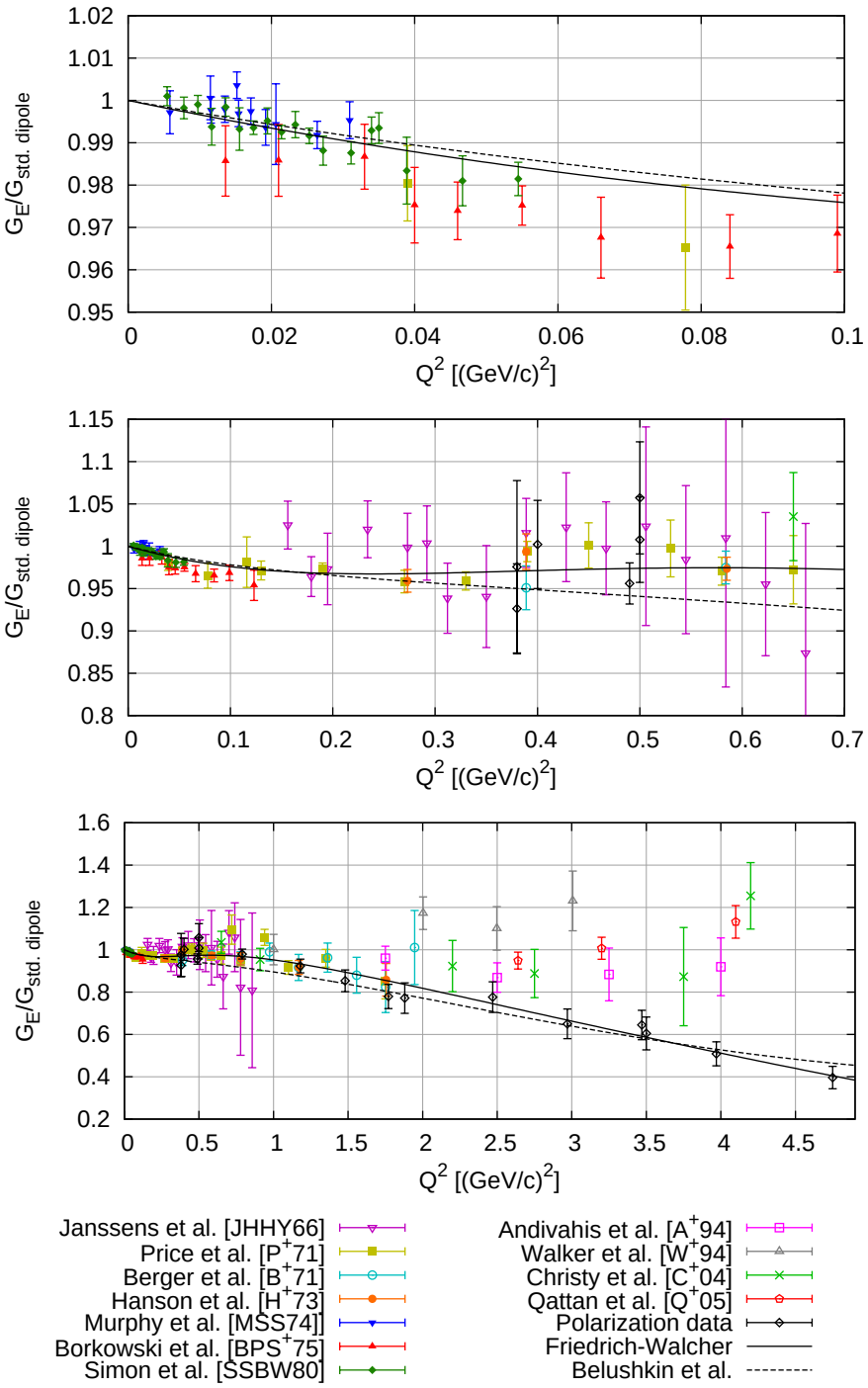

Figure 1.3: World data set of G_E, normalized to the standard dipole. The curves represent the model by Friedrich and Walcher [FW03] (solid), and the calculation by Belushkin et al. [BHM07] (dashed). The slope of the data at low Q^2 is not reproduced by the calculation, as is the shoulder at higher Q^2. The uncertainty of the data in the Q^2 range above 0.3 $(\mathrm{GeV}/c)^2$ is rather large. Therefore, the existence of a dip is only poorly established. Data points labeled "Polarization data" correspond to G_E values given in [FW03] from the polarized measurements [P$^+$01; J$^+$00; G$^+$01; M$^+$98; D$^+$01].

detail. It contains a precise description of the radiative tail to extract the first order cross section from the measurements.
Chapter 6 describes the experimental procedure to extract the cross sections from the measured counting rates. The cuts applied to the data and the matching of experiment and simulation are discussed. The chapter also covers the determination of the luminosity, the normalization using the luminosity monitor and further corrections to the data.
The data are analyzed by fitting models for the form factors, which are described in chapter 7. These models include several flexible polynomial and spline models, dipole models, the Friedrich-Walcher parametrization and the Gari-Krümpelmann model which has a footing in physical considerations.
The result of the fits for the cross sections are presented in chapter 8, which also covers considerations about the model selection and the determination of the statistical errors.
Chapter 9 presents the results for the form factors and for the proton electric and magnetic radius. After a discussion of the statistic and systematic confidence bands, the form factors extracted by the fit of the models and by Rosenbluth separation are presented and compared to previous data. The second part of the chapter describes the extraction of the radius including a discussion of the model dependency.
Chapter 10 summarizes the results of this work and gives an outlook for possible future experiments to extend the covered Q^2 range and to resolve remaining uncertainties.

2 Theoretical foundations

2.1 Cross section of elastic electron-proton scattering[1]

The kinematics of the elastic scattering of an electron on a target at rest is depicted in fig. 2.1.

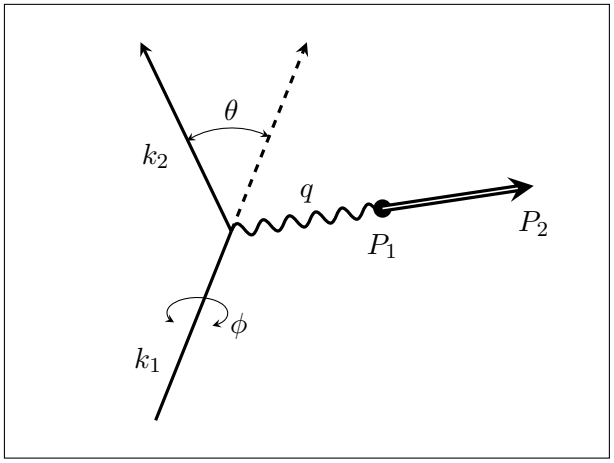

Figure 2.1: The kinematics for the elastic scattering of an electron on a target at rest.

The incident electron has a four-momentum[2] $k_1 = (E_1 = E, \vec{p_1})$. It is scattered in the direction $\Omega = (\theta, \phi)$ with four-momentum $k_2 = (E_2 = E', \vec{p_2})$. In the scattering process, the four-momentum $q = k_1 - k_2$ is transferred to the target via the exchange of a virtual photon. The target of mass M is initially at rest, $P_1 = (M, \vec{0})$.
The unpolarized cross section is independent of the azimuthal scattering angle ϕ. Therefore, it has two degrees of freedom, e.g. the energy of the incoming electron E and the scattering angle θ. The virtual photon in the scattering process has a negative four-momentum squared, it is space like. Therefore, the negative of q^2

$$Q^2 = -q^2 = 4EE' \sin^2 \frac{\theta}{2} > 0 \tag{2.1}$$

[1] For a more detailed treatment of this subject, refer to [DG89].
[2] Units are such that $\hbar = 1$, $c = 1$.

is used for convenience. The photon has the polarization

$$\varepsilon = \left(1 + 2\left(1+\tau\right)\tan^2\frac{\theta}{2}\right)^{-1}. \tag{2.2}$$

The transition currents of the electron, j^μ, and of the target, J^μ, are

$$\begin{aligned} j^\mu &= -e\bar{u}_{k_2}\gamma^\mu u_{k_1} \\ J^\mu &= e\bar{u}_{P_2}\Gamma^\mu u_{P_1}, \end{aligned} \tag{2.3}$$

where $u = (\sqrt{E+M}, \vec{\sigma}\cdot\vec{p}/\sqrt{E+M})^T\chi$. Here, $\vec{\sigma}$ are the Pauli matrices, and χ is a spinor. In terms of these currents, the Born invariant transition amplitude is given as

$$\mathcal{M} = j_\mu \frac{g^{\mu\nu}}{q^2} J^\nu = j_\mu \frac{1}{q^2} J^\mu. \tag{2.4}$$

For a target with internal structure like the proton, the vertex has to be parametrized by introducing appropriate form factors Γ_i. Since there are three independent Lorentz vectors, P_1^μ, P_2^μ, and γ^μ, the most general form is

$$\Gamma^\mu = P_1^\mu\Gamma_1 + P_2^\mu\Gamma_2 + \gamma^\mu\Gamma_3. \tag{2.5}$$

In the case of a free on-shell particle, the form factors Γ_i depend on Q^2 only. Because u_{P_1} and $\bar{u}_{P_2}$ satisfy the free Dirac equation, one obtains from current conservation, i.e. from

$$q_\mu \bar{u}_{P_2}\Gamma^\mu u_{P_1} = 0, \tag{2.6}$$

that $\Gamma_1 = \Gamma_2$. Using the Gordon decomposition and with the proton mass m_p and the anomalous part of the magnetic moment (in units of μ_K), $\kappa = \mu_p - 1$, Γ^μ can be rewritten as

$$\Gamma^\mu = \gamma^\mu F_1\left(Q^2\right) + i\sigma^{\mu\nu}q_\nu\frac{\kappa}{2m_p}F_2\left(Q^2\right). \tag{2.7}$$

Here, the Dirac and Pauli form factors are used. They are preferred in Vector Meson Dominance (VMD) models and in perturbative quantum chromodynamics (pQCD). Using these definitions, the unpolarized cross section for the elastic scattering of an electron on a proton with internal structure is given in the one-photon approximation as

$$\left(\frac{\mathrm{d}\sigma}{\mathrm{d}\Omega}\right)_0 = \left(\frac{\mathrm{d}\sigma}{\mathrm{d}\Omega}\right)_{\mathrm{Mott}}\left[\left(F_1^2 + \tau\left(\kappa F_2\right)^2\right) + 2\tau\left(F_1 + \kappa F_2\right)^2\tan^2\frac{\theta}{2}\right], \tag{2.8}$$

with the dimensionless quantity $\tau = Q^2/(4m_p^2)$ and where

$$\left(\frac{\mathrm{d}\sigma}{\mathrm{d}\Omega}\right)_{\mathrm{Mott}} = \frac{4Z^2\alpha^2E'^2}{Q^4}\frac{E'}{E}\left(1 - \beta^2\sin^2\left(\frac{\theta}{2}\right)\right) \tag{2.9}$$

is the recoil-corrected Mott cross section[3], which is the cross section for the scattering of a spin-$\frac{1}{2}$-particle on a scalar point-like target. The relations

$$\begin{aligned} G_E &= F1 - \tau\kappa F2, \\ G_M &= F1 + \kappa F2 \end{aligned} \tag{2.10}$$

translate the Dirac and Pauli form factors into the Sachs form factors. They were first proposed by Yennie et al. [YLR57]. Sachs et al. [ESW60; Sac62] conjectured that this choice might prove more physically meaningful than F_1 and F_2.

In the Breit frame, defined as $P_1^B + P_2^B = (2E_B, \vec{0})$, the transition current reduces to

$$J_B = e\chi_{p_2}^T \left(2M \cdot G_E, i\vec{\sigma} \times \vec{q} G_M\right) \chi_{p_1}. \tag{2.11}$$

In this frame, G_E and G_M are regarded as the Fourier transform of the spatial charge and magnetization distribution.

With the Sachs form factors, the cross section is given by

$$\begin{aligned} \left(\frac{\mathrm{d}\sigma}{\mathrm{d}\Omega}\right)_0 &= \left(\frac{\mathrm{d}\sigma}{\mathrm{d}\Omega}\right)_{\mathrm{Mott}} \left[\frac{G_E^2\left(Q^2\right) + \tau G_M^2\left(Q^2\right)}{1+\tau} + 2\tau G_M^2\left(Q^2\right) \tan^2\frac{\theta}{2}\right] \\ &= \left(\frac{\mathrm{d}\sigma}{\mathrm{d}\Omega}\right)_{\mathrm{Mott}} \frac{\varepsilon G_E^2 + \tau G_M^2}{\varepsilon\left(1+\tau\right)}. \end{aligned} \tag{2.12}$$

The choice of the Sachs form factors eliminates the mixed term in the cross sections, which now depends on the squares of G_E and G_M only.

In the static limit $Q^2 = 0$, the form factors normalize to the charge and magnetic moment of the proton in units of the electron charge and of the nuclear magneton μ_K, $G_E(0) = 1$ and $G_M(0) = \mu_p$.
The standard method to extract the form factors from measured cross sections is the Rosenbluth separation [Ros50]. It exploits the linear structure in ε of eq. (2.12) by disentangling the form factors at fixed Q^2 values from several measurements at different ε values (see subsection 9.2.2). The advances in computer power over the last decades open the possibility for an alternative method, namely, a multi-parameter fit of form factor models directly to the cross section data.

2.2 Radiative corrections

Nature does not allow us to measure the lowest order cross section directly since higher orders, as depicted as Feynman graphs in fig. 2.2, always contribute to the scattering process. It is common practice to divide these contributions into groups with an additional virtual (v1-v5 in fig. 2.2) or real photon (r1-r4). However, this grouping is problematic: Divergences in one group cancel against

[3] At the energy scales of this experiment, β is very close to unity. Hence, the approximation of the term $(1-\beta^2\sin(\theta/2))$ in eq. (2.9) with $\cos^2(\theta/2)$ is valid with an error below 0.002%.

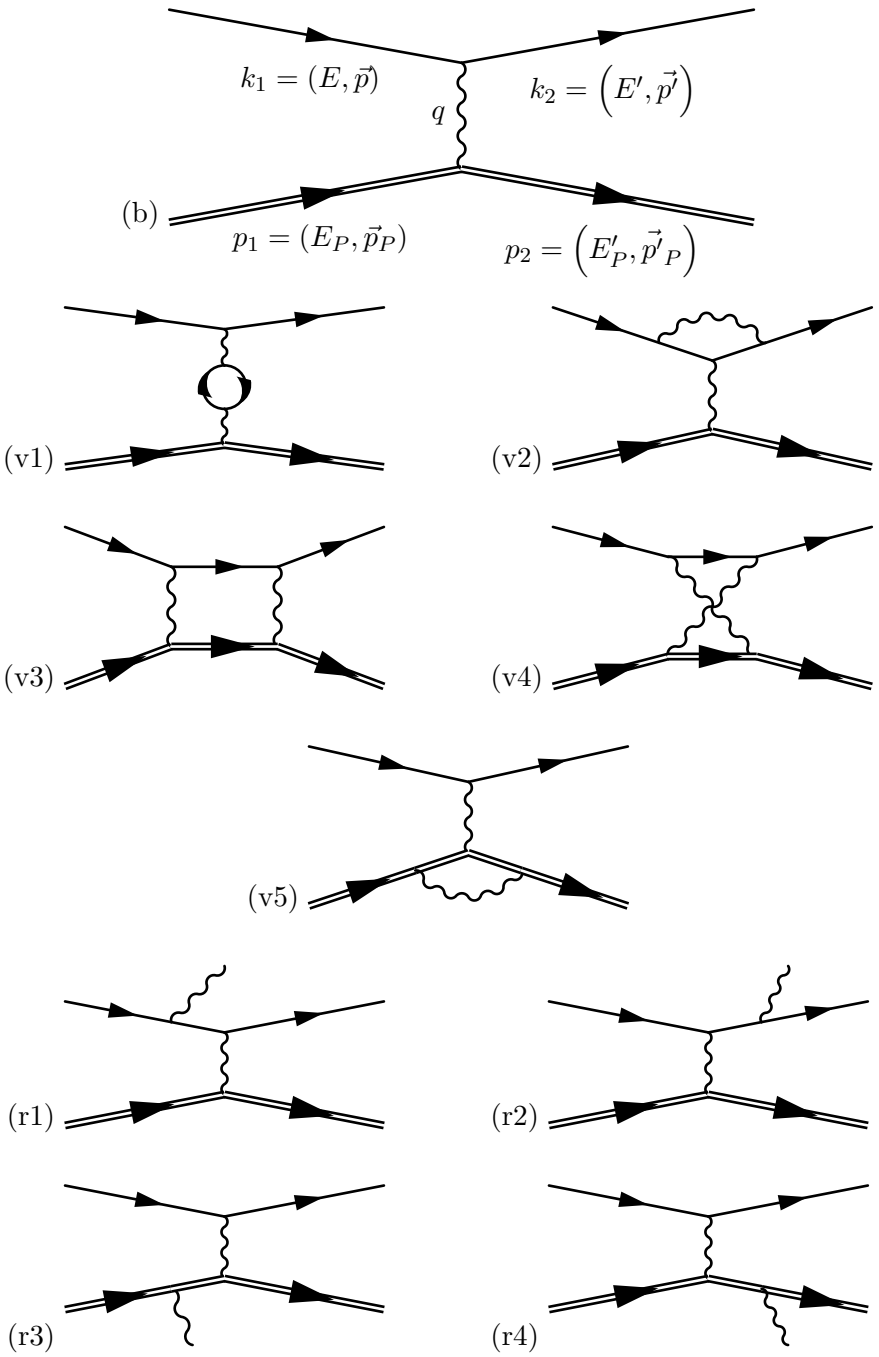

Figure 2.2: Feynman graphs of leading and next to leading order for elastic scattering. (b) leading order, (v1-v5) next to leading order with an additional virtual photon, (r1-r4) leading order graphs with a radiated real photon.

divergences in the other group, hence all graphs have to be evaluated at once. This leads to an "internal"[4] correction to the leading order process

$$\left(\frac{\mathrm{d}\sigma}{\mathrm{d}\Omega}\right)_1 = \left(\frac{\mathrm{d}\sigma}{\mathrm{d}\Omega}\right)_0 (1+\delta)\,. \tag{2.13}$$

Here, $\left(\frac{\mathrm{d}\sigma}{\mathrm{d}\Omega}\right)_0$ is the cross section for one photon exchange alone (graph (b) in fig. 2.2) as given by eq. (2.12), while $\left(\frac{\mathrm{d}\sigma}{\mathrm{d}\Omega}\right)_1$ is the cross section when next to leading order contributions are taken into account (graphs v1-v5 and r1-r4 in fig. 2.2).
Vice versa, the non-radiative cross section $\left(\frac{\mathrm{d}\sigma}{\mathrm{d}\Omega}\right)_0$ can be determined in a first order approximation by identifying the experimental cross section with $\left(\frac{\mathrm{d}\sigma}{\mathrm{d}\Omega}\right)_1$ and dividing it by $(1+\delta)$.

The integrals over the internal four-momenta of the graphs v1,v2 and v5 are logarithmically divergent for large momenta. This can be treated theoretically by charge and mass renormalization. Details can be found in [MT00; V$^+$00].
Graph v2 leads to an infrared divergence, but it can be shown [BN37; JR54] that this cancels with corresponding divergences of the graphs r1-r4.

Results

In the following, the formulae for the contributions from different groups of graphs will be presented. For details of the calculation, see [MT00; V$^+$00].
The vacuum polarization (v1) gives rise to a term

$$\delta_{vac} = \frac{\alpha}{\pi}\frac{2}{3}\left\{\left(v^2-\frac{8}{3}\right)+v\frac{3-v^2}{2}\ln\left(\frac{v+1}{v-1}\right)\right\}, \tag{2.14}$$

$$\overset{Q^2\gg m_l^2}{\longrightarrow} \frac{\alpha}{\pi}\frac{2}{3}\left\{-\frac{5}{3}+\ln\left(\frac{Q^2}{m^2}\right)\right\}, \tag{2.15}$$

with $v^2 = 1+\frac{4m_l^2}{Q^2}$, where m_l is the mass of the particle in the loop. The approximation (2.15) is valid for loop-electrons. However, at the energy scales of this experiment and within the envisaged accuracy, the vacuum polarization via muon and tau loops has to be accounted for and must be evaluated with eq. (2.14).
The finite part of the electron vertex correction (v2, the infinite part cancels later on) is given in the ultra-relativistic limit by

$$\delta_{vertex} = \frac{\alpha}{\pi}\left\{\frac{3}{2}\ln\left(\frac{Q^2}{m^2}\right)-2-\frac{1}{2}\ln^2\left(\frac{Q^2}{m^2}\right)+\frac{\pi^2}{6}\right\}. \tag{2.16}$$

In the same limit, the contribution from real photon emission by the electron (r1, r2) yields:

$$\delta_R = \frac{\alpha}{\pi}\left\{\ln\left(\frac{(\Delta E_s)^2}{E\cdot E'_{el}}\right)\left[\left(\frac{Q^2}{m^2}\right)-1\right] -\frac{1}{2}\ln^2\eta+\frac{1}{2}\ln^2\left(\frac{Q^2}{m^2}\right)-\frac{\pi^2}{3}+\mathrm{Sp}\left(\cos^2\frac{\theta_e}{2}\right)\right\}, \tag{2.17}$$

[4] To distinguish from "external" corrections like bremsstrahlung in the target.

where $\eta = E/E'_{el}$, $\Delta E_s = \eta \cdot \Delta E'$. E'_{el} is the energy of an electron scattered elastically through an angle θ when no photon is emitted. An electron which radiates a photon has a lower energy than E'_{el}. $\Delta E'$ is the maximum difference to E'_{el} allowed by the radiative tail cut-off; it is called the cut-off energy. Details about the Spence function $\mathrm{Sp}(x)$ can be found in appendix B of [Fri00].

The contributions from the proton side (v3, v4, r3, r4) are complicated and an exact calculation requires the knowledge of the internal structure of the proton. Maximon and Tjon [MT00] divide the correction in three parts, one proportional to Z (δ_1), one to Z^2 (δ_2) and a third part in which they include all of the structure dependence ($\delta_{el}^{(1)}$). The last part is believed to be small for the kinematics of this work and is therefore neglected. The other two correction terms[5] are given by

$$\begin{aligned}
\delta_1 &= \frac{2\alpha}{\pi}\left\{\ln\left(\frac{4\left(\Delta E_s\right)^2}{Q^2 x}\right)\ln\eta + \mathrm{Sp}\left(1-\frac{\eta}{x}\right) - \mathrm{Sp}\left(1-\frac{1}{\eta x}\right)\right\}, \\
\delta_2 &= \frac{\alpha}{\pi}\left\{\ln\left(\frac{4\left(\Delta E_s\right)^2}{m_p^2}\right)\left(\frac{E'_P}{\left|\vec{p'}_P\right|}\ln x - 1\right) + 1\right. \qquad (2.18) \\
&\quad + \frac{E'_P}{\left|\vec{p'}_P\right|}\left(-\frac{1}{2}\ln^2 x - \ln x \ln\left(\frac{\rho^2}{m_P^2}\right) + \ln x\right. \\
&\quad \left.\left. -\mathrm{Sp}\left(1-\frac{1}{x^2}\right) + 2\mathrm{Sp}\left(-\frac{1}{x}\right) + \frac{\pi^2}{6}\right)\right\}, \qquad (2.19)
\end{aligned}$$

with

$$x = \frac{(Q+\rho)^2}{4m_P^2}, \qquad \rho^2 = Q^2 + 4m_P^2. \qquad (2.20)$$

For vanishing cut-off energies $\Delta E'$, the corrections δ_R, δ_1 and δ_2 get infinitely large. In this case, however, more photons than just one are emitted in each scattering event. It has been shown in [BN37; YFS61] that this can be approximately taken into account by exponentiation of the corresponding correction terms as well as for the vertex correction. For the vacuum polarization contribution, Vanderhaeghen et al. [V$^+$00] iterate the first order contribution to all orders, which does not lead to an exponentiation. In total, they find

$$\left(\frac{\mathrm{d}\sigma}{\mathrm{d}\Omega}\right)_{exp} = \left(\frac{\mathrm{d}\sigma}{\mathrm{d}\Omega}\right)_0 \frac{e^{\delta_{vertex}+\delta_R+Z\delta_1+Z^2\delta_2}}{\left(1-\delta_{vac}/2\right)^2}, \qquad (2.21)$$

which, for the kinematics used in the present work, is marginally different (below 0.05%) from the fully exponentiated form, which will therefore be used in the analysis of the measured cross sections[6]:

$$\left(\frac{\mathrm{d}\sigma}{\mathrm{d}\Omega}\right)_{exp}\left(\Delta E'\right) = \left(\frac{\mathrm{d}\sigma}{\mathrm{d}\Omega}\right)_0 e^{\delta_{vac}+\delta_{vertex}+[\delta_R+\delta_1+\delta_2](\Delta E')}. \qquad (2.22)$$

[5] The Z-dependence is divided out.

[6] Here, Z has been set to 1.

It will be described in subsection 5.2.1 how these higher-order contributions are accounted for in the determination of the first-order cross section from the measured data.

2.3 Coulomb distortion and two photon exchange

The Coulomb distortion, i.e. the scattering process via the exchange of many soft photons, and the related two photon exchange, where both photons have a sizable momentum, is not fully included in the radiative corrections. There is yet some theoretical uncertainty in the modeling of these two effects. For the two photon effect, the off-shell nucleon and its exited states have to be modeled. For a discussion of the Coulomb distortion, see [Fri00]. A complete treatment of these effects could not be the topic of this thesis.
Nevertheless, the Coulomb distortion can not be ignored completely, especially for the determination of the radius, as has been shown by Rosenfelder [Ros00]. He finds that the extracted radius is enlarged by about 0.018 fm when Coulomb distortion is accounted for. It has been found in [Fri00] that the correction by Rosenfelder is in agreement with the simple additional correction-factor $(1+\delta)$ given in a footnote by Tsai (see [Tsa61], footnote 22 and references therein):

$$\delta = Z\alpha\pi \frac{\sin\frac{\theta}{2} - \sin^2\frac{\theta}{2}}{\cos^2\frac{\theta}{2}}. \tag{2.23}$$

This correction has been applied to the measured cross sections and lowers them by at most 1.2% at 180°.

The two photon exchange (TPE) becomes more important at larger Q^2 and may explain part of the difference between polarized and unpolarized measurements at large Q^2 [GV03]. Therefore, a lot of theoretical work focuses on the energy scales above 1 GeV. In 2007, Arrington et al. [AMT07] have reanalyzed the world data set with a model for two photon exchange corrections and made two fits, one with the corrections applied and one without. The ratio of these fits will be used as an estimate of the two photon effect on the form factor ratio in the Q^2 region of this experiment. With this correction, it is possible to compare the form factor ratio with previous polarized measurements, where the contribution of TPE on the result is believed to be small.

2.4 Proton radius

The electric and magnetic root mean square radii of the proton are related to the low-Q^2 behavior of the form factors as can be seen by expanding the form factors in terms of Q^2,

$$G\left(Q^2\right)/G\left(0\right) = 1 - \frac{1}{6}\left\langle r^2\right\rangle Q^2 + \frac{1}{120}\left\langle r^4\right\rangle Q^4 - \ldots, \tag{2.24}$$

hence

$$\left\langle r^2 \right\rangle = -\frac{6}{G\left(0\right)} \left. \frac{\mathrm{d}G\left(Q^2\right)}{\mathrm{d}Q^2} \right|_{Q^2=0} . \tag{2.25}$$

Therefore, the radius can be determined from the slope of the form factors at Q^2=0.

3 Accelerator and Experimental setup

In this chapter, an overview of the accelerator and detector facilities used in the experiment will be given. Important aspects regarding the drift chambers, pA-meter and angle setup will be discussed in detail in later chapters.

3.1 Accelerator

MAMI, the Mainz Microtron [HFK+76; Jan06; K+08], is a normal conducting continuous wave electron accelerator. It consists of a cascade of three race track microtrons (RTMs) and a fourth stage, a harmonic double sided microtron (HDSM). A schematic floor plan is depicted in figure 3.1.

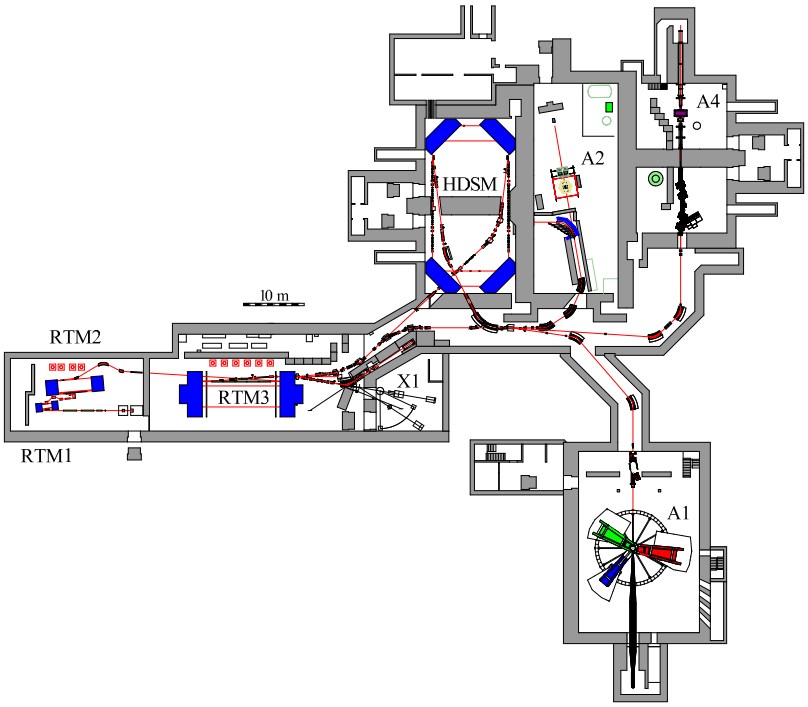

Figure 3.1: Overview of the MAMI facilities with the accelerator stages and experimental halls. The A1 hall with the 3-spectrometer facility is situated in the lower right. From [K+08].

The accelerator is equipped with two electron sources: A thermionic source, which can provide currents in excess of 100 μA, and a polarized source that

makes use of the photoelectric effect on a GaAs crystal using polarized light.
A linear accelerator injects the electrons with 3.97 MeV into the first RTM. Each of the three RTMs contains a normal conducting accelerator segment and two large high precision conventional magnets which recirculate the beam back into the accelerator segment. In the first RTM, the beam is recirculated 18 times, raising the electron energy to 14.86 MeV. The second RTM boosts this to 180 MeV in 51 turns.
The beam may now bypass the rest of the accelerator and may be directed to the different experimental sites. Alternatively, it can enter RTM 3, which can boost the energy up to 855 MeV in 90 turns. Every other recirculation path can be instrumented with a kicker magnet which deflects the beam to the exit beam line system. Thus, the energy can be selected in 15 MeV steps.
The beam may then be injected into the fourth stage. The design of this HDSM stage is comprised of two anti-parallel accelerator segments, one of which is operated at the doubled frequency to suppress instabilities. The beam is recirculated by four magnets. The HDSM stage raises the energy up to 1.6 GeV in 43 recirculations.
The root mean square energy spread is 30 keV at 855 MeV and 110 keV at 1.5 GeV. For the measurements described in this work, an unpolarized beam with beam energies of 180, 315, 450, 585, 720 and 855 MeV was used.

3.2 3-spectrometer facility

The detector setup of the A1-collaboration at MAMI is called the 3-spectrometer-facility[1]. The three high resolution magnetic spectrometers, labeled A, B and C, can be operated in single, double or triple coincidence mode. A photograph of the experimental hall with the spectrometers is depicted in figure 3.2, a detailed description can be found in [B$^+$98]. The spectrometers can be rotated around a central pivot to measure at different scattering angles. In the course of this work, the control system was extended to remote setting of the spectrometer angles from the counting room (see appendix A). This was indispensable for the large number of angle changes (more than 400) planned in this work.

3.2.1 Magnetic system

The magnetic system of spectrometer A and C is comprised of a quadrupole, a sextupole, and two dipoles. This system enables the high resolution measurement of particle momentum and angle inside a relatively large acceptance (up to 28 msr). Spectrometer B consists of only a single dipole in a clamshell configuration, leading to a slim design with higher spatial resolution but smaller acceptance (5.6 msr); for out-of-plane measurements, spectrometer B can be tilted, but this was not needed in this experiment. The main features of the

[1] A misleading name: Several additional permanent [Ach04] or temporary spectrometers are available.

Figure 3.2: The A1 hall. The three big spectrometers A (red, left), B (blue, middle), C (green, right) are visible. The short orbit spectrometer SOS is positioned in front of the target, in the middle of the picture. The thin upstream beam-line pipe comes in from the right. As a dimension scale: A person is slightly taller than the concrete block on the lower left edge.

	Spec. A	Spec. B	Spec. C
Configuration	QSDD	Clamshell D	QSDD
Maximum momentum (MeV/c)	735	870	551
Reference momentum (MeV/c)	630	810	459
Central momentum (MeV/c)	665	810	490
Maximum solid angle (msr)	28	5.6	28
Momentum acceptance	20%	15%	25%
Momentum resolution	10^{-4}	10^{-4}	10^{-4}
Angular resolution at target [mrad]	< 3	< 3	< 3
Position resolution at target [mm]	3-5	1	3-5
Length of central path [m]	10.75	12.03	8.53

Table 3.1: Main parameters of the spectrometers A, B, and C.

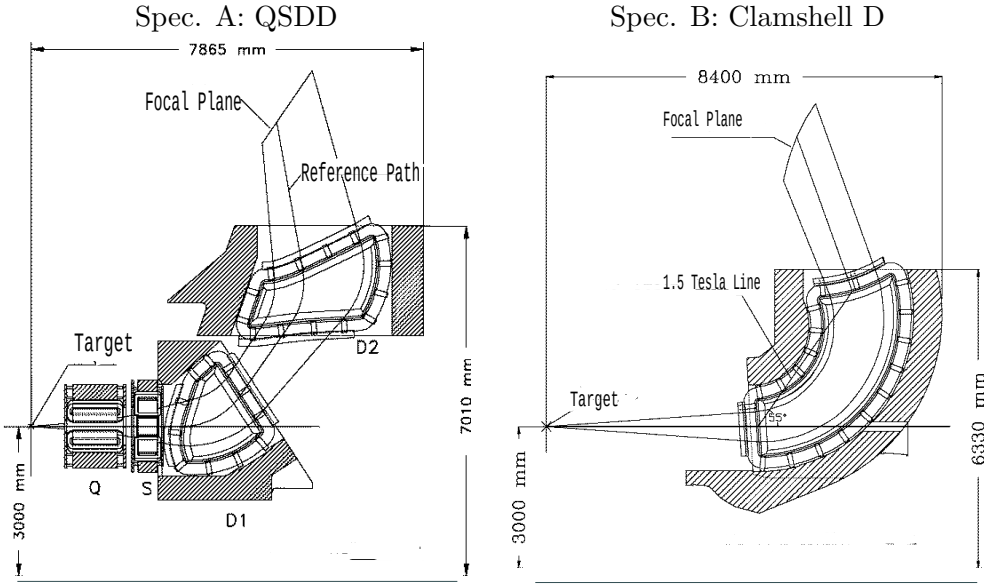

Figure 3.3: Dimensions and magnet arrangement of spectrometer A and B. Spectrometer C is a scaled-down version of spectrometer A. Modified version, original from [Sch94].

spectrometers are summarized in table 3.1; figure 3.3 shows the dimensions and magnet arrangements for spectrometers A and B.

3.2.2 Detector system

Each of the three spectrometers is equipped with similar detector systems consisting of two scintillator planes, two packets of two vertical drift chamber layers (VDC) and a gas-Čerenkov detector. The scintillators are used for triggering, particle identification and for a time reference. The drift chambers are used

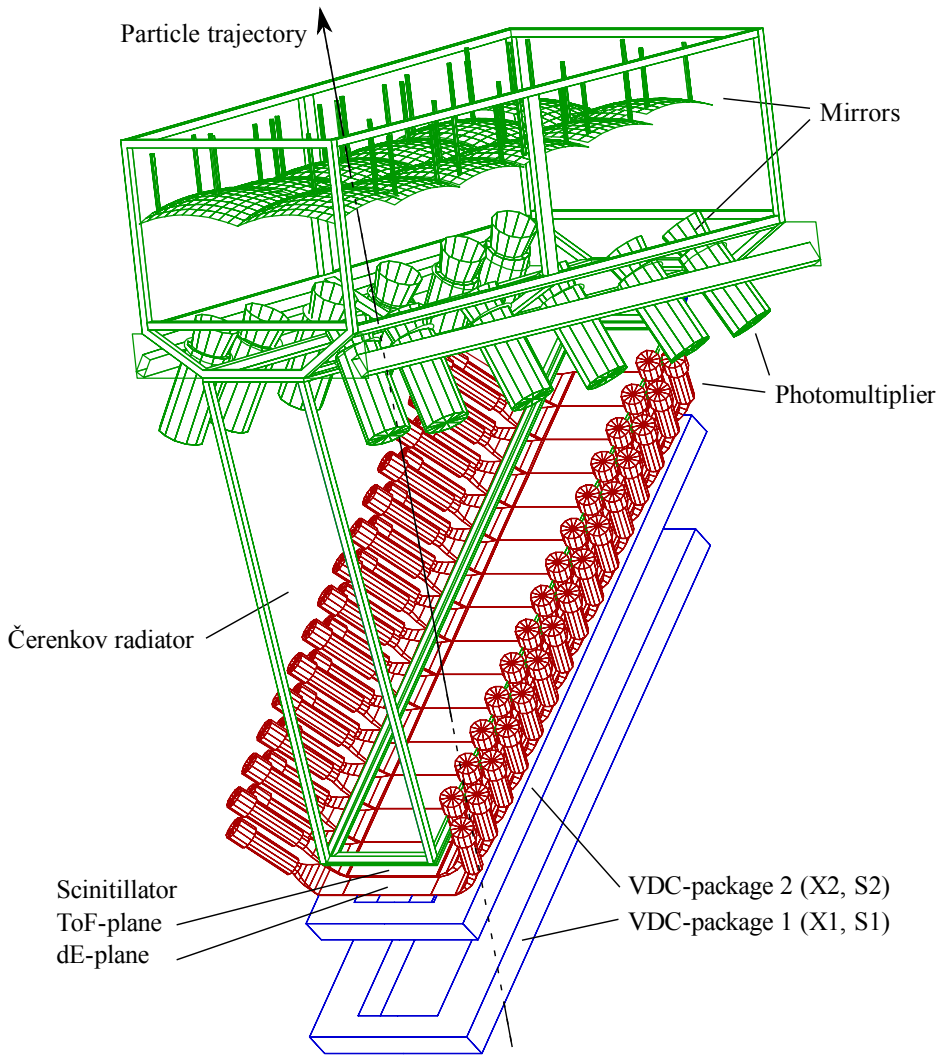

Figure 3.4: Drawing of the detector package of the three spectrometers. A particle first passes the four VDCs (blue), then two layers of scintillators (red) and a Čerenkov detector (green). Modified version, original from [B+98].

for the reconstruction of the particle trajectory. The Čerenkov detector distinguishes between pions (and heavier particles) and electrons. Figure 3.4 shows a drawing of the detector package.

Scintillators

The two scintillator planes are segmented (15 segments for A and C, 14 for B). The segmentation improves time resolution and allows for a rough position estimation of the particle track. The first plane (dE-Plane) is 3 mm thick, the second plane (ToF-plane) 1 cm. Normally, a coincidence between dE and ToF-plane is demanded for a trigger signal, with the ToF-plane providing the

timing. For efficiency measurements and for measurements with low momentum protons or deuterons, the logic can be switched to dE or ToF only. The different energy deposition in the two layers makes it possible to separate heavier from minimum ionizing particles. The timing information is used for the coincidence logic between the spectrometers and as a common stop signal for the Time-to-Digital converters of the VDCs.

Vertical drift chambers

The vertical drift chambers are used for the reconstruction of the particle trajectory inside the detector system. The spatial resolution is better than 200 μm (FWHM) in the dispersive and 400 μm in the non-dispersive direction. A detailed description is given in subsection 6.2.2. Continuing the efforts started in [Ber04], in preparation for this experiment the VDC system of A and B was refurbished (see appendix E).

Čerenkov detector

The Čerenkov detector is realized as a gas detector. The detector volume is filled with Decafluorobutane, R 3-1-10, in which passing electrons or positrons with energies larger than 10 MeV produce Čerenkov light. A mirror system reflects these photons to an array of photomultipliers. Pions with less than 2.7 GeV do not produce Čerenkov light. Therefore, the Čerenkov detector discriminates between electrons and heavier particles.
In spectrometer A, the Čerenkov detector can be replaced with a focal plane polarimeter. Details can be found in [P$^+$02; Pos00].

3.3 Target system

The target system is enclosed in a vacuum scattering chamber located on the rotation axis of the spectrometers. A target ladder holds several interchangeable solid state materials like graphite, polyethylene, HAVAR foil, copper etc. of varying thicknesses. Additionally, a luminescent screen (an Al_2O_3 plate with a cross hair printed on) is mounted. It is used for beam position calibration. The target ladder has a vertical translation degree of freedom that is actuated by an electric motor to select the target material.
The normal lid of the barrel-shaped scattering chamber can be exchanged for two different target constructions: A high-pressure gas target and a cryogenic target. Figure 3.5 shows the latter, which was filled with hydrogen as a proton target for this experiment.

The cryogenic target system is comprised of two loops. An inner loop ("Basel-loop") is filled with the target gas, which is liquefied before the beginning of the beam time. The completely liquefied material is continuously recirculated by a fan. The loop contains an interchangeable target cell; two types were used in this experiment: A long, cigar shaped cell (see figure 3.5) and a round cell with a diameter of 2 cm. A heat exchanger couples the inner loop to the

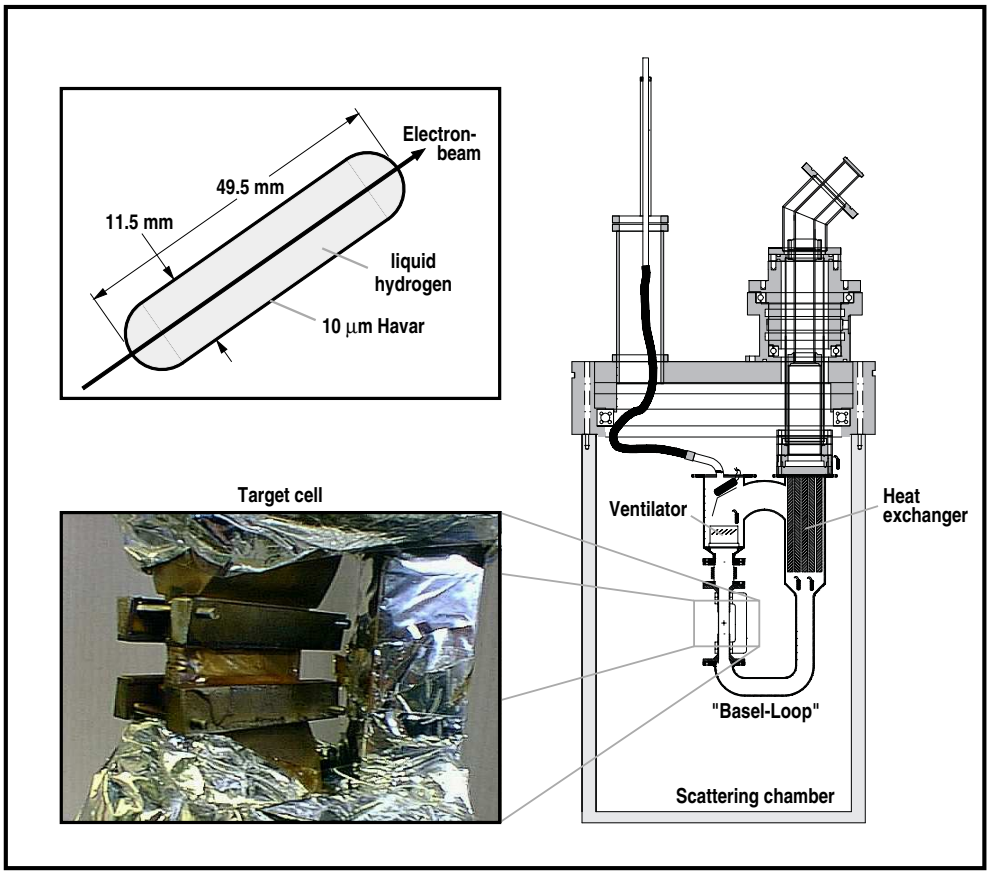

Figure 3.5: Top left: Schematics of the "long" target cell. Lower left: Photo of the installed cell. Right: Schematics of the target setup installed in the scattering chamber. Figure from [Pos00].

outer loop, which is coupled to a Philips compressor. The outer loop is also filled with hydrogen and works like a heat pipe: Hydrogen is liquefied at the Philips compressor. It flows down to the target, cooling down the target heat exchanger. The warmed up hydrogen then evaporates and returns to the Philips compressor.
The hydrogen inside the inner loop is subcooled to ensure that the beam load does not substantially change the density of the hydrogen by local heating above the boiling point. Nevertheless, for higher currents the beam is rastered in the transverse directions to reduce the effective power density.

3.4 Additions to the standard experimental setup

3.4.1 pA-meter

In the normal setup, the beam current is measured with a Förster probe located in a part of RTM 3 where all recirculations of the beam pass through.

Accordingly, the accuracy of the measurement is best with the highest number of recirculations, i.e. for a beam energy of 855 MeV. For 180 MeV, the beam does not pass the probe at all.
For measurements at small energies and currents, a pA-Meter was installed at the collimator called INT0KOLLI12, right before the linear accelerator segment. When the beam is deflected on the collimator, a beam induced current can be measured. When the deflection magnet is switched off, i.e. when the beam passes through the collimator and is injected into the accelerator, some of the beam current is still lost at the collimator. This offset has to be subtracted from the measured value when the beam is deflected to be fully absorbed by the collimator. The true beam current is a function of the difference of these two measurements. At the position of the collimator, the beam has an energy of 100.15 keV and is already chopped and bunched, so that the complete phase space is accepted by the rest of the accelerator. Though this current measurement is in such an early stage of the accelerator, the current at this position is essentially the same as in the experimental hall: Any significant beam loss would increase the radiation levels in the accelerator hall, which are carefully monitored; any excess in radiation would automatically shut off the accelerator.

3.4.2 Beam position stabilization

In [Ber04], it was shown that a shift of the beam position on the target results in a drift of the measured cross section. The beam is normally stabilized by the circulation in RTM 3, which dampens beam position changes introduced in the earlier stages of the accelerator. This self-stabilization is less effective with lower recirculation number, i.e. lower energies and is absent in the case of an incident beam energy of 180 MeV when the beam bypasses RTM 3. To eliminate beam position drifts, a beam-position control system has been installed by the MAMI group [Deh10]: The beam position is measured with two cavities in front of the target. Their signal is digitized and a correction current for the beam steering dipoles in the beam line is generated. The cavities need high beam currents for adequate sensitivity. Therefore, the beam has to be switched to a diagnostic mode where the beam is modulated as a train of high current pulses with a very low duty cycle. These periods have to be excluded from the cross section measurements. During the data taking, the A1 computer system periodically disables the data acquisition and generates a signal to the MAMI control system to start the adjustment process. When the correction has been performed, MAMI signals back to the A1 system and data acquisition is resumed. The analysis tool chain has been modified to account for these pauses in the data acquisition.
The system was installed in the beginning of the second measurement period and was used for all later measurements. After the installation of the system, there was no beam position drift detectable.

4 Measuring program

At a given four-momentum-transfer squared,

$$Q^2 = 4EE' \sin^2 \frac{\theta}{2}, \tag{4.1}$$

the relative contributions of G_E and G_M to the cross sections depend on the polarization of the virtual photon

$$\varepsilon = \left(1 + 2\,(1+\tau) \tan^2 \frac{\theta}{2}\right)^{-1}. \tag{4.2}$$

To disentangle the form factors from the measured cross sections using the traditional Rosenbluth technique, it is mandatory to measure at different ε for a given Q^2 value. While this constraint does not have to be fulfilled strictly when employing a global fit, the range and number of different ε values in a given Q^2 range determine the accuracy of the separation.
Figure 4.1 displays the region in the ε-Q^2-plane accessible by the accelerator and detector setup in the planned measurements[1]. The colored areas are excluded because of the various experimental limitations (see figure description).

To vary ε at constant Q^2, both the scattering angle and the incident beam energy have to be changed. A beam energy change takes about six hours with the Mainz setup, which is quick in comparison to other accelerator facilities but still costly to be done a large number of times. Thus, the measuring program was organized to minimize beam-energy changes. Since the energy gain in RTM 1 and RTM 2 is fixed, the minimum beam energy of MAMI is achieved when the beam passes RTM 3 without further acceleration, resulting in a 180 MeV beam. The beam time allocation permitted to measure at six energies, spread out evenly between 180 MeV and 855 MeV in 135 MeV steps. In this experiment, no use was made yet of the 1.5 GeV stage of MAMI[2].

At each beam energy, the measured angle range was maximized. The geometric designs of target and spectrometers allow each spectrometer to cover different, but overlapping angular ranges. To maximize the angular range covered by the data set and the internal redundancy in the data, all three spectrometers were used in parallel. While Spectrometer A and C switch roles between "production spectrometer" (changing angle from run to run) and "luminosity monitor" (at a

[1] To help the readability, only the centers of the overlapping acceptances are marked.
[2] While the HDSM stage of MAMI C was already commissioned for productive use, there was no experience with the quality of the beam, and it was not yet possible to extract the beam at energy levels between 0.855 and 1.5 GeV.

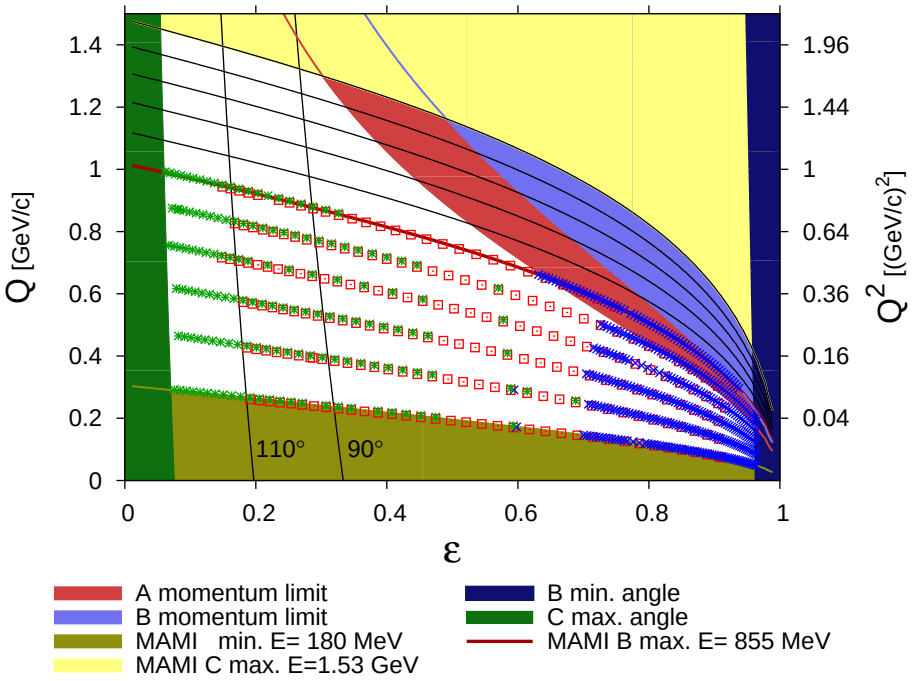

Figure 4.1: The accessible kinematical region in the ε-Q^2-plane. Colored regions are excluded because of minimum/maximum beam energy (dark/light yellow), maximum detectable momentum of spectrometer A and B (light red/blue), minimum angle of B (dark blue) and maximum angle of C (dark green). The center of the acceptances of the different kinematical settings are denoted with symbols (squares/crosses/stars (color red/blue/green) correspond to spectrometer A/B/C). The symbols are slightly shifted vertically to distinguish overlapping measurements. The near-vertical black lines denote spectrometer angles of 90° and 110°. The red line represents the maximum energy of MAMI B. The black near-horizontal lines represent a possible future extension using MAMI C energies. To stretch the low-Q^2 part, the (left) y-axis is presented linear in $Q = \sqrt{Q^2}$.

fixed angle)[3], spectrometer B was always used to take data. The spectrometer angle is changed each time only by a fourth of the acceptance, i.e. by 2.5° for A and C and by 0.5° for B, so that each angle is measured four times with the same spectrometer but with different parts of the spectrometer acceptance. Spectrometer A is used in the range between 25° and 110°[4], spectrometer C extends this to over 130°. The slim construction of spectrometer B allows it to reach scattering angles down to 15.5°.

The program for the detector simulation developed in [Ber04] was extended to aid the optimization of the parameters of the experiment: Beam current, event prescaling[5], measurement duration and concurrent angles of the spectrometers. It calculates the maximum beam current and optimal scaler values at which the rate of recorded events is below 500 Hz for each spectrometer and each wire of the VDC chambers triggers with less than 1000 Hz. When the field of a spectrometer is changed, the magnets have to settle. Since this takes some time, the momentum was adjusted only every second angle change in order to keep the elastically scattered electrons at the same place in the focal plane.
For most of the individual points, the required time to achieve the envisaged statistics of below 0.2% is around 30 minutes. For the small angle measurements, the cross section difference to the luminosity-measuring spectrometer is very large. Therefore, since both spectrometers have to achieve the desired statistics, these kinematics take considerably longer. Most settings were divided in either 15 or 20 minutes long sub-measurements. This reduces the statistical accuracy per measurement (which is compensated by the higher number of measurements), but increases the accuracy of the luminosity and facilitates the search for time dependent errors.
The measurements were done in three beam time periods, summarized in table 4.1.

[3] A similar technique, but limited to spectrometer C as the luminosity monitor, was employed in [Flo98; F$^+$99].

[4] Due to the construction of the target, the angle of A had to be limited to 90° for the long and to 110° for the short target cell.

[5] The experiment allows prescaling of the triggers, so that only every nth event is recorded. Only recorded events produce significant dead time. The prescaling helps to accommodate the largely different event rates of the different spectrometers at different scattering angles.

	August 2006	November 2006	May 2007
Duration	10 days	11 days	17 days
Setup/ calibration/ misc.	2 days	2 days	6 days
Incident energies [MeV]	585, 855	180, 720	315, 450, 720
Target cell used	long	short	long
Setup changes	152	173	217
Individual measurements	700	1008	1260
Real measurements	358	490	574

Table 4.1: Overview of the beam times. Setup changes are changes of momentum and/or angle of at least one spectrometer. The individual measurements also contain the luminosity measurements by one of the spectrometers and those which where later excluded because of obvious errors.

5 Simulation of the cross section measurement

5.1 Overview

The basic quantity measured in a scattering experiment is a counting rate. The number of (true) events n detected over a period of time T is related to the cross section by

$$n = \int_{\Delta\Omega} \int_{\Delta E'} \int_{T} \frac{\mathrm{d}\sigma}{\mathrm{d}\Omega \mathrm{d}E'} \left(\theta, E'\right) A\left(\Omega, E', t\right) L\left(t\right) \mathrm{d}\Omega \mathrm{d}E' \mathrm{d}t, \tag{5.1}$$

with A describing the acceptance of the spectrometer and L the luminosity. The acceptance is primarily given by the geometry of the spectrometers. Also, detector efficiency and resolution and the energy loss in the target and detector system have to be accounted for. A simulation of the experiment can fulfill these demands. Since the acceptance is assumed to be constant over the short measurement times, the integrals in eq. (5.1) can be rewritten as

$$n = \int_{T} L\left(t\right) \mathrm{d}t \cdot \int_{\Delta E'} \int_{\Delta\Omega} A\left(\Omega, E'\right) \frac{\mathrm{d}\sigma}{\mathrm{d}\Omega \mathrm{d}E'} \mathrm{d}\Omega \mathrm{d}E'. \tag{5.2}$$

The first integral is handled by the program package Lumi++.
The second integral is evaluated by the simulation software Simul++. It can simulate the accepted phase space ($\frac{d\sigma}{d\Omega} = 1$) or alternatively generate events according to a given cross section. It mimics the behavior of the data analysis package Cola++, so that the same histogram definitions can be used. It is based on Monte Carlo sampling, which relates the integral of a function F over a sufficiently small volume (a bin) to a sum of N (pseudo) randomly sampled points ([PTVF92], section 7.6):

$$\int_{V} F\left(\Omega\right) d\Omega \approx V \cdot \langle F \rangle \pm V \sqrt{\frac{\langle F^2 \rangle - \langle F \rangle^2}{N}}. \tag{5.3}$$

The angle brackets denote the arithmetic mean over N sample points,

$$\langle Y \rangle = \frac{1}{N} \sum_{i=1}^{N} Y\left(x_i\right). \tag{5.4}$$

5.2 Generator

As described earlier, the extraction of the first order Born cross section $\frac{d\sigma}{d\Omega}_0$ of the process $ep \longrightarrow e'p'$ also requires the calculation of a (radiation) correction factor. This factor depends on the kinematics and cut-off energy $\Delta E'$ in the spectrum of the scattered electrons:

$$\left(\frac{\mathrm{d}\sigma}{\mathrm{d}\Omega}\right)_{exp} = \left(\frac{\mathrm{d}\sigma}{\mathrm{d}\Omega}\right)_0 \cdot \mathrm{corr}\left(\Delta E', E, \theta\right), \tag{5.5}$$

or, differential in the scattered electron energy

$$\left(\frac{\mathrm{d}\sigma}{\mathrm{d}\Omega \mathrm{d}E'}\right)_{exp} = \left(\frac{\mathrm{d}\sigma}{\mathrm{d}\Omega}\right)_0 \cdot \frac{\mathrm{d}\,\mathrm{corr}}{\mathrm{d}E'}, \tag{5.6}$$

where $\frac{\mathrm{d}\,\mathrm{corr}}{\mathrm{d}E'}$ gives rise to the so called radiative tail. Since the correction factor varies over the large acceptance of the spectrometers, a single correction factor per spectrometer setting is not very accurate. The best way to extract the cross section is to simulate the measured spectrum on the basis of an assumed cross section, a peak shape and on the (known) energy loss via radiation. Division of the measured count rate by the luminosity integral and by the simulation then directly gives the ratio of the true cross section to the cross section assumed in the simulation without further corrections (see chapter 6).

A generator algorithm has to produce events with the correct weight in an efficient manner. This does not only incorporate the computational cost of the algorithm. The error term of eq. (5.3) depends on the variation of the function to be integrated inside the volume V. Through clever manipulation of the event distribution, the variance of the function can be minimized (Importance sampling, see [BL98]), thus, for a given error in the estimation of the integral, fewer events are required than for equally distributed events. The generator is based on a generator for events in a virtual Compton scattering experiment described in [Jov03]. In its original form, it was limited to a description of the shape of the tail, without correct global normalization. In the course of this work, it was extended to also describe accurately the peak region with the correct normalization. In the following, the details of the algorithms are explained. It can be separated in two parts, an outer "driver" that generates the radiative tail and an inner part which calculates the cross section.

5.2.1 Radiative tail generator

For each event, a vertex position, a scattering angle and an azimuthal angle is generated pseudo-randomly.

Electron contribution

Then the generator follows the principles laid out in Vanderhaeghen et al. [V$^+$00]: First, neglecting the proton contribution, the only part of the radiative correction δ (see chapter 2.2) that is dependent on the energy of the radiated photon and therefore gives rise to the radiative tail is:

$$\delta(\Delta E_s) = \frac{\alpha}{\pi} \ln\left(\frac{(\Delta E_s)^2}{E \cdot E'_{el}}\right)\left[\ln\left(\frac{Q^2}{m^2}\right) - 1\right]. \tag{5.7}$$

As already defined in chapter 2.2, E is the incoming electron energy, E'_{el} is the energy of an electron scattered elastically through the generated angle, Q^2 is the momentum transfer for this reaction and ΔE_s is the energy of the radiated photon in the c.m. system of photon and proton.

In the exponentiated form of the correction, δ is one term in the sum in the exponent. Separating this part, it is possible to rewrite $\exp(\delta(\Delta E_s))$ as

$$\left(\frac{(\Delta E_s)^2}{E \cdot E'_{el}}\right)^a = \left(\frac{\eta^2 (\Delta E')^2}{E \cdot E'_{el}}\right)^a = \eta^a \left(\frac{\Delta E'}{E'_{el}}\right)^{2a}, \tag{5.8}$$

using

$$\begin{aligned} a &= \frac{\alpha}{\pi}\left[\ln\left(\frac{Q^2}{m^2}\right) - 1\right] \\ \eta &= E/E'_{el} \\ \Delta E_s &= \eta \Delta E', \end{aligned} \tag{5.9}$$

where $\Delta E'$ is again the energy difference between E'_{el} and the final energy of the outgoing electron in the laboratory. Using a $\Delta E'$ distribution $I\left(E', \Delta E', t = 2a\right)$ which satisfies

$$\int_0^{\Delta E'} I\left(E'_{el}, x, t = 2a\right) \mathrm{d}x = \left(\frac{\Delta E'}{E'_{el}}\right)^t, \tag{5.10}$$

and weighting the event with η^a, it is clear that sampling this distribution accounts correctly for the radiative events, independent of up to where the spectrum is integrated. The distribution that has this property is given by

$$I(E'_{el}, \Delta E', t) = \frac{t}{\Delta E'}\left(\frac{\Delta E'}{E}\right)^t. \tag{5.11}$$

Its integral is normalized to 1.

To generate events according to this distribution, the generator starts with a uniformly distributed random number r between 0 and 1. From this, it calculates a ΔE:

$$\Delta E = E'_{el} \cdot r^{\frac{1}{t}}.$$

The distribution $J\left(E'_{el}, \Delta E', t\right)$ of this new random number ΔE is given by

$$J\left(E'_{el}, \Delta E', t\right) = \left(\frac{\mathrm{d}\Delta E'}{\mathrm{d}r}\right)^{-1} = \left(E'_{el}\frac{1}{t}r^{\frac{1}{t}-1}\right)^{-1}. \tag{5.12}$$

Solving equation (5.12) for r,

$$r = \left(\frac{\Delta E'}{E'_{el}}\right)^{t},$$

and back substitution yields

$$J\left(E'_{el}, \Delta E', t\right) = \frac{t}{E'_{el}}\left(\frac{\Delta E'}{E'_{el}}\right)^{t-1} = \frac{t}{\Delta E'}\left(\frac{\Delta E'}{E'_{el}}\right)^{t}. \tag{5.13}$$

Comparison of equations (5.11) and (5.13) shows that for $t = 2a$, this is the needed distribution. Therefore, generating events after this recipe with a weight of η^a yields the correct radiative tail.

Proton contribution

The proton contribution has two terms that contribute to the radiative tail. The first one is contained in δ_1:

$$\delta_1 = \frac{2\alpha}{\pi}\left(\ln\left(\frac{4\left(\Delta E_s\right)^2}{Q^2 x}\right)\ln\eta + \dots\right), \tag{5.14}$$

Similar calculations as before yield an exponent b,

$$b = \frac{2\alpha}{\pi}\ln\eta,$$

and a correction factor for the weight

$$\left(\frac{4E^2}{Q^2 x}\right)^{b}.$$

The second term contributing to the peak shape is contained in δ_2:

$$\delta_2 = \frac{\alpha}{\pi}\left(\ln\left(\frac{4\left(\Delta E_s\right)^2}{m_p^2}\right)\left(\frac{E'_P}{|\vec{p}_P|}\ln x - 1\right)\right), \tag{5.15}$$

giving rise to a exponent c,

$$c = \frac{\alpha}{\pi}\left(\frac{E'_P}{|\vec{p}_P|}\ln x - 1\right),$$

and a correction factor for the weight

$$\left(\frac{4E^2}{m_p^2}\right)^c.$$

Collecting all parts, the generator uses

$$t = 2a + 2b + 2c, \tag{5.16}$$

and a weight factor

$$\eta^a \cdot \left(\frac{4E^2}{Q^2 x}\right)^b \cdot \left(\frac{4E^2}{m_p^2}\right)^c. \tag{5.17}$$

5.2.2 Cross section generator

This part can be subdivided into two steps: Generation of a photon direction and calculation of the lowest order contribution to the $ep \longrightarrow ep\gamma$ reaction.

Generation of photon direction

In principle, the generation of the photon direction is easy: One has to simply generate a uniformly distributed direction, which is a rather standard technique. However, such a naive approach is very inefficient: The cross section for photon emission varies strongly with the angle when the photon is radiated in the direction of the outgoing or incoming electron, with a very sharp drop at the exact directions.
As has been noted before, a high variance leads to a large error term in eq. (5.3). Importance sampling is a better approach: Photon angles are generated according to a distribution which approximates the correct cross section. The transformation from a uniform distribution to this new distribution gives rise to a Jacobian, which has to be applied to the weight of the event. By design, this Jacobian and the original cross section cancel to a large extent. In the result, the average weight for each event will be nearly constant, minimizing the error term.
An approximation for the Bethe-Heitler part of the cross section is given by the sum of individual cross sections for radiation off the incoming or outgoing electron, neglecting the interference:

$$\begin{aligned}
\left(\frac{\mathrm{d}\sigma}{\mathrm{d}\Omega}\right)_{\text{approx.}} &= \left(\frac{1}{2}\left(\frac{\mathrm{d}\sigma}{\mathrm{d}\Omega}\right)_e + \frac{1}{2}\left(\frac{\mathrm{d}\sigma}{\mathrm{d}\Omega}\right)_{e'}\right) \\
\frac{\mathrm{d}\sigma}{\mathrm{d}\Omega_e} &= \frac{1}{\mathrm{N}\left(E,\vec{p}\right)} \cdot \frac{1-\cos^2\theta_{e,\gamma}}{\left(\frac{E}{|\vec{p}|} - \cos\theta_{e,\gamma}\right)^2} \\
\mathrm{N}\left(E,\vec{p}\right) &= -4 - 2\frac{E}{|\vec{p}|} \cdot \ln\left(\left(\frac{E}{|\vec{p}|} - 1\right) / \left(\frac{E}{|\vec{p}|} + 1\right)\right)
\end{aligned} \tag{5.18}$$

and the same expressions for E', p', $\theta_{e'\gamma}$. E (E') is the incoming (outgoing) electron energy, $\vec{p}$ ($\vec{p'}$) the corresponding momentum and $\theta_{e\gamma}$ ($\theta_{e'\gamma}$) the angle

between the incoming (outgoing) electron and the photon. The generator now selects with equal probability whether the photon is radiated from the incoming or outgoing electron.
Then, the transformation method is used to generate random values with a distribution according to eq. (5.18): The cumulative distribution[1] is given by

$$\begin{aligned} F\left(\theta_{e,\gamma}\right) &= \frac{\int_{-1}^{\cos(\theta_{e,\gamma})} \frac{\mathrm{d}\sigma}{\mathrm{d}\Omega}_{e} \mathrm{d}\cos\theta_{e\gamma}}{\int_{-1}^{1} \frac{\mathrm{d}\sigma}{\mathrm{d}\Omega}_{e/e'} \mathrm{d}\cos\theta_{e\gamma}} \\ &= \frac{1}{\mathrm{N}\left(E,\vec{p}\right)} \left(\frac{1-\left(\frac{E}{|\vec{p}|}\right)^2}{\frac{E}{|\vec{p}|}-\cos\theta_{e,\gamma}} - \cos\theta_{e,\gamma} \right. \\ &\quad \left. -2\frac{E}{|\vec{p}|} \ln \frac{\frac{E}{|\vec{p}|}-\cos\theta_{e,\gamma}}{\frac{E}{|\vec{p}|}+1} - 2 + \frac{E}{|\vec{p}|} \right). \end{aligned} \tag{5.19}$$

A uniformly distributed number r between 0 and 1 is now transformed by solving $r = F(\theta_{e,\gamma})$ to the new random variable $\theta_{e\gamma}$ with the correct distribution (see [PTVF92], section 7.2). The required inversion of F is realized numerically via a bisection method.
The event has to be weighted with the inverse of $\left(\frac{\mathrm{d}\sigma}{\mathrm{d}\Omega}\right)_{\text{approx.}}$. The upper two plots of fig. 5.1 depict the different steps of this part of the generator: The approximated angular distribution generated and the result when the weight is applied. In the upmost plot one can see the two peaks around the electron angles. The two-dimensional close-up around the forward peak reproduces the expected drop in the middle of the peak. Multiplying with the weight achieves a flat distribution.

Lowest order of $ep \longrightarrow ep\gamma$

The innermost part of the generator calculates the Feynman graphs of the lowest order describing the Bethe-Heitler (radiation from the electron, graphs r1 and r2 in fig. 2.2) + Born (radiation from the proton, graphs r3 and r4) processes for the now fixed kinematic. Here, a Jacobian for the transformation $\mathrm{d}\Omega_k^{Lab}$ to $\mathrm{d}\Omega_k^{c.m.}$ has to be taken into account. It is calculated numerically using finite differences.
The cross section calculated with these graphs is infrared divergent. This is accounted for by a modification of the propagators. Their denominators are

$$\begin{aligned} \text{Bethe-Heitler}: &\quad 2k\cdot q', \quad -2k'\cdot q' \\ \text{Born}: &\quad -2p\cdot q', \quad p'\cdot q', \end{aligned}$$

were $k(k')$ is the four-vector of the incoming (outgoing) electron and q' the four-vector of the radiated photon evaluated in the c.m. system. Here, q' is replaced with $q'_{mod} = q'/\left|\vec{q'}\right|$. Hence, the calculation yields the correct cross

[1] When the photon is radiated from the outgoing electron, again, the appropriate substitutions $E \to E'$ etc. have to be applied.

section multiplied with a factor $K^2 = \left|\vec{q}'\right|^2$ since the matrix element enters quadratically into the cross section. One order of K is then divided out at the cross section level, the remaining order has to be accounted for later on when the different parts of the generator are combined.

Combination

The soft photon limit ($|q| \to 0$) of the lowest order yields the correction $\delta_R + \delta_1 + \delta_2$ (without exponentiation). This contribution has to be replaced by the full calculation above. Differentiation for ΔE gives the term

$$\frac{t}{\Delta E'}, \tag{5.20}$$

which has to be divided out. In combination with the remaining order of K, this gives the factor

$$\frac{\Delta E'}{tK}, \tag{5.21}$$

which is numerically stable (it becomes $1/(t \cdot \eta)$ for diminishing ΔE). The lower part of figure 5.1 depicts the result of this final step.

5.3 Other aspects of the simulation

5.3.1 External radiation

When the cryo target is used, the incoming beam has to pass through different layers of matter until the scattering process occurs. This includes the walls of the target and the liquid hydrogen inside the target. Additionally, the cold target acts as a cold trap. "Snow", frozen water and nitrogen from the residual gas inside the vacuum chamber, can form on the target. The outgoing electron has to pass part of the hydrogen, the wall of the target, possibly snow and then the windows between spectrometer and vacuum chamber and a short distance of air between them. In all these layers, the electron loses energy by external bremsstrahlung and ionization of the atoms which adds to the radiative tail. These processes have to be folded with the internal bremsstrahlung spectrum; the simulation does this numerically.

5.3.2 Resolution

The resolution of the vertical drift chambers, the characteristics of the electronics and the limited knowledge of the transport inside the magnetic system give rise to specific error distributions for the extracted kinematical properties of the detected particles at the target. In the simulation, these distributions are modeled with parametrizations for the in-plane and out-of-plane angles, for the momentum and for the vertex resolution, i.e. the resolution of the reaction vertex along the beam axis. While the latter is modeled with a simple Gaussian,

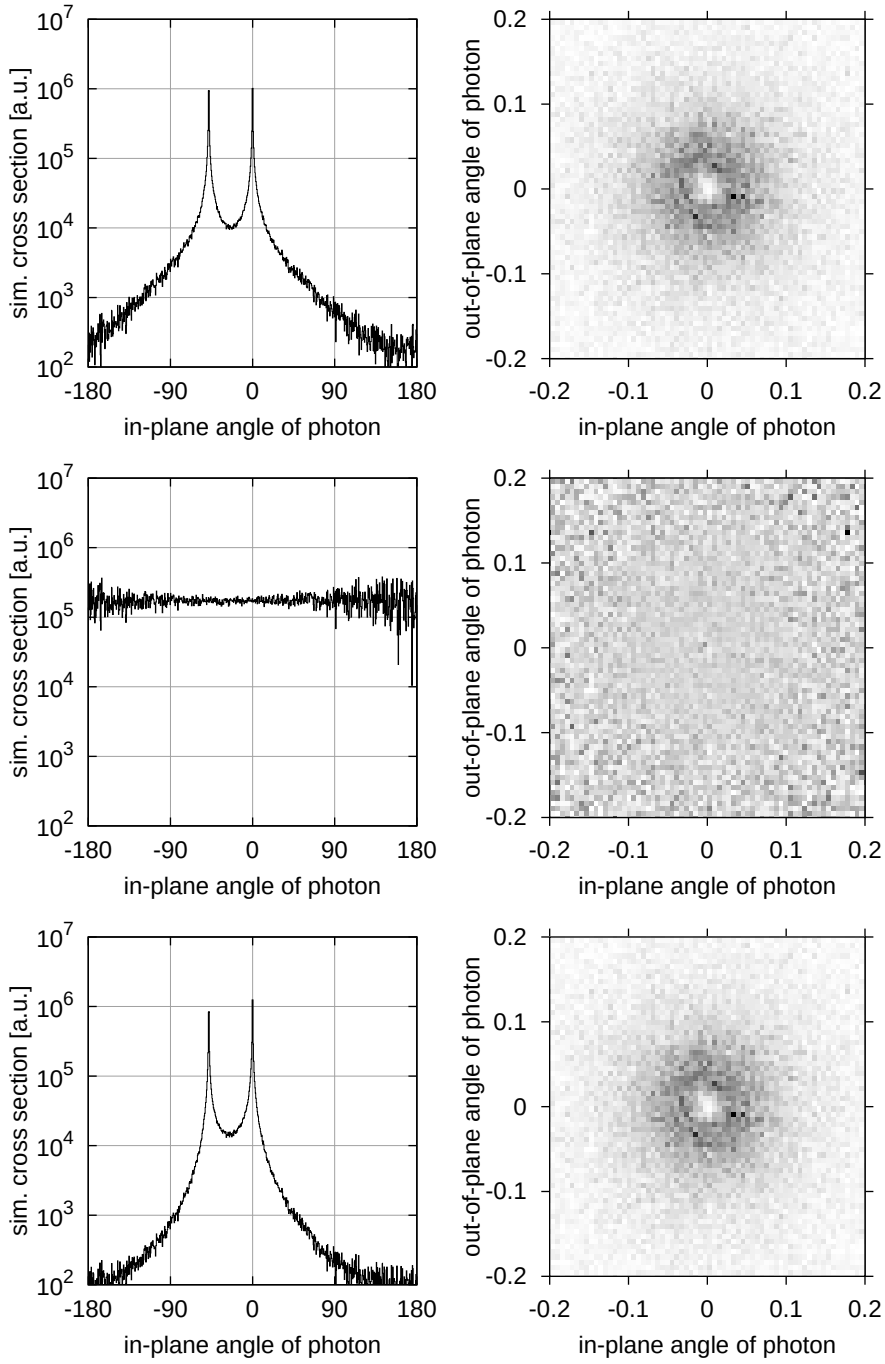

Figure 5.1: Different stages of the generator. Left: Distribution of events vs. the scattering angle. Right: Close-up of the area around the forward peak. The sharp drop of the cross section due to helicity conservation is clearly visible. Top: Distribution of events generated according to an appropriate, approximate distribution function. Middle: Same as top, now weighted by the inverse of the distribution function; the result should be uniform. Bottom: After multiplication with the correct weight from the Feynman graph calculation.

the simulation employs a sum of Gaussians with different weights and widths to model the momentum and angle resolution. The additional Gaussians allow the modeling of the longer tails of these distributions in contrast to a single Gaussian.

5.4 Test of the description of the radiative tail

The measured data allow a check of the description of the tail. Figure 5.2 shows a comparison of the measured $\Delta E'$ spectrum and the simulated tail. Background from the target walls complicate the situation, this will be dealt with in detail in section 6.4. For the comparison of the tail simulation with measured data, this background is suppressed by a vertex cut. Such cut is problematic for a cross section determination, as described in chapter 6.4, but it is well suited for this comparison. The resolution parameters mentioned above have to be optimized for this comparison. Details can be found in section 6.3. Figure 5.3 depicts comparisons of the integrated strength for different kinematical setups.

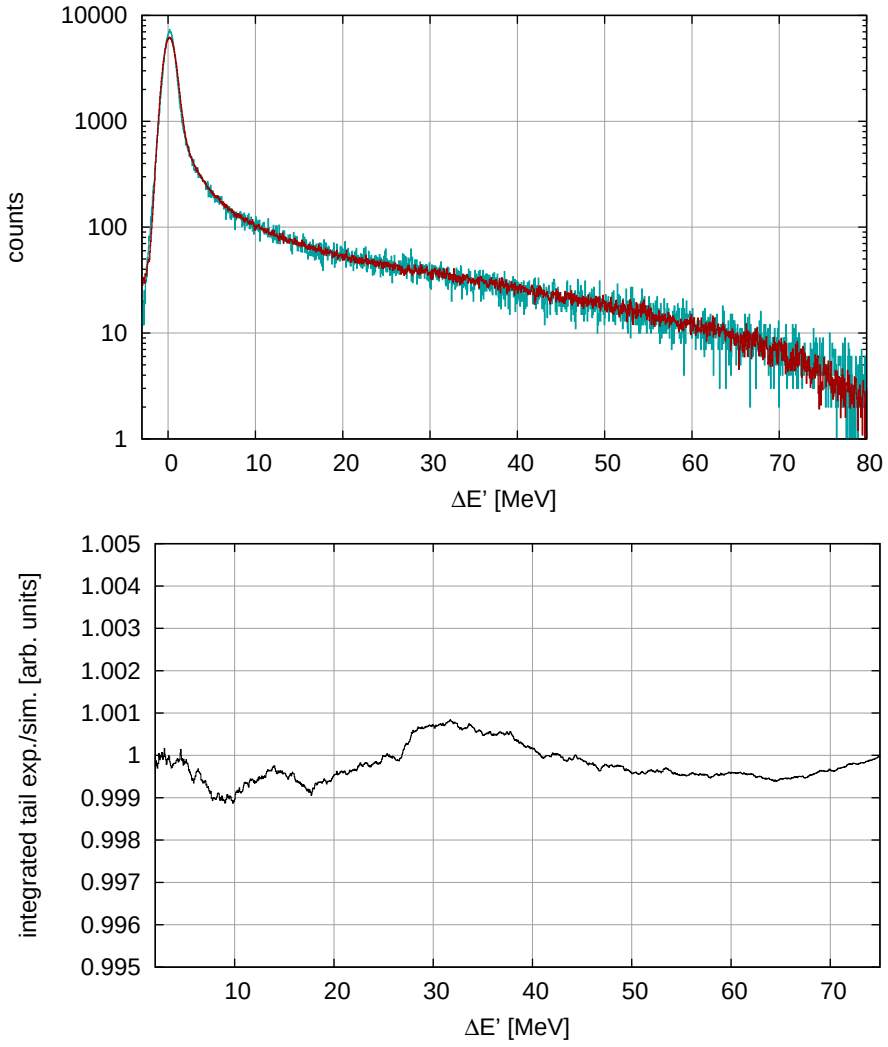

Figure 5.2: Top: Comparison of experimental (cyan) and simulated (red) $\Delta E'$ histogram. Bottom: Ratio of the integral of the experimental data to the integral of the simulation integrated up to the cut-off energy $\Delta E'$. The ratio varies by less than 0.1% for cut-off energies up to 75 MeV. Data: Spectrometer A, 53°, 855 MeV incident beam energy.

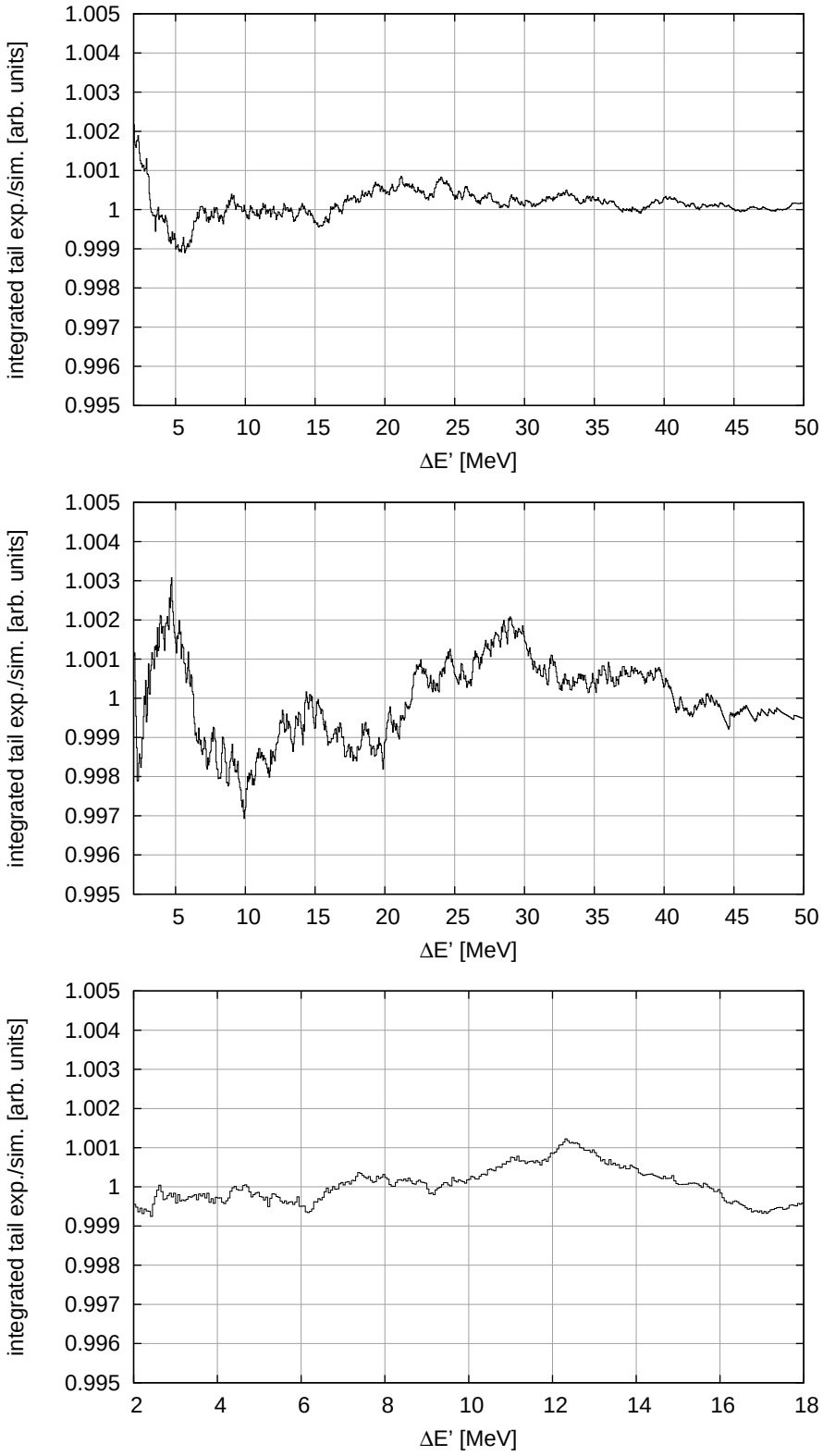

Figure 5.3: Same as fig. 5.2 for spectrometer A at 73° and 585 MeV (top), spectrometer B at 54° and 855 MeV (middle) and spectrometer C at 118° and 180 MeV (bottom).

6 The cross section data

6.1 Overview

The experiment aims at measuring the elastic electron-proton cross section in the kinematical region accessible with MAMI. The cross section is measured as the integral over the spectrometer acceptance. Complete knowledge of the exact transfer function of the magnetic system of the spectrometers would allow a further subdivision of the large acceptances. However, the experiment proved that this function is not known exactly enough for the level of precision the experiment aims at. Cuts on the phase space would be especially hard to control when the spectrometer angles change. From this it follows that the experiment is limited to a measurement of the cross sections integrated over the complete spectrometer acceptance. This cross section is determined relative to the cross section implemented in the simulation as

$$\sigma_{\mathrm{rel,exp}} = \frac{A - B}{\sigma_{\mathrm{sim}} \mathcal{L}}. \tag{6.1}$$

Here, A is the number of counts in the peak region (see subsection 6.2.1) integrated to the cut-off energy $\Delta E'$, B is the estimated background in this region, σ_{sim} is the simulated cross section integrated over the acceptance of the spectrometers (see chapter 5 and section 6.3) and $\mathcal{L} = \int \mathcal{L}_{\mathrm{eff}} \mathrm{d}t$ is the time-integrated effective, i.e. prescaling and dead-time corrected, luminosity.
With the existing setup, the absolute normalization, which includes the knowledge of the target length, current calibration and detector efficiency, can be determined only on the few-percent level. This is not sufficient for the accuracy aimed at in this experiment. Therefore the global normalization will be left floating in the final analysis.
The next sections describe the determination of A, B and $\mathcal{L}$.

6.2 Data preparation

Besides the events one is interested in, the system also records background events and random triggers from cosmic rays. To minimize background and erroneous trajectories, cuts have to be applied. This is described in subsection 6.2.1.

The detector information stored in the data files is interpreted and analyzed by the software package *Cola++*[1], which has been developed in the A1-collaboration. In a single-arm experiment, the main tasks are:

- Calculate the particle trajectories in the detector system from the VDC information.
- Transform these trajectories using the transfer matrix to the particle coordinates at the target. This gives the directions, vertex positions and relative momenta of the particles.
- Calculate the true momentum of the particle from the reference momentum and from the momentum of the particle relative to the reference momentum (the reference momentum is calculated from the field setting and given by a parametrization file).
- Calculate derived properties and fill histograms accordingly.

The first of these steps is very critical: If the parametrized description of the VDC is not optimal, a certain amount of good events are lost. The parametrization is dependent on TDC offsets and on the drift velocity of the electrons in the VDC gas mixture. Subsection 6.2.2 describes the procedure to determine these values.
The transformation from the detector system to the target is done using a matrix formalism. Some details can be found in subsection 6.2.3.

6.2.1 Event identification

Electrons scattered elastically without the emission of a photon have an energy

$$E'(\theta) = \frac{E}{1 + \frac{E}{m_p}(1 - \cos\theta)}. \tag{6.2}$$

Internal and external bremsstrahlung as well as ionization reduce the energy of the detected electron. To identify the elastic reaction, one defines

$$\Delta E_{\text{exp}} = E'(\theta_{\text{exp}}) - E'_{\text{exp}}, \tag{6.3}$$

the difference of the detected energy E'_{exp} to the energy calculated from the detected scattering angle, $E'(\theta_{\text{exp}})$. The histogram for ΔE_{exp} shows a peak near zero, with the radiative tail to the right (see top plot of fig. 6.1; note the logarithmic scale). A cut around this peak down to a cut-off energy $\Delta E'$ selects the elastic reactions.

The momentum acceptance of the spectrometer is given by the extent of the detector plane. Since it is difficult to control the efficiency (including angular acceptance) at the edges of the detector plane, the uppermost and lowermost

[1] Cindy OnLine Analysis in C++, [DMW01]. Further details about the software used in this work can be found in appendix F.

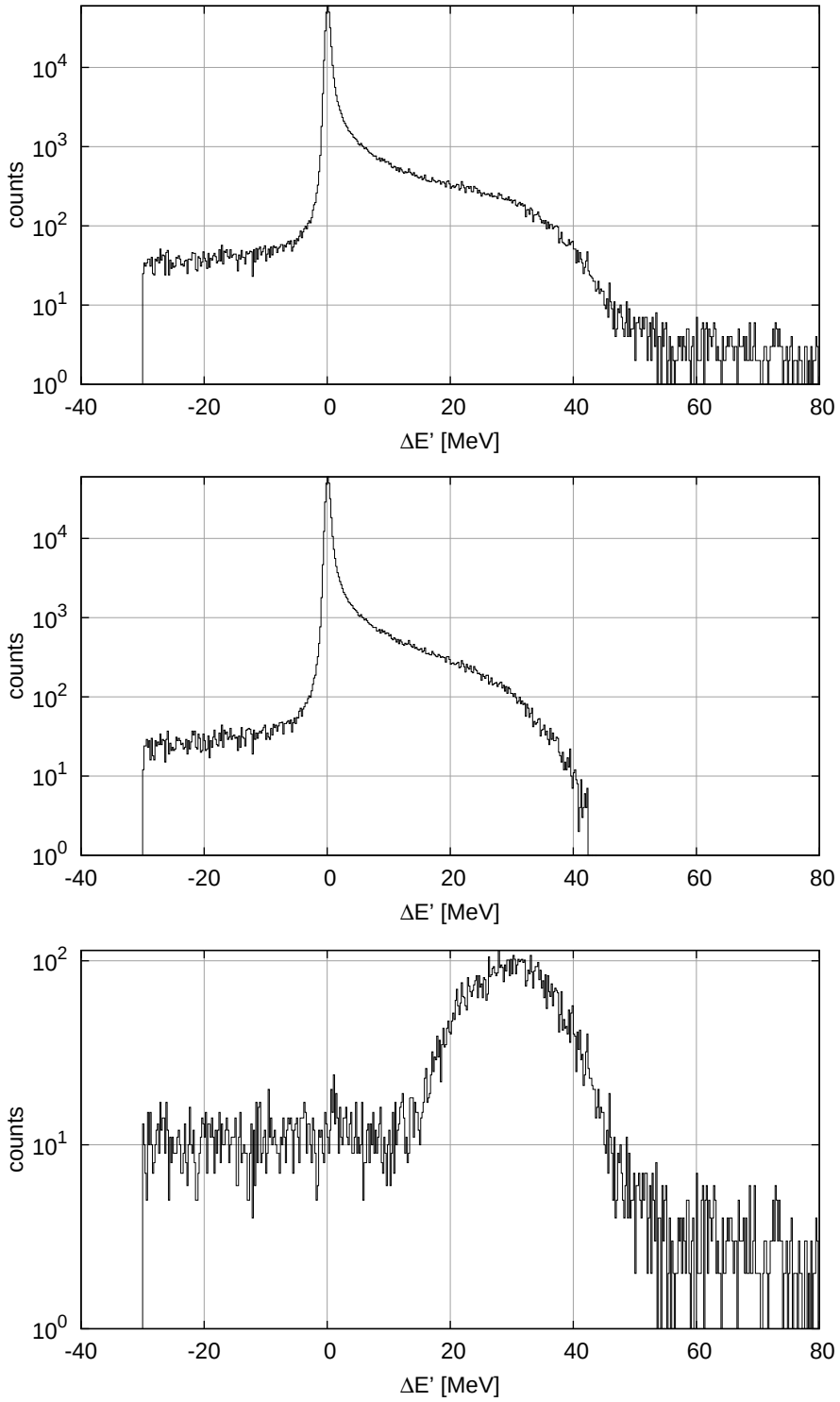

Figure 6.1: $\Delta E'$ histograms of the measurement with spectrometer A at 90.5° at an incident energy of $E = 585$ MeV. Top: Spectrum without any cut. Middle: After all cuts except a cut in $\Delta E'$. Bottom: Events that are rejected by the cuts. Random events give rise to the nearly constant level between -30 and 15 MeV. The bump around 30 MeV stems from events detected near the edge of the detector plane, which are cut away.

Cut	spec. A	spec. B	spec. C
Δp_c	$-10\% < \Delta p_c < 9\%$	$\lvert\Delta p_c\rvert < 7.3\%$	$\lvert\Delta p_c\rvert < 12.3\%$
Φ_0	$\lvert\Phi_0\rvert < 6.5°\%$	$\lvert\Phi_0\rvert < 3°\%$	$\lvert\Phi_0\rvert < 6.7°\%$
Θ_0	$\lvert\Theta_0\rvert < 5°\%$	$\lvert\Theta_0\rvert < 3°\%$	$\lvert\Theta_0\rvert < 6.5°\%$
Snout cut y_{snout}	–	$\lvert y_{\text{snout}}\rvert < 30, \text{mm}$	–

Table 6.1: Overview of the cuts used in the analysis.

accepted momenta are cut out. The measured relative momentum is Δp_c, the deviation of the particle momentum from the central momentum[2]. To reduce background, cuts around the nominally accepted in-plane (Φ_0) and out-of-plane (Θ_0) angles were applied. In order not to loose good events, these cuts have been chosen sufficiently broad. The cuts are summarized in table 6.1, figure 6.1 shows the effect of the cuts on the $\Delta E'$-spectrum.

For spectrometer B, an additional cut has to be introduced. Here, particles can be detected whose trajectory between target and spectrometer is outside of the acceptance defined by the collimator, when they hit the long snout in front of the collimator, whereby they may be scattered back into the acceptance. Fortunately, they are easily identified by the horizontal component of the intersection of the particle trajectory and the plane of the entrance of the snout (y_{snout}). Figure 6.2 shows the two-dimensional histogram of the horizontal offset at the collimator y_{colli} versus y_{snout}. The events around $y_{\text{snout}} = 0$ correspond to good events. One can see a shadow on the right and a dimmer shadow on the left. In the final analysis, the cut $|y_{\text{snout}}| < 30\,\text{mm}$ was applied. As one can see in fig. 6.3, which shows the distribution of the events that are cut away by this cut, the back-scattered electrons are located in the radiative tail. Their particular energy spectrum would not be accounted for by the ansatz for the background used in this work (see subsection 6.4) and would therefore be left as a contribution to the elastic scattering events in the tail region in particular at low electron energy.

6.2.2 VDC optimization

Each spectrometer is equipped with two packages of vertical drift chambers (VDCs). Each package consists of two individual VDC planes, one with wires perpendicular to the dispersive plane ("X"-chambers) and one with diagonal wires (40° rotation, "S"-chambers). The timing information from these vertical drift chambers is used to reconstruct both the intersection point and the angles of the trajectory to the focal plane.

A schematic view of a VDC is shown in figure 6.4. A VDC consists of a plane of alternating signal and potential wires with a pitch of 2.5 mm, sandwiched between two cathode planes of aluminized foil in 12 mm distance. The potential

[2]For spectrometers A and C, the central momentum is not the reference momentum (see table 3.1). Here, the relation $\Delta p_c = (1 + \Delta p_{\text{ref}}) \cdot 630/665 - 1$ is used for A and $\Delta p_c = (1 + \Delta p_{\text{ref}}) \cdot 459/490 - 1$ for C.

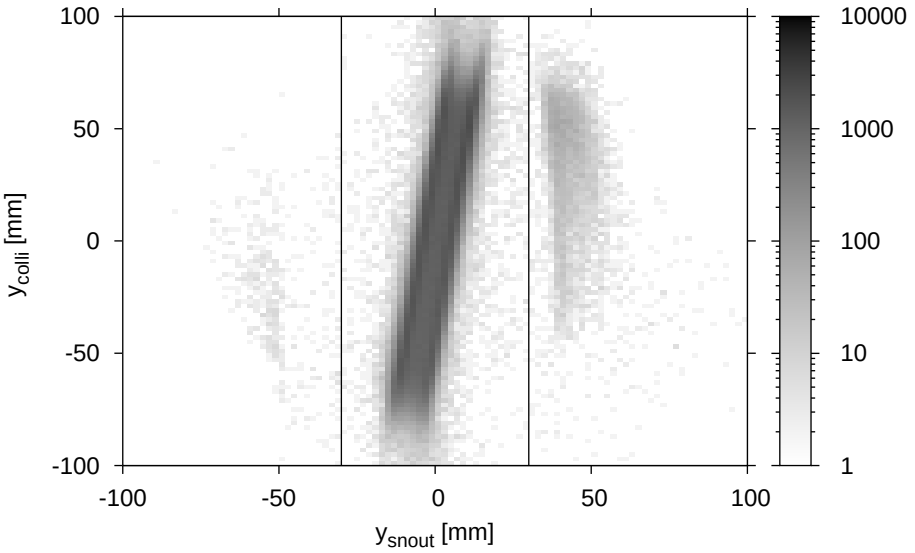

Figure 6.2: Histogram of y_{colli} vs. y_{snout} of the measurement with spectrometer B at 32.5° at an incident energy $E = 180\,\text{MeV}$. The gray scale is logarithmic to emphasize the side bands. The events around $y_{\text{snout}} = 0$ correspond to good events, the side bands result from back scattering from the snout walls. The black vertical lines denote the cut used in the analysis.

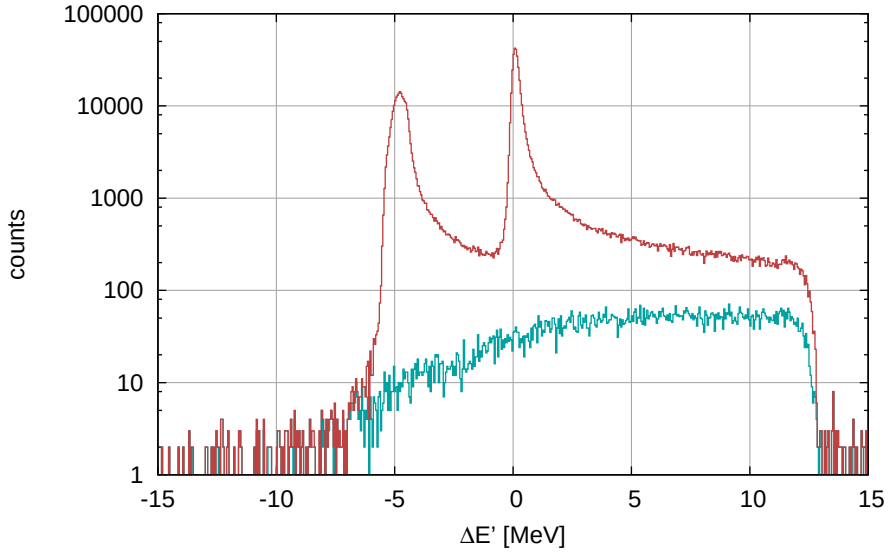

Figure 6.3: $\Delta E'$ histogram of the same measurement shown in figure 6.2. The events that were cut away (cyan) contribute mainly in the region of the elastic tail of the complete data set (red, with peaks). — The peak at $-5\,\text{MeV}$ stems from elastic scattering off the nuclei in the entrance and exit walls of the cryogenic target cell.

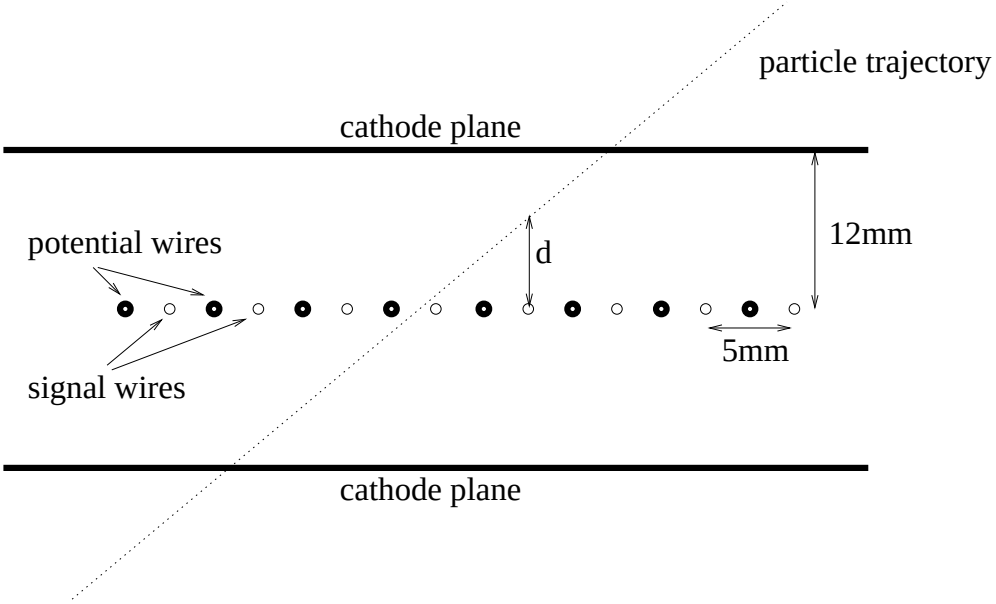

Figure 6.4: Schematic view of a vertical drift chamber. The cut is perpendicular to the wires.

wires are grounded directly, while the signal wires have zero potential through the input impedance of the preamplifier electronics. The cathode planes are set to a potential of about -6 kV with respect to the wires. The volume is filled with an argon-isobutane mixture with a small admixture of ethanol. A passing charged particle generates electron-ion-pairs along its trajectory. While the ions drift to the cathodes, the free electrons are accelerated to the high field strength area around the wires, where the number of primary electrons is magnified due to secondary collisions (gas amplification). When the electrons reach the signal wire, the current is strong enough to be digitized. The potential wires are thicker. Therefore, the field strength is lower and no sufficient gas amplification takes place there.
The VDC system is operated in a common stop mode: The TDCs connected to each signal wire are started when the electron clouds reach the wires and they are stopped by the (delayed) signal from the scintillator system.
The timing information of an event is translated into distances from the wires (for details, see [Dis90; Ber04]). To this end, the algorithm needs two parameters, a time offset corresponding to a zero drift time and the drift velocity. These parameters depend on the gas mixture and pressure, on the applied high voltage and on the trigger setup. The exact values vary over time and need to be determined and controlled.
The algorithm used to find the trajectories also estimates an error. This error estimate is histogrammed. The shape and especially the position of the maximum of the histogram is a good indicator for a correct determination of the offset and drift time.

Due to the sheer number of settings in this experiment it is not feasible to optimize the offsets and drift velocities by hand. Therefore, an automatic fit program has been created from a stripped-down version of the analysis package Cola++. The algorithm determines the goodness of the tested parameter combination from the peak position of the error histograms. The exact position of the peak is not the main focus here. Rather, the robustness against statistical fluctuations is important for a successful fit. The following algorithm proved to be a robust estimate of the peak position:

- First, in the error histogram, the bin with the maximum value is searched.
- Then, the algorithm searches in both directions from the maximum the bins where the histogram has dropped to 80% and 30% of the maximum value. This identifies the region of the peak slopes on both sides.
- A straight line is fitted to both sides of the peak from the 80% to the 30% point.
- The x-coordinates of these two lines at the average height of the four points are calculated and the middle between these two coordinates is taken.

Using this peak-position algorithm, the drift velocity and the offsets which minimize the peak position can be determined for each individual measurement with standard algorithms.
The drift velocities found by this optimization are shown in figure 6.5. While most of the measurements yield very similar velocities, there are obvious structures within the 180 MeV and 315 MeV measurement periods. After some search it was found that these structures coincide with the replacement of the isobutane bottle. It is very likely that some admixture of another gas changed the drift time. A possible source is insufficient flushing of the pipe system after swapping of the bottles. However, considering the small volume of the pipe system in comparison to the volume of the VDCs and the duration of the effect, this appears unlikely. On the other hand, the isobutane bottles themselves contain impurities. While these are minimal, it is possible that they accumulate at the top of the bottle, so they are released in a higher concentration when the bottle is fresh. A test at a later beam time showed that the blow-off of about 0.5 kg of isobutane cures this problem.

Figure 6.6 shows the change of the error estimate when the drift velocity is off by 5% or if one of the TDC offsets is wrong by 10 channels (5 ns). The worsening of the error estimate is obvious, therefore, this is an efficient way to determine these important quantities.

In order to account for the drifts of the drift velocity and of the TDC offsets, the values found by the optimization were described with appropriate functions of time. By taking these functions in the final analysis, individual outliers are suppressed.

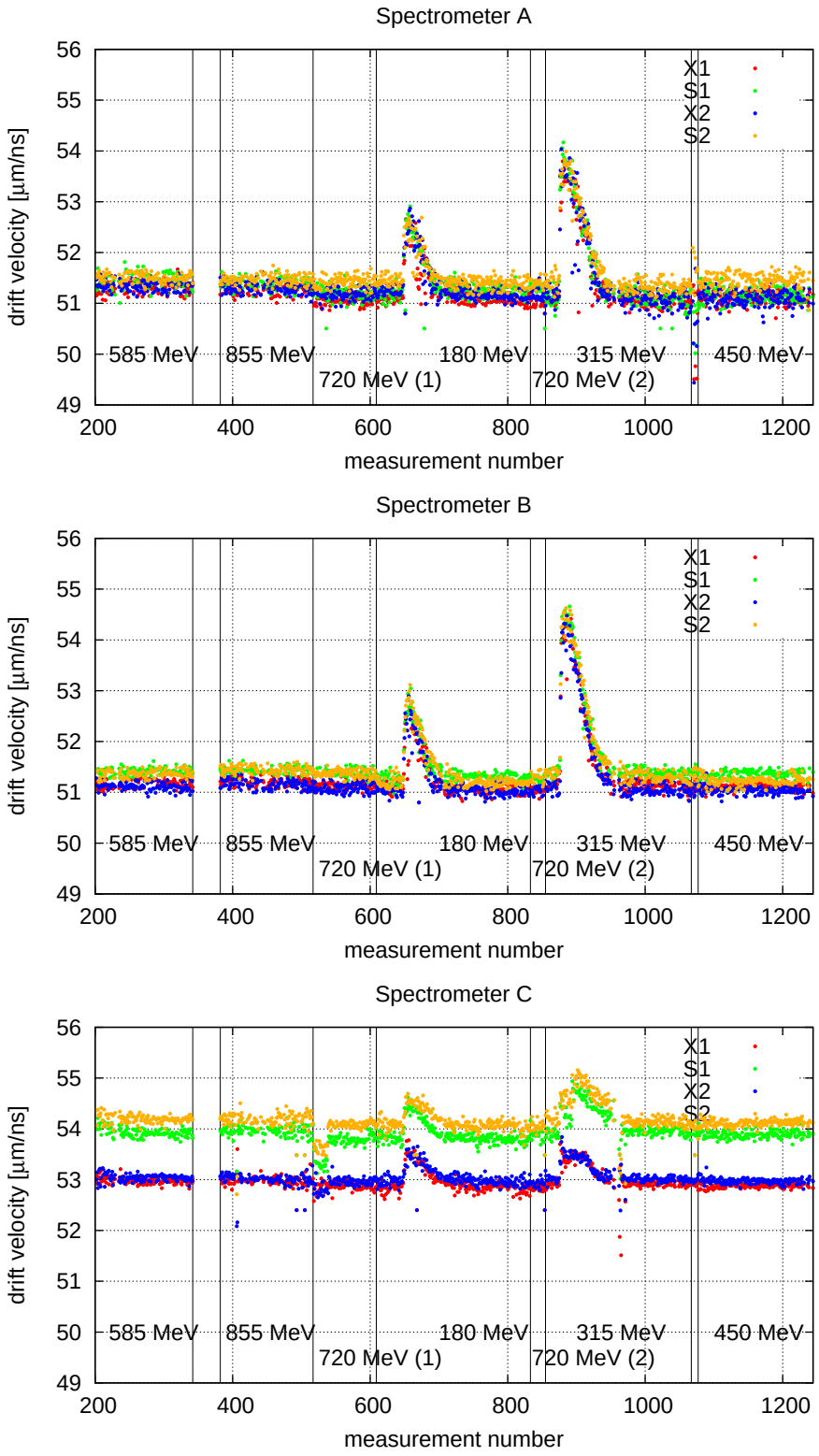

Figure 6.5: The drift velocities as determined by the fit procedure. The measurements are numbered sequential in time. The vertical lines separate measurements at different beam energies. The concurrent, sudden rise of the drift velocities coincide with the replacement of the isobutane supply bottle.

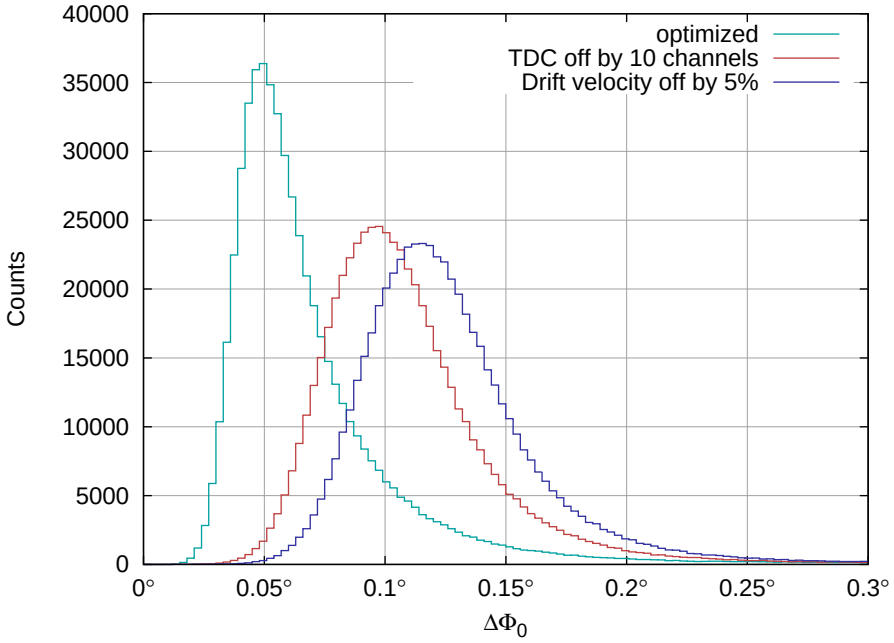

Figure 6.6: Distribution of the estimated error in the non-dispersive angle Φ_0. The cyan line shows the optimized case. When the TDC offset is changed by 10 channels (5 ns), the error is much larger (red curve). The result is even worse when the drift velocity is wrong by 5% (blue curve), which is comparable to the magnitude of the effect seen when the isobutane bottle is changed.

6.2.3 Matrix optimization

The determination of the trajectory by the VDC yields four values (two positions and two angles), the so called "focal plane coordinates". They are then translated to target coordinates: Two angles, the momentum and the position perpendicular to the central plane of the spectrometer. This transformation is parametrized in a matrix formalism. In essence, the functional dependency of a target coordinate $t_i \in \{\theta,\ \phi,\ y_0,\ \Delta p\}$ is described by a polynomial expansion in terms of the detector or focal plane coordinates $f_j \in \{\Theta_0,\ \Phi_0,\ X,\ Y\}$:

$$t_i = \sum_a \sum_b \sum_c \sum_d M_{abcd,i} f_1^a f_2^b f_3^c f_4^d. \tag{6.4}$$

Here, it is assumed that the perpendicular beam coordinates are zero (or known). The coefficients were determined by a fit to sieve-slit data (details of the process can be found in [Kor94]). When the VDC package is removed for maintenance, the position may change slightly when it is mounted again. To accommodate such changes without a complete redetermination of the matrix, the formalism allows for the specification of offsets which are subtracted from f_j.

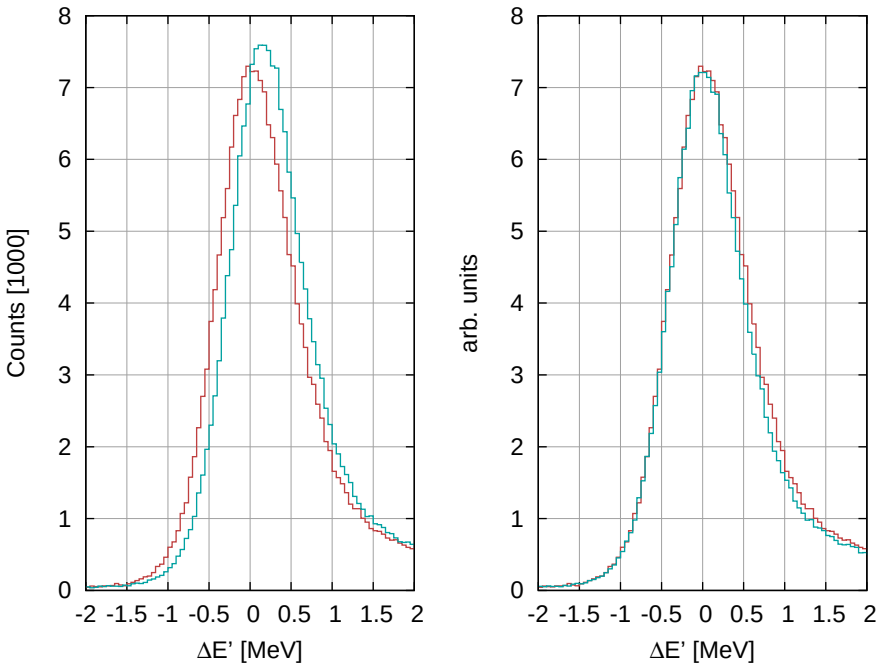

Figure 6.7: The effect of the matrix optimization, here on a measurement with spectrometer A at 70.5° and 450 MeV incident beam energy. Red: Data analyzed with unoptimized matrix. Cyan: With optimized matrix. The peak shifts to the right due to a change in the reconstructed scattering angle. Left: Original data. Right: Cyan peak is rescaled and shifted to make the reduced width more apparent. The FWHM gets smaller by about 7%.

Using sieve slit measurements taken at the beginning of each beam time, the offsets and some low order coefficients were optimized. Figure 6.7 shows a comparison of the $\Delta E'$ histogram before and after the optimization. In this case, the full width at half maximum could be reduced by 7%.

6.3 Determination of resolution and central momentum

In the simulation, the accuracy of the determination of the particle coordinates is parametrized in the target reference frame, i.e. the simulation contains parametrizations for the resolution in the vertex position, in the momentum and in the in-plane and out-of-plane angles. These parametrizations include parameters for the width of the distributions, which depend on the kinematics of the setup and which have to be determined for each setup individually.
Additionally, the peak position in the $\Delta E'$ histogram has to match between experiment and simulation, otherwise the cut in $\Delta E'$ would fail to select the equivalent part of the peak and tail region in both the experiment and the simulation. The peak position is given by the relative momentum (determined

in first order by the focal plane coordinate X) and by the momentum of the reference trajectory, which itself depends on the fields of the magnets. These are measured using Hall probes and, for the dipole fields which define the momentum, an NMR (Nuclear Magnetic Resonance) system which is more precise and does not drift due to radiation damage. To measure the field strength with NMR, inhomogeneities of the field at the position of the probe must be below a certain level, otherwise no resonance can be found. This is fulfilled for spectrometer A and C, but not for B, where correction coils have to be employed to suppress inhomogeneities caused by the clamshell design. Unfortunately, the NMR probe of spectrometer B only found a resonance in rare cases, so for most settings, only Hall probe measurements are available. The Hall probe, designed for the fast and coarse measurement needed in the initial steps of the field-change procedure, has only limited resolution and is not calibrated very well. Despite extensive efforts, the cause of the problems with the NMR system in spectrometer B could not be determined.
Additionally, precise reconstruction of the momentum needs precise knowledge of the transfer matrix. In any case, the conversion from field to momentum is not perfect. So, for all spectrometers, the exact momentum has to be found by comparing the peak positions of experiment and simulation (the incident energy is known within 0.1 MeV or better).

The determination of the momenta and resolutions is done in a two step process: The first step is to find the vertex resolution and, together with this, a possible target offset. For this, a standard non-linear least-squares optimization is performed, for which the derivatives of χ^2 with respect to the parameters have to be calculated numerically: For each variation of the parameters, the simulation is run, and the vertex histograms of experiment and simulation are compared. Since the analysis of the measured data is not dependent on these values, only the simulation has to be updated at each fit iteration.
In the second step, the momentum and the remaining resolutions are optimized. To this end, the spectra of $\Delta E'$, of the angles, and of Δp (the momentum relative to the reference momentum) are compared. Since the momentum value changes the data analysis, both data and simulation have to be updated at each step.
An example for the excellent matching between experiment and simulation is shown in figure 6.8. Figure 6.9 shows the difference between the "true" reference momentum determined from the known incoming energy by the described procedure and the reference momentum determined "online" from the measurements of the magnetic fields. For spectrometer B, large deviations around 1.5 MeV are found. This is easily understood from the fact that for spectrometer B, only the uncalibrated values of the Hall measurement were available. In fact, in the rare cases where the NMR locked on to a resonance and gave a field measurement, the Hall probe and NMR probe differed by approximately 1.5 MeV. The slope of the differences for spectrometer B is caused by non-linearities of the Hall probe and by the effect explained in appendix D.

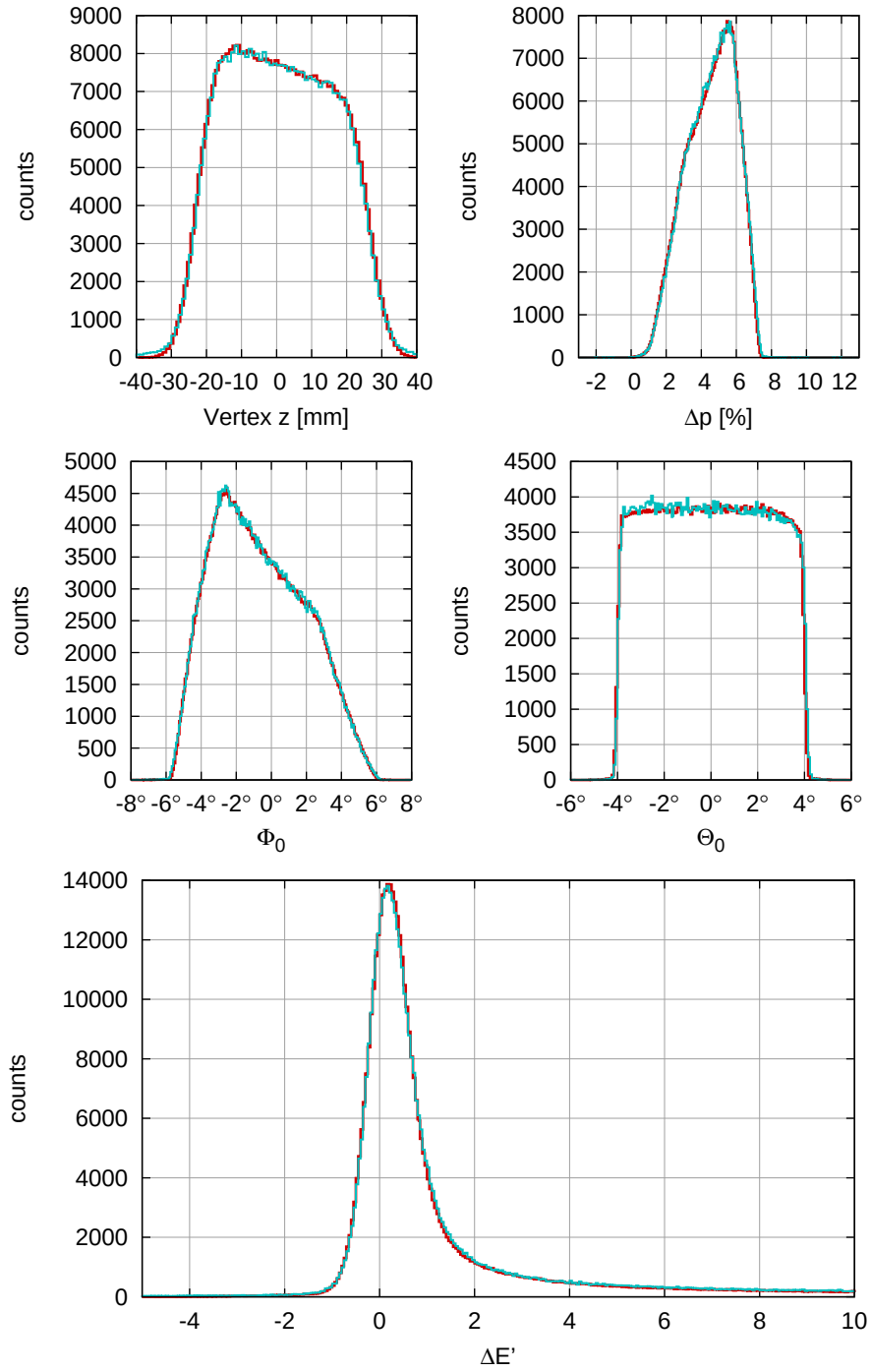

Figure 6.8: Comparison of vertex (top left), Δp (top right),Φ_0 (middle left) and Θ_0 (middle right) and $\Delta E'$ spectra of experiment (cyan) and simulation (red) for the measurement with spectrometer A at 43° and with 450 MeV incident beam energy.

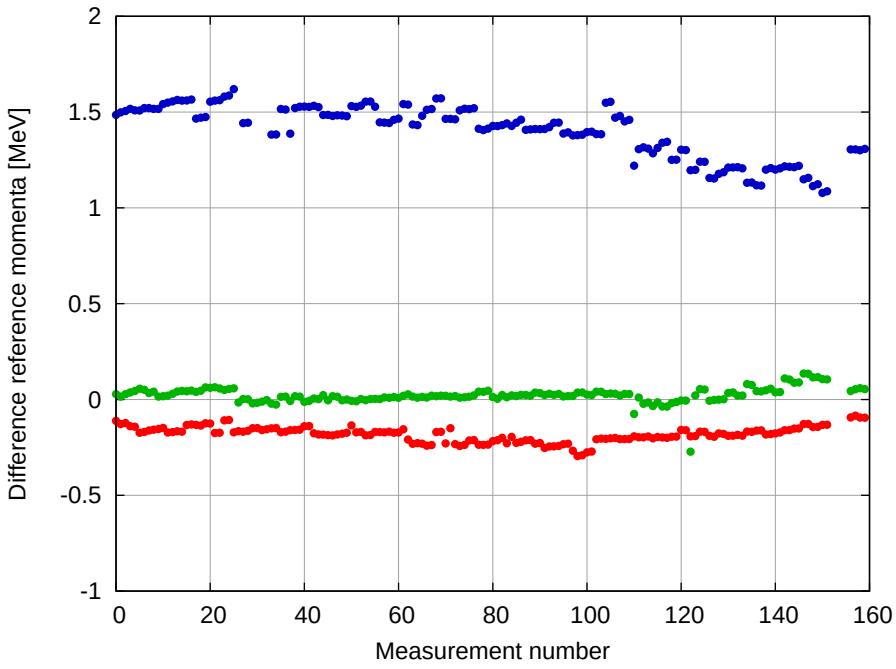

Figure 6.9: The difference of the fitted momentum to the momentum determined by the measurement of the magnetic fields for the measurements at 450 MeV incident beam energy. For A (red) and C (green), where the momentum is determined by the NMR, the difference is very small, whereas for B (blue), where only the Hall measurement can be used, the difference goes up to 1.5 MeV.

6.4 Background subtraction

As mentioned in section 3.3, the liquid hydrogen is contained in a cryo cell. The electron beam has to pass through the walls of this cell, a thin foil made of HAVAR, an alloy of several metals. So, besides the scattering off hydrogen one is interested in, scattering also occurs on the nuclei of the wall atoms[3]. This produces background in the energy region of the elastic peak of the hydrogen. Due to the difference in recoil, the peak from elastic scattering off the proton sits on the tail of the elastic peaks from the wall nuclei. At higher momentum transfer, this background mainly comes from quasi-elastic scattering, which, more or less by definition, sits under the elastic hydrogen peak, broadened by the Fermi momentum of the nucleons in the initial state and shifted by the separation energy. Due to the different masses m_i of the nuclei of HAVAR, the elastic background peak is a superposition of several peaks at positions

$$E_i' = \frac{E}{1 + \frac{E}{m_i(1-\cos\theta)}}. \tag{6.5}$$

Since the reconstruction of the $\Delta E'$ histogram assumes $m_{\text{target}} = m_p$, the peaks from the wall-nuclei are broadened.

Isolated inelastic peaks are either very small (at low Q^2) or they are already outside the region of the elastic proton-peak (at large Q^2).

The background that is under the proton peak has to be separated or subtracted from the data. A separation with kinematical cuts would be possible in a coincidence experiment. In a single arm experiment like in this work this is not possible. The only possibility to reduce or eliminate the background would be a cut in the vertex position. Such a cut however is very problematic: The vertex resolution and accuracy depends strongly (see appendix C) on the spectrometer angle and is almost impossible to handle, at least at the level of precision this experiment aims at: An estimation of the target length could not be attained with sufficient precision. Also, the assumption that the target length seen by one spectrometer is constant during one energy setting could not be maintained.

The approach for handling the background in this work consists of an estimation of the contributions by simulation. To this end, the simulation package was extended by models to simulate the elastic and quasi-elastic scattering on the wall nuclei, including their radiative tails. Both contributions are constructed to give the correct shape, while the amplitude is fitted to the data.

The generators for both contributions first select, according to the composition of HAVAR, a type of nucleus on which the scattering occurs. The elastic generator then calculates the radiative tail similar to the hydrogen generator, but without the explicit calculation of the Feynman graphs. The quasi-elastic generator additionally generates a nucleon. The kinematics are calculated relativistically, the Fermi momentum distribution is approximated by a sphere in momentum space. The elementary cross section is calculated according to

[3] HAVAR mainly consists of cobalt, chrome, iron, tungsten, molybdenum and manganese.

the de Forest off-shell cross section prescription [de Fo83]. Figure 6.10 depicts example spectra for both generators.

For each measurement, the amplitudes a of the two background types are determined by a fit of the sum of the simulated background $\Delta E'$-spectra and the simulated hydrogen spectrum to the measured spectrum by minimizing

$$\chi^2\left(a_{\text{sim.}}, a_{\text{el.}}, a_{\text{q.el.}}\right) = \sum_i \left(\frac{d_i - \left(a_{\text{sim.}} s_i + a_{\text{el.}} e_i + a_{\text{q.el.}} q_i\right)}{\Delta d_i} \right)^2, \tag{6.6}$$

where d_i is the measured count rate and s_i, e_i, q_i are the values of the simulated hydrogen, elastic background and quasi-elastic spectrum in the ith bin. Figure 6.11 displays a measured spectrum and the difference spectrum, i.e. the data histogram minus the three simulated and scaled spectra. One sees the excellent agreement in the tail, while there are slight imperfections in the replication of the immediate peak region by the simulation around the steep fall offs of the hydrogen peak, which, however, level out to zero in the integral. The ratio of the integrals of the background-corrected data and the integrated simulation of the hydrogen peak in the tail region is depicted in figure 6.12 for three measurements. This figure shows that within a large range, the choice of the cut-off energy has an effect of at most a couple of per mill. The background is largest for the small-angle settings at 180 MeV; for spectrometer B, the background contribution reaches 10%. However, for most of the setups, the background is below 4%.

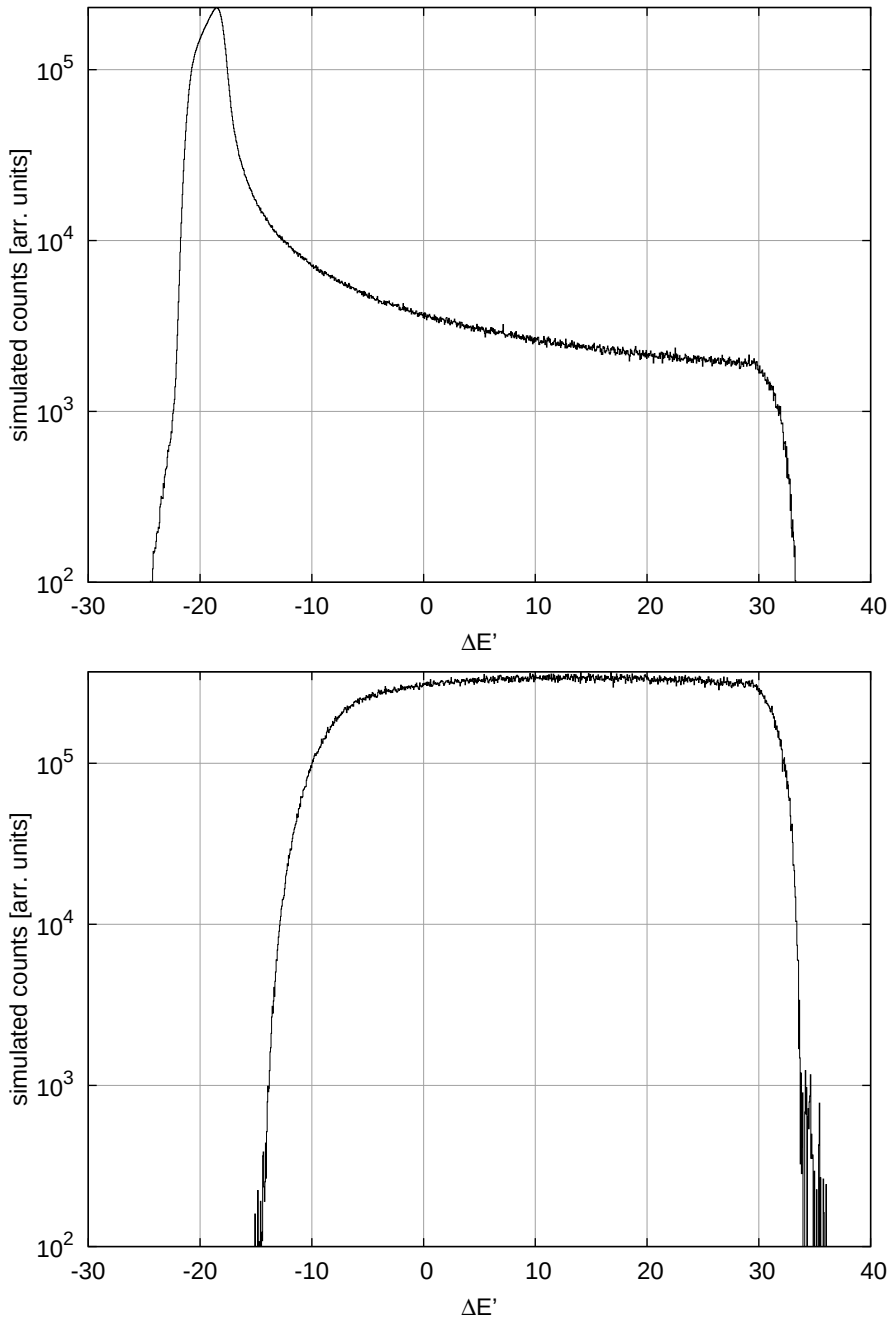

Figure 6.10: The simulated spectra of the elastic (top) and quasi-elastic (bottom) background for spectrometer B at 25.5° and 450 MeV incident beam energy ($Q^2 = 0.038$ (GeV/c)^2). The amplitudes are fitted to the measured spectrum.

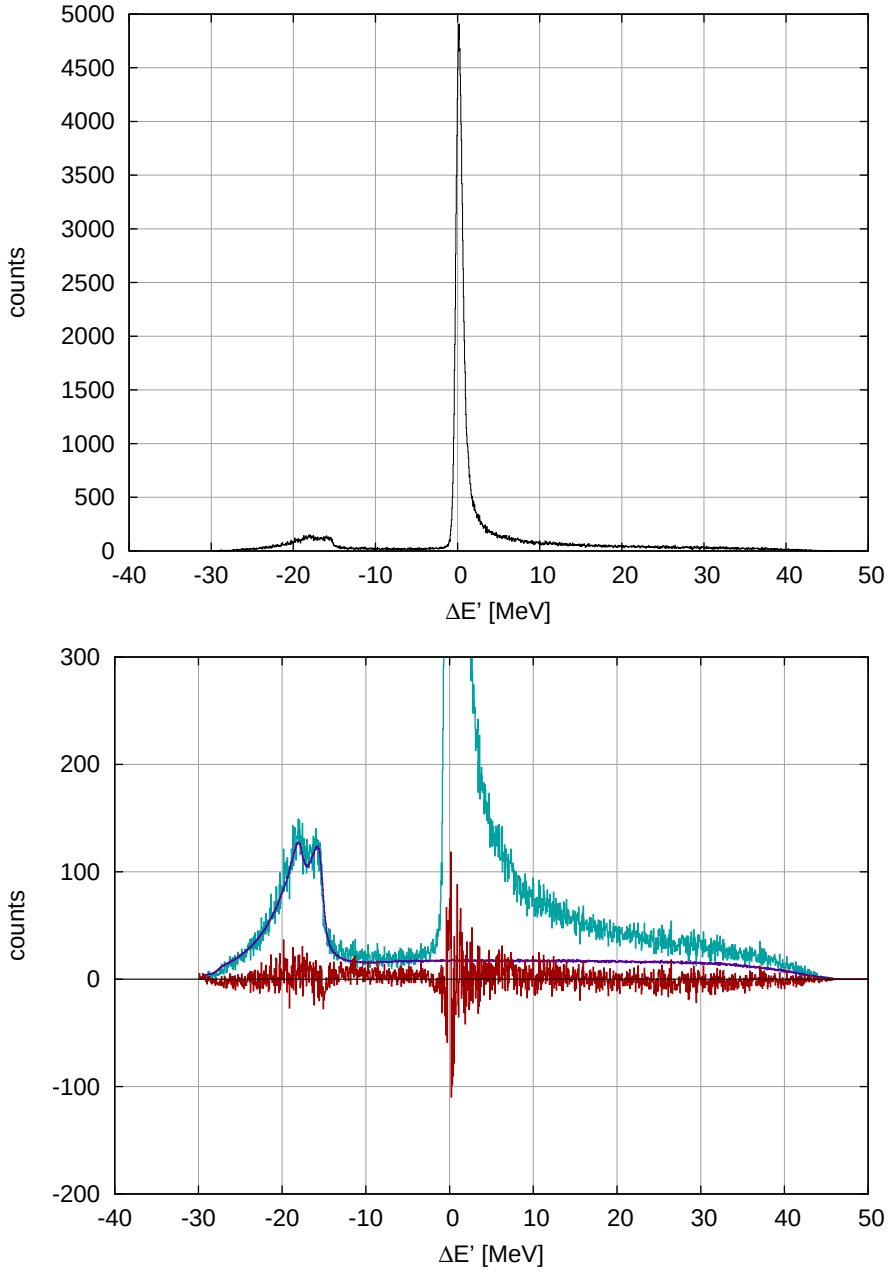

Figure 6.11: Top: $\Delta E'$ spectrum measured with spectrometer B at 25.5° and 450 MeV incident beam energy. Bottom: Same spectrum (cyan), background estimate (blue) and difference of the data to the sum of simulated hydrogen peak and background (red).

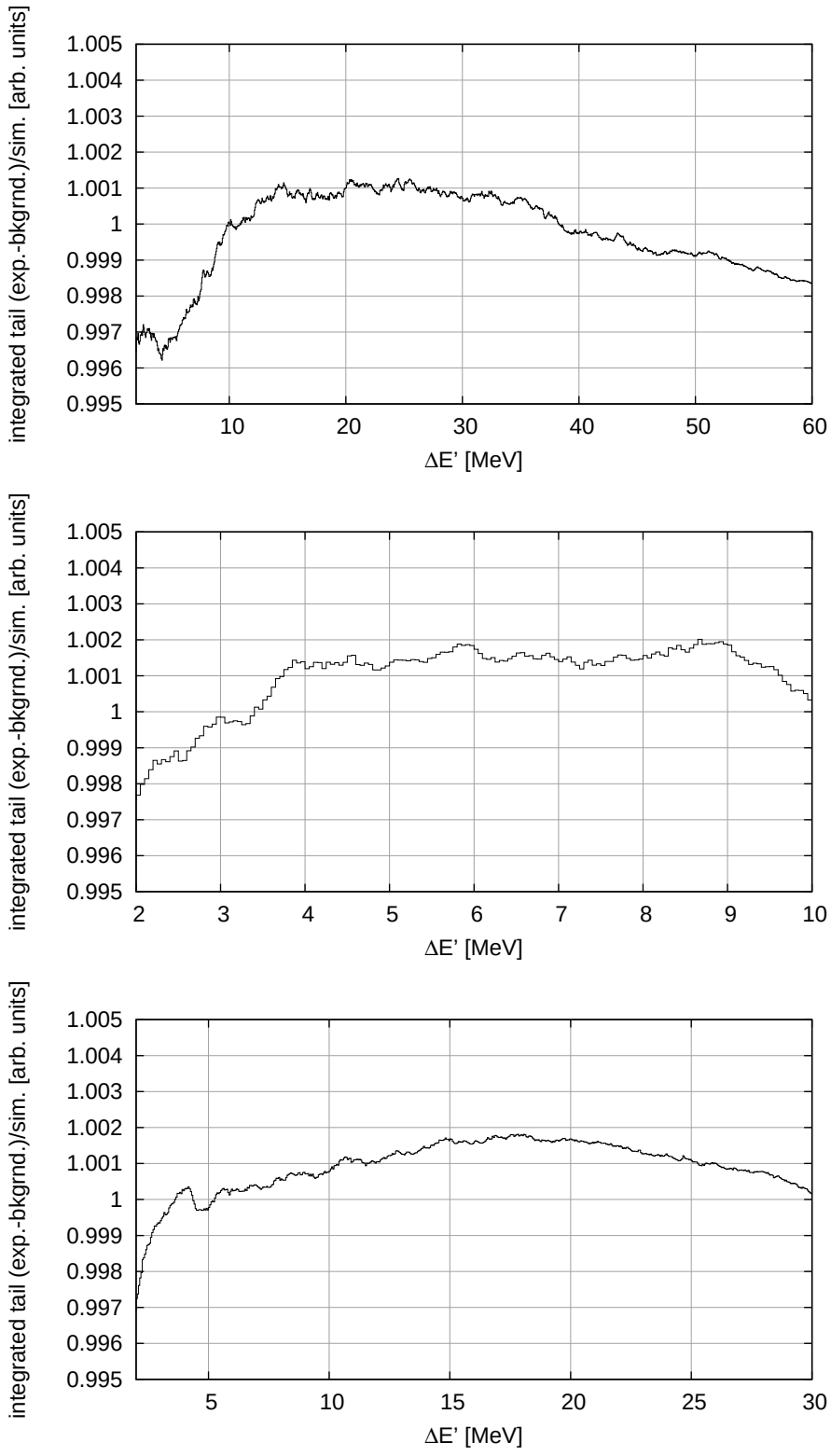

Figure 6.12: The ratio of background-corrected data to simulation in the tail region. Top: Spectrometer A at 88° and 855 MeV incident beam energy. Middle: Spectrometer B at 49° and 180 MeV. Bottom: Spectrometer C at 73° and 585 MeV.

6.5 Luminosity

The integrated luminosity is defined as the number of electrons, N_e, impinging on the target in the duration of the measurement, T, multiplied by n_T, the areal density of the target nuclei:

$$\mathcal{L} = N_e n_T. \tag{6.7}$$

The number of electrons can be calculated from the charge Q_e hitting the target, i.e. from the integrated beam current I,

$$N_e = \frac{Q_e}{e} = \frac{1}{e}\int_T I\mathrm{d}t, \tag{6.8}$$

where e is the electron charge. In this experiment, the beam current I is either measured with the Förster probe or with the pA-meter, which gives more stable results (see subsection 6.5.1).
The areal density of the protons n_T is given by the areal density of the hydrogen molecules n_{H_2} and the number of atoms in a hydrogen molecule $z = 2$. With Avogadro's constant $N_A \approx 6.022 \cdot 10^{23}\,\mathrm{mol}^{-1}$, the mass-volume-density ρ, the thickness x, and the molar mass M_{H_2} of the target, n_T is determined by

$$n_T = z \cdot n_{\mathrm{H}_2} = 2\frac{N_A}{M_{\mathrm{H}_2}}\rho \cdot x. \tag{6.9}$$

The target density ρ is calculated from continuous pressure and temperature measurements. These values are nearly constant during a cross section measurement.

To avoid local overheating of the liquid hydrogen due to the heat load of the passing electron beam, at high currents the beam is rastered over the (curved) frontal face of the target. The small change in the effective target thickness x due to this rasterization is accounted for by the simulation. The absolute length of the cooled-down cryo cell is hard to determine on the sub-percent level. Uncertainties in its determination enter as a constant factor in the global normalization which will be taken as a fit parameter anyhow; it is gratifying to note, however, that the normalizations of the different blocks of measurements are in the expected range and do not depend strongly on the form factor model used in the fit (see appendix G).

The luminosity has to be corrected for prescaling and dead time. This is done with the program *LumiTNG*, a rewrite of *Lumi++*. (The rewrite was necessary to implement the special treatment of the pauses caused by the beam position stabilization (see subsection 3.4.2)). It also calculates the effective measurement time and the integrated Förster probe values.

6.5.1 pA-meter calibration

The design of the experiment aims at a determination of the luminosity by the measurements done with one of the spectrometers (at constant angle) as

luminosity monitor as described in the next subsection. In this case, no current-measurement is needed. However, the measurement of the beam current provides a cross check. Furthermore, an anomaly in the 315 MeV data (see subsection 6.6.2) makes it impossible to use the luminosity measurements with the spectrometer for this energy, instead the analysis has to rely on the normalization from the beam current. The pA-meter provides precise measurements even for extreme low currents and low beam energies where the standard Förster probe works badly (if at all).
The pA-meter measures the current on a collimator positioned right before the first linear-accelerator segment. For a beam-current measurement, the collimator current is measured with the beam once deflected onto the collimator and once not, so that the beam passes through the collimator and enters the rest of the accelerator. The actual beam current should be proportional to the difference of these two values.
The pA-meter measurement is calibrated against the Förster probe. These measurements were done over a large range of currents using a beam energy of 855 MeV, maximizing the number of return paths in RTM 3 and hence the precision of the Förster-probe measurement.

The Förster probe (also called fluxgate magnetometer) measures the magnetic field of the electron beam by cancellation with the field of a coil. The current to produce the compensation field is the measurement signal, which is converted into a frequency. The output signal is counted to integrate the beam current over the measurement time. The signal fed into the frequency converter can be reduced by a fixed factor f, allowing to measure both high and low currents with good precision. In the normal analysis, f is taken to be exactly the design value 100. Since the calibration measurements span both ranges, this factor was tested by fitting the two ranges separately. For the complete data range, we make the ansatz

$$i_{\text{Förster}}\left(i_{\text{pA}}\right) = \begin{cases} m \cdot i_{\text{pA}} + b_{\text{lr}}, & \text{low range} \\ f \cdot m \cdot i_{\text{pA}} + b_{\text{hr}}, & \text{high range} \end{cases}, \tag{6.10}$$

i.e. with the same slope for both ranges (apart from f), but different offsets. The low-range offset b_{lr} is small, and, within the uncertainty, compatible with zero. This offset is most likely caused by the limited precision of the Förster probe for low currents and is set to zero in the final calibration. The high-range offset is larger, but still compatible with 0. Setting f to 100 and b_{hr} also to 0, the fit of only m does not reproduce the data. This is demonstrated in figure 6.13 which shows the deviation of the data and of a fit of eq. (6.10) with free f from a fit with fixed $f = 100$ and $b_{hr} = 0$. The change in the behavior above 1000 nA, where the switch between low range and high range occurs, is obvious. The fit with both offsets b set to zero gives a proportionality factor of $m = 2.0682 \pm 0.0019$ and $f = 98.77 \pm 0.10$.

Non-linearities in the frequency converter may introduce deviations from the linear relation (6.10). In a fit with a quadratic term, this term is found to be compatible with zero. Therefore, the relation between beam current i_{beam} and pA-meter current is taken to be strictly linear.

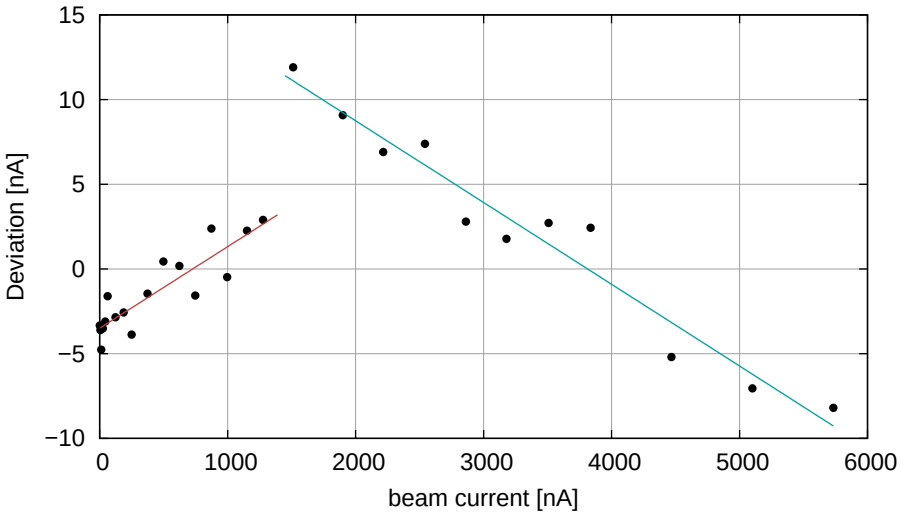

Figure 6.13: Deviation of the beam currents measured by the Förster probe and of a fit with free f from a fit with fixed f and b_{hr}. The fit with free f does explain the data in the low range(red) and high range (cyan) of the Förster probe.

It has to be noted that also for the measurements where a normalization with the luminosity monitor is not possible the exact knowledge of the proportionality factor m is not needed, since it only affects the global normalization, which is subsumed in the normalization parameters of the global fit.

The 315 MeV data were measured with several different beam currents. However, several cross section measurements were done at each beam current. Now, the average of the beam current measurements for each constant-beam-current group is calculated. The scattering of the individual current measurements of each group from the average is an indication of the precision of the measurement. The superior performance of the pA-meter at low beam energies and low currents is demonstrated in figure 6.14, where the ratio of the individual measurement to the average value is depicted for both pA-meter and Förster probe.

6.5.2 Luminosity monitor

For all measurements, one of the three spectrometers was used as a luminosity monitor, i.e. this spectrometer stayed with the same field at the same angle, thus measuring the count rate for a fixed momentum transfer for a time where many runs at different angles were taken with the other spectrometers. This spectrometer thus monitors the constancy of the luminosity. In the course of the measurements at one energy, only a few changes of the monitor angle are necessary to ensure that its event rate is high enough.
Each measurement of the luminosity monitor is analyzed in the same way as the

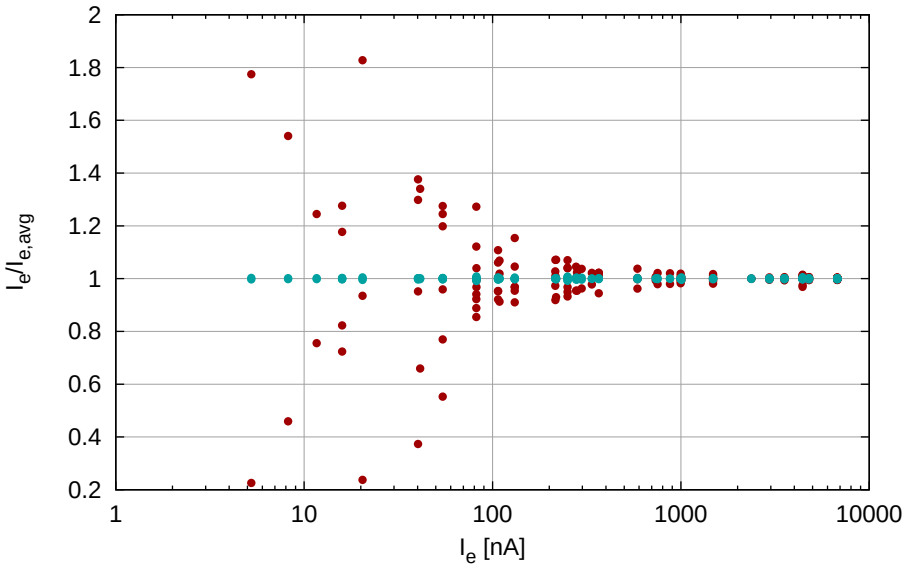

Figure 6.14: The current-measurements of the 315 MeV beam time, grouped by constant setup of the electron source of the accelerator. Depicted is the ratio of the individual measurement to the average current of a group, for pA-meter (cyan) and Förster probe (red). While the scattering of the pA-meter values is barely visible, the Förster probe values scatter significantly, the more the lower the beam currents. At higher beam energies, the performance of the Förster probe is considerably better.

normal cross section measurements, that is, the normal procedure of background subtraction, dead time correction and normalization to the estimated luminosity is performed.

From the n individual results, the average cross section is calculated:

$$\sigma_{\mathrm{lum,avg}} = \frac{1}{n}\sum_{i=1}^{n}\sigma_{\mathrm{lum},i}. \tag{6.11}$$

The cross section values $\sigma_{\mathrm{exp},i}$, measured with the other spectrometers, are now normalized:

$$\sigma_{\mathrm{exp,norm},i} \quad = \quad \sigma_{\mathrm{exp},i}\cdot\frac{\sigma_{\mathrm{lum,avg}}}{\sigma_{\mathrm{lum},i}}. \tag{6.12}$$

Hence, the common factors in the luminosity, i.e. beam current, target density and target length, cancel out and uncertainties in their determination play no role apart from the overall normalization, which will be taken as a fit-factor in the final analysis anyhow.

In this procedure, the statistical error of the normalized data is enhanced by the statistical error of the luminosity measurement:

$$\frac{\Delta\sigma_{\mathrm{exp,norm},i}}{\sigma_{\mathrm{exp,norm},i}} = \sqrt{\left(\frac{\Delta\sigma_{\mathrm{exp},i}}{\sigma_{\mathrm{exp},i}}\right)^2 + \left(\frac{\Delta\sigma_{\mathrm{lum},i}}{\sigma_{\mathrm{lum},i}}\right)^2}. \tag{6.13}$$

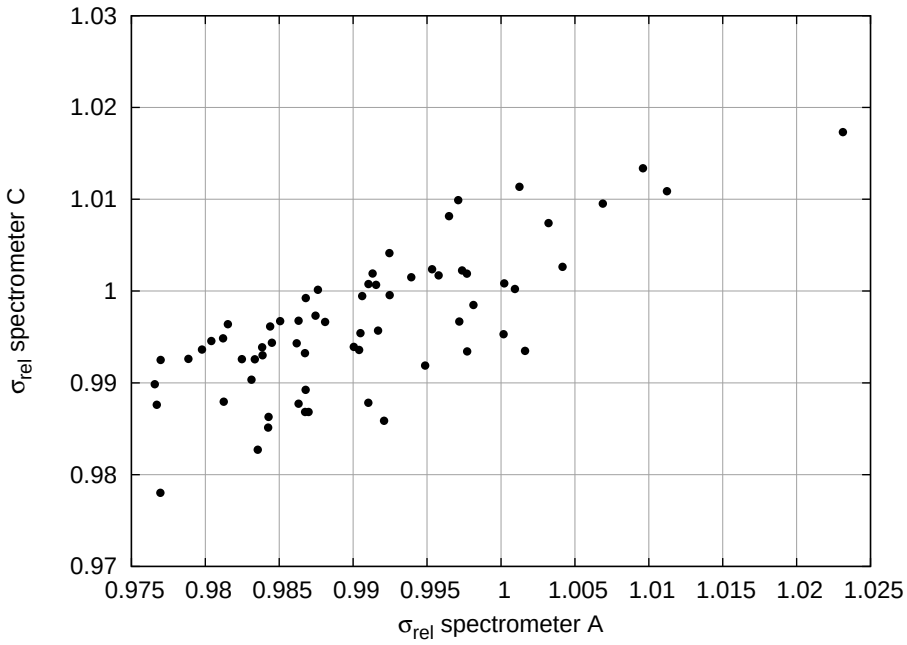

Figure 6.15: Relative cross sections measured with spectrometer A versus those measured with spectrometer C in the same run. The angle of spectrometer C is fixed. The correlation is obvious.

For higher currents, where the beam and the current read-out is stable, the effect of the normalization to the luminosity monitor is small, though visible. For 180-MeV-measurements with very small currents and a less stable beam the normalization is indispensable as can be seen from figures 6.15 and 6.16. The former figure shows the relative cross sections measured with spectrometer A plotted against those measured in parallel with spectrometer C. The correlation is clearly visible, the correlation coefficient is $r = 0.997$, though the spread in the data from spectrometer A due to the deviation from the standard dipole is still present. Figure 6.16 demonstrates the result of the normalization to the luminosity monitor. The luminosity normalization is applied to all measurements where possible (see subsection 6.6.2).

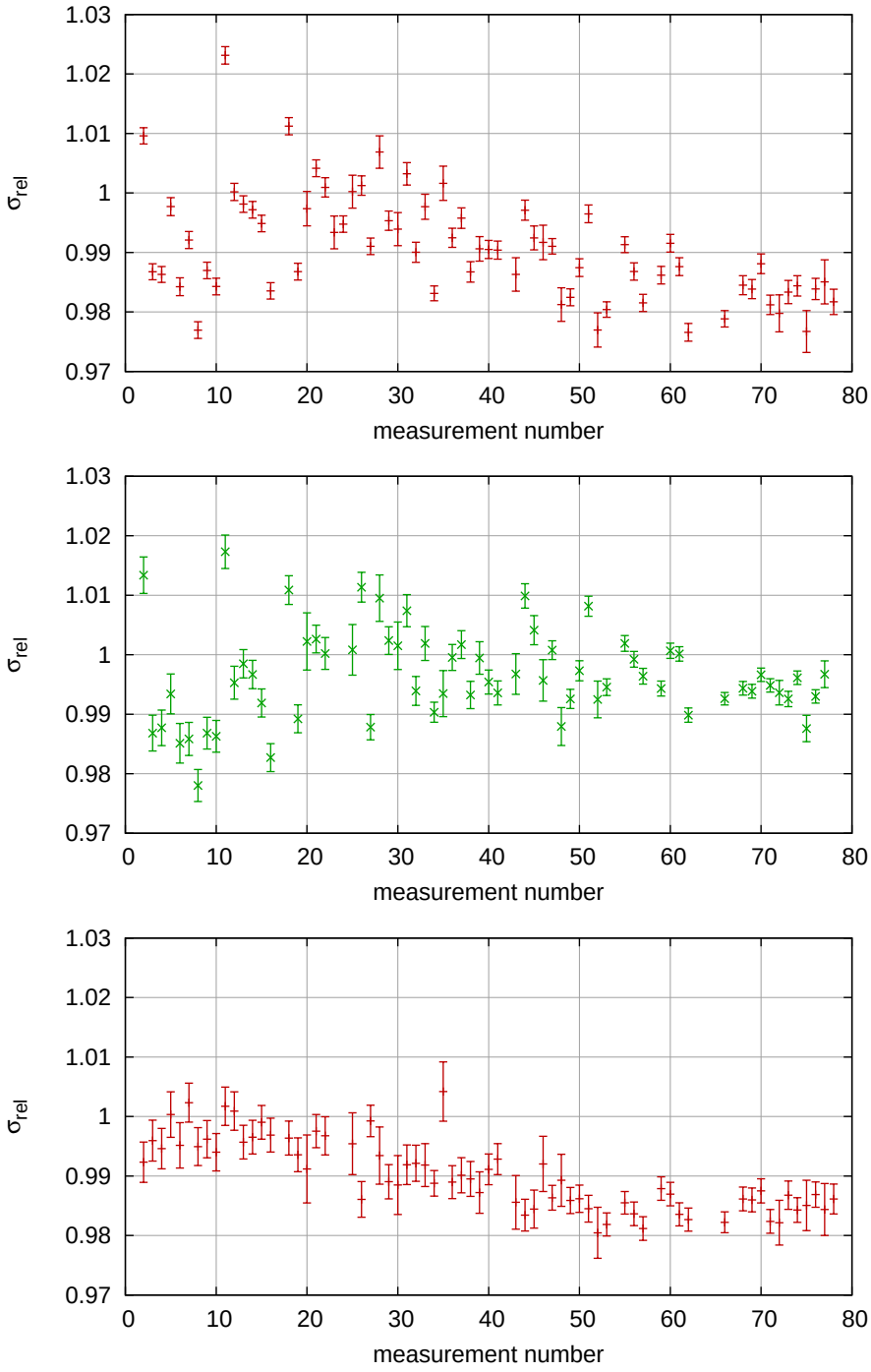

Figure 6.16: The effects of the luminosity-monitor normalization for the 180 MeV data. Top: Uncorrected (relative) cross sections measured with spectrometer A vs. time (number of measurement, scattering angles vary from 35.5° to 85.5°). Middle: Measurements of the luminosity-monitor spectrometer C at a fixed angle of 73°. The correlation is obvious (see also figure 6.15). Bottom: Corrected data from spectrometer A. The scattering of the data is significantly reduced, the remaining tendency in the data shows the deviation from the standard dipole.

6.6 Further corrections and anomalies

The level of statistical precision achieved in this experiment together with the conceptual design of overlapping acceptances made several anomalies apparent, which would have been missed in a traditional type of experiment. Some of them are handled automatically by the way the data are analyzed. These are described in appendix B. For others, the cause could be understood and corrections could be calculated (subsection 6.6.1). However, the cause for an anomaly in the 315 MeV data could not be found, therefore these data need a particular treatment (see subsection 6.6.2).

6.6.1 Corrections

In the course of the analysis it was found that the acceptances of spectrometers A and C are not completely given by the sheer geometry of the collimators, instead, they depend to some extent on the the vertex position. A corresponding correction has been determined and is now included in the simulation package. Details can be found in appendix C.

Furthermore it was found that the magnetic field of spectrometer C influences the measurement with spectrometer B when the spectrometers are close to each other: Then the field of the quadrupole of spectrometer C influences the trajectories of the scattered electrons on their way to spectrometer B. The handling of this problem is explained in appendix D.

6.6.2 315-MeV-anomaly

The 315 MeV data exhibit problems with spectrometer C which served as luminosity monitor. For the first half of the beam time, the cross sections, though measured at a constant angle, show a drift and there were jumps which are not correlated to the behavior of the cross sections measured with the other spectrometers. A closer look revealed that one of the VDC wires in spectrometer C was “hot”, i.e. it fired almost constantly. This may skew the result of the trajectory determination and thus may lead to lost trajectories if such wire is not excluded from the analysis. However, even after exclusion, the strange cross section behavior persisted.
A reduction of the data set to those events where this wire had no signal showed no drift, but then the number of events is so drastically reduced that the effect may be hidden in the statistical uncertainty. This also prohibits to use the reduced data set for normalization and such a cut would be questionable anyhow, since there is no good argument why the ratio of “good” to “bad” events should be constant in time. However, the vanishing of the effect with a cut on “good” events is an indication that the strange behavior is not caused by some unaccounted dead time due to the dead wire, since the dead time would still affect the reduced data set.
More likely is some kind of interference of the firing wire with the rest of the

electronics. While the ultimate cause could not be determined, the problem vanished half way through the beam time.
For the 315 MeV data set, this problem makes a normalization to the luminosity monitor impossible, and the analysis was performed with the luminosity determined by the pA-meter. Accordingly, this data subset may have a larger (statistical) error since for the pA-meter measurement, the cross section measurement has to be interrupted, hence it does not register beam current fluctuations while the cross section measurement is performed.

6.7 Results

The described procedures yield 1422 cross section measurements. Due to the division by the simulation, the internal and external radiation has been taken into account and one gets cross sections relative to the cross section calculated from the standard dipole, integrated over the acceptances of the spectrometers. They will now be analyzed by global fits of different models (see chapter 7). The cross section results of these fits, which also fix the normalization, are presented in chapter 8, the cross section values are listed in appendix K.1.

7 Parametrizations for the form factors

For a direct fit of the measured cross sections, an ansatz has to be made for the description of the form factors. Care has to be taken that the final results do not depend on a particular choice of the form factor parametrization. The model bias can only be judged in the context of an appropriate selection of models of different kinds. In the following, the models used in this work will be discussed. All models are normalized to 1 at $Q^2 = 0$. — For the magnetic form factor G_M the factor μ_p has been suppressed to improve readability.

7.1 Dipole

The standard dipole

$$G_{\text{standard dipole}}(Q^2) = \left(1 + \frac{Q^2}{0.71\,(\text{GeV}/c)^2}\right)^{-2} \tag{7.1}$$

emerged from the measurements by Hand et al. [HMW63]. For a long time, it was the accepted form for the electric form factor of the proton, and – scaled with $\mu_{p/n}$ – also for the magnetic form factor of both the proton ("scaling relation") and the neutron, and it is found in many text books (e.g. [PRSZ04]). While the choice of the dipole form was originally purely phenomenological, the related exponential fall-off in r-space comes about as the probability function of a quantum mechanical particle trapped in a narrow potential well.
In the present analysis, the scaling relation is not enforced. Instead different parameters for the electric and magnetic form factor are used:

$$G^{E,M}_{\text{dipole}}(Q^2) = \left(1 + \frac{Q^2}{a^{E,M}}\right)^{-2}. \tag{7.2}$$

With only two free parameters, a^E and a^M, this model is very rigid, and it will be seen that it is not able to describe the data of this experiment, as was the case already for earlier data (e.g. Simon et al. [SSBW80]).

7.2 Double dipole

A somewhat more flexible ansatz consists of the sum of two dipoles:

$$G^{E,M}_{\text{double dipole}}(Q^2) = a_0^{E/M}\left(1 + \frac{Q^2}{a_1^{E/M}}\right)^{-2} + \left(1 - a_0^{E,M}\right)\left(1 + \frac{Q^2}{a_2^{E/M}}\right)^{-2}. \tag{7.3}$$

The model is invariant under the exchange

$$a_1^{E,M} \Leftrightarrow a_2^{E,M}, \quad a_0^{E,M} \Leftrightarrow (1 - a_0^{E,M}). \tag{7.4}$$

This ambiguity might cause problems for the optimization algorithm.

7.3 Polynomials

7.3.1 Simple polynomial

A polynomial is a simple model without assumptions for the devolution of the form factors except some level of continuity or smoothness. The constant term is fixed to 1 by the normalization constraint $G^{E,M}(0) = 1$. With a polynomial of the order n, the form factors are parametrized as:

$$G^{E,M}_{\text{polynomial,n}}(Q^2) = 1 + \sum_{i=1}^{n} a_i^{E,M} \cdot Q^{2 \cdot i}. \tag{7.5}$$

Since the form factors drop rapidly with Q^2, a rather high order is needed to describe them adequately over a larger Q^2 range.

7.3.2 Polynomial $\times$ dipole

In order to free the polynomial from the necessity to describe the gross behavior of the form factors, the latter may be accounted for by multiplying the polynomial by the standard dipole:

$$G^{E,M}_{\text{polynomial}\times\text{dipole,n}}(Q^2) = G_{\text{standard dipole}}(Q^2) \times \left(1 + \sum_{i=1}^{n} a_i^{E,M} \cdot Q^{2 \cdot i}\right). \tag{7.6}$$

In principle, it is possible to optimize also the parameter of the dipole. It was found, however, that this additional freedom does not improve the fits while the fit consumes much more computer time.

7.3.3 Polynomial + dipole

A variation of the aforementioned splitting-off of the gross behavior of the form factors is the sum of a polynomial and the standard dipole instead of the product:

$$G^{E,M}_{\text{polynomial+dipole,n}}(Q^2) = G_{\text{standard dipole}}(Q^2) + \left(\sum_{i=1}^{n} a_i^{E,M} \cdot Q^{2 \cdot i}\right). \tag{7.7}$$

While the multiplication parametrizes the relative deviation from the standard dipole, the sum parametrizes the absolute deviation.

7.3.4 Inverse polynomial

A variation of the polynomial model is the inverse polynomial ansatz as in [Arr04]:

$$G^{E,M}_{\text{inv. poly.,n}}(Q^2) = \frac{1}{1 + \sum_{i=1}^{n} a_i^{E,M} \cdot Q^{2 \cdot i}}. \tag{7.8}$$

7.4 Splines

In polynomial models, the behavior of the model in different Q^2 regions is highly correlated. Therefore, possible shortcomings in the description of the data in one Q^2 region may influence negatively the description in other regions. Functions that decouple the behavior in different Q^2 regions to a greater extent are splines.
A spline is a function that is assembled piecewise from polynomials of a certain (low) order n. The points where the polynomial pieces join are called knots. There, an $(n-1)$-times continuous differentiability is enforced. If the knots are equidistant, the spline is called uniform.
A spline ansatz has multiple advantages. Depending on the number of knots, a spline can be very flexible. Nevertheless, the fit converges even for a large number of knots very quickly since each parameter essentially only affects a limited part of the curve.
The knots have to be chosen appropriately for the Q^2 range of the data.
It is clear that a spline is not suited for extrapolations.

7.4.1 Plain uniform cubic spline

Cubic splines are assembled from polynomials of the third order. Due to the continuity constraints, a cubic spline with k knots ($k-1$ polynomials with four parameters each) has only $k+2$ parameters. The spline segment between the ith and $(i+1)$th knot can be written in matrix notation as:

$$S_i(t) = \frac{1}{6} \begin{bmatrix} t^3 & t^2 & t & 1 \end{bmatrix} \begin{bmatrix} -1 & 3 & -3 & 1 \\ 3 & -6 & 3 & 0 \\ -3 & 0 & 3 & 0 \\ 1 & 4 & 1 & 0 \end{bmatrix} \begin{bmatrix} p_{i-1} \\ p_i \\ p_{i+1} \\ p_{i+2} \end{bmatrix}. \tag{7.9}$$

Here, $t \in [0,1]$ denotes the position between the two knots Q_i^2 and Q_{i+1}^2:

$$t = \frac{Q^2 - Q_i^2}{Q_{i+1}^2 - Q_i^2}. \tag{7.10}$$

To enforce the normalization constraint, the ansatz is chosen as

$$G^{E,M}_{\text{spline}}(Q^2) = 1 + Q^2 \cdot S^{E,M}(Q^2). \tag{7.11}$$

7.4.2 Cubic spline × dipole

Following the same considerations as in subsection 7.3.2, it might be advantageous to multiply the spline ansatz with the standard dipole. This leads to the ansatz

$$G^{E,M}_{\text{spline}\times\text{dipole}}(Q^2) = G_{\text{standard dipole}}(Q^2) \cdot \left(1 + Q^2 \cdot S^{E,M}(Q^2)\right). \tag{7.12}$$

7.5 Friedrich-Walcher parametrization

In their analysis of the world form factor data, Friedrich and Walcher [FW03] used an ansatz that is composed from a smooth part and a "bump". The smooth part is identical to the double dipole ansatz:

$$G_S\left(Q^2, a_0, a_1, a_2\right) = a_0 \left(1 + \frac{Q^2}{a_1}\right)^{-2} + (1 - a_0)\left(1 + \frac{Q^2}{a_2}\right)^{-2}. \tag{7.13}$$

The bump contribution consists of a Gaussian in Q^2 with an amplitude a_b, position Q_b and a width σ_b. If $Q_b \neq 0$, the Taylor expansion of the Gaussian has odd powers, which is not allowed for form factors. This is circumvented by adding another Gaussian which is mirrored at $Q^2 = 0$, as has been done by Sick [Sic74] for a model-independent analysis of nuclear charge distributions in r-space. The bump contribution is hence described by:

$$G_b\left(Q^2, Q_b, \sigma_b\right) = e^{-\frac{1}{2}\left(\frac{Q-Q_b}{\sigma_b}\right)^2} + e^{-\frac{1}{2}\left(\frac{Q+Q_b}{\sigma_b}\right)^2} \tag{7.14}$$

To attribute the full normalization to the smooth part, the bump contribution is multiplied by Q^2. The complete model is therefore:

$$G^{E,M}_{\text{Friedrich}-\text{Walcher}}(Q^2) = G_S\left(Q^2, a^{E/M}_{0,1,2}\right) + a^{E/M}_b \cdot Q^2 G_b\left(Q^2, Q^{E/M}_b, \sigma^{E/M}_b\right) \tag{7.15}$$

7.6 Extended Gari-Krümpelmann model

While all previous models are just mathematical functions for the description of the data, the extended Gari-Krümpelmann model [GK92; Lom01; Lom02; Lom06] – actually a group of models which differ only in details – is based on physical considerations. In this work, the version called DR-GK'(1) ([Lom01]) respectively GKex(01) ([Lom02; Lom06]) is selected, since it had the best results in [Lom06] for existing proton form factor data when the normalization of the data sets is not varied.
Under the assumption that QCD is the fundamental theory of the strong interaction, the electromagnetic form factors can be calculated in perturbative QCD (pQCD) for very high momentum transfers. For small momentum transfers, the confinement property of QCD leads to an effective hadronic description with

vector meson dominance (VMD), the coupling of a photon to a vector meson which itself couples to the nucleon.
Earlier models that were based solely on VMD introduced multiple, phenomenological poles of higher mass besides the ρ, ω and ϕ-poles. Gari and Krümpelmann limit the VMD contributions to these three poles, but enforce the asymptotic Q^2 behavior dictated by the scaling behavior of pQCD by additional terms. In the model used here, the dispersion integral approximation of the ρ meson contribution is replaced by an analytical form. The model was extended to include the $\rho'(1450)$-pole (for details see [GK92; Lom01]).
As has been described in section 2.1, the form factors can be written either as the Sachs form factors G_E and G_M or as the Dirac and Pauli form factors F_1 and F_2, which can be divided into an isoscalar and an isovector component:

$$2F_{1,2}^{p} = F_{1,2}^{is} + F_{1,2}^{iv}, \qquad 2F_{1,2}^{n} = F_{1,2}^{is} - F_{1,2}^{iv}. \tag{7.16}$$

The model GKex(01) is formulated in terms of these four form factors with the poles for ρ, ρ', ω, ω' and ϕ mesons:

$$\begin{aligned}
F_1^{iv}\left(Q^2\right) &= \frac{N}{2}\frac{1.0317 + 0.0875\left(1+Q^2/0.3176\right)^{-2}}{\left(1+Q^2/0.5496\right)}F_1^{\rho}\left(Q^2\right) \\
&\quad + \frac{g_{\rho'}}{f_{\rho'}}\frac{m_{\rho'}^2}{m_{\rho'}^2+Q^2}F_1^{\rho}\left(Q^2\right) + \left(1 - 1.1192\frac{N}{2}\frac{g_{\rho'}}{f_{\rho'}}\right)F_1^{D}\left(Q^2\right), \\
F_2^{iv}\left(Q^2\right) &= \frac{N}{2}\frac{5.7824 + 0.3907\left(1+Q^2/0.1422\right)^{-1}}{\left(1+Q^2/0,5362\right)}F_2^{\rho}\left(Q^2\right) \\
&\quad + \kappa_{\rho'}\frac{g_{\rho'}}{f_{\rho'}}\frac{m_{\rho'}^2}{m_{\rho'}^2+Q^2}F_2^{\rho}\left(Q^2\right) + \left(\kappa_{\nu} - 6.1731\frac{N}{2} - \kappa_{\rho'}\frac{g_{\rho'}}{f_{\rho'}}\right)F_2^{D}\left(Q^2\right), \\
F_1^{is}\left(Q^2\right) &= \sum_{\alpha=\omega,\omega',\phi}\frac{g_{\alpha}}{f_{\alpha}}\frac{m_{\alpha}^2}{m_{\alpha}^2+Q^2}F_1^{\alpha}\left(Q^2\right) + \left(1 - \frac{g_{\omega}}{f_{\omega}} - \frac{g_{\omega'}}{f_{\omega'}}\right)F_1^{D}\left(Q^2\right), \\
F_2^{is}\left(Q^2\right) &= \sum_{\alpha=\omega,\omega',\phi}\kappa_{\alpha}\frac{g_{\alpha}}{f_{\alpha}}\frac{m_{\alpha}^2}{m_{\alpha}^2+Q^2}F_2^{\alpha}\left(Q^2\right) \\
&\quad + \left(\kappa_s - \kappa_{\omega}\frac{g_{\omega}}{f_{\omega}} - \kappa'_{\omega}\frac{g_{\omega'}}{f_{\omega'}} - \kappa_{\phi}\frac{g_{\phi}}{f_{\phi}}\right)F_2^{D}\left(Q^2\right).
\end{aligned} \tag{7.17}$$

In this model, the form factors F_i^{α} ($\alpha = \rho$, ω, ω', ϕ, meson-nucleon) and F_i^{D} (quark-nucleon) are parametrized as:

$$\begin{aligned}
F_1^{\alpha,D}\left(Q^2\right) &= \frac{\lambda_{1,D}^2}{\lambda_{1,D}^2+\tilde{Q}^2}\frac{\lambda_2^2}{\lambda_2^2+\tilde{Q}^2}, \\
F_2^{\alpha,D}\left(Q^2\right) &= \frac{\lambda_{1,D}^2}{\lambda_{1,D}^2+\tilde{Q}^2}\left(\frac{\lambda_2^2}{\lambda_2^2+\tilde{Q}^2}\right)^2,
\end{aligned} \tag{7.18}$$

$$
\begin{aligned}
F_1^{\phi}\left(Q^2\right) &= F_1^{\alpha}\left(Q^2\right) \cdot \left(\frac{Q^2}{\lambda_1^2 + Q^2}\right)^{\frac{3}{2}}, \\
F_2^{\phi}\left(Q^2\right) &= F_2^{\alpha}\left(Q^2\right) \cdot \left(\frac{\lambda_1^2}{\mu_\phi^2}\frac{Q^2 + \mu_\phi^2}{\lambda_1^2 + Q^2}\right)^{\frac{3}{2}},
\end{aligned} \tag{7.19}
$$

with

$$
\tilde{Q}^2 = Q^2 \frac{\ln\left[\left(\lambda_D^2 + Q^2\right)/\lambda_{\mathrm{QCD}}^2\right]}{\ln\left(\lambda_D^2/\lambda_{\mathrm{QCD}}^2\right)}. \tag{7.20}
$$

The parametrization fulfills the normalization constraint[1] for $Q^2 = 0$. The constants κ_ν, κ_s and the masses m_ρ, m_ω, m_ϕ, $m_{\rho'}$ and $m_{\omega'}$ are taken as $\kappa_\nu = 3.706$, $\kappa_s = -0.12$, $m_\rho = 0.776\,\mathrm{GeV}$, $m_\omega = 0.784\,\mathrm{GeV}$, $m_\phi = 1.019\,\mathrm{GeV}$, $m_{\rho'} = 1.45\,\mathrm{GeV}$ and $m_{\omega'} = 1.419\,\mathrm{GeV}$.
There remain at most 14 free parameters: Eight couplings (four g_α/f_α, four κ), four cut-off masses (λ_1, λ_2, λ_D and μ_ϕ), the mass λ_{QCD}, which gives the size of the logarithmic Q^2 behavior, and the normalization parameter N for the dispersion relation part of the ρ meson.
In [Lom02], at most 12 of these parameters were varied, since either the ω' meson contribution was neglected or N and λ_{QCD} were fixed to $N = 1$ and $\lambda_{\mathrm{QCD}} = 0.150$, the physical value. The latter constraints are also used in the present work. Still, the fitting of the model was very time-consuming due to the logarithmic terms and slow convergence to the optimum.

[1] In this model, μ_p is neither suppressed nor does it show explicitly, i.e. $G_m(0) = F_1^p(0) + F_2^p(0) = 1 + \kappa_p = \mu_p$.

8 Fit of the form factor models to the cross sections and selection of the models

The experimentally determined cross sections are analyzed using a direct fit of the different models for the form factors.
As has been mentioned before, it is almost impossible to determine the global normalization down to a sub-percent level directly from a precise knowledge of all relevant properties of the experiment. Therefore, the normalization is left floating, i.e. for each data group a scaling parameter is included in the fit (details see appendix G). Overall, 31 normalization constants are used as free parameters in addition to the model parameters in the fit to a total of 1422 cross sections.

The fit minimizes the function

$$\chi^2 = \sum_i \left(r_i - n_i \cdot \frac{\int_{A_i} \left(\frac{\mathrm{d}\sigma}{\mathrm{d}\Omega}\right)_{\text{model}} \mathrm{d}\Omega}{\int_{A_i} \left(\frac{\mathrm{d}\sigma}{\mathrm{d}\Omega}\right)_{\text{std. dipole}} \mathrm{d}\Omega} \right)^2 / (\Delta r_i)^2. \tag{8.1}$$

Here, r_i is the ratio of the ith measured cross section to the standard dipole, A_i is the acceptance of measurement i, and Δr_i is the statistical error of r_i. n_i is the normalization constant for the data group to which measurement i belongs. $\left(\frac{\mathrm{d}\sigma}{\mathrm{d}\Omega}\right)_{\text{model}}$ and $\left(\frac{\mathrm{d}\sigma}{\mathrm{d}\Omega}\right)_{\text{std. dipole}}$ are the cross sections calculated from the fit model and from the standard dipole, respectively.
The integration over the acceptance is done numerically.

8.1 Scaling of the statistical errors

Besides the errors of counting statistics and dead time estimation, different additional effects contribute to the statistical error. These include the normalization to the luminosity measurement and the uncertainty of the current measurement for the 315 MeV data (see subsection 6.6.2), the statistical error of the background estimation and undetected slight variations of the detector and accelerator performance. To estimate these effects, one can inspect for specific data groups[1] the distribution of the deviation of the data points from the fit, divided by the error from the counting statistics and normalization.

[1] Grouped by incident beam energy and spectrometer the data is measured with.

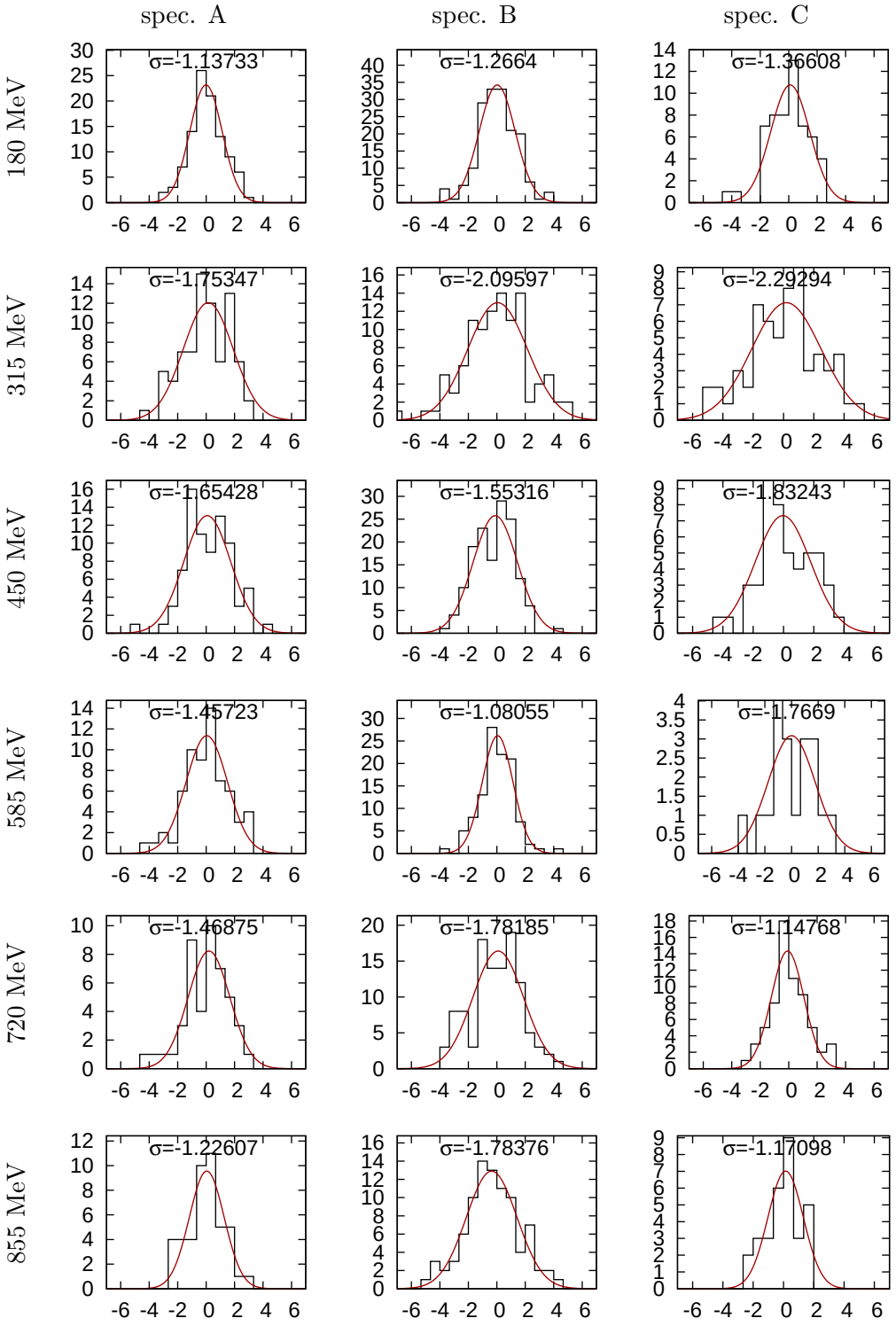

Figure 8.1: The distribution of the deviations of the data points from the spline fit, divided by the estimated statistical errors, with the data grouped by energy and spectrometer. The distributions for the 315 MeV data are significantly wider, since these data could not be normalized to the luminosity measurement.

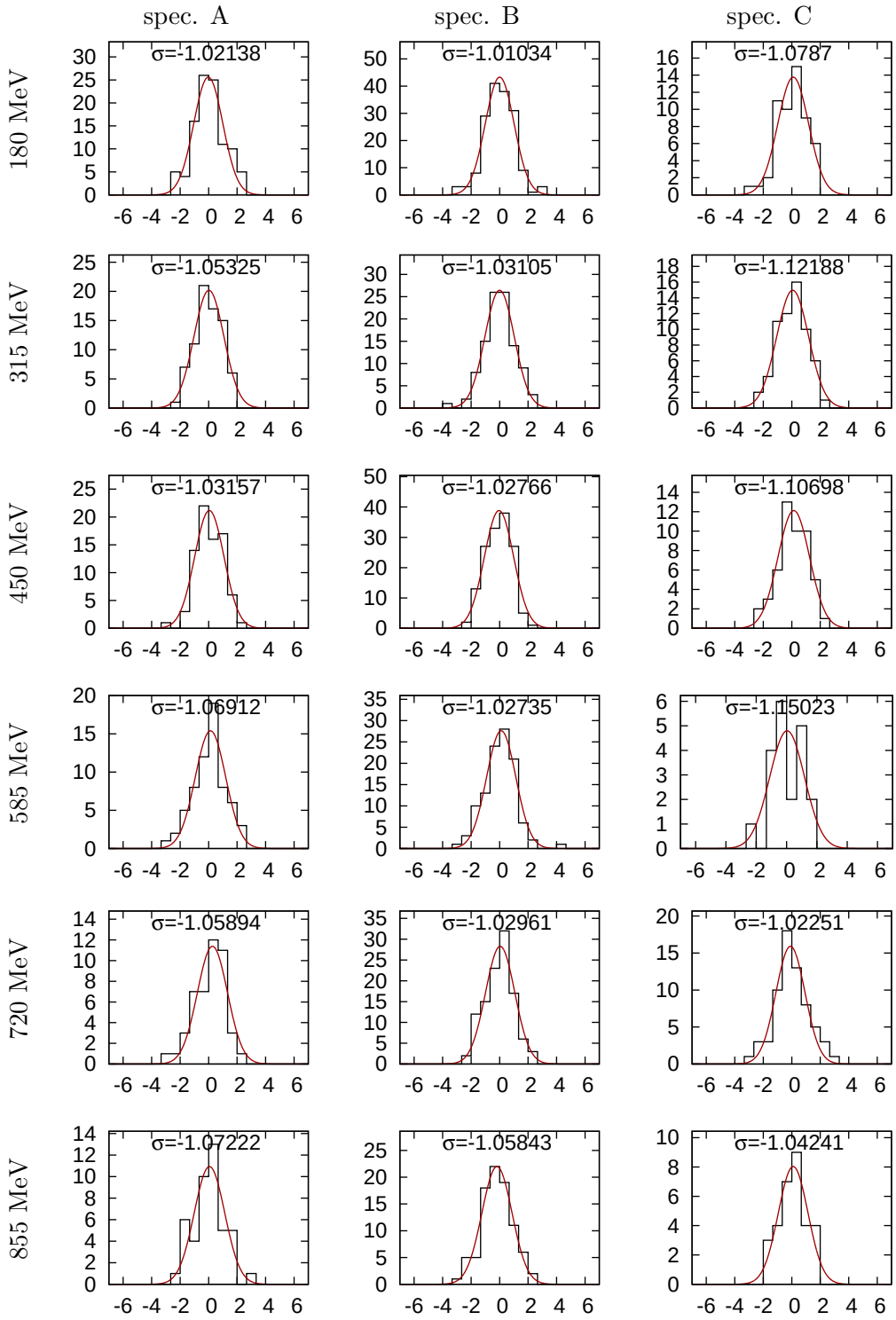

Figure 8.2: Like fig. 8.1, but with the errors scaled.

The results are presented in figure 8.1 for the fit with the spline model with 8 parameters per form factor. The widths of the distributions were determined by a fit of Gaussians.

The errors of the different data groups are then scaled by these widths, and the fit is redone; after one iteration, some of the width are now significantly below 1. The scaling factors of those groups are subsequently reduced until all widths are above one. Therefore, the final χ^2 per degree of freedom is expected to be slightly larger than unity (in fact, to achieve a reduced χ^2 of unity for the best models, the statistical error would have to be increased additionally by less than 7%).

The final distributions of the deviations are depicted in figure 8.2.

By this scaling of the errors, single cross sections calculated from the fit change at most by 0.3%.

8.2 Determination of model parameter number and model selection

The spline and polynomial models allow for a varying number of parameters. For the determination of the optimal number, one encounters the basic fact that it is not possible to determine simultaneously which model describes the data and how statistically pure a data sample is. In the extreme case, a model goes through all data points, i.e. it interpolates the data. The choice of the number of parameters is therefore a trade-off: With too few parameters, the model cannot describe the data and deduced quantities cannot be trusted; on the other hand, a fit with too many parameters starts to follow local deviations instead of averaging out fluctuations.

To find the optimal number of parameters, the reduced χ^2,

$$\chi^2_{\text{red}} = \frac{\chi^2}{\text{number of data points} - \text{number of parameters}}, \tag{8.2}$$

is used.

In figure 8.3, χ^2_{red} is shown as a function of the number of parameters N_p for the different models for the form factors. A plateau is reached at around ten parameters per form factor. In each group, the model with the standard dipole multiplied in reaches the plateau with one to two parameters less. Interestingly, for the spline models χ^2_{red} starts to drop again when the parameter number reaches twelve; the fits then start to show oscillations at a Q^2 above 0.4 $(\text{GeV}/c)^2$.

The number of parameters were selected as the lowest number where the plateau was surely reached. While not directly visible in the χ^2 value, the polynomial $\times$ dipole model starts to oscillate at higher Q^2 for orders above 9, so an order of 8 has been selected. The inverse polynomial reaches the plateau already with 7 parameters. Table 8.1 summarizes the used parameter numbers.

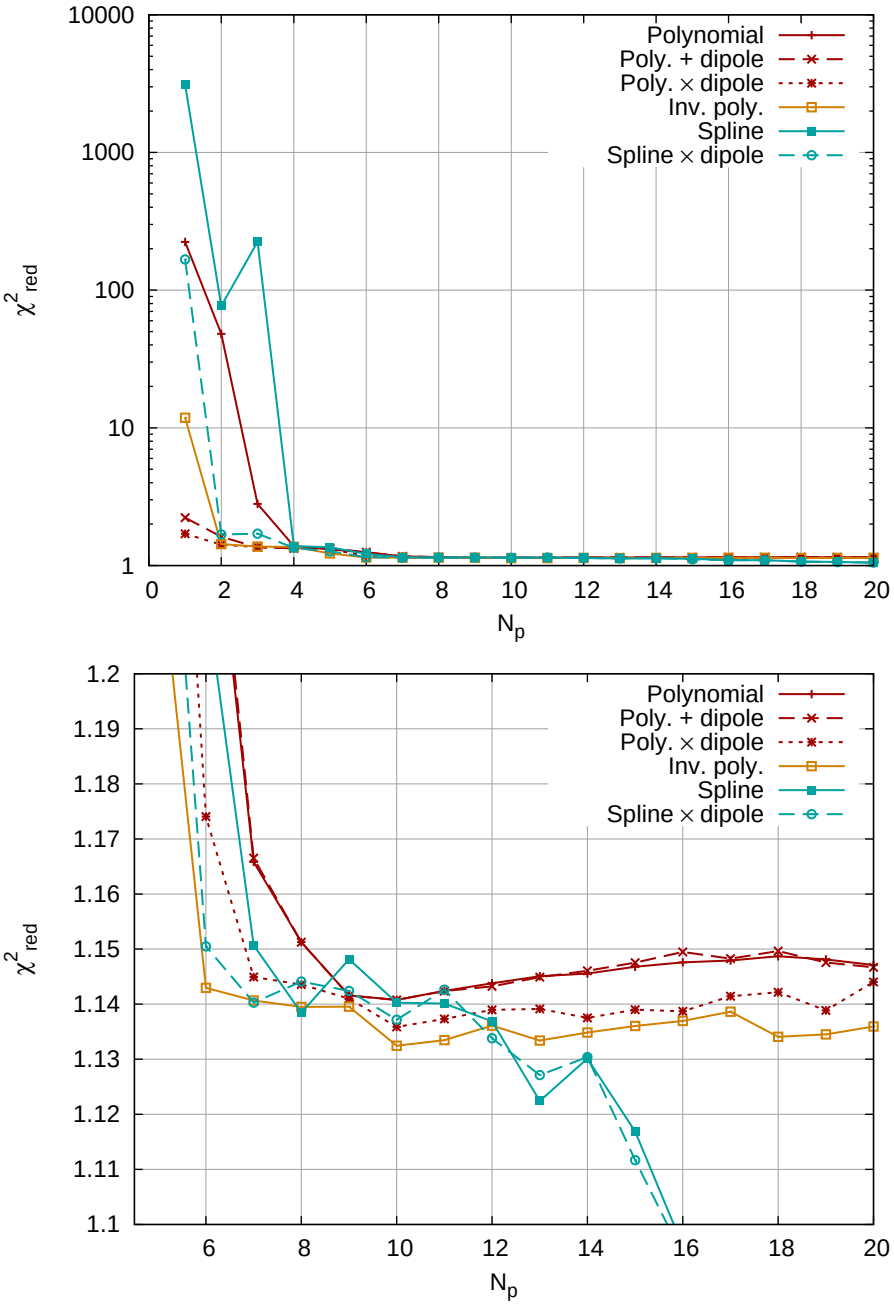

Figure 8.3: Dependence of χ^2_{red} on the number of parameters N_p of the form factor parametrizations for different polynomial and spline models.

	Poly.	Poly. + dip.	Poly. × dip.	Inv. poly.	Spline	S. × dip.
Order	10	10	8	7	8	7

Table 8.1: Selected orders for polynomial and spline models.

Model	χ^2	Number of parameters	χ^2_{red}
Single dipole	3422	$2 \times 1 + 31$	2.4635
Double dipole	1786	$2 \times 3 + 31$	1.2893
Polynomial	1563	$2 \times 10 + 31$	1.1399
Poly. + std. dipole	1563	$2 \times 10 + 31$	1.1400
Poly. × std. dipole	1572	$2 \times 8 + 31$	1.1436
Inv. poly.	1571	$2 \times 7 + 31$	1.1406
Spline	1565	$2 \times 8 + 31$	1.1385
Spline × std. dipole	1570	$2 \times 7 + 31$	1.1403
Friedrich-Walcher	1598	$2 \times 7 + 31$	1.1588
extended Gari-Krümpelmann	1759	$14 + 31$	1.2777

Table 8.2: The achieved total χ^2, the number of parameters and χ^2_{red} for the different models used in this thesis.

The flexible spline and polynomial models reach χ^2 values below 1600 (for 1422 data points). This is the baseline against which one can test the other models. Table 8.2 lists the achieved χ^2 value and number of parameters of the different models. The single-dipole fit results in a χ^2 of more than 3400, and, looking at a comparison of the data and the fit, the failing of this model is obvious (figure 8.4). The double dipole achieves a χ^2 of 1786, which is much closer to the results with the flexible models. Nevertheless, the model dependency analysis (appendix H) shows that the extraction of the radius by the double dipole is not reliable and, depending on the exact shape of the form factor, the deviations of the fit from the true value can be large.

The Friedrich-Walcher model reaches a χ^2 that is less than 2.5% larger than the best flexible model, well below the width of the χ^2 distribution ($\sigma_{\chi^2} \approx 58$); it is therefore included in the analysis.

The extended Gari-Krümpelmann model achieves a χ^2 of 1759, which is only slightly better than the double dipole. This fit is rather complicated and it seems that there are ambiguities in the solutions. Since the calculation and convergence is very slow due to the large number of logarithms and to the numerical properties of the model, it was not possible to perform a full study of this model. Such a study would need to vary the starting conditions and constraints. For a reliable fit of this model, it may be necessary to fix the 31 normalization parameters beforehand with one of the flexible models. Then, form factors can be extracted with the standard Rosenbluth technique (see subsection 9.2.2) and subsequently be used as data for a fit.

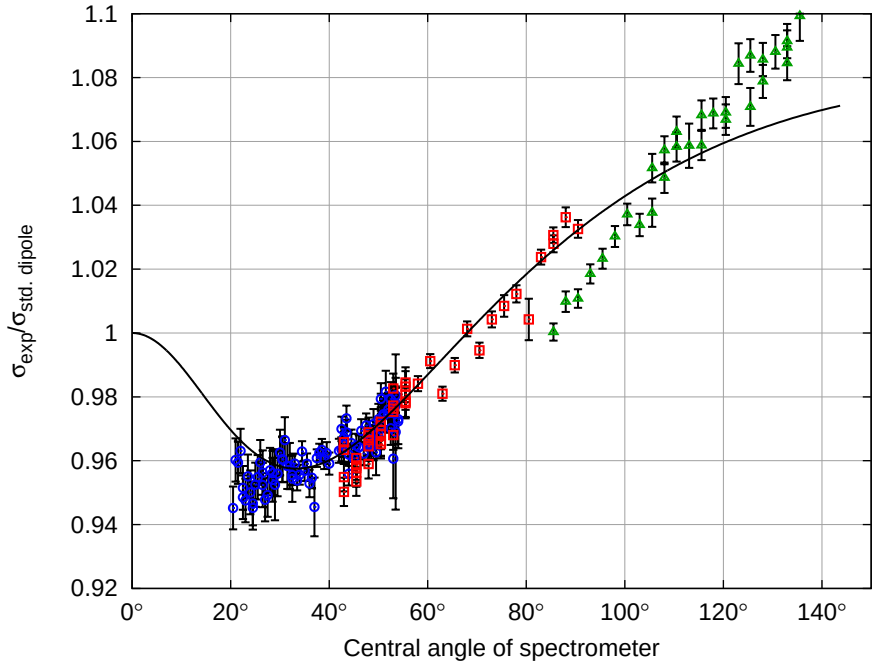

Figure 8.4: The single-dipole fit compared to the measured cross sections for an incident beam energy of 855 MeV. Here, as in the following figures, the data measured with spectrometers A, B and C are shown in red (squares), blue (dots) and green (triangles). Obviously, the single dipole cannot describe the rise of the cross section (compared to the standard dipole) at larger scattering angles. Since the normalization per data set is floating, these data sets are shifted down in order to minimize χ^2 (most visible for the data measured with spectrometer C).

8.3 Fits to the cross sections

Figures 8.5 to 8.10 show the normalized cross section data with the scaled statistical errors compared to the fits. To emphasize the precision of better than 0.4% (average) per data point, the cross sections are divided by the cross section given by the standard dipole. It has to be noted that the normalization parameters depend slightly on the fit. Therefore, to compare the data to a fit, the normalization of that fit should be used. However, the models that achieve a small χ^2 yield very similar normalizations, so it is reasonable to present the data normalized to the spline model only, which has the smallest χ^2_{red}. For the flexible models, the maximum difference in a normalization parameter is 0.26%, and the average standard deviation is 0.073% (see appendix G). The largest difference for the "good" models occurs for the 855 MeV data, where the (less flexible) Friedrich-Walcher model shifts the data slightly upwards, namely by 0.7% for the data measured with spectrometer C. To judge the size of this effect, in figure 8.10, the data points are additionally plotted with the

normalizations from the Friedrich-Walcher model (orange crosses).

For the models that do not achieve a χ^2 below 1600, i.e. the double-dipole and the extended Gari-Krümpelmann model, the differences in the normalization are larger (up to 1.6% in the case of the double-dipole fit). Both models would shift the cross sections down, therefore both fit curves are below the data with normalizations from the spline fit.

The analyses with the "good" models yield cross sections which differ by less than 1% for almost all of the Q^2 range of the data. In the high-Q^2 range, the fits start to diverge. Above 0.55 $(\mathrm{GeV}/c)^2$, only data from 720 MeV and 855 MeV contribute. Therefore, the separation into G_E and G_M is not well fixed. In the Q^2 region covered only by 855 MeV data, the allocation of the cross section strength to the electric or magnetic part is undetermined, giving rise to the larger spread of the models.

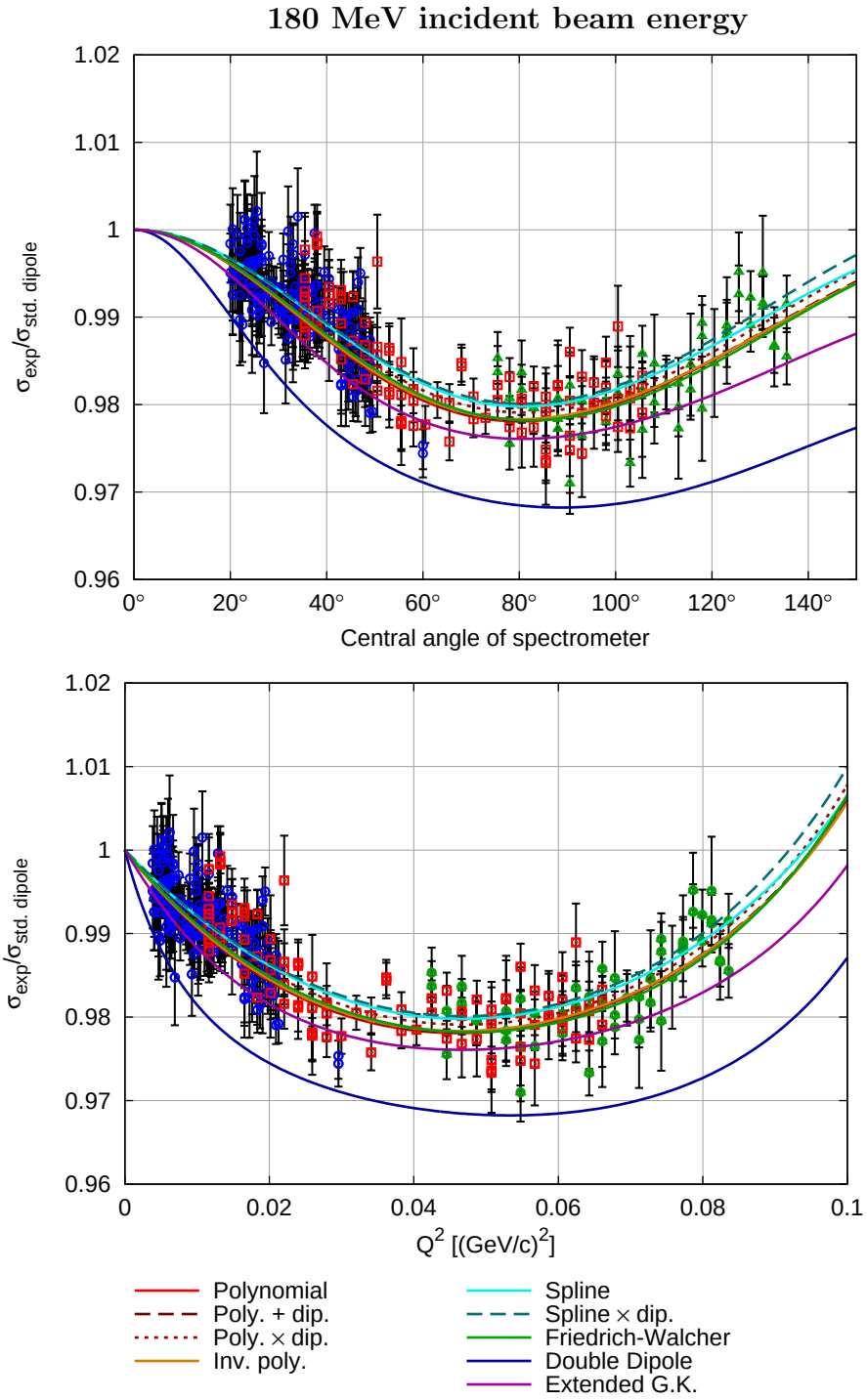

Figure 8.5: The measured cross sections and the fits for 180 MeV incident beam energy, divided by the cross section calculated from the standard dipole, as functions of the scattering angle (top) and of Q^2 (bottom). The normalization parameters of the data are taken from the spline fit. The fits that achieve a good χ^2 differ by at most 0.3%. The normalization parameters from the double-dipole fit would shift the data down by up to 1.6%. Accordingly, its curve lies below the data with the normalizations from the spline fit. (Symbols/colors as in fig. 8.4)

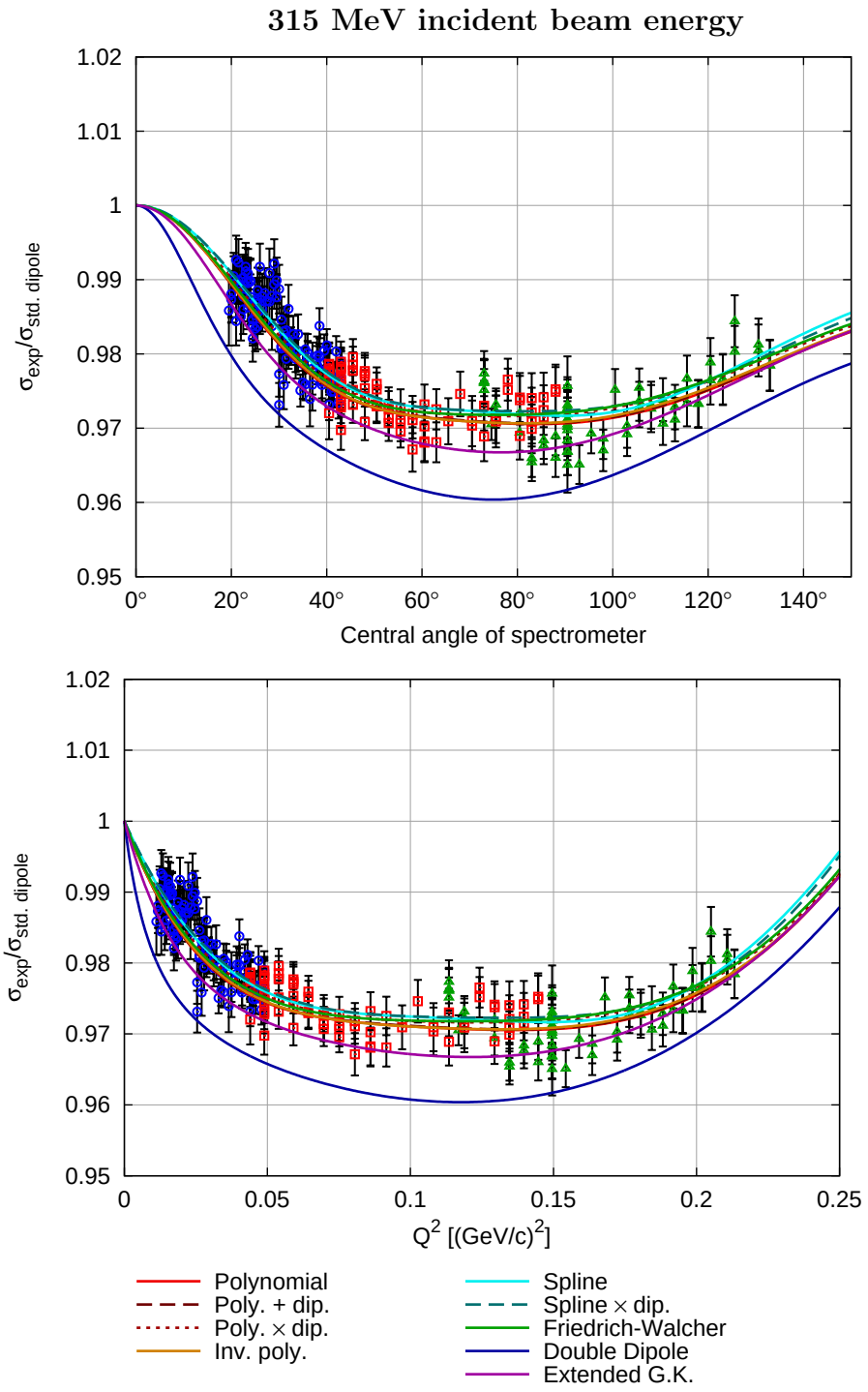

Figure 8.6: Same as fig. 8.5, but for 315 MeV incident beam energy. The difference between the models is smaller than for the 180 MeV data.

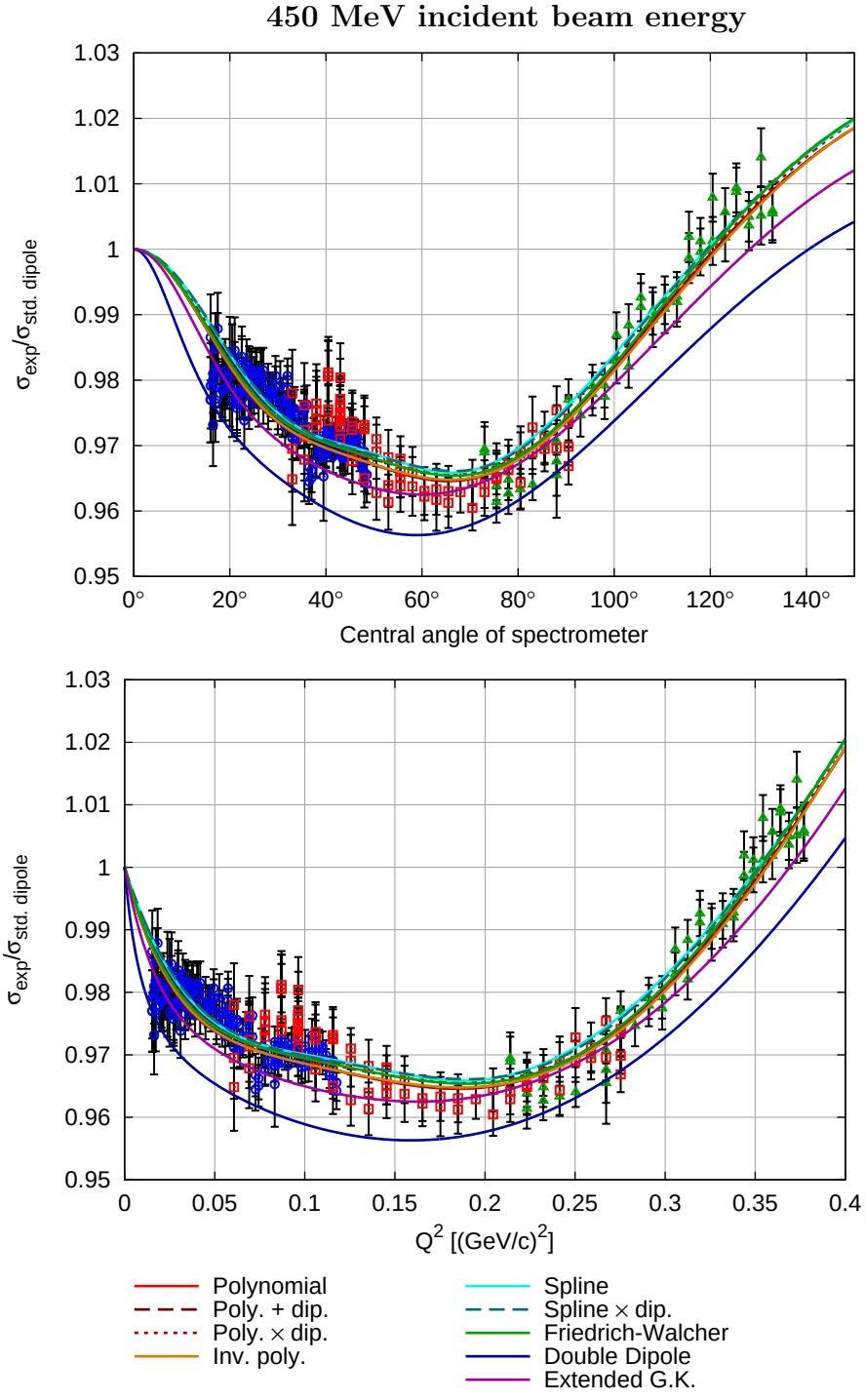

Figure 8.7: Same as fig. 8.5, but for 450 MeV incident beam energy.

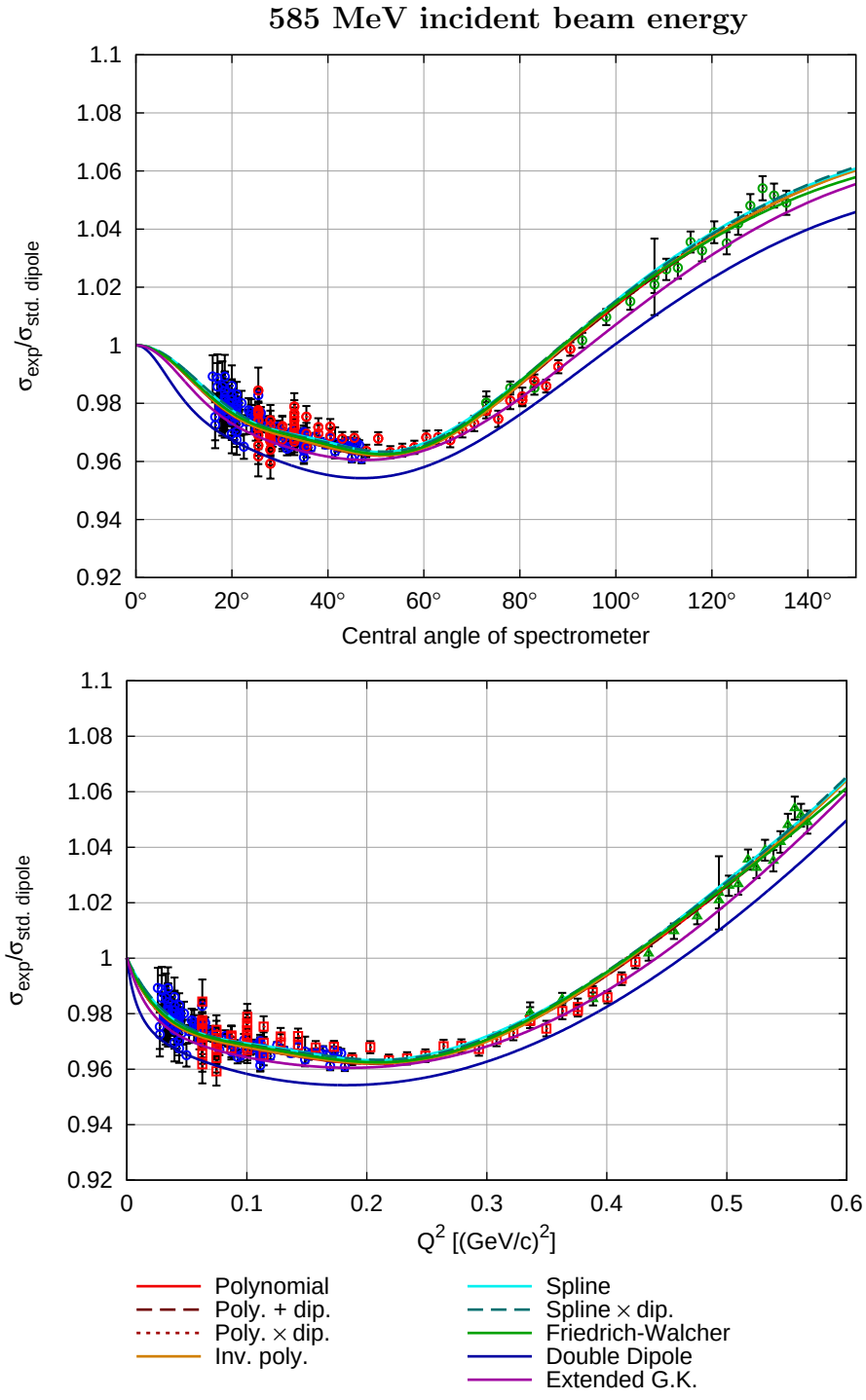

Figure 8.8: As fig. 8.5, but for 585 MeV incident beam energy.

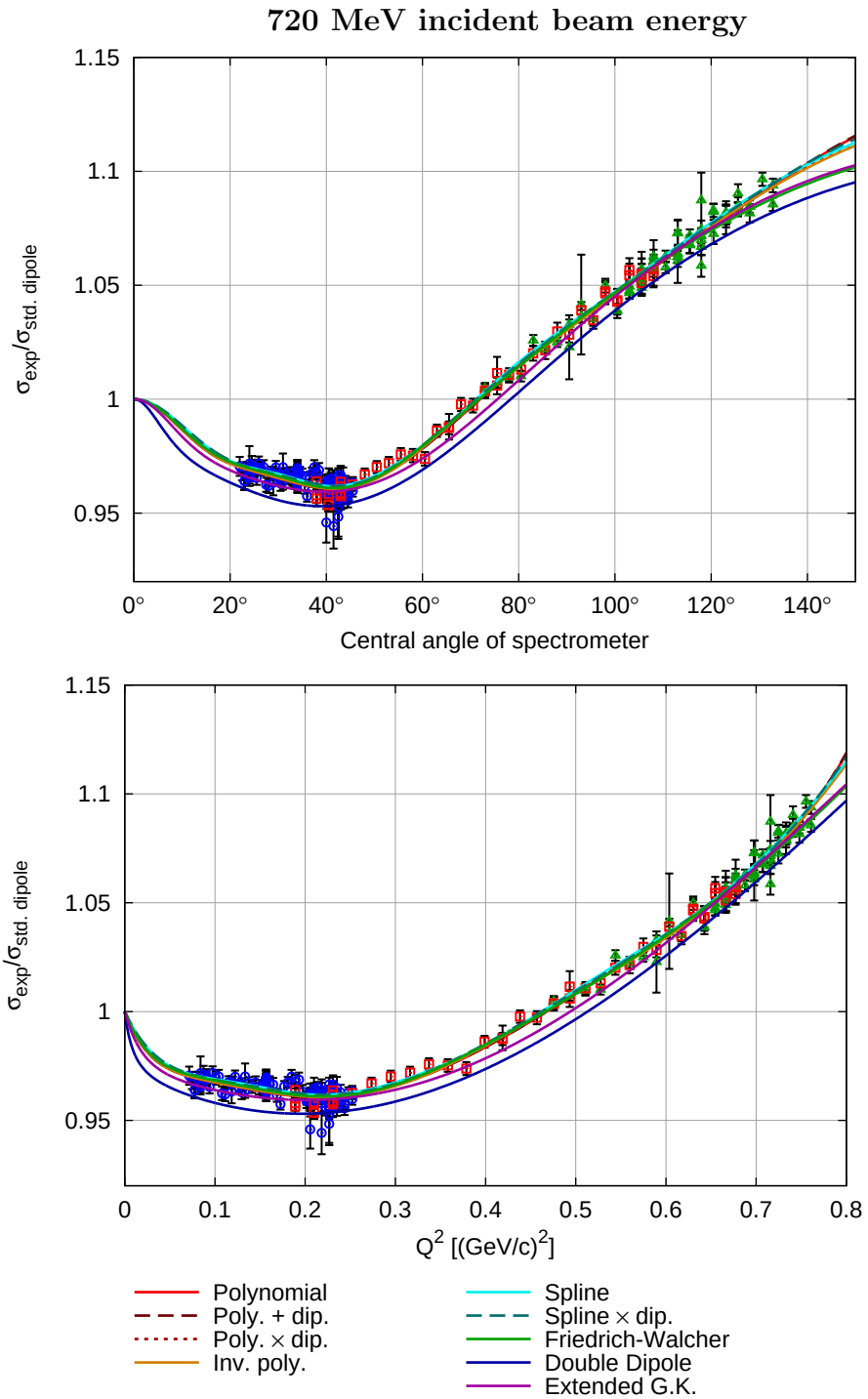

Figure 8.9: Same as fig. 8.5, but for 720 MeV incident beam energy. The "good" fits begin to diverge at Q^2 values above the data. Here, the form factor separation breaks down since there are only data from one energy (855 MeV).

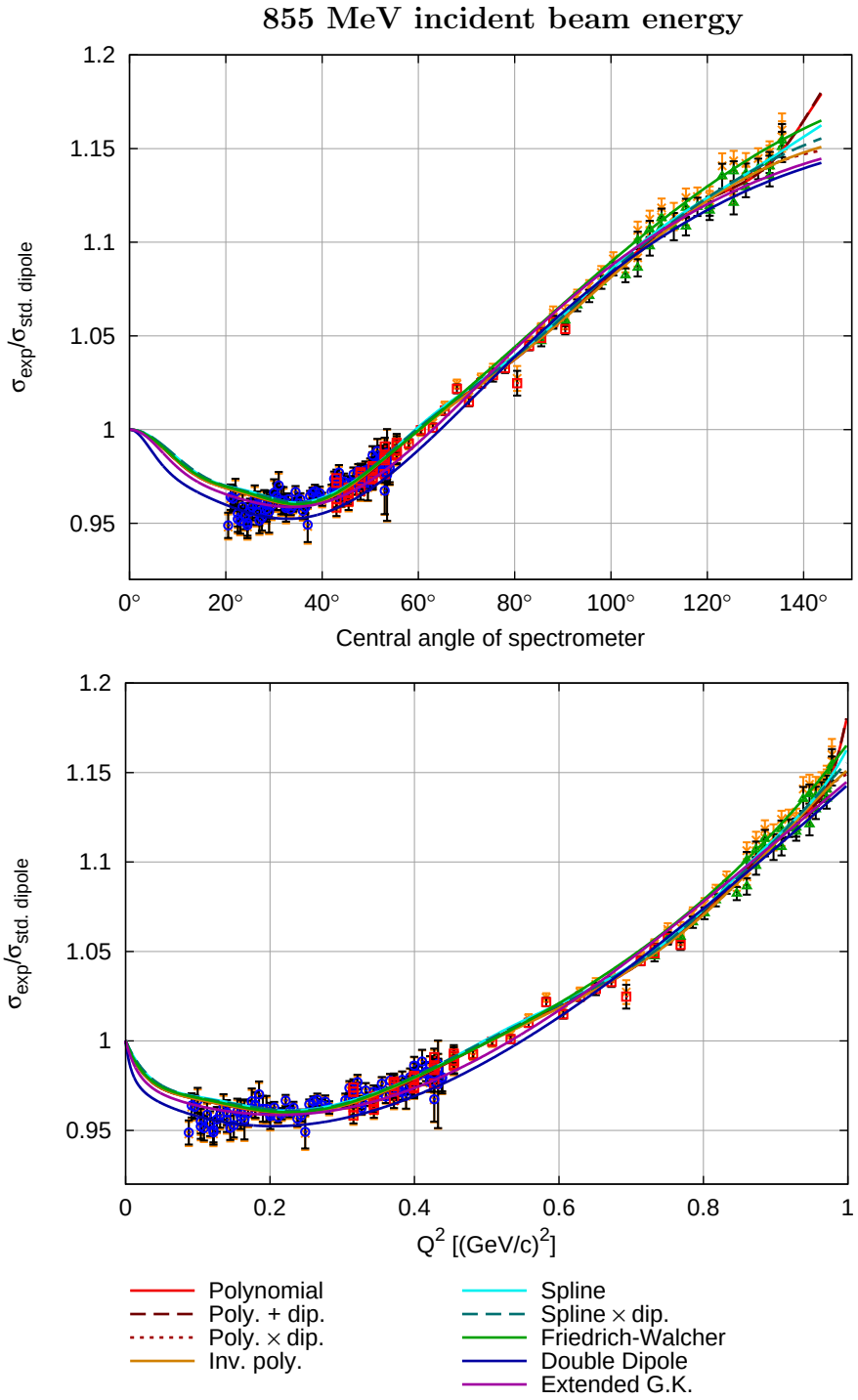

Figure 8.10: Same as fig. 8.5, but for 855 MeV incident beam energy. The orange (crosses) data points are normalized according to the Friedrich-Walcher fit; they differ from the data normalized with the more flexible models only above 90° (0.7 GeV/c)^2) and here by less than 0.7%. — The behavior of the flexible models beyond the 1 (GeV/c)^2 range is heavily influenced by just the highest points, as can be seen by the steep rise of the polynomial model to "catch" the last data point.

9 Results for the form factors and for the rms radii

9.1 Determination of the errors on the extracted form factors and radii

There are several contributions to the final error for the form factors and radii: The statistical error of the data, uncertainties from the experimental setup and systematical uncertainties from the model and from theory.

9.1.1 Statistical errors

Pointwise confidence band

The statistical uncertainties of the measured cross sections give rise to a statistical uncertainty of the extracted form factors. This uncertainty is expressed as a confidence band (or error band) to a given confidence level around the optimal fit.
Usually, this is taken as the symmetrical confidence band around the best fit, with a width calculated with standard error propagation. A model f, which describes the quantity y at the position x and which depends on a parameter vector $\vec{p}$, can be written as

$$y = f(x, \vec{p}). \tag{9.1}$$

The fit to the data y_i gives best fit parameters $\hat{\vec{p}}$. The parameters $\hat{\vec{p}}$ have uncertainties and correlations, described by the covariance matrix $\mathbf{V}(\vec{p})$ with $V_{i,j}(\vec{p}) = \mathrm{cov}(p_i, p_j)$. Standard error propagation[1] now gives the variance of y at the point x by

$$\sigma_y^2(x) = V(y(x)) = (\frac{\partial f}{\partial p_1}, \frac{\partial f}{\partial p_2}, \dots)^T \mathbf{V}(\vec{p}) (\frac{\partial f}{\partial p_1}, \frac{\partial f}{\partial p_2}, \dots). \tag{9.2}$$

Further details can be found in appendix I. By this method one constructs the pointwise confidence band with 68.3% confidence level (in case of Gaussian errors, the 1σ-errors), i.e. one expects the true value $y_{\mathrm{true}}(x)$ to be within the band with 68.3% probability at a given x (or Q^2 in our case):

$$P[f(x, \hat{\vec{p}}) - \sigma_y(x) \leq y_{\mathrm{true}}(x) \leq f(x, \hat{\vec{p}}) + \sigma_y(x)] = 0.683. \tag{9.3}$$

[1] In the case $\mathrm{cov}(p_i, p_j) = 0$ for $i \neq j$, this can be written as the more familiar $\sigma_y^2 = \sum_i \left(\frac{\partial y}{\partial p_i} \sigma_{p_i} \right)^2$.

To obtain the confidence band for a different confidence level, the width of the band has to be scaled accordingly.
This method is exact for models which are linear in the parameters. However, in the case at hand, the cross sections described by a form factor model do not depend linearly on the parameters. It is not easy to determine if a linear approximation is good enough in the parameter range which has to be exhausted to give the desired confidence level. Therefore, a different approach using Monte Carlo techniques has been taken.

Monte Carlo method

It is possible to estimate the confidence bands with Monte Carlo techniques: Taking the best fit to the data, one can calculate points on the fit curve at the original kinematical positions. Now, a large number (about 50 000) of pseudo data sets are generated: The calculated points are randomized according to the statistical errors of the original data. Additionally, the normalization of each normalization group is varied randomly according to a Gaussian with a width of 5% (it has been tested that the choice of this width has negligible influence on the result).
In essence, these data sets simulate the outcome of 50 000 experiments with 1422 cross section measurements each, under the assumption that the best fit represents the truth.

Each data set is now fitted with the model used in the original fit. From each fit result, the radii and the form factor values at a large number of different Q^2 are calculated. At each Q^2 and for the radii, the confidence band is now constructed around the best fit such that 68.3% of the 50 000 fits are inside the band. Figure 9.1 displays the input (best fit), the distribution of the form factor values and the constructed confidence band for the spline $\times$ dipole model.

This method has the benefit that the full parameter interdependence and the non-linear nature of the model is taken into account. The confidence band constructed by the Monte Carlo method agrees very well with the one calculated directly from the covariance matrix for almost all models (for a comparison see appendix I.4).

Simultaneous confidence bands

For a comparison with theoretical models, the pointwise confidence band is not well suited. More useful is the simultaneous confidence band, where one expects the true value to be inside the band with a probability β (the chosen confidence level) for all x, or at least for a certain range X of x:

$$P[f(x,\vec{\hat{p}}) - l(x) \leq y_{\text{true}}(x) \leq f(x,\vec{\hat{p}}) + u(x) \text{ for all } x \in X] = \beta. \tag{9.4}$$

The exact analytical treatment is involved. However, with the assumption that the shape of the pointwise and simultaneous confidence band is similar, one can determine a scaling factor using Monte Carlo techniques. For 68.3% confidence level, the factor is found to be around 2.3 for the flexible models and slightly less for the stiffer ones. Details on the procedure and scaling factors for different confidence levels can be found in section I.5 of the appendix.

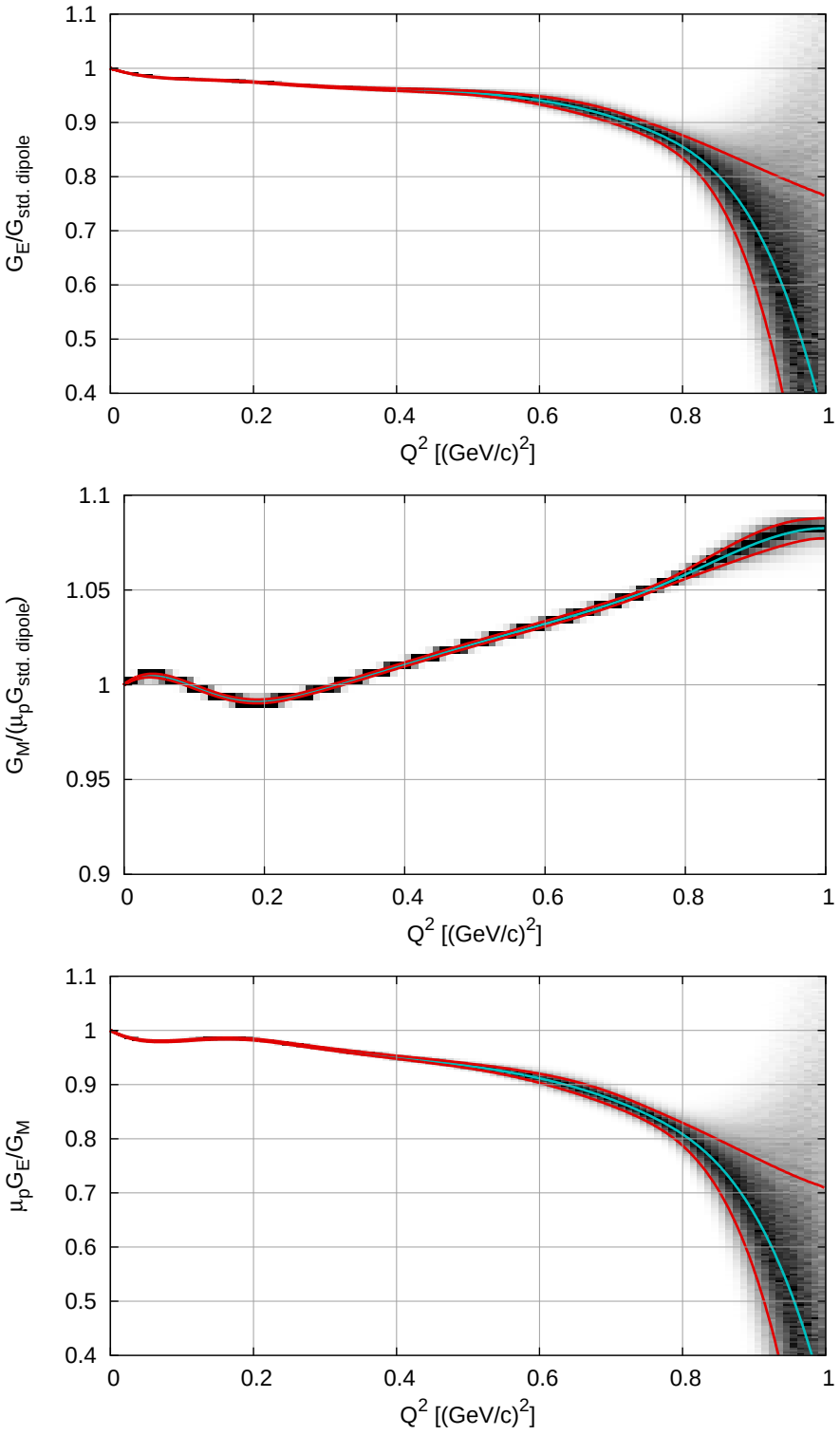

Figure 9.1: The distribution of $G_E(Q^2)$, $G_M(Q^2)$ and $\mu_p G_E/G_M(Q^2)$ determined from 50000 pseudo-data sets calculated and analyzed with the spline $\times$ dipole model. The pseudo data account for the statistical error and normalization uncertainties of the cross sections. The cyan (inner) line represents the best fit, the red (outer) lines the pointwise confidence bands to a confidence level of 68.3%.

9.1.2 Systematic errors

The systematic errors are divided in two groups: Experimental errors and theoretical errors. While a global shift has no effect because it is subsumed in the fitted normalization, drifts in the course of time transform into changes in the slope of the data versus the scattering angle or Q^2, which will influence the outcome of the fits. Therefore, such trends in the data have to be estimated. The experimental errors have several sources:

- Energy cut in the elastic tail. This can be estimated by varying the cut-off energy. It changes the form factor results by at most 0.2% for high Q^2 and by less than 0.1% for $Q^2 < 0.55$ $(\mathrm{GeV}/c)^2$.
- Drift of the normalization. This might occur due to unaccounted dead time effects in the detectors or electronics when the event rate changes. From the long time experience with the detector setup, this error on the cross sections is estimated to be below 0.05%.
- Efficiency change due to different positions of the elastic peak on the focal plane. The detector efficiency is position-dependent because of different wire tension, missing wires or quality of the scintillators. Since the position of the electron trajectories in the focal plane changes only slightly in the course of the experiment, this effect on the cross sections is estimated to be at most 0.05%.
- The vertex-dependent acceptance correction for spectrometers A and C. A comparison of the 720 MeV data, measured with the long and short target cells, leads to a (cross section) uncertainty below 0.1%.
- The background estimation. Depending on the size of the background below the elastic hydrogen peak, this error is estimated to be between 0.1% and 0.5%.

While the first point can be tested directly by varying the cut-off energy used in the fit, the other uncertainties have to be applied by hand to the data. To this end, the cross sections are grouped by the energy and by the spectrometer they are measured with. For each group, a factor, interpolating linearly from 0 for the smallest angle to the full estimated uncertainty[2] at the maximum angle of the group, is multiplied onto the cross sections. The slope of this linear factor was kept constant for all energies. The so modified cross sections were then fitted with the form factor models. To determine an upper and a lower bound, the fit was repeated with the negative of the slope. The so found uncertainties are combined quadratically with the uncertainties from the radiative tail cut-off.

The theoretical systematic errors are harder to determine. The absolute value of the radiation correction itself should be correct on the sub-percent level. Therefore, any slope introduced by the radiation correction should be contained in the slope-uncertainty discussed above, up to a negligible rest; it is therefore not considered.

[2] Since the effects are independent, the estimated uncertainties are added quadratically.

The Coulomb distortion is corrected only approximately. To evaluate its effect, the amplitude of the correction was scaled by ± 50%. The so modified cross sections are fitted with the different models. The differences of the extracted form factors to the results for the data with the unmodified correction gives the widths of the theoretical confidence bands presented in this work.
The two photon exchange (TPE) is not included, and the data have to be interpreted as such. No error estimate for the neglect of the two photon exchange has been included. For the form factor ratio, an estimate of the TPE effect is given by a comparison of the fits by Arrington et al. [AMT07] (see section 2.3). There, the ratio G_E/G_M drops by at most 5% (at 1 $(\mathrm{GeV}/c)^2$) when the TPE correction is applied.

In the plots presented in this work, the bands from the systematic experimental and the theoretical uncertainties are added linearly to the statistical confidence bands.

9.2 Results for the form factors

9.2.1 Fits and their confidence bands

Figures 9.2 to 9.9 display the results of the fits with the different models for the form factors and for their ratio, including the confidence bands. The extended Gari-Krümpelmann fit is not included here, since the fits are too slow and unstable to generate the confidence bands.
The Q^2 range covered by the individual energies are indicated by black lines.

For all models, the confidence bands for G_E get broader with increasing Q^2. This is caused by the lower number of energies covering the region and by the decreasing contribution of G_E to the cross section. For G_M, this effect is less pronounced, since the increasing contribution of G_M to the cross sections compensates the decreasing number of contributing energies.
It is obvious that the confidence bands of the flexible models get large above 0.75 $(\mathrm{GeV}/c)^2$, especially for G_E. Here, only the large-angle data of 855 MeV incident beam energy contribute, and no separation is possible. Therefore, the form factor values extracted in that region are unreliable.

The resulting parameters of the different models can be found in appendix J. Numeric values for the extracted form factors and their error estimates are tabulated in appendix K.2.2 for 46 Q^2 values between 0.005 and 1.000 $(\mathrm{GeV}/c)^2$.

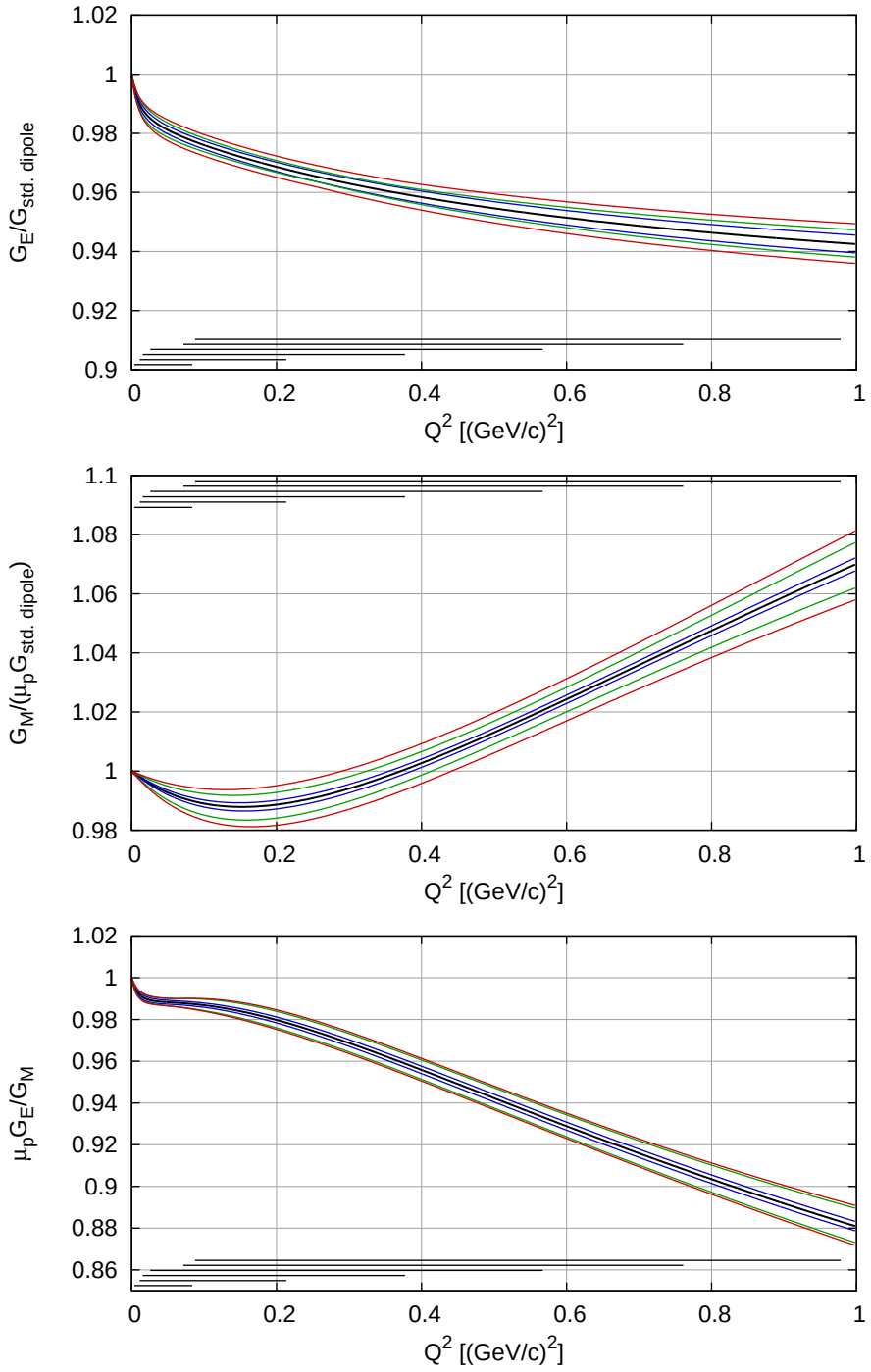

Figure 9.2: G_E (top), G_M (middle) and G_E/G_M (bottom) determined by the double-dipole fit. The black (innermost) line is the best fit. The blue lines represent the statistical pointwise confidence band (68.3% confidence level), while the green lines also account for the experimental systematical errors and the red (outermost) lines also for the theoretical errors (the different errors are added linearly). The straight black lines at the edge of each plot indicate the Q^2 regions covered by the different energies (bottom to top: 180 MeV to 855 MeV).

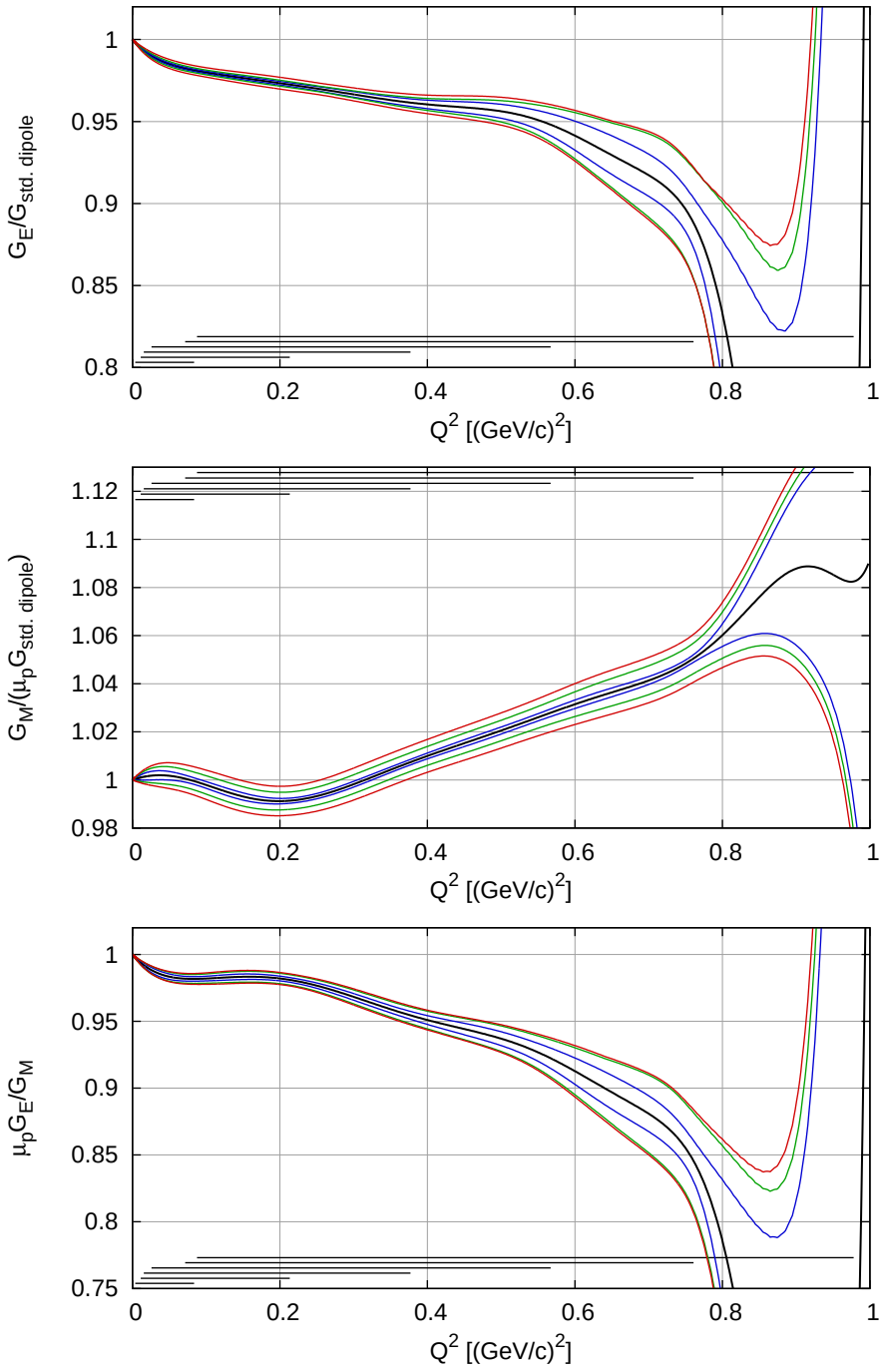

Figure 9.3: Same as fig. 9.2, but for the polynomial model.

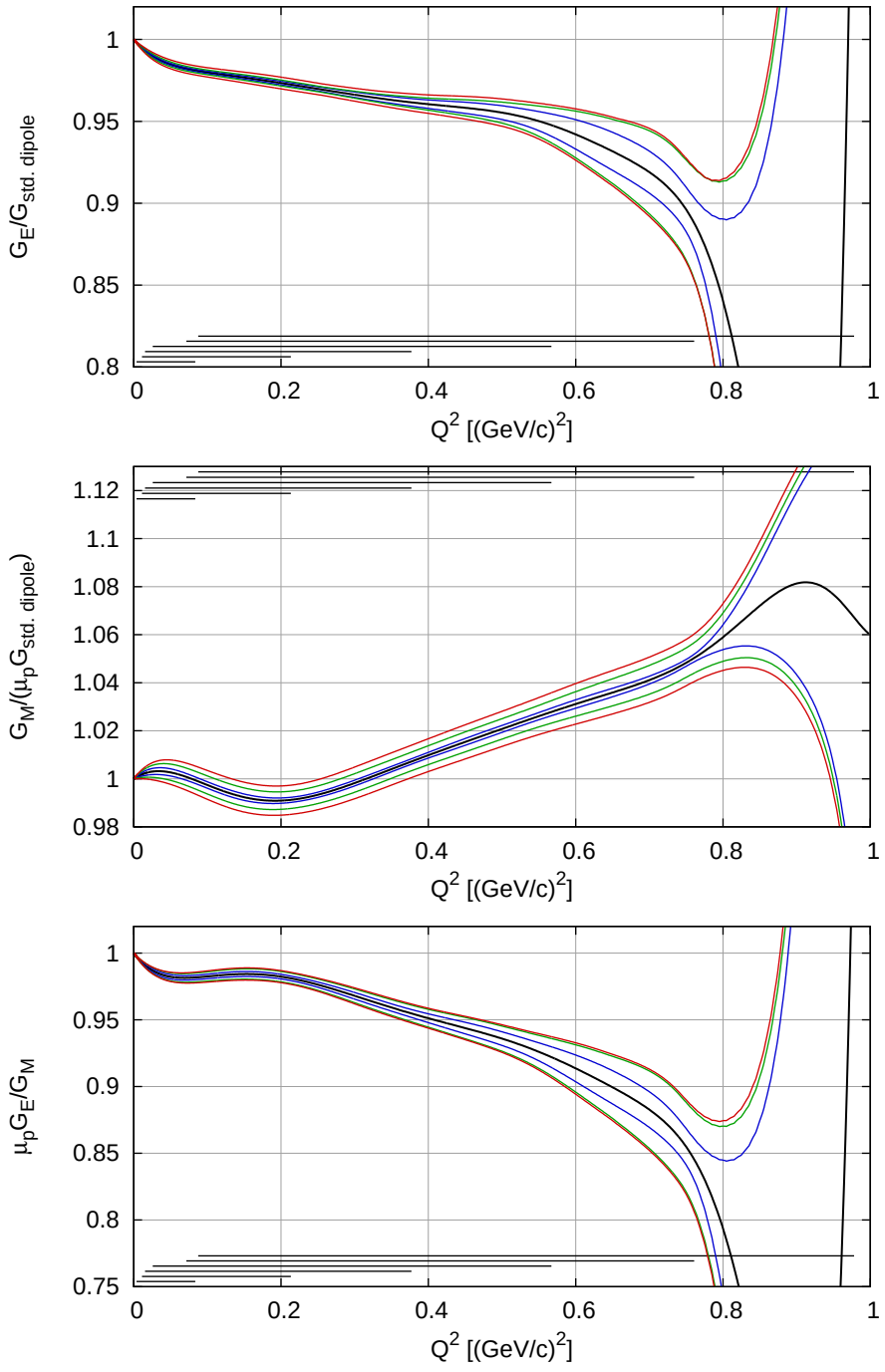

Figure 9.4: Same as fig. 9.2, but for the polynomial + dipole model.

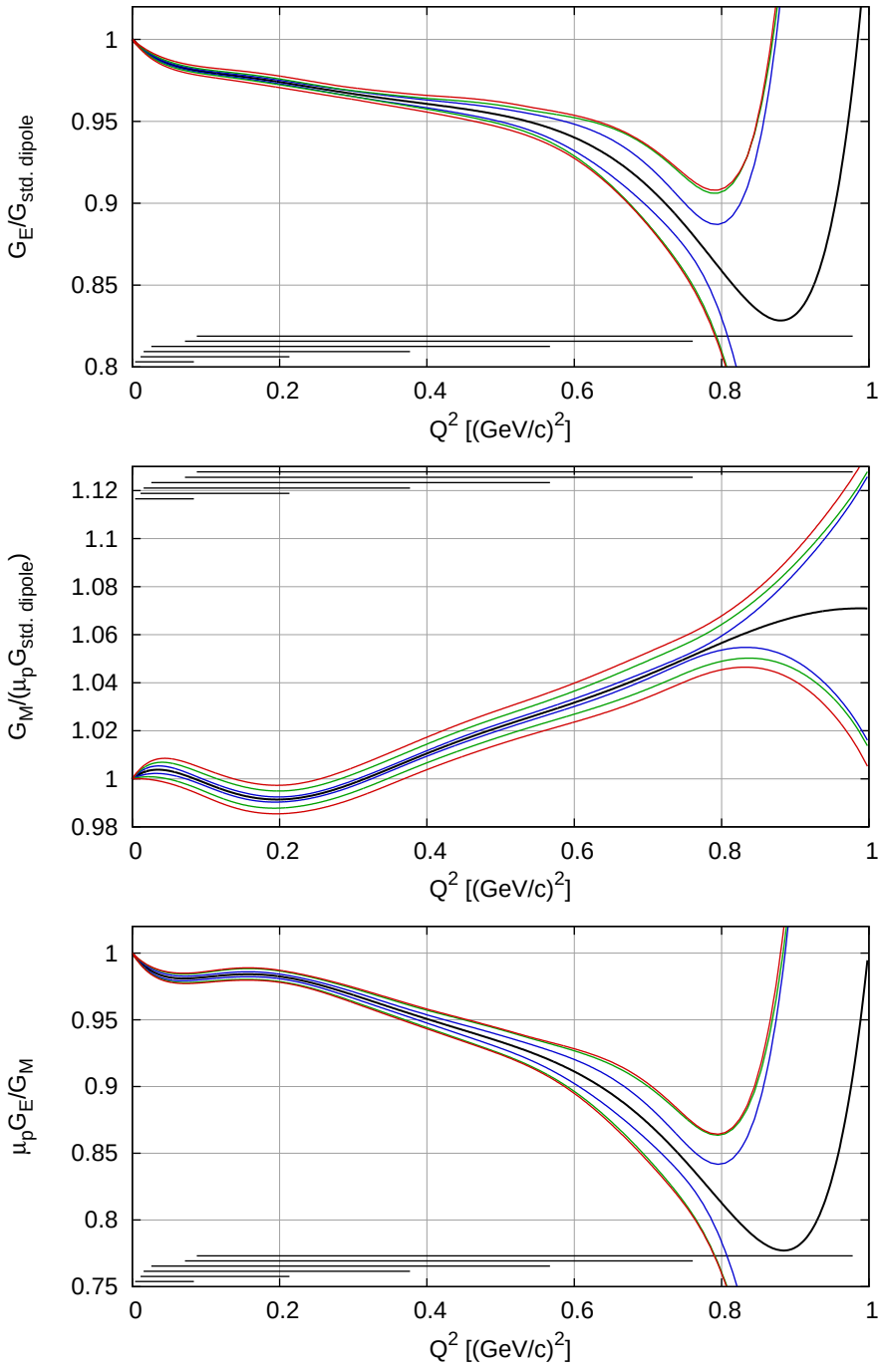

Figure 9.5: Same as fig. 9.2, but for the polynomial × dipole model.

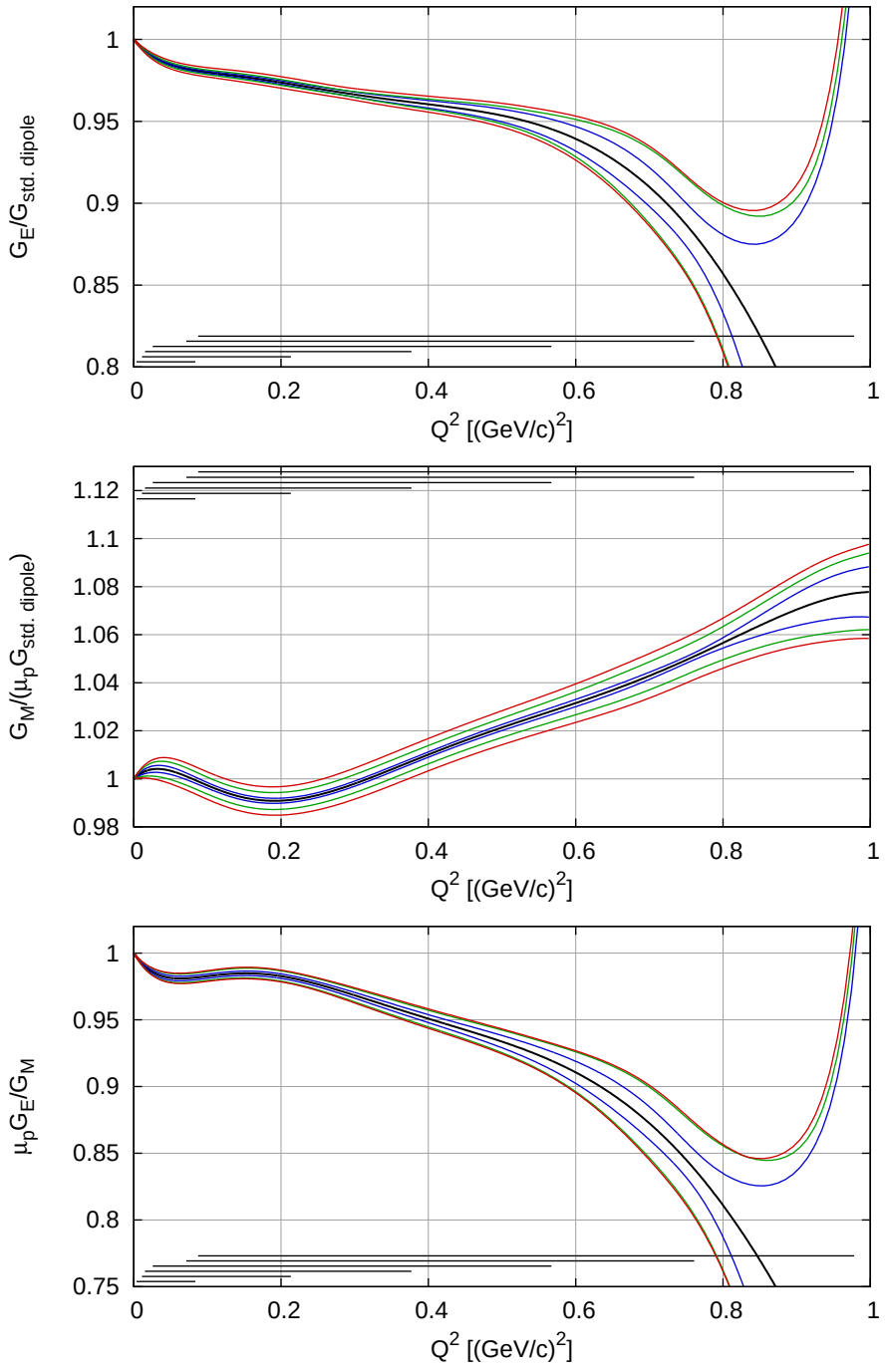

Figure 9.6: Same as fig. 9.2, but for the inverse polynomial model.

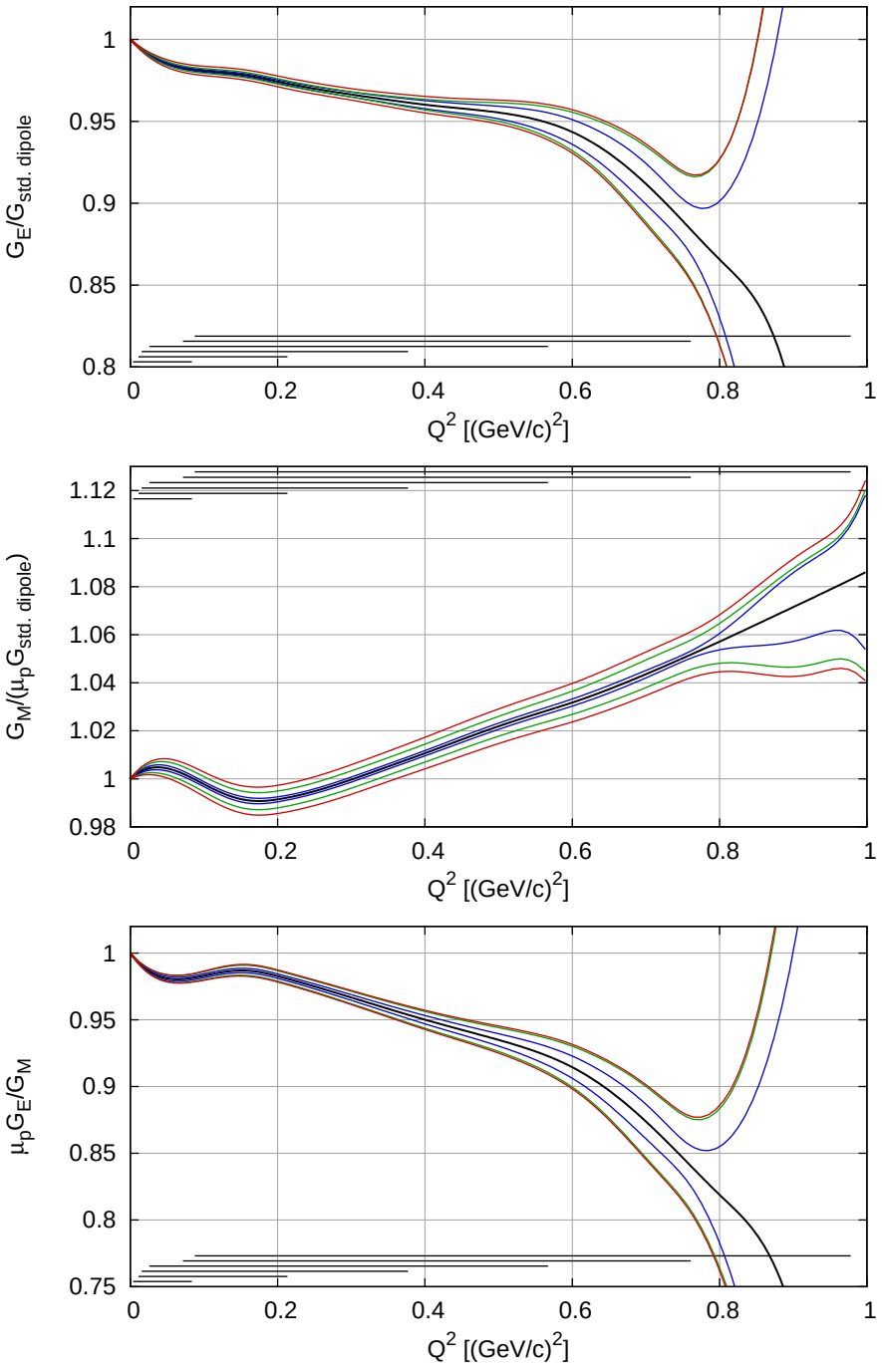

Figure 9.7: Same as fig. 9.2, but for the spline model.

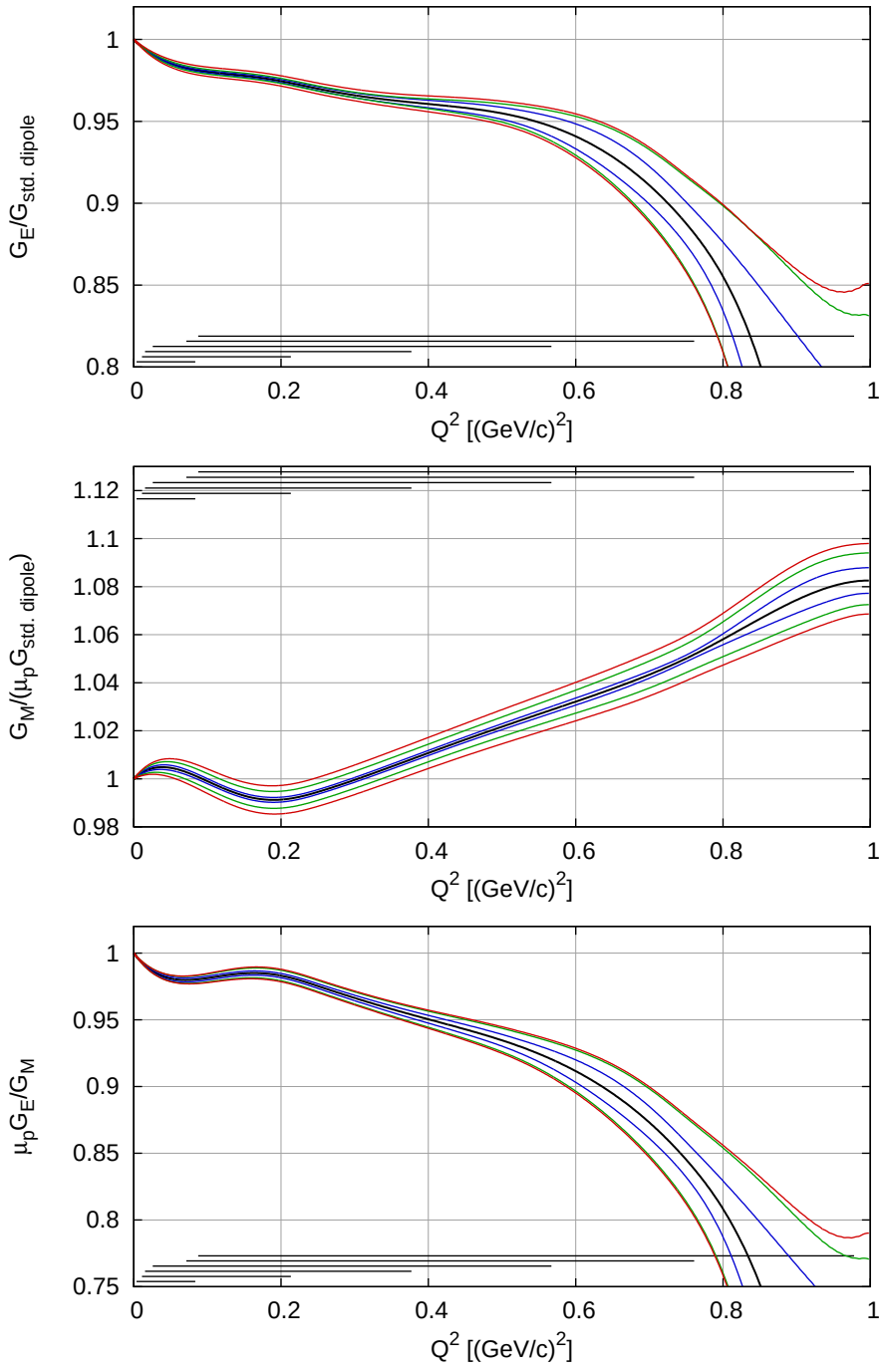

Figure 9.8: Same as fig. 9.2, but for the spline × dipole model.

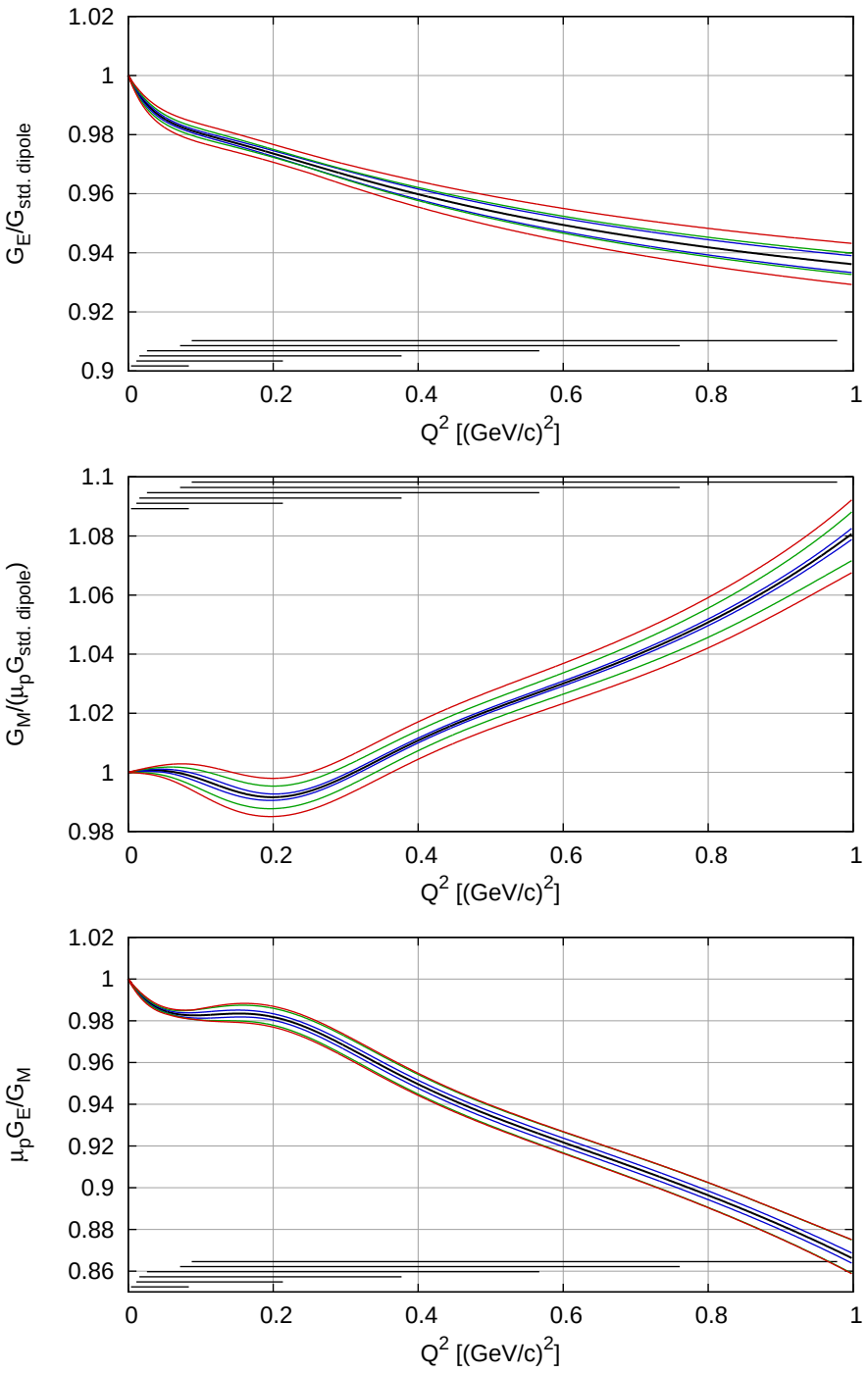

Figure 9.9: Same as fig. 9.2, but for the Friedrich-Walcher model.

9.2.2 Rosenbluth separation

Fixing the cross sections with the normalizations of the different data groups determined by one of the flexible fits, it is possible to extract G_E and G_M by the standard Rosenbluth technique. Writing the cross section (eq. (2.12)) as

$$\sigma_{\text{red}} = \varepsilon\,(1+\tau)\left(\frac{\mathrm{d}\sigma}{\mathrm{d}\Omega}\right)_0 / \left(\frac{\mathrm{d}\sigma}{\mathrm{d}\Omega}\right)_{\text{Mott}} = \left(\varepsilon G_E^2\left(Q^2\right) + \tau G_M^2\left(Q^2\right)\right) \tag{9.5}$$

shows that, for constant Q^2, the reduced cross section σ_{red} depends linearly on ε with $G_E^2(Q^2)$ as slope and $\tau G_M^2(Q^2)$ as y-intercept[3].
To judge the deviation from a straight line, a separation of G_E and G_M requires data at at least three different ε values.

Due to the large number of measurements with overlapping acceptances, one can define a set of narrow-spaced Q^2 values (see table K.3 in the appendix) such that each measured cross section can be attributed to one Q^2 out of this set. The cross section measured in one setting is projected to that Q^2 value which is nearest to the central Q^2 of the acceptance. Since the cross sections are measured as the ratio to the form factor implemented in the simulation (the standard dipole), the projection is performed automatically by multiplication with the standard-dipole cross section at the Q^2 to project to. The error of projection is given by the change of the ratio between central Q^2 and selected Q^2. The error is below 0.15% at the highest Q^2 presented here, and considerably less for lower Q^2.

The numerical values of the Rosenbluth separation are given in table K.3 in the appendix K.2.1 for 77 Q^2 values.

Figure 9.10 compares the form factor values from the Rosenbluth separation with the result of the global fit (spline model). For the lowest Q^2 points, where G_M is less well determined, $G_M/(\mu_p G_{\text{std. dip.}})$ was not determined by the fit, but for each point set once to 1 and once to 1.05, as one would expect G_M to be in that range and not larger. For each point, the range in G_E of the two fits and the errors of the individual fits are combined to produce the error of G_E shown in the figure. The unconstrained points are presented in red for reference. The use of the prior knowledge that the magnetic form factor can not differ much from μ_p at small Q^2 helps to reduce the error bars on G_E considerably.

The agreement of the Rosenbluth-separated form factors with those from the global fits has been tested by calculating a reduced χ^2 from the differences of the Rosenbluth data points to the global fit. The rather large value of 2.2 is found[4]. Fits of polynomials (order 10) to G_E and G_M from the Rosenbluth separation yield also χ^2_{red} values above 2. To put these numbers into perspective, one has to note that the χ^2_{red}-distribution is much wider for the fit to the Rosenbluth-separated form factors, due to the lower number of degrees of freedom. In fact,

[3] This is one formulation of the so called Rosenbluth separation. It is also possible to use an other variant of eq. (2.12) with $\tau(\frac{1}{1+\tau} + 2\tan^2(\theta/2))$ as the x-axis. Then, the slope is G_M^2 and the y-intercept $G_E^2/(1+\tau)$.

[4] With similar numbers for a comparison of G_E or G_M alone.

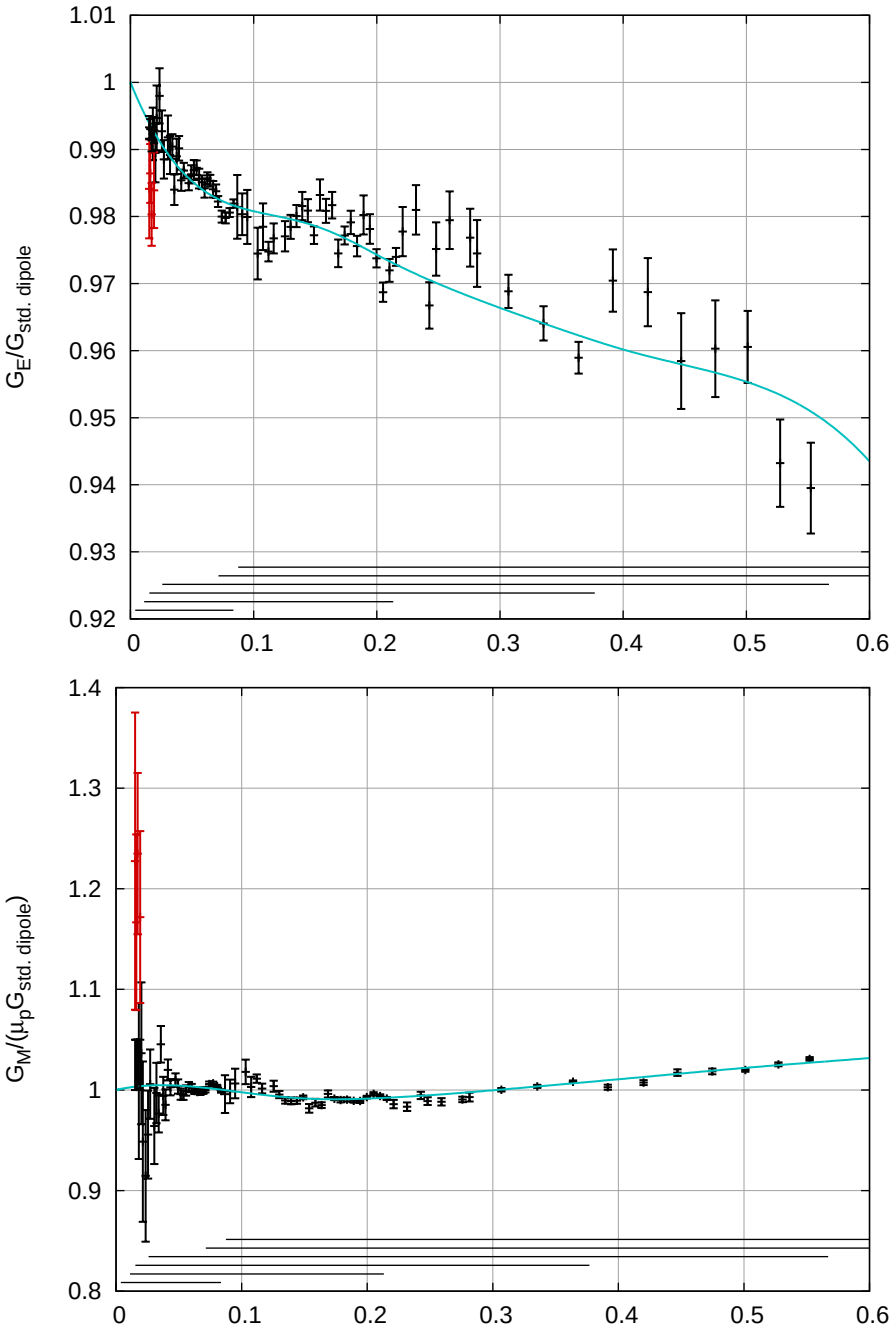

Figure 9.10: G_E and G_M determined via the Rosenbluth separation technique (black points) compared to the spline fit (cyan curve). For the lowest points, $G_M/(\mu_p G_{\text{std. dip.}})$ was set to 1 and 1.05 (the results of an unconstrained fit are shown in red). For details see text.

interpreting the deviation of the flexible fits from the expectancy value 1 as pure statistical, χ^2_{red} values up to 1.7 for the fit to the Rosenbluth-separated form factors would have the same probability as χ^2_{red} values up to 1.14 for the global fits.

While the "ingredients" of the global fit and the Rosenbluth separation are in principle similar, the explicit Rosenbluth separation is fundamentally different from the global fit since it has to a) contract the large acceptance of the measurements to single Q^2 points and acts b) on sub-samples of the complete data set. The consequences of this differences have not been studied fully, however, the robustness (see section 8.7 of [Jam06]) of both estimators, i.e. the sensitivity to unaccounted non-Gaussian errors of the input data, has been tested. To this end, statistically pure pseudo data are generated from the spline fit and then perturbed with systematic errors. It was found that the Rosenbluth separation is much more sensitive.
In fact, attributing, at variance with the above remark on the χ^2_{red}-distribution, all of the χ^2-difference to systematic errors, a systematic, that is "not normal distributed", shift of 5% of the measured cross sections by only 0.5% yields a χ^2-difference comparable to the difference seen for the measured data. We therefore conclude that the global fit is a much more robust estimator of the form factors with respect to non-normal errors in the measured cross sections.

Figures 9.11 to 9.13 show the relative deviations of the measured σ_{red} from the Rosenbluth fit for Q^2 values from 0.02 to 0.55 in steps of 0.01 $(\text{GeV}/c)^2$. For this investigation, the measured cross sections are attributed to all Q^2 values that are inside the middle half of the respective acceptance. Due to the narrow steps in Q^2 in comparison to the large acceptance of the spectrometers, this results partly in the attribution of one measured cross section to more than one Q^2 value. At the level of statistical accuracy of this experiment, no systematic deviations from the straight line, which would be a hint to insufficiencies in the measurement or theory (e.g. unaccounted two photon effects), are visible; this was tested by fitting polynomials of second order, where the coefficient of the quadratic term was found to be compatible with zero.

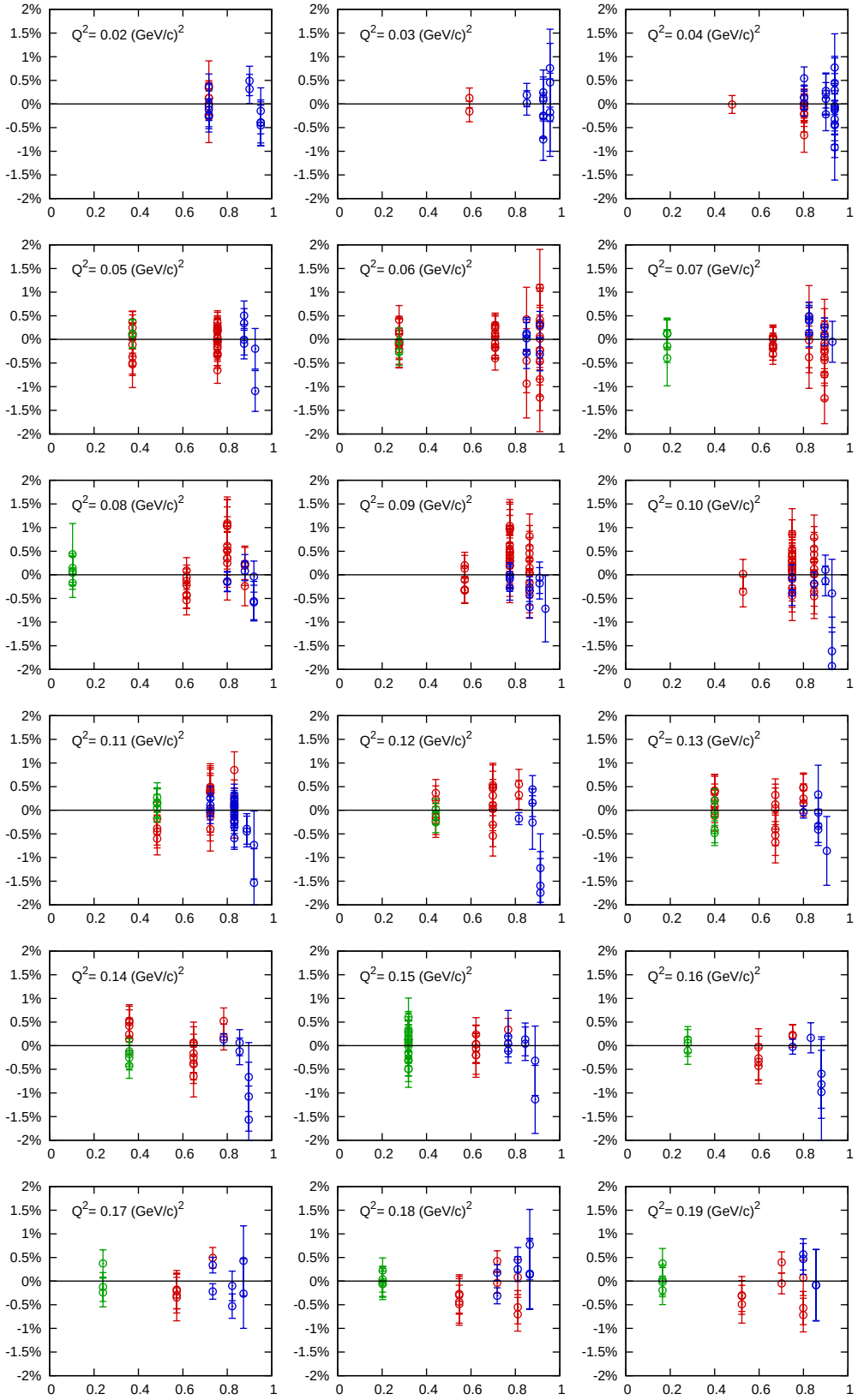

Figure 9.11: The relative deviation of the measured σ_{red} from the Rosenbluth straight-line fit. x-axis: ε. y-axis: Deviation.

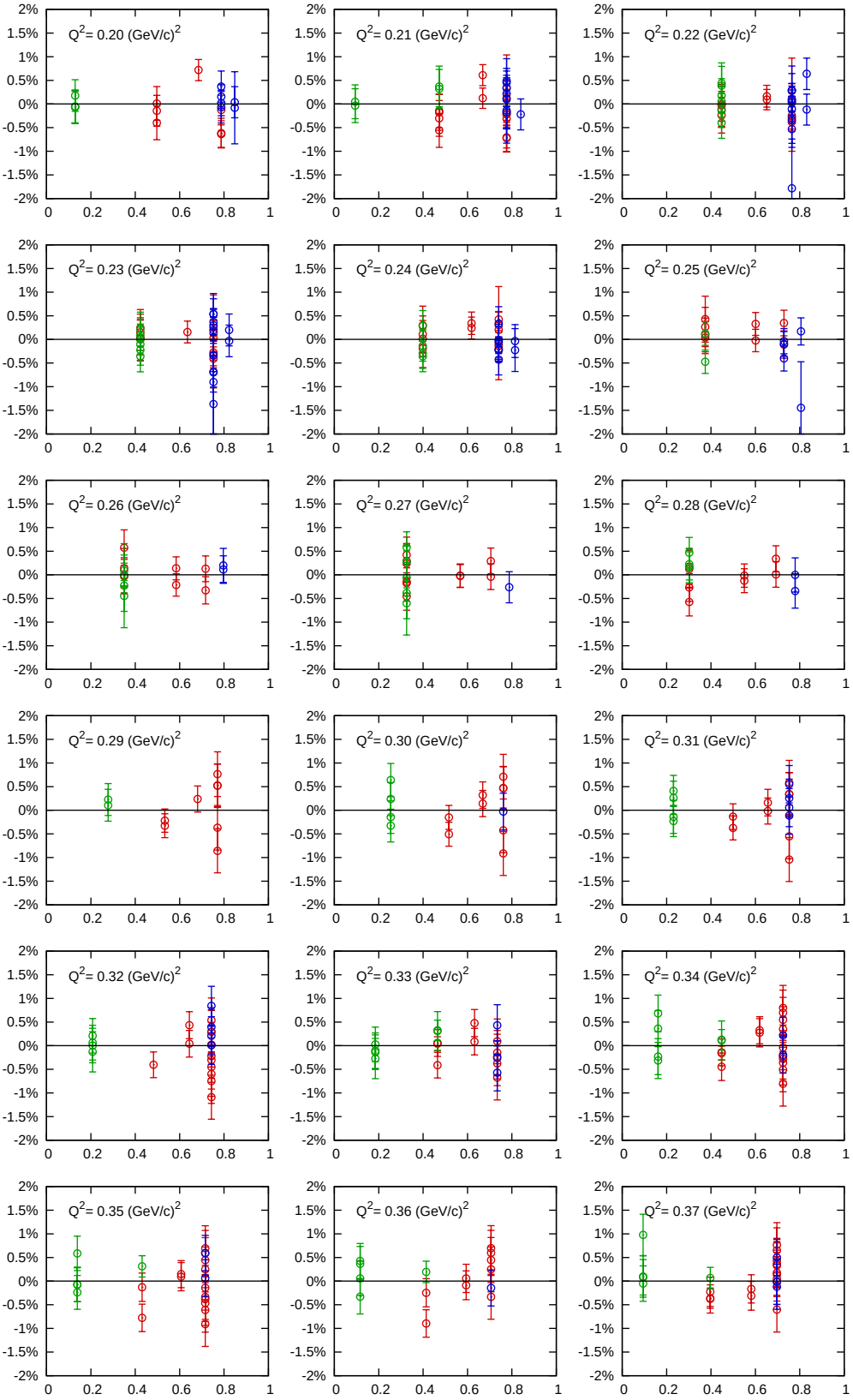

Figure 9.12: 9.11 continued.

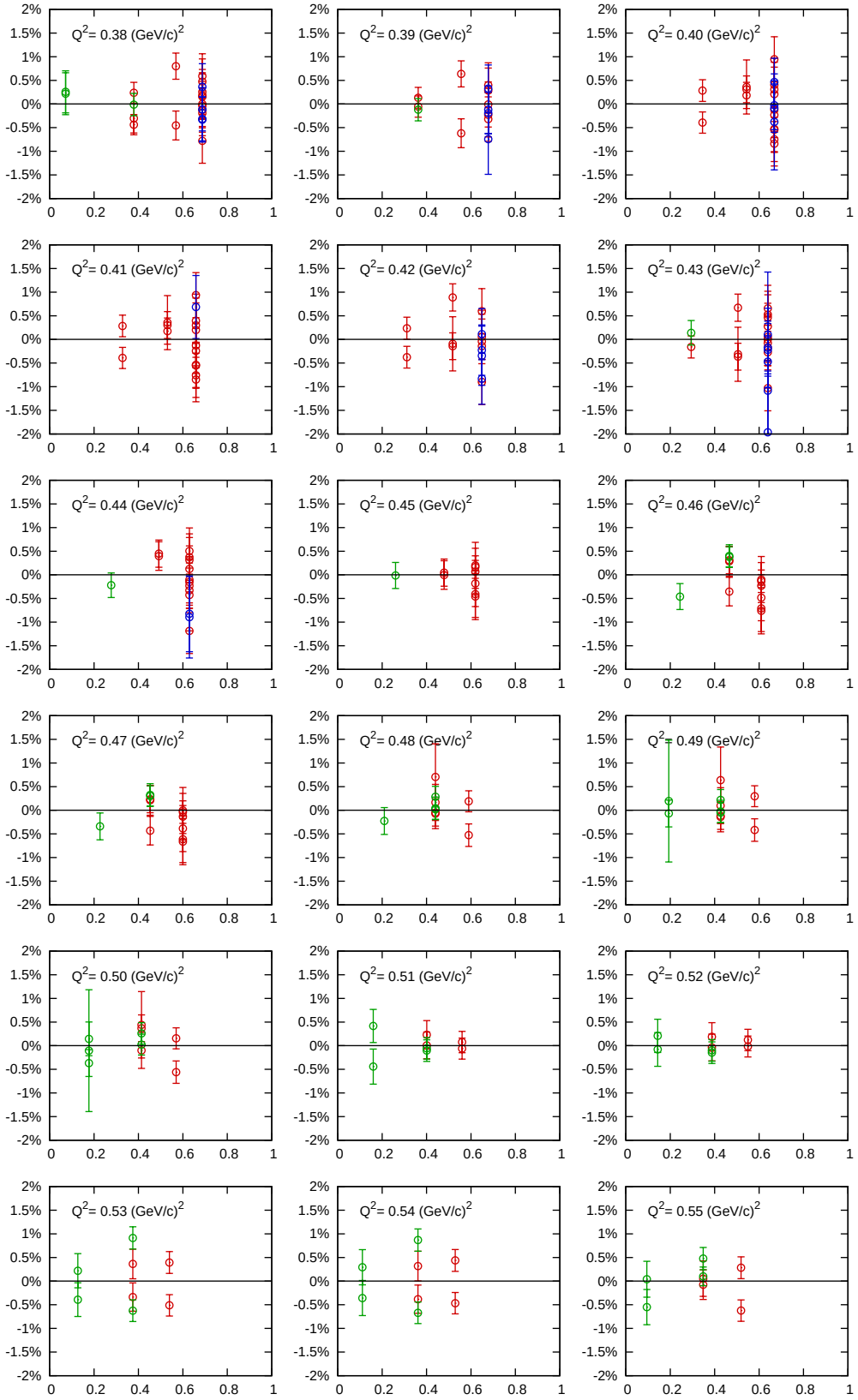

Figure 9.13: 9.11 continued.

9.2.3 Comparison of the models and discussion of the result

All models give very similar form factors, in particular in the Q^2 region where several energies contribute. This is demonstrated by figure 9.14, which shows the ratio of G_E and G_M from the different fits to the results from the polynomial fit. Up to 0.5 $(\mathrm{GeV}/c)^2$, all flexible models and the Friedrich-Walcher model agree on the 0.1% level. This means that the form factors are extracted essentially model-independently by the super-Rosenbluth-fit, as very different models have been tested. Above 0.5 $(\mathrm{GeV}/c)^2$, the less flexible models (double-dipole, Friedrich-Walcher, Gari-Krümpelmann) are no longer able to describe the data at this level of precision, while the flexible models can do so and they all agree to within better than 0.5% up to about 0.75 $(\mathrm{GeV}/c)^2$. However, since in the Q^2 range between 0.55 and 0.75 $(\mathrm{GeV}/c)^2$ only data from the highest two energies contribute to the fit and since they have only a small separation in ϵ, the separation of the cross section into G_E and G_M is very susceptible to slightest unaccounted uncertainties in the data and the flexible models might just follow such deviations.
Above 0.75 $(\mathrm{GeV}/c)^2$, there are only cross sections from 855 MeV, hence there is no information which would allow a separation of G_E and G_M, and the different models "interpret" the cross sections in that range very differently, according to their functional form.

Figure 9.15 shows the electric form factor determined by the different fits, divided by the standard dipole. In the upper plot, the different large-Q^2 behavior of the flexible and of the stiff models already seen in the ratio-plot is clearly visible. The flexible models slope down above 0.55 $(\mathrm{GeV}/c)^2$, while the less flexible models continue with (about) the same slope as in the lower Q^2 region. The erratic behavior of the flexible models above 0.75 $(\mathrm{GeV}/c)^2$ is obvious.
In the lower plot, which focuses on the low-Q^2 region, two aspects are visible: a) The results from all fits start with large downward slope (compared to the standard dipole). This slope changes significantly around 0.05 $(\mathrm{GeV/c})^2$, from where on it is almost stable up to 0.55 $(\mathrm{GeV}/c)^2$. b) Between 0.1 and 0.2 $(\mathrm{GeV}/c)^2$, there appears a slight bump, slightly stronger in the spline models than in the others. However, a smooth shape without a bump would be inside the combined confidence bands (see figures 9.2 to 9.9).

In figure 9.16, the magnetic form factor extracted by the different models is presented. In the Q^2 range between 0.1 and 0.55 $(\mathrm{GeV}/c)^2$, the fits of the Friedrich-Walcher model and of the flexible models are almost identical. For higher Q^2, the fit of the Friedrich-Walcher model falls slightly below the fits of the flexible models, however, for G_M, the difference between the flexible models and the Friedrich-Walcher model is much smaller than for G_E.
In the low-Q^2 region (lower plot), all models except the double dipole model exhibit the same principal phenomenology: A bump around 0.04 $(\mathrm{GeV}/c)^2$, followed by a dip around 0.2 $(\mathrm{GeV}/c)^2$. While the fit of the Gari-Krümpelmann model finds a different shape as the flexible models for both structures, the fit of the Friedrich-Walcher model gives almost the same dip, but a smaller bump. It has to be noted that the first bump below 0.1 $(\mathrm{GeV}/c)^2$ is an artifact of the

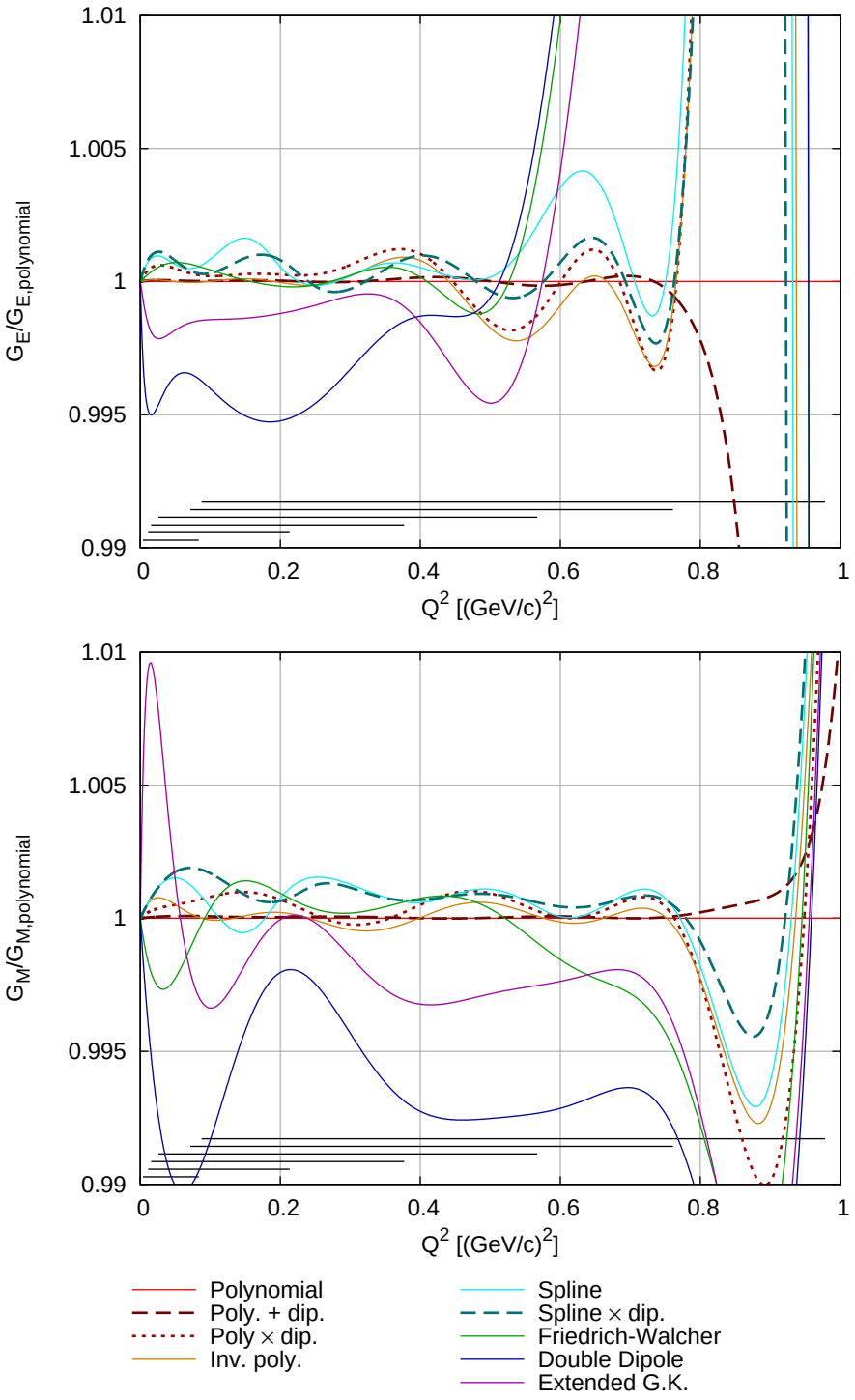

Figure 9.14: Ratio of the results of the different fits to the results of the polynomial fit. Top: G_E. Bottom: G_M.

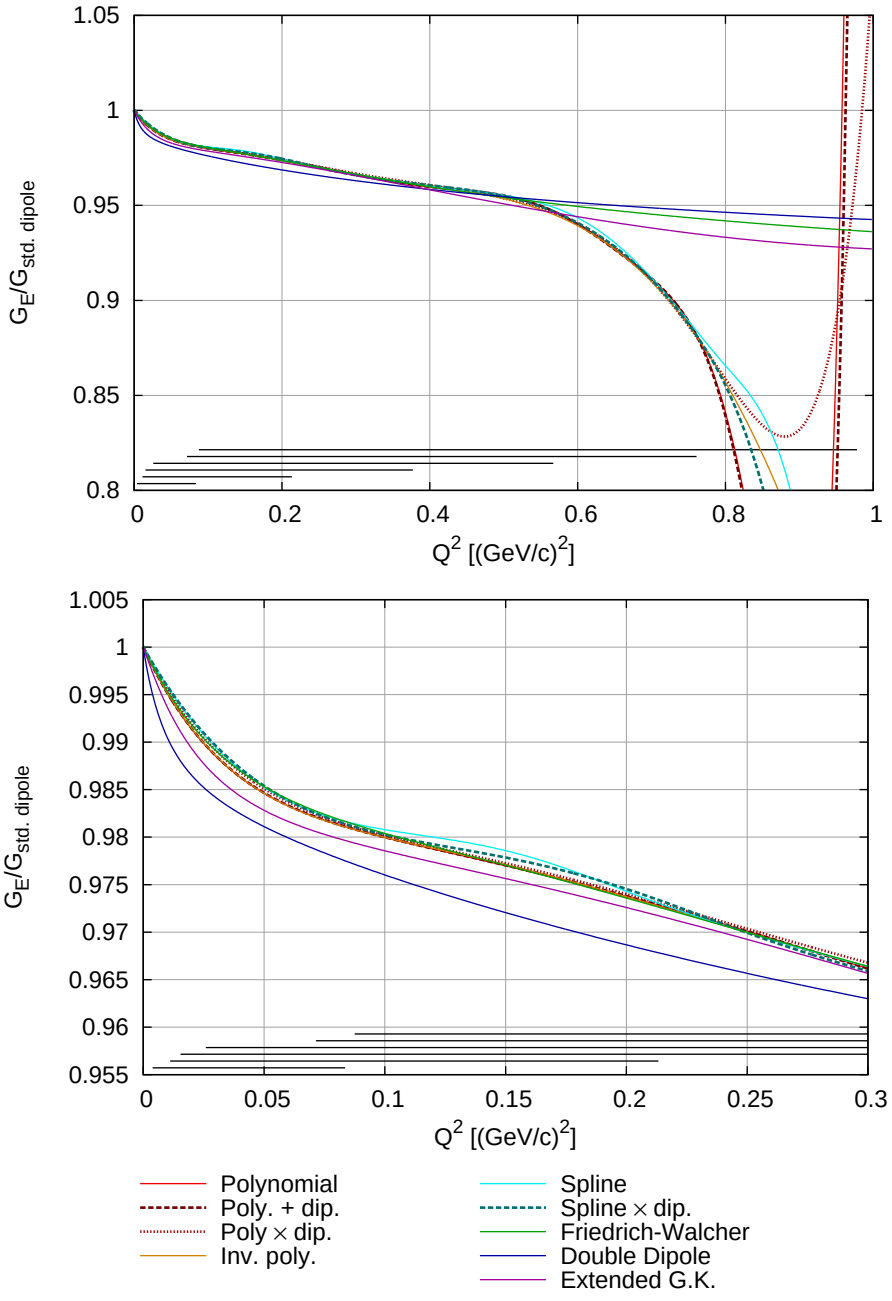

Figure 9.15: G_E determined by the different fits.

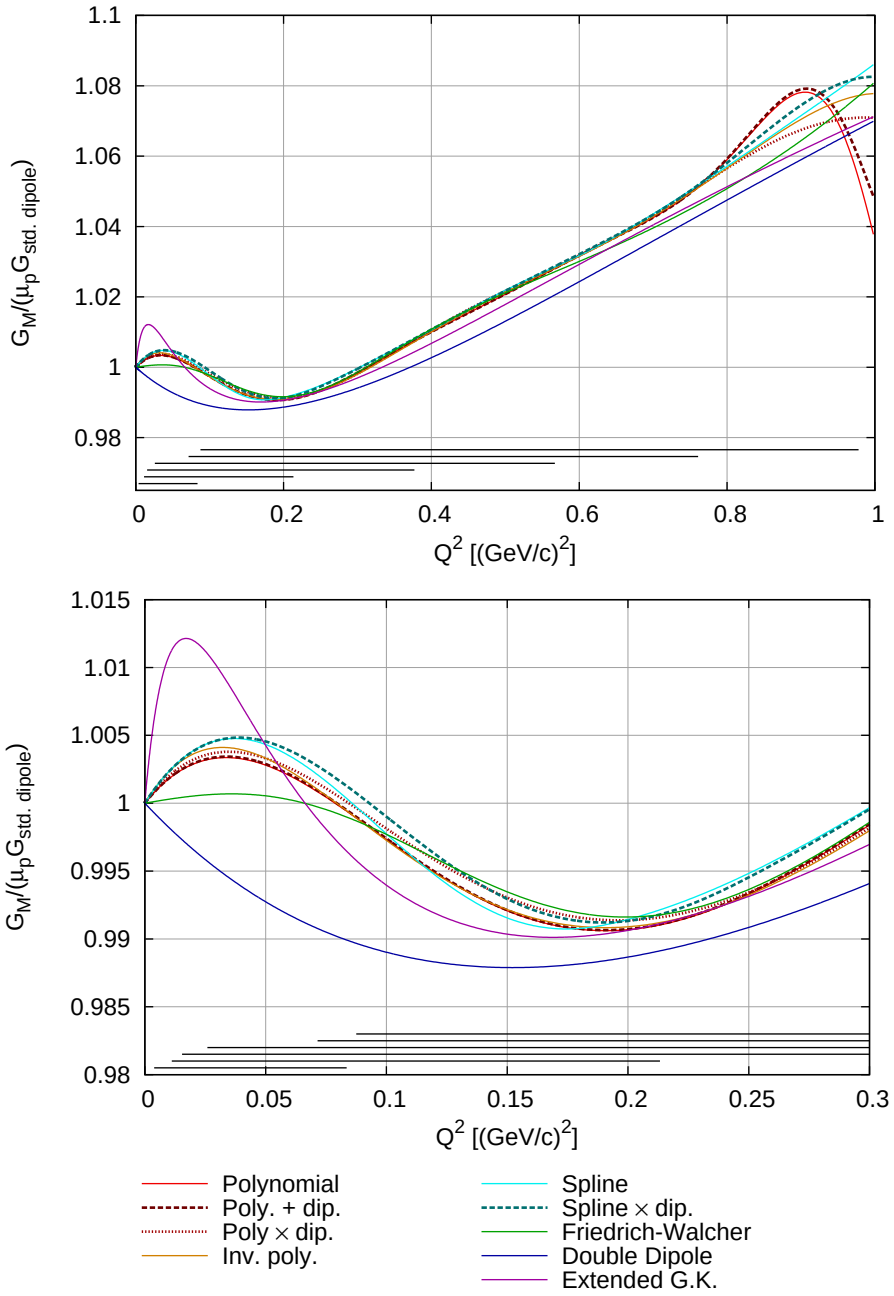

Figure 9.16: G_M determined by the different fits.

way the data is presented and is just an indication that the slope at $Q^2 = 0$ (and therefore the magnetic radius) is smaller than the slope of the standard dipole. Normalization to a dipole with a different parameter (and therefore slope) would eliminate this bump. However, the depression around 0.2 $(\mathrm{GeV}/c)^2$ cannot be explained that way and might be taken as an indication for a pion cloud.
One has to keep in mind that momentum transfers below 0.05 were measured in forward direction in this experiment. Hence, the contribution of G_M to the cross section is small and the determination of G_M is very sensitive to small uncertainties in the data.

9.2.4 Comparison with existing data

The form factors determined in this experiment are now compared with existing data. Table 9.1 gives an overview of the different data sets taken into account.

Figures 9.17 to 9.19 show the form factors extracted by the spline model (as an example for the flexible models) and the Friedrich-Walcher model (as an example for the stiffer models) in comparison to the previous data points (the confidence bands for the Friedrich-Walcher model have been omitted to avoid cluttering and to keep the plots legible). Shown here are also the fits to previous data by Arrington [AMT07] (without the two photon exchange correction) and by Friedrich and Walcher [FW03].

Figure 9.17 compares the results of the fits for the electric form factor, normalized to the standard dipole, to the previous data which are plotted only with their statistical errors. As can be seen in the top plot, the results of the fits agree on a 2% level with the previous data, up to 0.57 $(\mathrm{GeV}/c)^2$. At larger Q^2, the less flexible models follow the trend of the previous data points while the flexible models follow the data of this work and show a downward slope.

In the low-Q^2 region, it is obvious that the Borkowski et al. [BPS$^+$75] data and the other data points have different normalizations; the Borkowski data seem to be lower in comparison to the fit and the other data points by about 1%, which is clearly within their normalization uncertainty. If one allows for such a shift of the Borkowski data, the fits agree reasonably well with the existing data up to 0.38 $(\mathrm{GeV}/c)^2$.

The previous data are by far not precise enough to make any statement about the indication for a bump around 0.15 $(\mathrm{GeV}/c)^2$ seen in the results of the flexible fits.

The fits to the data of this work do not follow the upward shift of the Price and Janssens data sets above 0.38 $(\mathrm{GeV}/c)^2$. Following these data, the Arrington and Friedrich-Walcher parametrizations rise above 0.4 $(\mathrm{GeV}/c)^2$, however they still stay below most of the previous data points between 0.38 and 0.6 $(\mathrm{GeV}/c)^2$.

Measurement	Q^2 range $[(\mathrm{GeV}/c)^2]$	Reference
G_E		
$H(e,e')$	0.006 – 0.03	Murphy et al. [MSS74]
	0.01 – 0.05	Simon et al. [SSBW80]
	0.014 – 0.12	Borkowski et al. [BPS$^+$75]
	0.04 – 1.75	Price et al. [P$^+$71]
	0.16 – 0.86	Janssens et al. [JHHY66]
	0.39 – 1.95	Berger et al. [B$^+$71]
	0.4 – 5.5	Christy et al. [C$^+$04]
$d(e,e'p)$	0.27 – 1.76	Hanson et al. [H$^+$73]
G_M		
$H(e,e')$	0.014 – 0.12	Borkowski et al. [BPS$^+$75]
	0.04 – 1.75	Price et al. [P$^+$71]
	0.16 – 0.86	Janssens et al. [JHHY66]
	0.39 – 1.95	Berger et al. [B$^+$71]
	0.4 – 5.5	Christy et al. [C$^+$04]
	0.49 – 1.75	Bosted et al. [B$^+$90]
	0.67 – 3.00	Bartel et al. [B$^+$73]
$d(e,e'p)$	0.27 – 1.76	Hanson et al. [H$^+$73]
G_E/G_M		
$\vec{H}(\vec{e},e'p)$	0.16 – 0.59	Crawford et al. [C$^+$07]
$H(\vec{e},e'\vec{p})$	0.23 – 0.49	Ron et al. [R$^+$07]
	0.32 – 1.77	Gayou et al. [G$^+$01]
	0.37 – 0.44	Pospischil et al. [P$^+$01]
	0.38 – 0.50	Milbrath et al. [M$^+$98]
	0.40	Dieterich et al. [D$^+$01]
	0.49 – 3.47	Jones et al. [J$^+$00]
	0.50 – 3.48	Punjabi et al. [P$^+$05]

Table 9.1: Compilation of the earlier form factor measurements shown in figures 9.17 to 9.19.

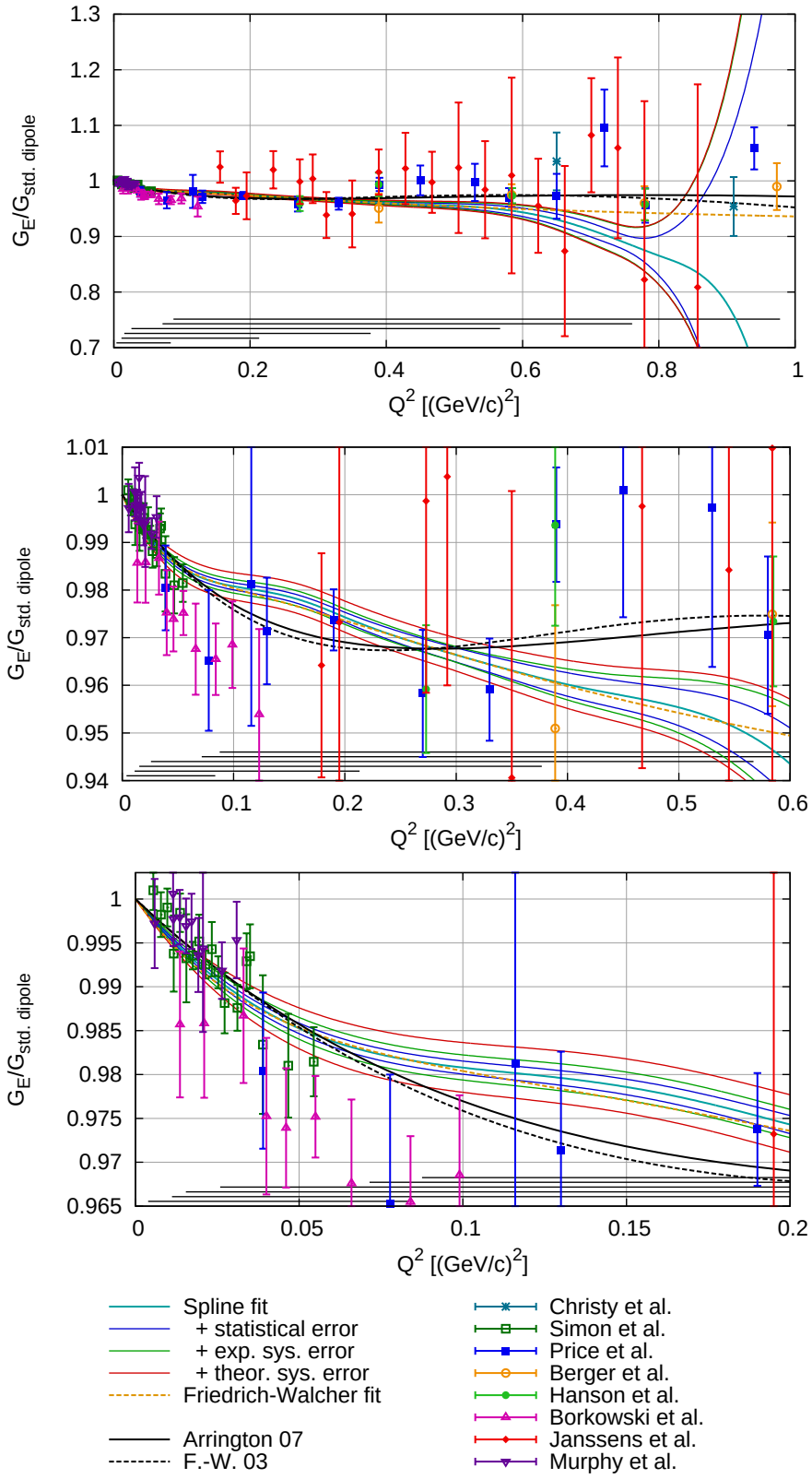

Figure 9.17: The electric form factor G_E determined with the spline and with the Friedrich-Walcher model in comparison to the previous data. To compress the data range, the form factor is divided by the standard dipole.

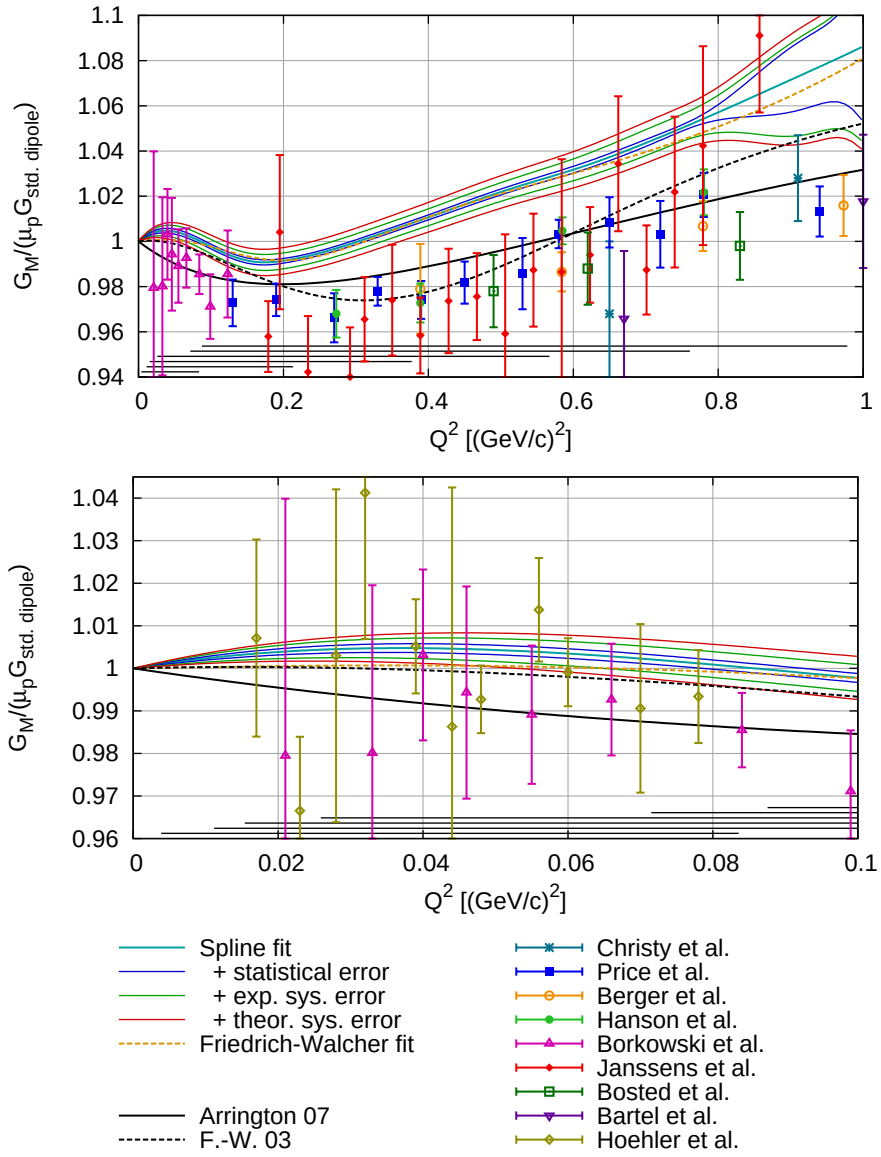

Figure 9.18: The magnetic form factor G_M determined with the spline and with the Friedrich-Walcher model, normalized to $\mu_p G_{\text{std. dipole}}$, in comparison to previous data.

Figure 9.18 shows the same comparison for the magnetic form factor. Looking at the close-up (lower plot), again, the Borkowski et al. [BPS$^+$75] data is about 1% lower than the fits to the new data. In the close-up, results from a dispersion-relation analysis by Höhler [H$^+$76] is included, which are slightly higher than the Borkowski et al. [BPS$^+$75] data and agree within their errors with the present result.

While the agreement between the fits and the previous data is good at low Q^2 if one accepts a normalization error of 1% for the Borkowski et al. [BPS$^+$75]

data, the fits, i.e. the new data, lie above the previous data in the Q^2 range from 0.2 to 0.8 $(\mathrm{GeV}/c)^2$ by nearly constant 4%. It has to be noted that Brash et al. [BKLH02] found 1.5 to 3% higher G_M values in their analysis of the previous world data, when they used the G_E/G_M-ratio measured in polarized measurements as a constraint for the Rosenbluth separation. Some of the difference may also be caused by a different treatment of the internal radiation correction, especially the proton vertex contribution. Unfortunately, the publications are not all clear on what kind of radiation corrections were applied.

Figure 9.19 shows the form factor ratio measured in polarization experiments compared to fits to the previous data and to the present result from the global fits. In the lower plot, the TPE correction (see section 2.3) is applied to the fits.

Around 0.4 $(\mathrm{GeV}/c)^2$, the fits to previous data are higher than most of the polarization measurements. It has to be noted here that the fits to previous data fall below the previous (Rosenbluth-separation) G_E data points in that region, i.e. that those data points indicate an even larger ratio.
The discrepancy is especially large for the high precision data sets by Ron et al. [R$^+$07]. Unpublished, preliminary data from the Jefferson Laboratory [Hig10; ZH10], in the range from 0.35 to 0.7 $(\mathrm{GeV}/c)^2$, with uncertainties below 2%, give ratios which are notably below those given by the old fits, and therefore by the old data sets for G_E and G_M. The TPE correction reduces this discrepancy only slightly. Therefore, it has to be noted that the previous G_E and G_M data are incompatible with the polarized measurements, and they can not be reconciled with the TPE correction used here.

By contrast, the fits to the new data of this work are in excellent agreement with these high precision polarization measurements up to 0.6 $(\mathrm{GeV}/c)^2$. However, the polarization measurements do not support the downward slope of the flexible fits at higher Q^2, which, anyhow, is not well established by the present data (see subsection 9.2.3), and it has to be mentioned that this downward slope also does not match with the high-Q^2 results from polarization measurements [P$^+$01; J$^+$00; G$^+$01; M$^+$98; D$^+$01].

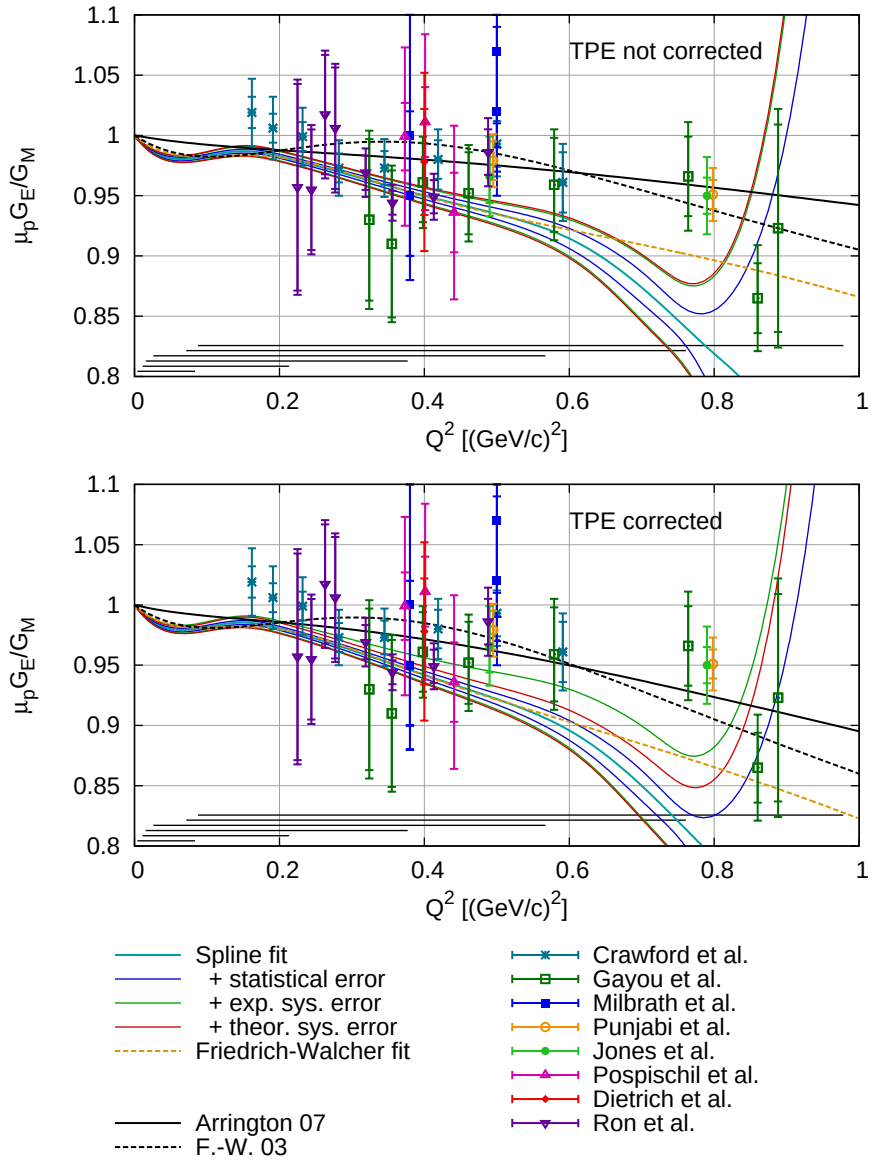

Figure 9.19: Ratio of the electric to the magnetic form factor determined with the spline and the Friedrich-Walcher model. Top: Fits without two photon exchange (TPE) correction. Bottom: Fits corrected for TPE by the ratio of the Arrington et al. [AMT07] fits (see text). The data points shown here are measured in polarized experiments. Not shown are unpublished preliminary results from the Jefferson Laboratory [Hig10; ZH10], which are in excellent agreement with the new fits.

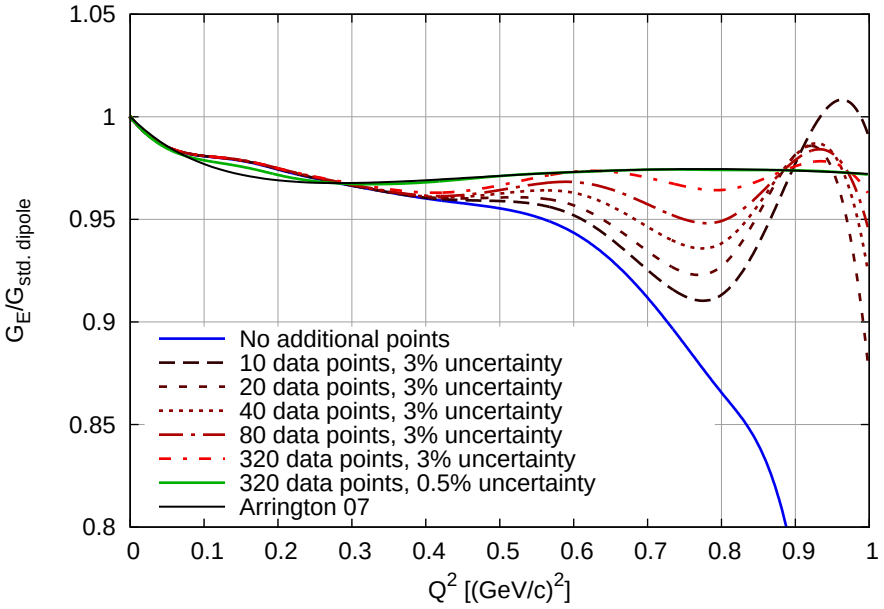

Figure 9.20: G_E extracted with additional pseudo data points. Shown are the best fit curve without pseudo data (blue), curves (shades of red, dashed) with increasing number of pseudo data points from the Arrington-07 parametrization (black) with constant uncertainty, and a curve with pseudo data points with smaller uncertainty (green). The pseudo data points are distributed uniformly between 0 and 1 $(\mathrm{GeV}/c)^2$.

9.2.5 Inclusion of external data

In the light of the problems of the previous data, an inclusion in the analysis of the present data has questionable merit. In any case, the existing data points inside the Q^2 region covered by the present experiment have only a marginal effect: Due to their low number and their larger errors, their influence on the minimization of χ^2 is minimal. Reduction of the errors of the additional data points increases their impact. However it leads to oscillations of the flexible models inside the data range, when the fit is locally pulled away from the optimal solution for the new cross section data.

One possibility with which one might circumvent this oscillatory behavior is to create dense pseudo data points from a parametrization of the old data. While this approach has no statistical value, because the weight of the old data is now arbitrary, it is a test of the stability of the fit procedure. The result is as one would expect: With increasing number of pseudo data points, or larger weight, the fit continuously shifts away from the optimal solution without the addition of external data toward the parametrization for the additional data. This is shown in figure 9.20, where different numbers of points calculated from the (not TPE corrected) Arrington-07 parametrization have been included, finally with highly reduced errors.

A similar effect can be seen when external data at Q^2 higher than 1 $(\mathrm{GeV}/c)^2$ are included. While the less flexible models are too fixed by the low-Q^2 data of this experiment to change in a significant way, the polynomial[5] models can describe the additional data, but with heavy oscillations between the individual points. When dense pseudo data points are created and included as outlined above, the flexible fits can describe these also, but flexibility in the low-Q^2 region is lost and the description of the data of this work gets worse. This can be compensated by a larger number of parameters, but then the fit is essentially unchanged for low Q^2 and the parametrization for the pseudo data points is replicated at large Q^2.

[5]The large gaps between the external data points force rather large knot distances for the spline models. With such knot distances, the description of the data at low Q^2 would deteriorate considerably.

9.3 Determination of the electric and magnetic rms radii

According to eq. (2.25), the electric and magnetic root mean square (rms) radii, $\langle r_e \rangle$ and $\langle r_m \rangle$, are given by the slopes of the corresponding form factors at $Q^2 = 0$. Therefore the accuracy with which they are determined by the measurement is given by the accuracy of the data in particular at low Q^2. Since the accuracy of G_E is high at low Q^2, $\langle r_e \rangle$ will be determined with good precision, while G_M, due to its small contribution to the cross section at low Q^2, is poorly determined here. At any rate, the determination of $\langle r_e \rangle$ and $\langle r_m \rangle$ correspond to an extrapolation of G_E and G_M to $Q^2 = 0$, and one has to ask the question to which extent the result depends on the ansatz for the fit model, in particular on its flexibility, which is certainly different for the different functional forms and which also depends on the number of parameter, N_p, i.e. on the order of the polynomial or number of knots in the splines, respectively.

9.3.1 Determination of the radii from the global fits

Figure 9.21 displays the dependency of the extracted electric and magnetic radii on N_p. It has to be noted that for both the electric and the magnetic radius the polynomial and the polynomial + dipole model produce a stable result for $N_p > 9$. The polynomial $\times$ dipole model works comparably well for the electric radius for $N_p > 8$, but shows erratic behavior for the magnetic radius for $N_p > 9$. The inverse polynomial, which has a quicker convergence to the χ^2 plateau, also deteriorates quicker into such an erratic behavior for $\langle r_m \rangle$. Nevertheless, these models agree quite well for both radii when one confines oneself to N_p at the beginning of the plateau.
The erratic behavior of the magnetic radius stems from the less stringent determination of the magnetic form factor at low Q^2, where the magnetic contribution is very small and where, with enough flexibility (large N_p), the fit follows smallest statistical deviations, resulting in large uncertainties. Low N_p give the fit enough stability to extrapolate G_M from higher Q^2 values, where the magnetic contribution is sizable, down to $Q^2 = 0$. It has to be noted that in previous determinations of $\langle r_m \rangle$, only low order Q^2 terms have been used (up to Q^4 in [SSBW80]).

The spline fits (here based on polynomials of third order) tend to give a smaller electric radius than the rest of the models, they additionally exhibit a depression in the value of the radius for N_p around 10. This difference between the result from the splines and the polynomials was further investigated, but no conclusive cause was found. It has to be noted (see the model dependency analysis in appendix H) that for some input models the spline models have a bias to smaller radii.
The curvature of a spline is limited by the order of the base polynomial. Therefore, also splines based on polynomials of fourth and fifth order were tested[6]. They produce larger radii, as can be seen from figure 9.22.

[6] Higher orders would reduce the spline fit to a simple polynomial fit.

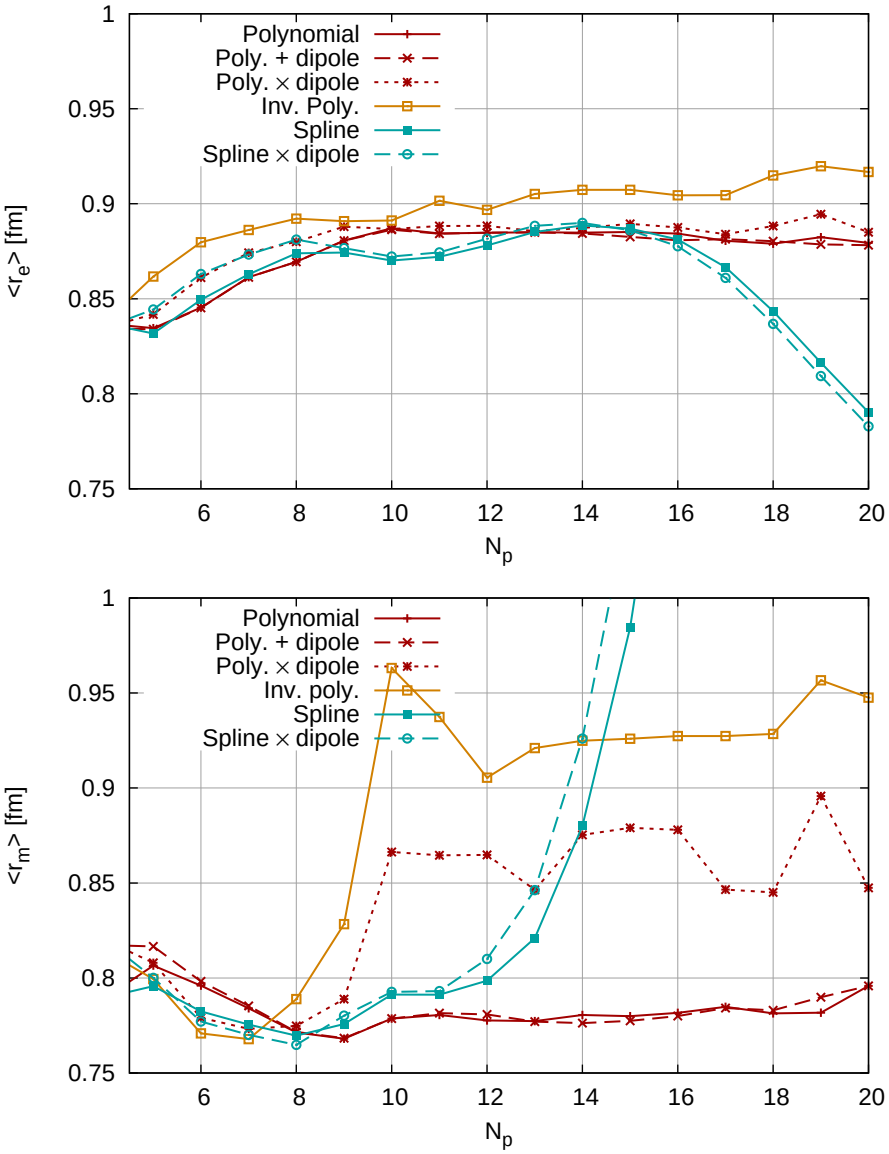

Figure 9.21: The dependence of the extracted electric (top) and magnetic (bottom) radius of the different flexible models on the number of parameters.

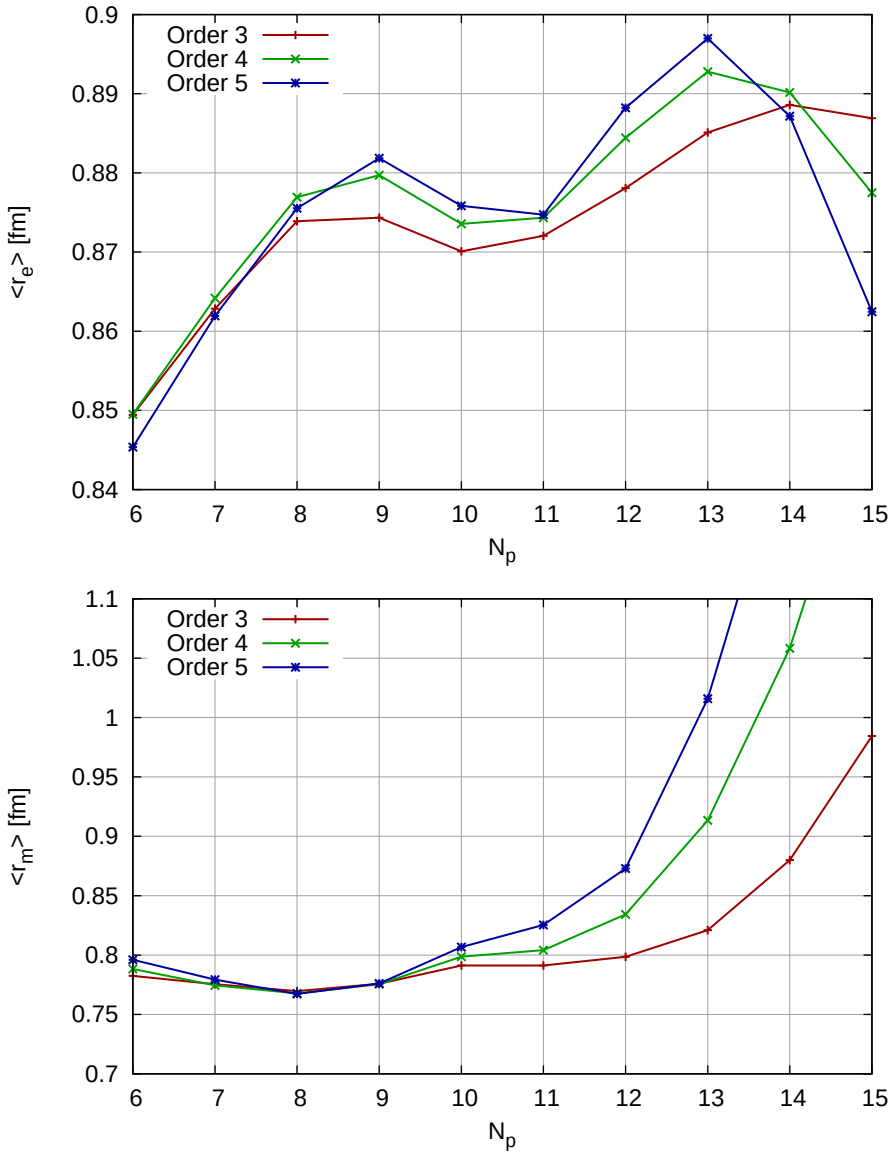

Figure 9.22: The electric and magnetic rms radii, extracted by the spline model with polynomials of third, fourth and fifth order as base functions.

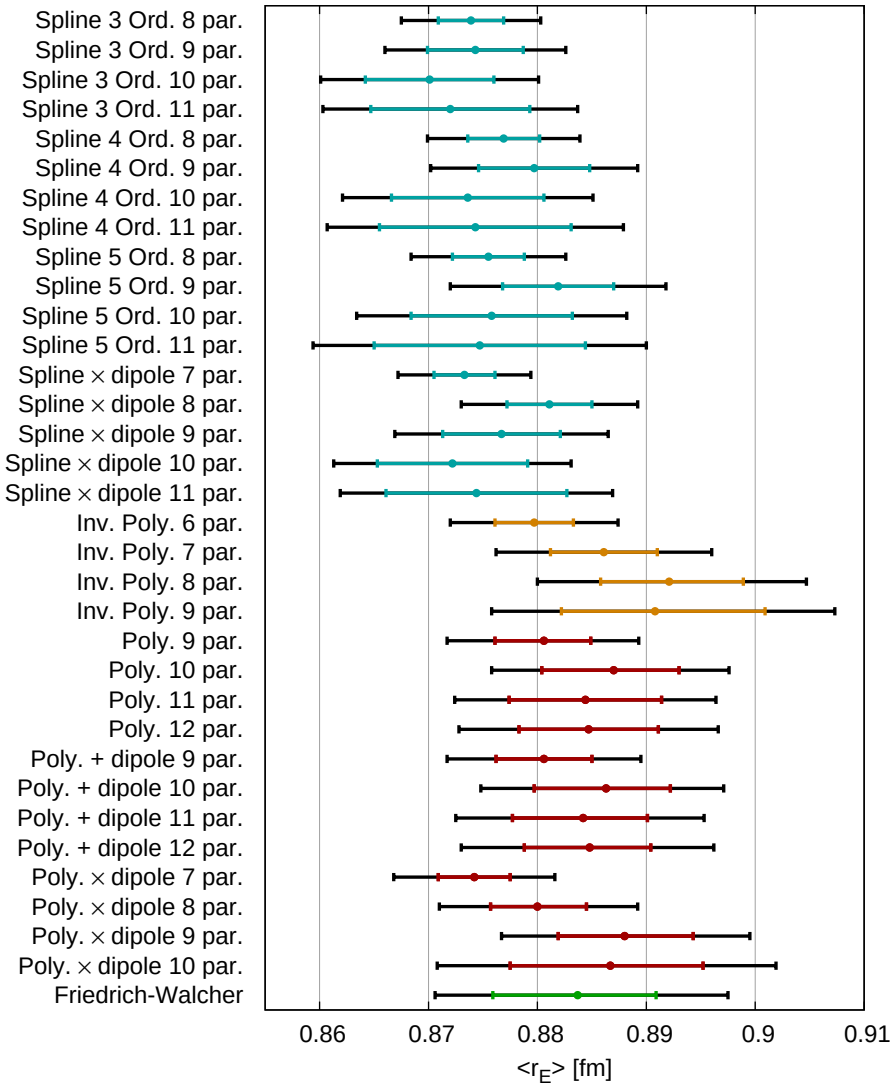

Figure 9.23: The electric rms radius as extracted by the different models. Colored: Statistical error. Black: Linearly added systematic error.

Focusing on the χ^2-sum of points below $Q^2 = 0.06\,(\mathrm{GeV}/c)^2$ (543 data points), the spline fits yield a χ^2 around 581, while the rest of the models give around 576. While this also points to a less good fit of the low-Q^2 region by the spline models, it is not statistically significant since the $\Delta\chi^2$ of 5 lies well within the 1σ-width of the χ^2 distribution ($\sigma_{\chi^2}(N_{\mathrm{d.o.f}} \approx 543) \approx 33$).

To estimate the model dependency for the extracted radii, the radii are determined with all models described before and for some variation in N_p. The results are shown in figures 9.23 and 9.24.

The results for the charge radius fall apart into two groups according to the model of the analysis, namely those determined with the spline-based models

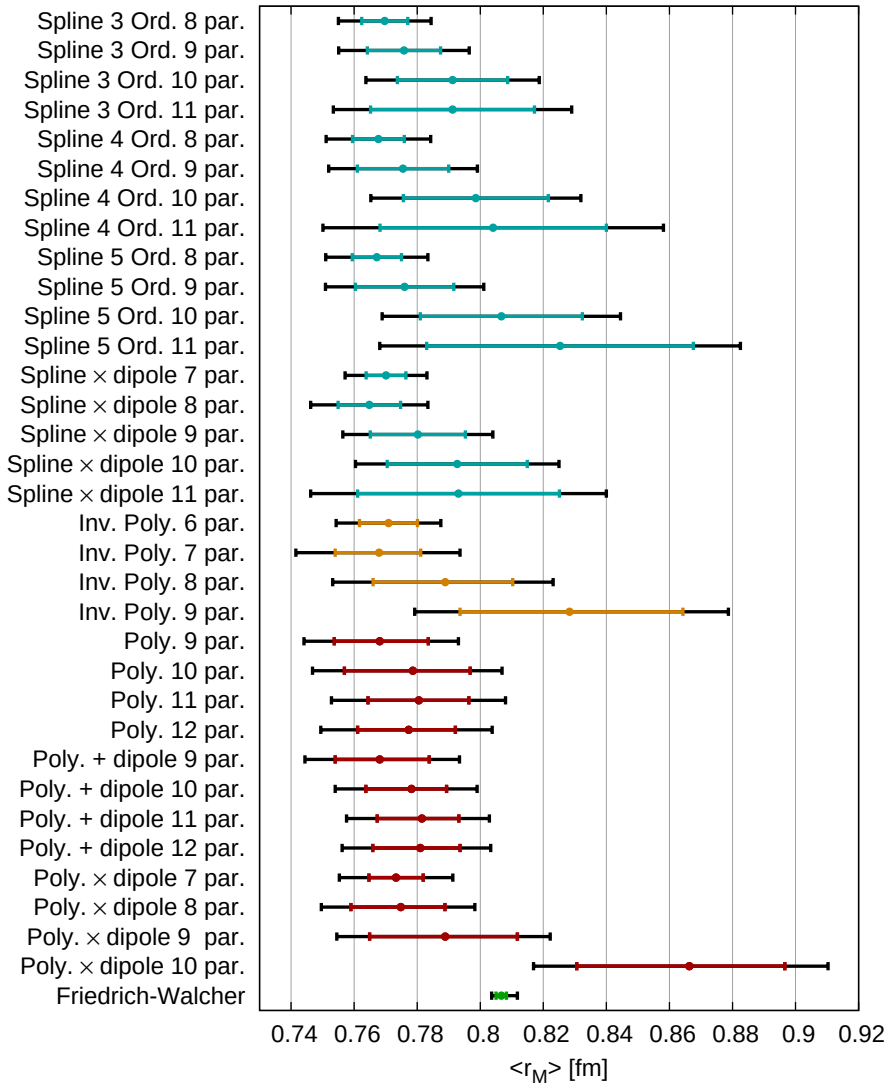

Figure 9.24: The magnetic rms radius as extracted by the different models. Colored: Statistical error. Black: Linearly added systematic error.

Group		radius
Spline	$\langle r_e \rangle$	$0.875 \pm 0.005_{\text{stat.}} \pm 0.004_{\text{syst.}} \pm 0.002_{\text{model}}$ fm
	$\langle r_m \rangle$	$0.775 \pm 0.012_{\text{stat.}} \pm 0.009_{\text{syst.}} \pm 0.004_{\text{model}}$ fm
Polynomial	$\langle r_e \rangle$	$0.883 \pm 0.005_{\text{stat.}} \pm 0.005_{\text{syst.}} \pm 0.003_{\text{model}}$ fm
	$\langle r_m \rangle$	$0.778^{+0.014}_{-0.015\ \text{stat.}} \pm 0.010_{\text{syst.}} \pm 0.006_{\text{model}}$ fm

Table 9.2: The electric and magnetic rms radii $\langle r_e \rangle$ and $\langle r_m \rangle$ determined from the two groups of models, namely the spline and the polynomial group.

and those from the polynomial-based models. For each group, the electric and magnetic radius has been determined as the weighted average and an additional model error has been determined from the weighted variance. The results for $\langle r_e \rangle$ and $\langle r_m \rangle$ are summarized in table 9.2.

The final result is the (unweighted) arithmetic average of the values of the two groups. An additional model error (labeled "group"), accounting for the difference of the two groups, is attributed to the result. Since it cannot be assumed that this error is normal-distributed, it is taken as half of the difference of the two groups. The final result from these flexible models is

$$\begin{aligned} \langle r_{e,\text{flexible}} \rangle &= 0.879 \pm 0.005_{\text{stat.}} \pm 0.004_{\text{syst.}} \pm 0.002_{\text{model}} \pm 0.004_{\text{group}} \text{ fm}, \\ \langle r_{m,\text{flexible}} \rangle &= 0.777 \pm 0.013_{\text{stat.}} \pm 0.009_{\text{syst.}} \pm 0.005_{\text{model}} \pm 0.002_{\text{group}} \text{ fm}. \end{aligned}$$

The results of the fit of the Friedrich-Walcher parametrization is not included in this average. It yields

$$\begin{aligned} \langle r_{e,\text{F.-W.}} \rangle &= 0.884^{+0.007}_{-0.008\ \text{stat.}}\ ^{+0.007}_{-0.005\ \text{syst.}} \text{ fm} \\ \langle r_{m,\text{F.-W.}} \rangle &= 0.807 \pm 0.002_{\text{stat.}}\ ^{+0.004}_{-0.001\ \text{syst.}} \text{ fm}. \end{aligned}$$

It is in agreement with the charge radius found by the flexible models, but differs for the magnetic radius. The very small error bar for the magnetic radius is an indication that the Friedrich-Walcher parametrization is not flexible enough to express the shape of the data for the magnetic form factor at smaller Q^2, i.e. it is completely fixed by the large-Q^2 data. The statistical errors have to be interpreted in the usual way, that is, with 68.3% probability the true value of the electric radius is inside the error without any constraint on the magnetic radius (and vice versa).

9.3.2 Determination of the charge radius from 180 MeV data alone

For small Q^2, the contribution of the magnetic form factor to the cross section is small. Hence, the adoption of a parametrization for G_M makes it possible to extract the charge radius from the 180 MeV data alone: The (small) G_M contribution is estimated from a G_M parametrization and subtracted from the cross section. The resulting values for G_E are fitted using a simple model like a low order polynomial or inverse polynomial. This technique is similar to

the method employed by Simon et al. [SSBW80], where G_M was set to $\mu_p G_E$ (scaling relation) and has been applied here only as a kind of consistency check. In the present work it is used with different parametrizations, different cut-off values in Q^2 and different G_M-models. The normalization was left floating, but the fit recovered the normalization given by the global fit on the 0.1% level. This approach yields radii between 0.870 and 0.895 fm, with most values around 0.880 fm, thus in excellent agreement with the final result of the global fit.

10 Conclusion and Outlook

10.1 Conclusion

A high-precision measurement of the elastic electron-proton scattering cross section was performed at the MAMI 3-spectrometer-facility in the Q^2 range from 0.004 to 1 $(\mathrm{GeV}/c)^2$. Employing a direct fit of a selection of different form factor models to the measured cross sections, the electric and magnetic form factor were extracted. All flexible models give very similar results, indicating that there is no model bias for the form factor extraction. The high internal consistency of the data and the results prove the validity of the global fit approach. These two points are further supported by a model dependency analysis where the analysis method and the validity of the different fit models was tested with pseudo data generated from popular parametrizations.

The aim of this work was twofold. First, the analysis of the previously existing data by Friedrich and Walcher [FW03] did reveal some bump-structure in the electromagnetic form factors which theory seems to be unable to reproduce. Second, the electromagnetic rms-radii of the proton should be measured with high precision in order to clarify the comparison with the Lamb shift measurements.

While our measurement does not support the bump-structure in G_E revealed by the Friedrich-Walcher analysis of the previous data, it is found that the electric form factor shows several characteristic deviations from the dipole. This is emphasized in figure 10.1, where the slope of the form factor relative to that of the standard dipole is shown. One observes three striking features: In the first segment, below 0.1 $(\mathrm{GeV}/c)^2$, the slope of G_E is significantly steeper than that of the standard dipole. In the second segment, the slopes are very similar. The flexible models show a third region, above 0.5 $(\mathrm{GeV}/c)^2$, where the slope is again substantially larger.

The steeper slope at low Q^2 is a direct signature for the fact that the rms-radius is substantially larger than that of the standard dipole fit (see below). This large radius, which theory is not able to reproduce hitherto [BHM07], may be a hint to a pion cloud in the proton.
The change in the (relative) slopes around 0.1 $(\mathrm{GeV}/c)^2$ may also be taken as a hint that there are two different scales in the extension of the proton. It is interesting to see what theory can say about this change when looking at it within the precision of this experiment.
The third characteristic, the change in slope at 0.5 $(\mathrm{GeV}/c)^2$, is only revealed by the sufficiently flexible models. The stiffer models (double-dipole and Friedrich-

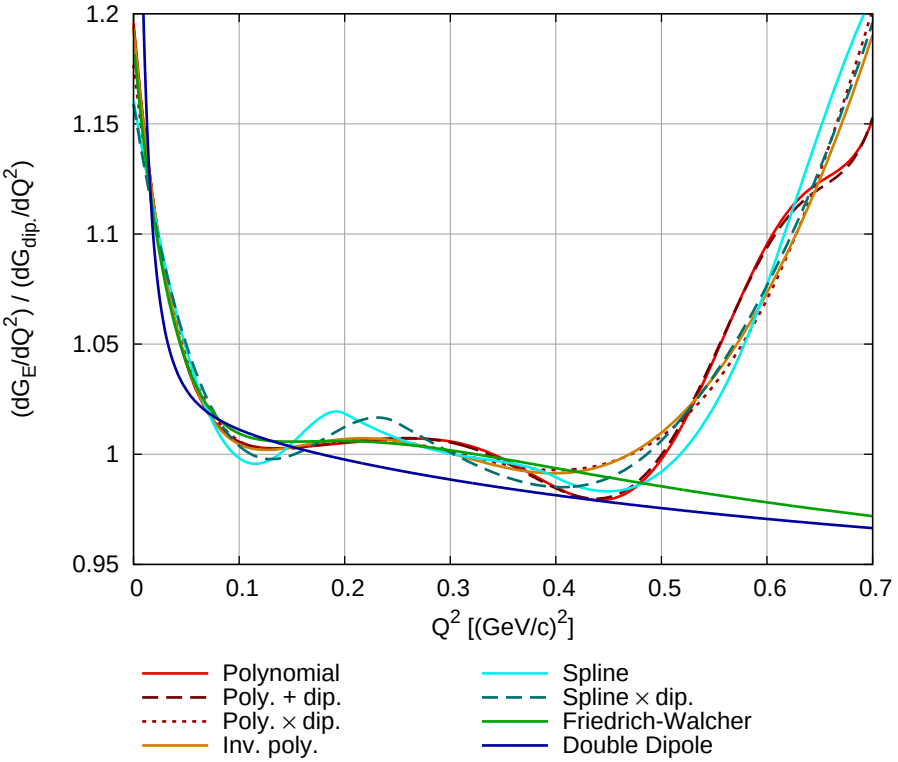

Figure 10.1: The derivative of the electric form factor, divided by the derivative of the standard dipole. Three regions of different behavior are visible: (1) A steep drop of the ratio up to 0.1 $(\mathrm{GeV}/c)^2$, where the slope of the fits is larger than the slope of the standard dipole. (2) A region where both slopes are similar (up to 0.5 $(\mathrm{GeV}/c)^2$). (3) A region where the flexible models again show a larger slope.

Walcher parametrization) are not able to follow this feature. While it is interesting to look for a possible physical explanation for this feature, one has to be aware that above 0.55 $(\mathrm{GeV}/c)^2$ only two energies contribute to the measurement and above 0.75 only one. Therefore, the separation into the small contribution from G_E and the larger contribution from G_M (which dominates the cross section in this Q^2 region and which does not show this behavior) may fully exhaust the possible uncertainties in the data in the determination of G_E. This will be checked by further measurements with MAMI C (see below). Nevertheless it might be worthwhile to think of dispersion contributions to the cross section, i.e. of two photon exchange with the proton being exited in the intermediate state. At these energies and relatively large angles, the magnetic excitation of the Δ should be quite likely. This is left as an open question.

G_M exhibits a structure (relative to the standard dipole) around 0.2 $(\mathrm{GeV}/c)^2$, which again might be taken as a hint for a pion cloud (see figure 9.16). However, there is no change in the slope around 0.5 $(\mathrm{GeV}/c)^2$.

The determination of the charge radius of the proton, i.e. the extrapolation of the form factor to $Q^2 = 0$, depends somewhat on the model used for the extraction. In the analysis of this experiment, a large number of models was used, which can be classified into two groups, the spline models and polynomial models. While several findings indicate that the radius extracted by the spline models is less reliable, the spline models cannot be excluded with certainty. This model-dependence is accounted for by an additional model error, which is equal to half of the difference of the results from the two groups. The charge radius is found to be

$$\langle r_e \rangle = 0.879 \pm 0.005_{\text{stat.}} \pm 0.004_{\text{syst.}} \pm 0.002_{\text{model}} \pm 0.004_{\text{group}} \text{ fm}.$$

This is far above the standard-dipole value, but it is in good agreement with the previous, Coulomb-distortion-corrected Mainz result (0.880 ± 0.015 fm [Ros00]) and results from Lamb shift experiments (0.883 ± 0.014 fm [Mv00], 0.890 ± 0.014 fm [U$^+$97; Kar99]). It has to be noted, however, that the Coulomb correction applied in the present work is only an approximation, and the radius might change slightly when a full calculation is applied.

The limited accessible kinematical region and the Q^2-scaling of the magnetic form factor contribution to the cross section lead to a significant larger error for the magnetic radius. It is found to be

$$\langle r_m \rangle = 0.777 \pm 0.013_{\text{stat.}} \pm 0.009_{\text{syst.}} \pm 0.005_{\text{model}} \pm 0.002_{\text{group}} \text{ fm},$$

hence substantially smaller than the standard-dipole value and also smaller than the results from previous measurements.

10.2 Outlook

To reduce the theoretical uncertainties of the results of this thesis, a full calculation of the Coulomb distortion and the two photon effect should be performed in the future and included in a new fit.

Further experiments can improve the present data set in three ways: With the installation of the variable energy extraction magnet on the HDSM stage of the Mainz Microtron (MAMI C), the extension to larger Q^2 is straight forward. The limit here will be the maximum electron momenta the spectrometers can handle, hence, low scattering angles cannot be measured at the higher energies. It may be possible to circumvent this by detecting the proton instead, a detailed study has to be performed in this regard. These measurements will be very important as they add data with more incident energies at larger Q^2 in order to clarify the situation with the steeper slope in G_E above 0.5 $(\text{GeV}/c)^2$.
To reduce systematic errors, only the short target and a smaller collimator should be used for spectrometers A and C – the count rate, though lower at higher energies, should still be sufficiently high. Furthermore, simultaneous measurements with spectrometers B and C should be avoided[1], at least at

[1] It may also be possible to shield spectrometer B from the field of spectrometer C.

small relative angles. Also, the algorithm for the magnetic field setup has to be revised.
Such an extension is on the agenda of the A1-collaboration for the near future.

It is not as straight forward to achieve a better determination of the magnetic form factor at small Q^2 with the MAMI facility. To enhance the contribution of the magnetic form factor to the cross section, one needs to measure at backward angles, hence at smaller incident beam energies. The latter are not currently available at the Mainz facility. However, the second race track microtron could be modified to deliver smaller energies. This is under investigation.

In the case of the electric form factor, a different approach is actively investigated: The idea is to use initial-state-radiation, i.e. the situation where the electron radiates a (hard) photon before the scattering occurs, to reach very low Q^2. The cross section is determined by measuring deep into the radiative tail. First feasibility studies for such a measurement were already performed at the Mainz linear accelerator [PFS$^+$89]. Preliminary calculations indicate that an exact reaction reconstruction is possible without measurement of the proton or photon. The validity of this method depends on the accuracy of the theoretical description of the radiative tail. Varying the kinematics, it is possible to test at the same time the theoretical description and to extract the electric form factor. If this method proves valid, it allows for a determination of the electric form factor down to $Q^2 = 0.0001$ (GeV/c)^2.

Appendix

A Remote control of the spectrometers

The measurement program encompasses a large number of individual measurements, differing in the magnetic field and in the angles of the spectrometers. While the magnetic field could be adjusted from the counting room, it was not possible to change the spectrometer angle remotely. Such feature was not deemed to be necessary in the original plans for the spectrometer setup, since the planned coincidence experiments needed such long measurement durations for a single setting that the interruption time for a hall access and a setting of the spectrometers by hand was reckoned to be more or less negligible. In addition, it was felt that the up to 400to heavy spectrometers should be moved only under the direct control of the experimentalist.
However, a hall access for moving the spectrometers has several disadvantages:

- The beam has to be switched off. In addition, to exclude any endangerment of a person in the experimental hall, one of the beam-line dipoles is switched off. The field of this magnet drifts for some minutes after it is switched on again. Also, for the time the beam is switched off, the target is not heated and the temperature of the liquid hydrogen drops. When the beam is turned on again, the temperature rises and hence the density drops to the old value. These effects make it mandatory to delay the start of the next measurement until the experimental setup has stabilized.
- In addition to the time needed for the actual movement of the spectrometers, beam time is lost for the communication with the accelerator operator and for the opening of the hall.
- The chance for a malfunction of the accelerator or detector setup is higher in a discontinuous operation than in a continuous one.

All in all, a change in spectrometer angle via hall access takes about 20 minutes. Together with the higher malfunction risk, this would have been prohibitive for the planned 500 angle changes of the $p(e, e')$-experiment. This program could only be executed with a remote control of the spectrometers.

A.1 Existing control

The spectrometers are connected to a common pivot right below the target vacuum chamber. The spectrometers themselves are seated on a steel ring. When a spectrometer has to be moved, a compressor mounted on each spectrometer pumps oil between the steel ring and the spectrometer pillow block. A geared motor drives a cogwheel that meshes with a chain around the steel ring to move the spectrometer.

Compressor and motor are controlled by a "speicherprogrammierbare Steuerung" (SPS, programmable logic control PLC) of the series S5 made by Siemens. It is composed of a central unit and several input/output modules connected over a serial bus system to interact with the user and the motor/compressor. The user-defined program is stored on an eprom. It interprets the user's input and controls and supervises the compressor and motor driver.

A.2 Design of the remote control

The following points were important for the concept of the remote control:

1. The existing method to control the spectrometers from inside the hall should be preserved.
2. In case of a disruption of the communication link between the spectrometer-mounted control system and the remote station, the control should go to a secure mode, i.e. the motion of the spectrometers has to stop.
3. Any collisions between the spectrometers and obstructions in the hall must be avoided. This includes collisions with the beam line, the target system and the walkway around the hall, but also collisions of the spectrometers among each other.

A.2.1 Changes to the SPS program

The SPS is equipped with a debug port that allows access to the memory and hence to the executed program. Unfortunately, no documented sources of the control program were available. To find a suitable point to attach the remote control, parts of the control codes had to be reverse engineered. Here, a strategy of minimal invasion was observed, which was supported by the design of the S5 series. The SPS has an internal, immutable main loop, the sequence:

- The input status of all attached modules is read in serially and saved in a special region of the random-access memory.
- The user-defined program is executed. To get the input status, the program accesses this memory and writes output commands to another memory block.
- This second block is written out to the output modules via the serial connection. Then the actual output change is performed by the attached modules.

To preserve as much as possible of the original program, the best route is to modify the memory copy of the input status with the remote control commands. This would emulate a true button press for the main program without the need to bridge the buttons electrically with e.g. a relay. It is possible to write to this memory range via the debugging connection, but erroneous behavior may occur

when the change is done while the user defined program is executed. Hence, the access has to be synchronized.

The user defined program consists of a simple main loop which calls consecutively a number of submodules. Using the debugging access, it is possible to change the ordering or add calls. For the synchronization, two new submodules were written:
The first module checks a certain memory location. This memory location is written to by the remote control to enable remote operation. If it is set, the module copies the input data from a remotely written memory range to the special memory copy of the inputs. The module is added to the beginning of the main loop so that later modules either see the true inputs (remote control off), or the inputs sent by the remote control.
The second submodule is called at the end of the main loop. It copies the memory range of the output to another memory range where it is read out by the remote control using the debugging port. This makes the status information from the local control circuit available on the remote control station.

A.2.2 Remote control hardware and software

The debugging port is a serial connection complying with the V24 standard. For the installation of the remote control, an electronics board was constructed and mounted in the counting room, which translates the three V24 channels to RS-232. The galvanic isolation is realized with optocouplers. The power supply of the spectrometer control has been equipped with a relay, so that the complete control logic can be switched on and off from the counting room. This is a precaution to allow remote reboot of the SPS when the internal microcontroller has crashed, e.g. due to radiation.

The software has two parts: A server component is running on the control computer where the converter electronics is attached to. It communicates via UDP with the GUI component which can be run on any computer on the network. The GUI component presents the status information read back from the spectrometer and has buttons to start/stop the compressor and motor.

A.2.3 Security aspects

The original programming of the SPS already provided for collision switches, but those were never equipped. Collision detection switches were now mounted on the spectrometers and connected to the provided inputs. They are actuated by blocks mounted on the steel ring to stop the spectrometers before a collision with the beam line can occur. Another switch prevents collisions between spectrometers B and C. A relay, which is powered by the control system of spectrometer C, distributes the signal of this switch to both spectrometers. This makes it mandatory to switch on spectrometer C when B has to be moved. All switches are normally closed and have forcibly guided contacts, reducing the risk of a collision due to hardware failures.

The switch mount plates have space for another switch that is triggered a little bit later. This allows for a hard switch off of the motor in the case the SPS crashes in an unsafe manor. The experience of the beam times shows, however, that this precaution was not necessary.

An unmonitored moving of the spectrometers would be reckless even with the installation of the collision switches. Temporary obstructions like ladders or stuck hoses have to be taken into account. Therefore, cameras were mounted on each side of the spectrometer platforms. The captured images are transmitted to the counting room via the normal IP network. The cameras are motorized so that the field of view can be controlled remotely.
The changes to the SPS software are patched in on demand using the debugging port. After a power outage or when the spectrometer control is power cycled, the original software is loaded from the eprom, and the spectrometer control is in a safe operation mode. The patched-in software modules also check whether the last communication with the remote control was recent. After a timeout, it does not copy the remotely set input values to the input memory area. This secures the transition to safe operation when the transmission from the remote control to the spectrometer control is disturbed.

B Anomalies

B.1 585-MeV-anomaly

The 585 MeV data set exhibits a strange anomaly. Figure B.1 depicts the measured cross sections, normalized to the standard dipole, as a function of time (number of measurement). The measurements with the three spectrometers are slightly shifted apart by multiplication with some factor. While the cross sections show a certain continuous variation according to the change of spectrometer angle, at least three "jumps" are visible around measurement numbers 20, 40 and 62, where the measurements of all three spectrometers change suddenly by the same amount. The data exhibit the same behavior whether they are normalized to the beam current measured with the Förster probe or with the pA-meter, ruling out a problem in the luminosity measurement. Several possible causes were tested and ruled out:

- The most probable cause of such jumps is a change of a target parameter like target density or position. However, these could be ruled out: A change in the target position might happen when the target is moved out and back in, e.g. when the screen is moved into the beam for a beam-position check. However, at at least one of the jumps, the target was not moved at all. The target pressure and temperature readings are stable over the complete measurement period, and a change of the density by this order of magnitude and short period of time would be very unlikely anyhow, especially since the jumps do not always coincide with a change in the beam current.
- A sudden change of beam position might cause such jumps. However, in the beam-position-monitor data, no indications of a beam-position jump was found.
- A further possible explanation is a beam loss after the Förster probe and pA-meter. This, however, should have been detected by an elevated radiation level.

While there is no indication for a sudden change in beam quality, such an occurrence could not be ruled out completely. However, some kind of timing or electric problem in the trigger logic appears more likely. For example, a "slightly" failing power supply of the PLU[1] module of the trigger logic, an FPGA[2], could cause glitches and hence missed events. This would possibly

[1] Programmable Logic Unit
[2] Field Programmable Gate Array

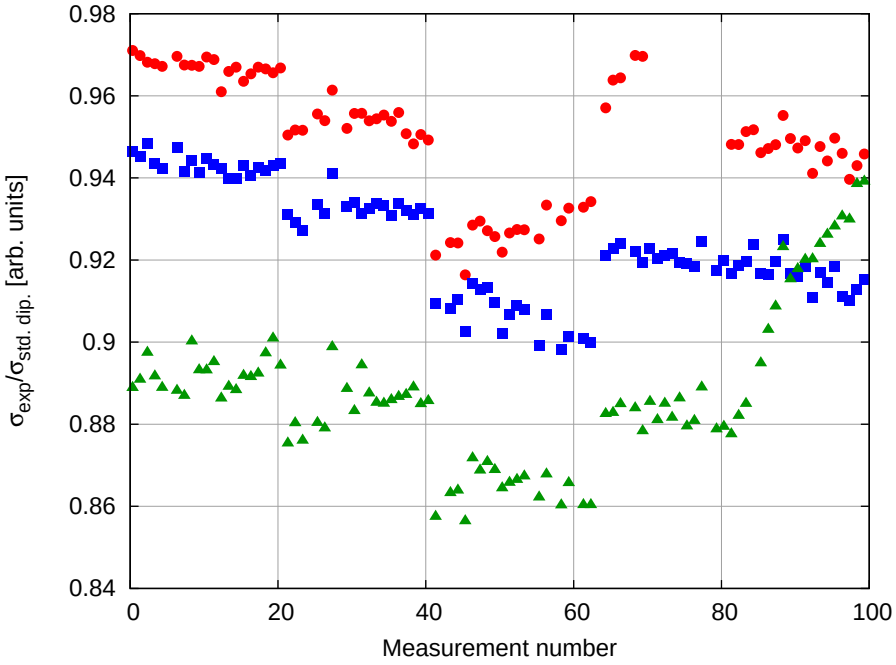

Figure B.1: The cross sections measured with 585 MeV incident beam energy, divided by the standard dipole cross section, plotted against time (number of measurement). The data measured with spectrometer A (red circles), B (blue squares) and C (green triangles) have slightly different normalizations to spread them apart. These data are normalized to the beam current measurement of the pA-meter. They show slightly different slopes due to the different changes in spectrometer angles, but exhibit three clear jumps around 20, 40 and 62.

correlate with the current drawn by the FPGA and therefore with the trigger rate.

This kind of error does not appear in any other of the data taking periods of this experiment and has not been observed in later beam times. However, in conventional experiments, with less redundancy in the measurements and lower statistics, it may have been missed entirely. It was not possible to reproduce the problem nor determine a cause.

Fortunately enough, one of the spectrometers was always used as a luminosity monitor. In fact, the "jumps" vanish completely when the data are normalized to the luminosity monitor, as can be seen in figure B.2. Therefore, this anomaly does not affect the analysis of the data.

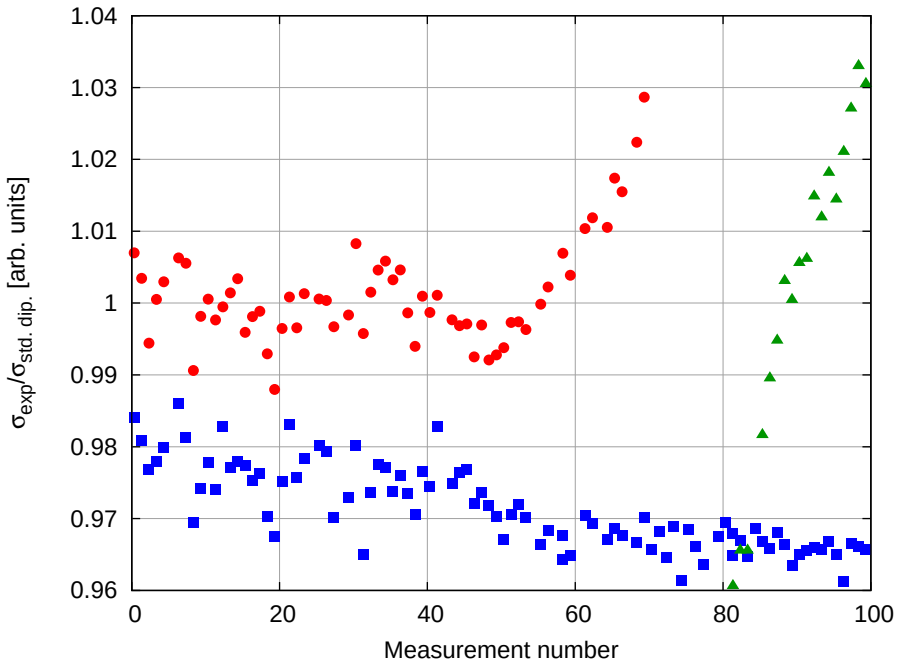

Figure B.2: Same as B.1, but normalized to the luminosity monitor. No "jumps" are visible anymore. The large slope of the data measured with spectrometer A after measurement number 50 and of the data of C stems from the change of the spectrometer angle, and thus of the deviation from the standard dipole fit they are normalized to (note that the scattering angle does not increase uniformly with the measurement number). The measurements of spectrometer C (up to measurement number 80) and of spectrometer A (over 80) which where used for the luminosity normalization are not displayed.

B.2 Quadrupole field

Another problem became apparent when the acceptance correction (see appendix C) was tested with varying cuts in the out-of-plane angle. The data points of spectrometer A for 855 MeV and 720 MeV break up into two groups according to whether they are measured below or above a certain spectrometer angle. When the cut is varied, the cross sections do not change in relation to other measurements of the same group, but the two groups are shifted against each other, an effect in the order of a few percent. A comparison of the spectra right before and after the "fault line" showed that the range of accepted out-of-plane angles gets slightly smaller.
While spectrometer B has only one dipole, i.e. the magnetic field is parametrized only by one parameter, spectrometers A and C have multiple magnets which have to be adjusted synchronously. The algorithm implemented for the magnet control calculates the required magnetic fields from the requested reference

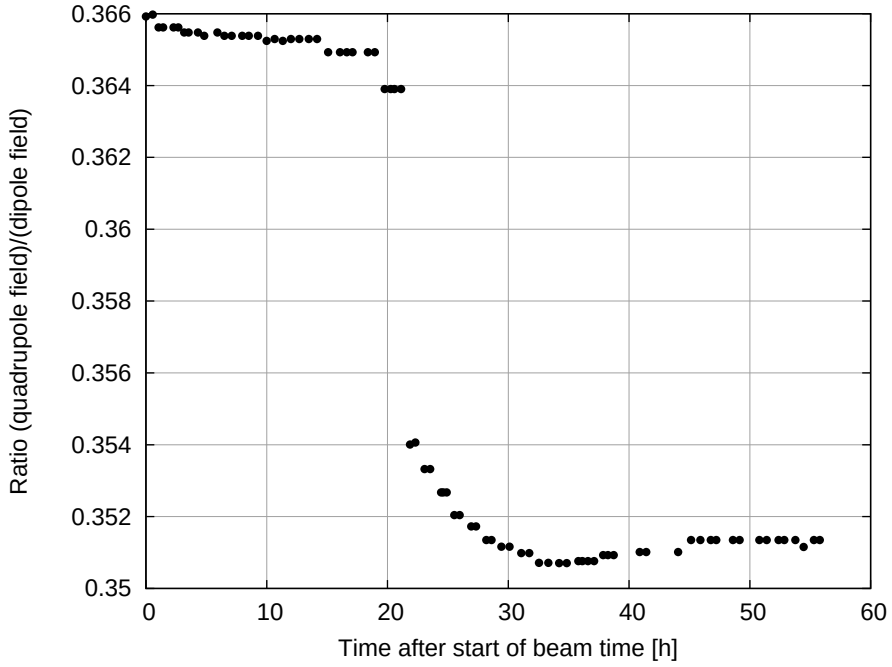

Figure B.3: The ratio of the quadrupole field to the dipole field of spectrometer A for the 720 MeV beam time. The x-axis is the time after the start of production measurements. The jump shortly after 20h beam time is clearly visible. It coincides exactly with the jump in the out-of-plane angle range.

momentum. The fields are converted to currents for the different coils and the power supplies are set accordingly. The dipole fields are then checked and fine-tuned with the NMR probe, while the fields of the quadrupole and sextupole are not fine-tuned at all.
If one now compares the Hall probe measurements of the quadrupole with that of the dipole, the ratio exhibits a jump about 20h after start of the beam time (see figure B.3). This coincides exactly with those measurements where the range of out-of-plane angles gets smaller. For measurements after that jump, the quadrupole has a smaller field in relation to the dipoles. The quadrupole is defocusing in the out-of-plane direction, a smaller field thus leads to a more narrow angle distribution. The effect is very subtle and can only be seen when comparing two histograms directly (figure B.4).

In a detailed study no other jumps for spectrometer A and no jumps at all for spectrometer C were found.

Since the acceptance is fixed by the geometry of the collimator in front of the spectrometer (for some subtle detail, however, see appendix C), this effect does not influence the extracted cross sections as long as no cut depending on the reconstructed target angles is applied.

To circumvent the problem in the future, the algorithm has to be extended to readjust all currents. It is unclear whether the resolution of the Hall probe is

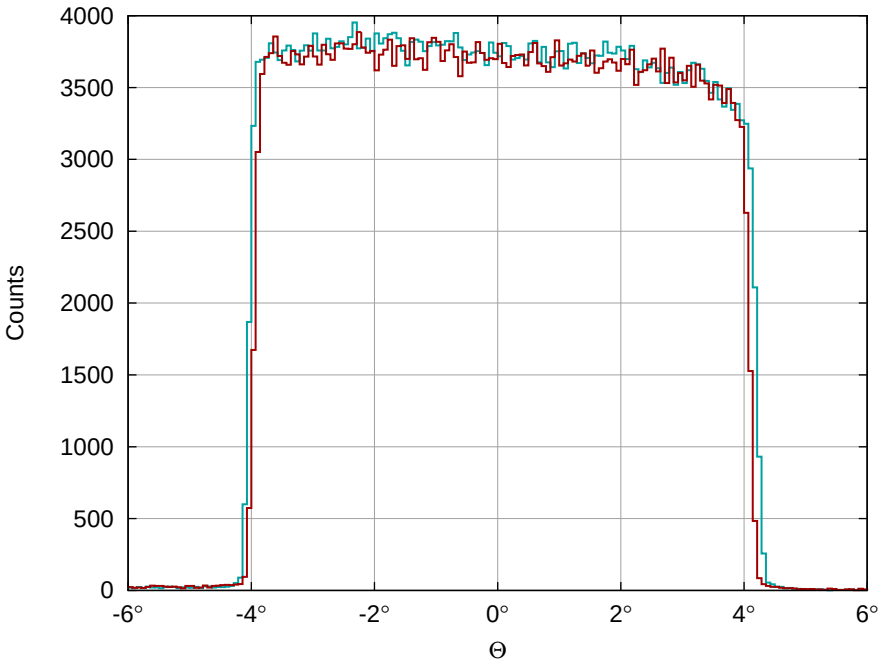

Figure B.4: Histogram of the out-of-plane angle Θ_0 of a measurement of spectrometer A directly before (cyan) and directly after (red) the jump (720 MeV data).

good enough for a fine-tuning of the quadrupole, especially for low reference momenta. Hence, future investigations have to evaluate whether an upgrade of the Hall probe is needed. Also, it is not clear whether the initial value for the quadrupole was off, or whether the dipole fine-tuning changed the field by an unadapted amount. The exact tuning procedure was not logged, so it is not possible to reconstruct how the fine-tuning procedure changed the initial dipole current.

C Acceptance correction for spectrometers A and C

Precise knowledge of the acceptance is a prerequisite for a precise determination of cross sections.
Normally, the acceptance is defined by the well known geometry of the collimator. However, for spectrometers A and C, there are particle trajectories for which the acceptance is not fully defined by this geometry. These are trajectories which pass the collimator, but then hit parts of the spectrometer before they can reach the detector system.
This happens only to trajectories which have very large in-plane angles Φ_0 which can happen if they originate from a vertex z far off the center (see figure C.1). The relevant coordinate here is not the position along the beam axis, but its projection to a plane parallel to the spectrometer collimator plane (see fig. C.2). Therefore, the effect depends on the target length itself (for the short target, the effect is much smaller) and on the actual spectrometer angle α. This would lead to a superimposed slope on the measured cross section. Thus, this effect in the measurement has to be accounted for also in the simulation.

To identify where collisions occur, the transport of charged particles inside the

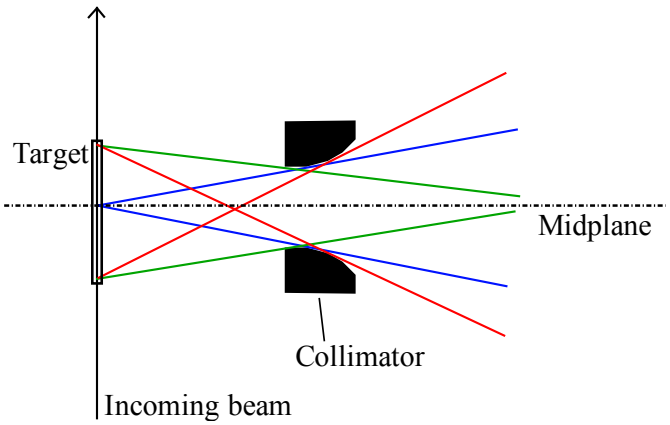

Figure C.1: Schematic (not to scale) of different trajectories. Blue: Trajectories from the middle of the target are all accepted. When the vertex has an offset along the beam line, the trajectories which cross the midplane before the collimator (red) may have very large angles and may collide with parts of the spectrometer geometry. Those on the other side of the acceptance (green) have smaller angles and do not collide inside the spectrometer.

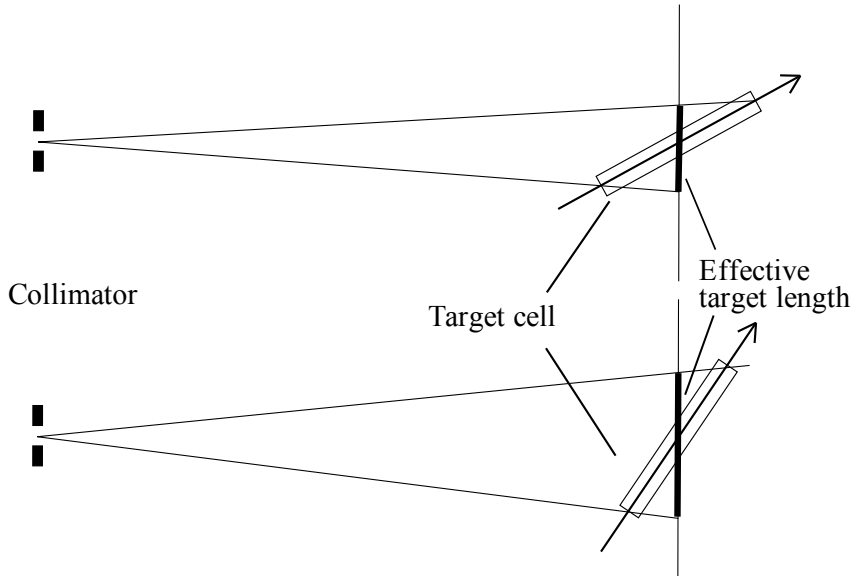

Figure C.2: Effective target length for two different spectrometer angles. The target appears smaller at smaller angles. At 90°, the length seen by the spectrometer is the true target length.

magnetic fields of the spectrometers were calculated. To this end, the program *gridtrace* ([Ber04], based on *qspin* [Pos00]), which solves the equation of motion by numeric integration, was adapted to calculate the particle transport in A and C.
Two possible collision points were found, namely a) the vacuum chamber inside the quadrupole magnet and b) the pole shoes of the first dipole.

a) Trajectories which have at the same time large out-of-plane and in-plane angels Θ_0 and Φ_0 may hit the tapered edges of the vacuum chambers inside the quadrupole magnet (see figure C.3). This leads to "missing corners" in a Φ_0-Θ_0-histogram (see figure C.4).

b) The electrons may hit the pole shoes of the first dipole. This effect gets stronger with higher relative momentum Δp (the difference to the momentum of a particle on the reference trajectory), because the focusing effect of quadrupole and sextupole is then smaller. The magnetic system behind the sextupole is not symmetric out-of-plane, which gives rise to an asymmetry in Θ_0: The effect is stronger when the trajectory is pointing downwards when entering the collimator, i.e. when the trajectories have a wide orbit in the up-deflecting dipoles.

To avoid this z-Φ_0-Θ_0-dependent acceptance, one may apply cuts in the data analysis to reduce the accepted phase space to a range where no trajectories are lost. Such a cut would either be dependent on the vertex position, or it would

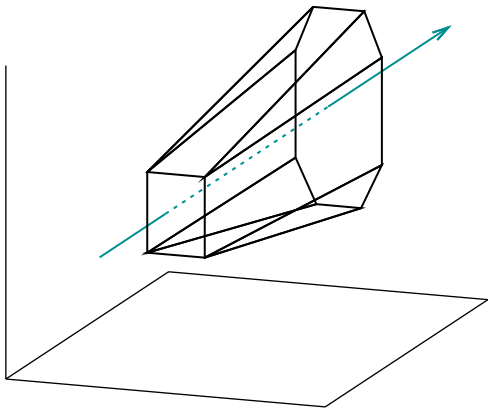

Figure C.3: Schematic drawing of the vacuum chamber inside the quadrupole of spectrometer A and C. The edges are tapered to make room for the quadrupole pole shoes outside of the chamber. The cyan arrow points away from the target into the spectrometer.

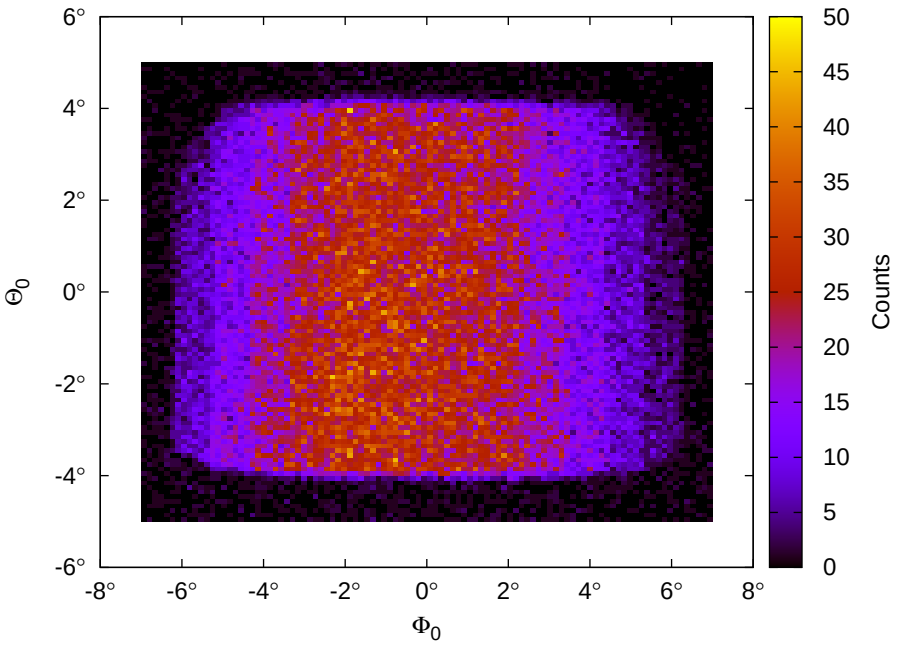

Figure C.4: Φ_0-Θ_0-histogram for a measurement of quasi-elastic reactions off a foil-stack target (5 foils with 1 cm distance). One can see the "missing corners", corresponding trajectories collide with the tapered edges of the vacuum chamber inside the quadrupole. Effect b) has been suppressed by a cut which only accepts $\Delta p < 0$.

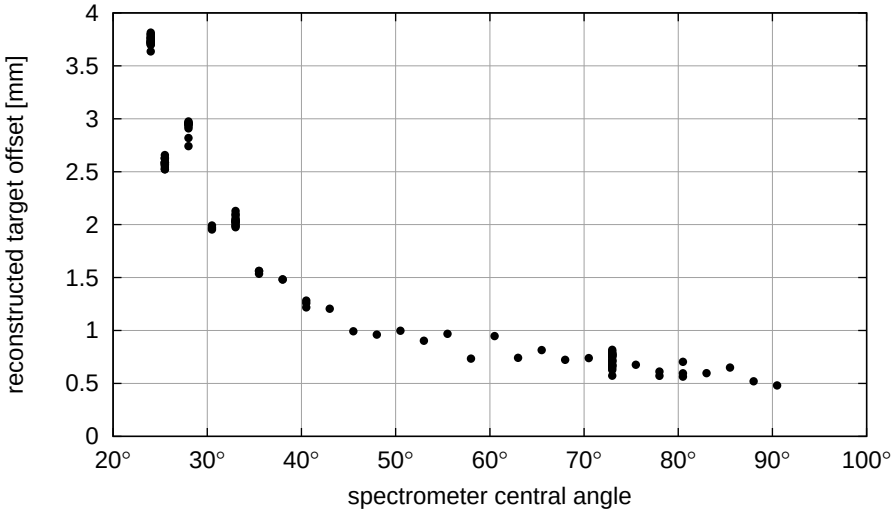

Figure C.5: Reconstructed offset of the target along the incident beam from the measurements of spectrometer A as a function of the central scattering angle. While the target was fixed, the reconstructed position of its center shows a dependency on the angle.

cut away a lot of "good" phase space. The latter is clearly undesirable, but the first possibility may look like a viable solution. However, it would be quite unreliable: With a change of the spectrometer angle, the vertex resolution changes, too. Also, the vertex reconstruction depends on the angle, as can be seen in fig. C.5, which shows the reconstructed target position (the true target position did not change). It is not feasible to match the simulation to this behavior in the experiment, hence a vertex-dependent cut would introduce uncontrollable, angle-dependent effects.

A viable alternative is to use the correct aperture in the simulation. The program *gridtrace* was further extended to test the calculated particle trajectory against the vacuum chamber and dipole geometry. While the geometry of the dipole is readily available as precise CAD drawings, the drawings for the vacuum chambers were not all available in the final version and had to be partly reconstructed from measurements from the outside of the chamber and from a comparison of measured data with the simulation.

A full numeric calculation of the particle trajectory for each event in a simulation is much too time-consuming. Therefore, the acceptance function was precomputed on a high performance cluster computer. This function depends on α, Φ_0, Θ_0, Δp and z. To compress the data, at each four-dimensional point $(\alpha, \Theta_0, \Delta p, z)$, the minimum and maximum Φ_0 is searched by bisection.
For each event in the simulation, the nearest points included in the table are looked up. The minimum and maximum Φ_0 are then linearly interpolated. Based on these values, the event is either accepted or discarded: A particle with an in-plane angle between these two values is taken to reach the detector.

D Influence of the quadrupole of spectrometer C on spectrometer B

Spectrometer B and C are located on the same side of the beam line (see figure D.1).
In the periods where spectrometer C was the designated luminosity monitor, it is at a fixed angle over a long period of time while spectrometer B is approaching spectrometer C with each angle change. When spectrometer B comes near to the minimal angle between B and C, spectrometer C is moved to the next, larger angle.

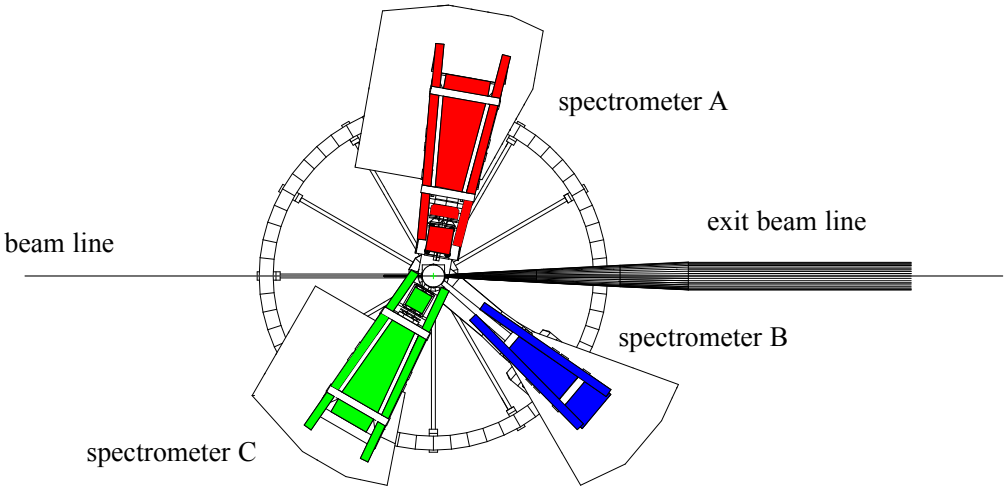

Figure D.1: Schematic of the spectrometer arrangement. Spectrometer B and C are on the same side of the beam line.

A closer look at the cross sections measured with spectrometer B reveals jumps of the order of 1 to 2% when spectrometer C is moved, i.e. when the angle between spectrometer B and C is increased by a large amount. When the spectrometers are close to each other, the measured cross sections are larger than anticipated from the rest of the measurements.
In addition, one observes that the energetic position of the hydrogen elastic peak also shows jumps on the same occasions: The measurements with spectrometer C close by show larger electron energies in spectrometer B (compared to the energy calculated from the angle) than those with spectrometer C further away. In contrast, the position of the elastic peak from the target walls barely changes when spectrometer C is moved (see figure D.2).

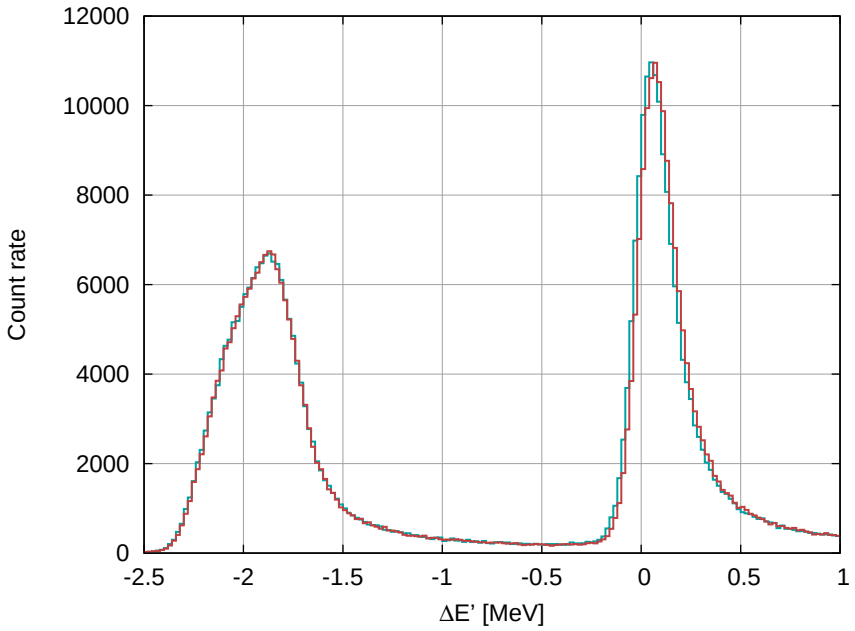

Figure D.2: $\Delta E'$ histograms measured with spectrometer B at 20° with spectrometer C close by (cyan) or further away (red). The left peak stems from electrons scattered elastically on the wall nuclei. The right peak corresponds to elastic scattering off hydrogen. While the left peak is not shifted, the hydrogen elastic peak shifts slightly (by around 15 keV) to larger energies when spectrometer C is close by.

Both effects can be explained with the influence of the fringe field of the quadrupole of spectrometer C on the trajectories going into spectrometer B: The field causes a deflection of the trajectories in the snout section of B, they are bent in the horizontal plane to larger scattering angles, i.e. away from the exit beam line. The collimator of spectrometer B is placed behind the snout at the entrance of the clamshell magnet. Hence, in first order, this deflection causes not a change of the absolute acceptance, but of the selected angular range. In effect, the spectrometer accepts smaller scattering angles than the geometry would indicate. The electrons at these angles have a larger energy and are produced with higher rate, because the cross section is larger for smaller angles. This explains both effects mentioned before. The size of the effect gets larger when spectrometer B is nearing spectrometer C and drops when spectrometer C is moved away from B to the next angle.

In principle, it is possible to calculate the size of the effect from the relative position of the hydrogen elastic peak to the peak from the target wall. However, this proved to be not precise enough. To correct for this effect quantitatively, it was studied in an additional data taking period. Spectrometer B was at a fixed angle (and therefore should measure constant electron energies and cross sections) and spectrometer C was varied both in field strength and angle. From

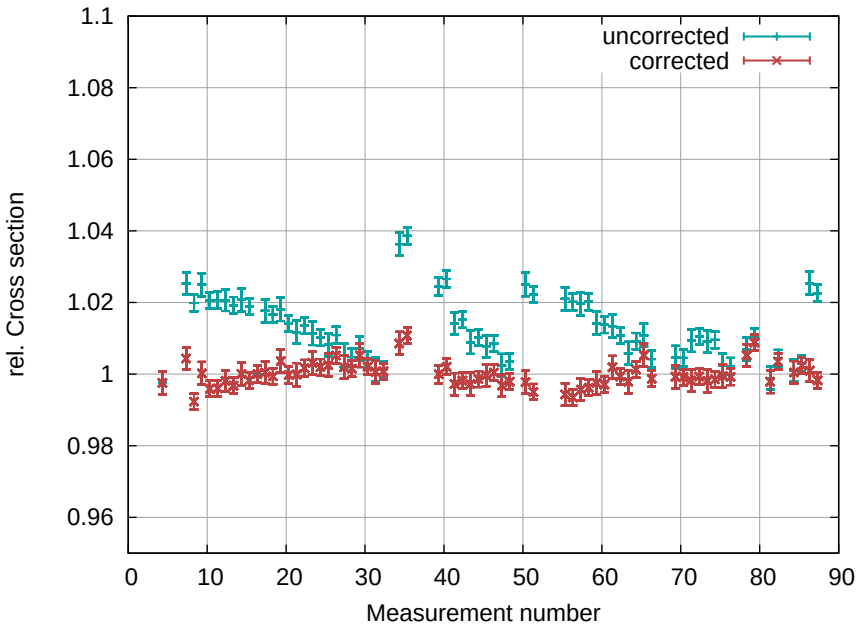

Figure D.3: Uncorrected (cyan) and corrected (red) relative cross section measurement with spectrometer B at a constant angle and momentum while spectrometer C is changed in field and angle. The empirical correction formula (eqs. (D.1) and (D.2)) compensates the spread within the statistical accuracy.

the change of the electron energy and cross section measured with spectrometer B, an empirical correction formula for the effective angle shift $\Delta\theta$ has been derived. This formula depends on the difference angle $\Delta\alpha$ and the ratio of the spectrometer fields, expressed by the central momenta p_C/p_B:

$$\Delta\theta = -3.271^\circ \cdot 1.201^{21.104^\circ - \Delta\alpha} \cdot \frac{p_C}{p_B}. \tag{D.1}$$

A negative sign indicates that the scattering angle of the accepted electrons is smaller than the angle spectrometer B is positioned at geometrically. This leads to a cross section modification

$$\frac{\Delta\sigma}{\Delta\Omega} = \frac{\Delta\sigma}{\Delta\Omega_{\text{exp.}}} \cdot \frac{\frac{\mathrm{d}\sigma}{\mathrm{d}\Omega}_{\text{theory}}(E,\theta)}{\frac{\mathrm{d}\sigma}{\mathrm{d}\Omega}_{\text{theory}}(E,\theta+\Delta\theta)}. \tag{D.2}$$

The angle correction $\Delta\theta$ is always smaller than 0.13°.
Since the correction depends on the ratio of the cross sections at nearby angles and since the effect is small, the choice for the theoretical cross section has no influence on the final result. In this work, the parametrization by Friedrich and Walcher is used. The correction is at most 1.8% for the kinematics in the experiment. Figure D.3 depicts the uncorrected and corrected cross sections measured in the additional beam time.

E Maintenance of the VDC in spectrometer A and B

In [Ber04], as preparatory work for this experiment, the efficiency of the vertical drift chambers (VDC) was studied with high spatial resolution. The work resulted in maps of the efficiency (see fig. E.1). Non-functional wires are visible as black lines. Additionally, one sees small areas where the efficiency is lower and which are not along the wire direction. It was assumed that in these areas the thin aluminum plating of the cathode planes had been damaged from sparks. In the preparation of the present experiment, the VDC systems of spectrometers A and B were uninstalled and opened inside the clean room of the A1 detector laboratory. In fact, on the cathode foils, the expected damaged areas were visible, and they were replaced with new foils.
At the same time, all wires were inspected visually and those which were identified as broken or exhibited visual imperfections were replaced. The construction of the VDC enables the coupling of an electric pulse capacitively onto the wires. This makes it possible to check the electrical connection of the wires to the preamplifier boards. Disrupted connections were repaired either by resoldering the wire or by patching broken circuit traces with conductive paint.

Although the wire repair was very successful, the change of the cathode foils had not the hoped-for effect. Data after the repair still exhibit most of the structures seen before. The cause for this is unclear. Although the wires did not exhibit visible defects in these regions, their surface may have been affected somehow. Further studies have to be performed to identify the physical cause. In the present experiment, care was taken that the measurements avoid the lowered-efficiency parts of the planes as much as possible.

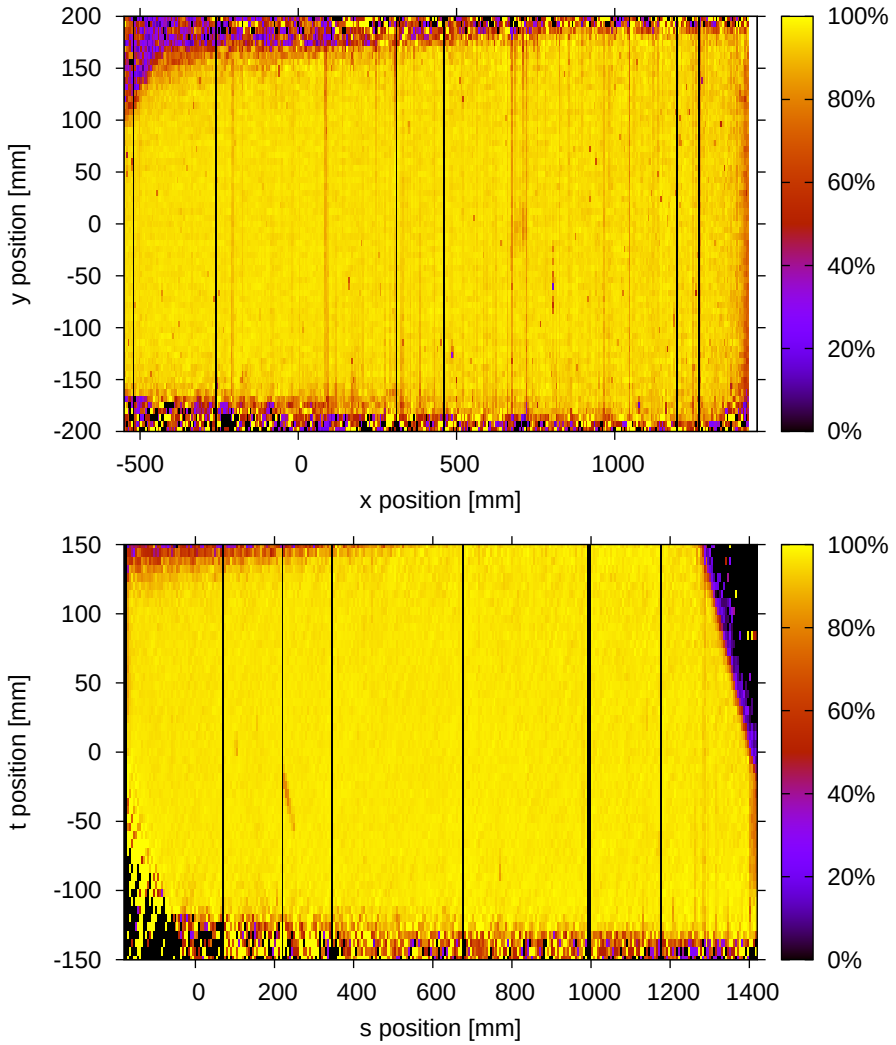

Figure E.1: The VDC efficiency maps before the repair attempt. Displayed are the X1 and S1 planes (see [Dis90]) of spectrometer A, which exhibit the worst structures. The vertical black lines (efficiency 0%) are due to broken wires. These have been repaired. Unfortunately, the areas where the efficiency is slightly reduced persist. The algorithm with which the efficiency is determined over-pronounces efficiency drops, the efficiency per wire is normally above 98%. For further details, see [Ber04].

F Software used in this work, computing time

The main analysis software packages, *Cola++* for the data processing and *Simul++* for the simulation, were developed in the A1-collaboration [DMW01]. Besides this, a lot of open-source tools were used. The most important ones are briefly discussed in the following:

- Normally, the configuration of data analysis and simulation is held in a single text file. Although this is very flexible and easy to use, the large number of different measurements and, accordingly, the large number of simulations, all with different parameters, made it mandatory to use a database system to hold the information. The relational database *PostgreSQL* [Pos] fits perfectly to our situation: The ability to create table views made it possible to hide the data tables behind an abstraction layer. This allowed for the implementation of an automatic control system: The views were extended with triggers which automatically copy the original data to a log table whenever a change is made. Hence the history of changes is preserved and it is possible to revert every parameter of the data analysis and simulation to an earlier stage.

- Most of the control logic, like dependency tracking, job distribution and data extraction, were written in *python* [van Ro95], a powerful scripting language. For fits, the *scipy* package was used [J$^+$]. It contains a wrapper around the *MINPACK* lmdif and lmder algorithms [MGH80]. Like most scripting languages, python is not well suited to perform large numbers of mathematical operations. However, it is possible to extend python with custom modules written in a compiled language like C++. To accelerate the fit procedures, the inner loop and the calculation of the model values were written in C++ and imported into the python code as a module. The powerful *boost* library [boo] was used to quickly generate the wrapping code. The author wants to strongly recommend the combination of python, boost and C++ for any project which needs fast prototyping and fast execution speeds.

- *Blender* [ble], a 3D content creation suite, was a valuable tool for the reconstruction of the vacuum chamber geometry. Some of the schematics were realized with *Inkscape* [ink], a powerful Scalable Vector Graphics (SVG) editor. Most plots were generated with *gnuplot* [WK].

- The layout of this work has been done with LaTeX [Lat] and the TeX distribution TeX live [Tex].

Most of the calculations of the analysis was performed on a blade cluster with 80 cores. Fortunately, the workload is embarrassingly parallel [Fos95], since the analysis of one of the 1422 data points is independent from all others. Therefore, the speedup to a single core was nearly a factor 80. The most time-consuming task is the matching of the simulation to the experiment (see section 6.3) which takes about 2.5 weeks of computing time on the cluster. The data analysis and simulation for all 1422 points takes slightly less than a week.
The time for the Monte Carlo calculations for the confidence bands depends strongly on the model: A typical iteration for the splines is finished in less than 5 seconds, while an iteration for the polynomial models takes up to 2 minutes (for comparison: A single fit of the extended Gari-Krümpelmann model takes at least 20 minutes, which excludes this model from such studies). The calculation of all confidence bands takes about 5 days.
All in all, a complete reanalysis of the data takes about a month of pure computation time.

G Determination of the normalization constants

One of the most difficult tasks in the measurement of a cross section is the absolute normalization. Despite large efforts, it is impossible to determine the absolute normalization to better than a few percent. Fortunately, theory tells us that the form factors G_E and G_M have to go to 1 and μ_p, respectively, for Q^2 going to zero, and it is possible to make use of this limit to determine the normalization from the measured data themselves, in particular if they have been measured down to sufficiently small Q^2. Thus, besides the parameters of the model used to describe the form factors, the fit also has to determine normalization constants for each group of data. Here, one group of data is comprised of the cross sections measured for one energy with one spectrometer for different angles.
The original design of the experiment called for 3 constants per energy: One normalization constant n_E, say for spectrometer A, and two constants to parametrize the efficiency difference between spectrometer A and B, and A and C, n_{AB} and n_{AC}[1]. In principle, each angle setting of the luminosity monitor leads to a different normalization constant. However, the measuring program provided for one of the other spectrometers to stay at a constant angle when the angle of the luminosity monitor is changed. These measurements allow the coupling of the different subgroups. Due to several shortcomings explained below, the number of normalization constants had to be enlarged.

Table G.1 lists the normalization groups for each energy: For each cross section measuring spectrometer, the angle ranges and the number of data points (in parenthesis) is given in the second column. The spectrometer serving as luminosity monitor and its angle is given in the third column. The necessary normalization parameters are listed in the 4th column and the number of parameters in the 5th. The 6th column lists the comments to that row given below.

Comments:

1. For 315 MeV, no normalization to the luminosity spectrometer was possible (see subsection 6.6.2).
2. It was planned to switch from spectrometer C to spectrometer A as luminosity monitor when spectrometer A reached its maximum angle. In order to couple the two luminosity groups, spectrometer B was left at a

[1] Due to different setups of the spectrometers from beam energy to beam energy, these are allowed to change when the beam energy is changed.

Energy [MeV]	Measurements	Luminosity monitor	Normalization parameters	Number of parameters	Comments
180	A: 35.5°(4), 35.5°-85.5°(69), 85.5°-105.5°(29) B: 20°-20.5°(4),20.5°-32°(69),32°-37.5°(33)	C: (60.5°, 73°, 90.5°)	$n_{E,C}$, n_{AB}, n_{AC}	5	2,3,4
	B: 33°-46.5°(41), 46.5°-60°(19) C: 75.5°-118°(38), 118°-135.5°(19)	A: 90.5°	$n_{E,A1}$, $n_{E,A2}$, n_{AB}, n_{AC}		
315	A: 40.5° − 88°(78) B: 19.5° − 43°(104) C: 73° − 133°(62)		n_E, n_{AA}, n_{AB} , n_{AC}	4	1,7
450	A: 33°-43°(22), 43°-90.5°(56),90.5°(2) B: 16°-19.5°(21), 19.5°-32°(56),32.5°-40°(17)	C: (60.5°, 73°), 90.5°	$n_{E,C1}$, $n_{E,C2}$, n_{AA}, n_{AB}, n_{AC}	6	2,3,7
	B: 32°-48.5°(52) C: 73°-133°(50)	A: 90.5°	$n_{E,A}$, n_{AB}, n_{AC},		
585	A: 25.5°-33°(27), 33° − 90.5°(37) B: 16°-21°(41), 21°-32°(56), 35°-40°(47)	C: 60.5°, 73°	$n_{E,C1}$, $n_{E,C2}$, n_{AB}, n_{AC}	5	2,3
	B: 31.5°-47°(21) C: 73°-135.5°(20)	A: 90.5°	$n_{E,A}$, n_{AB}, n_{AC},		
720	A: 38°-108°(46) B: 22°-34°(47)	C: 73°	$n_{E,C}$, n_{AB}, n_{AC}	6	2,6
	B: 30.5°-44.5°(36) C: 73°-128°(37)	A: 73°	$n_{E,A}$, n_{AB}, n_{AC},		
	B: 39.5°-45.5°(27) C: 103°-133°(28)	A: 73°	$n_{AB,2}$, $n_{AC,2}$,		
855	A: 43°-90.5°(45) B: 20.5°-44°(54), 35°-40°(47)	C: 85.5°	$n_{E,C}$,n_{AQ}, n_{AB}, n_{AC}	5	2,5
	B: 44°-54°(35) C: 85.5°-135.5°(31)	A: 85.5°	$n_{E,A}$, n_{AB}, n_{AC}		

Table G.1: Normalization constants (for details see text)

constant angle when the switch from spectrometer C to spectrometer A occurs. Unfortunately, the influence of spectrometer C on B (not known at that time) renders these measurements useless for this purpose, since spectrometer C is moved at these occasions (see appendix D). Therefore, the planned coupling is not possible and a different normalization constant has to be included in the fit for the measurements with A as luminosity monitor.

3. Across an angle-change of spectrometer C as the luminosity monitor, one of the other spectrometers made measurements at constant angle to couple the normalization of these two groups. However, some of these measurements were unusable for this purpose either because they had problems (e.g. low statistics, tripping of the VDC) or they were measured with spectrometer B (see comment 2). Therefore, it was not possible to couple all subgroups. Those where it was possible are marked in the table with parenthesizes.

4. Due to an error of the operators, the setup of spectrometer A was changed while it was the luminosity monitor. Though it was changed back to the nominal configuration, it can not be guaranteed that it measured exactly the same. Therefore, the measurements with spectrometer A as the luminosity monitor have to be divided in two subgroups with two normalization constants, $n_{E,A1}$ and $n_{E,A2}$.

5. The quadrupole anomaly described in section B.2 of the appendix has an influence on the acceptance correction of spectrometer A (see appendix C). The effect can be neglected for 720 MeV, where the acceptance correction is small (short target cell). However, for 855 MeV, measured with the long target cell, the change in the quadrupole behavior divides the measurements of spectrometer A in two groups. The relative normalization of these two groups is parametrized with n_{AQ}. The normalization difference of these two groups is found to be around 1%, about half of the acceptance correction. This is plausible since the acceptance correction stems from (lost) trajectories with extreme angles which are affected most by the focusing of the quadrupole magnet.

6. The main part of the 720 MeV measurements were performed in the second beam time with the short target. However, the last part had to be deferred to the last beam time and these data are measured with the long target. Accordingly, the normalization and the relative efficiencies may have changed. This makes it necessary to introduce two more constants, $n_{AB,2}$ and $n_{AC,2}$. No additional normalization parameter $n_{E,A}$ is needed, it is subsumed in these two constants.

7. A field change of the spectrometers is time consuming since the magnetic field has to be changed slowly, the magnets have to settle. To save beam time, the field was changed only every other angle-change. This leads to an alternating position of the elastic peak on the focal plane. A close inspection of the measured cross sections revealed that for 315 MeV and 450 MeV the cross sections measured with spectrometer A exhibit the

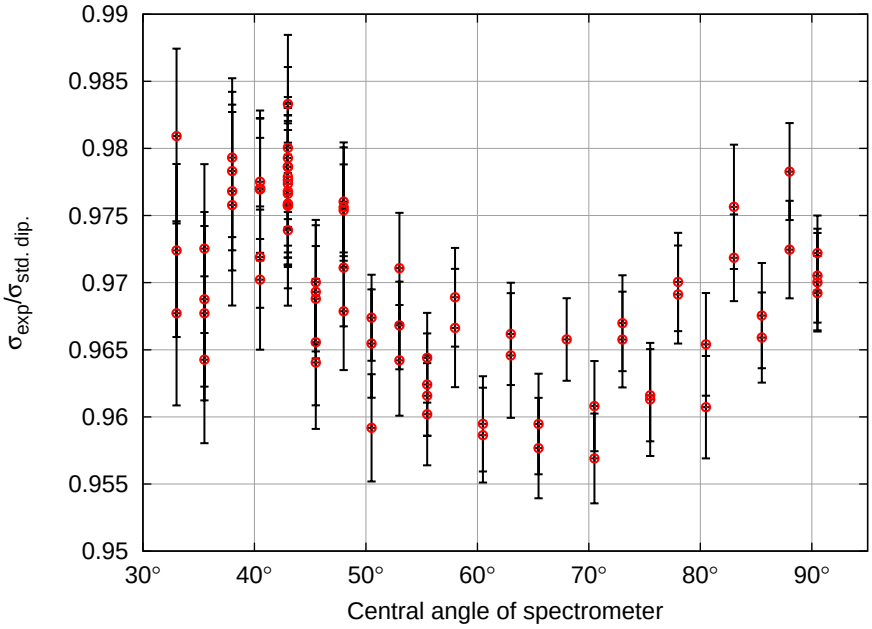

Figure G.1: The cross section measurements, divided by the dipole cross section, for 450 MeV incident beam energy. Here, the normalization parameter governing the efficiency difference between the focal plane positions has been omitted. The alternating pattern can be seen best for the data above 60°, where the points alternate between "low" and "high" from angle to angle.

same pattern (see figure G.1), i.e. the efficiency changes with the peak position on the focal plane. Such a dependency on the position on the focal plane may be caused by a failure in the setup of the photomultiplier voltages or by a worsening of the scintillators or VDC chambers between the beam times (these energies were measured last). The measurements were split according to the position on the focal plane. An additional parameter n_{AA} (different for the two energies) was used to describe the efficiency difference between these two sets. It corrects for a difference of 0.41% for the 315 MeV measurements and of 0.67% for 450 MeV, where the shift on the focal plane is larger. This correction has a negligible effect on the extracted form factors, but improves the total χ^2 by 89.

All in all, 31 normalization constants are included as free parameters into the fit to 1422 data points. Due to the high redundancy of the measurements, these constants are very well determined by the data. Their values are also essentially independent from the model used in the fits. For the fits of the flexible models, the difference between the lowest and the largest value of a normalization constant is at most 0.26%, with an average standard deviation of 0.073%. Including the fit of the Friedrich-Walcher model, the maximum difference is raised to 0.74% (from the normalization of spectrometer C at 855 MeV incident beam energy), with an average standard deviation of 0.074%.

H Model dependency analysis

The extraction of the form factors and the radii with a direct fit of models to the measured cross sections may introduce some model dependency. To test the models, artificial cross section data points are generated at the same kinematics as the measured cross sections from different previously existing form factor parametrizations. To this end, the (pseudo) data points[1] are moved away from the model value by a random number according to the width of the error estimate of the measured data. They are then group-wise rescaled by a randomly chosen normalization, with the grouping equal to that of the measured data. The normalization value was generated according to a Gaussian distribution with the width of 5%, which is significantly larger than the estimated normalization uncertainty of the measurement of 2%.

The selection of input models includes the standard dipole, the phenomenological Friedrich-Walcher parametrization [FW03] and three parametrizations by Arrington: Two from [Arr04] (a fit to unpolarized Rosenbluth data (called Arr. 03 R), and a fit to polarized measurements (called Arr. 03 P)), and the parametrization from [AMT07] to TPE-corrected cross sections (called Arr. 07). These data are then analyzed with the same models used in the analysis of the present data.

For each combination of input parametrization and model used for extraction, about 50 000 tests were performed. The results are analyzed in terms of the achieved reduced χ^2, the form factors and the extracted radii.

H.1 Reduced χ^2

The reduced χ^2 gives information whether the flexibility of the fit model is sufficient with respect to the input parametrization: Since the errors on the pseudo data are by construction true statistical errors on the otherwise correct cross section data, the average χ^2_{red} has to be 1 for a good fit. A χ^2_{red} well above unity indicates that the fit is not flexible enough to reproduce the input parametrization. An example for the χ^2_{red} histogram of two combinations is presented in figure H.1, once for the fit of the spline model to standard-dipole data and once for the fit of the single dipole model to the Friedrich-Walcher parametrization. The former combination leads to a χ^2_{red} of about 1.00, indicating that the fit model can describe the input data. On the other hand, the fit of the single

[1] While these data points calculated from parametrizations are not data in the classical sense, the word data is used in this chapter for the (randomized) values derived from the parametrizations, since they are treated like measured data.

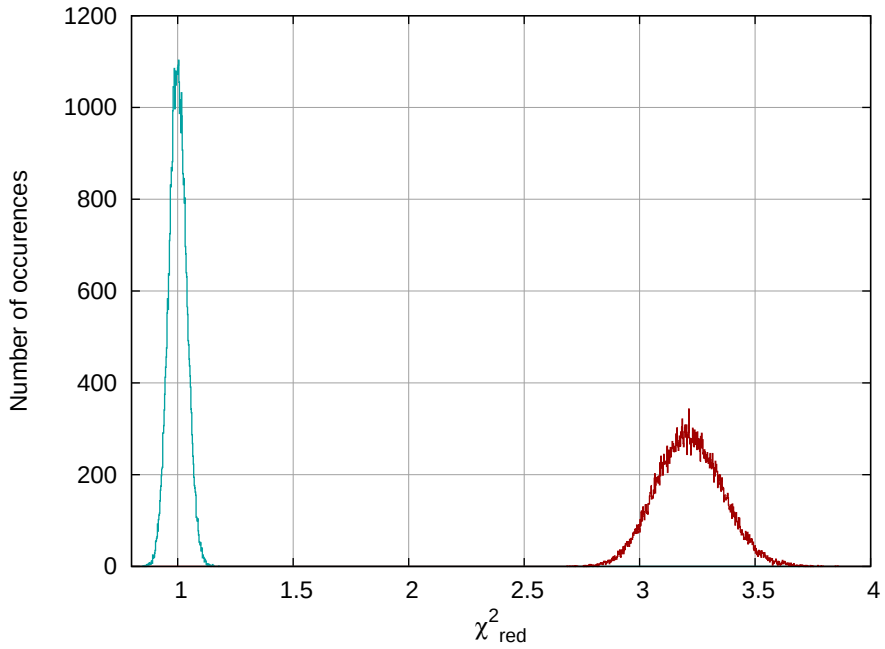

Figure H.1: Distribution of χ^2_{red} for the fit of the spline model to pseudo data derived from the standard dipole (cyan, left) and for the fit of the single-dipole model to Friedrich-Walcher data (red, right). The large χ^2_{red} for the latter combination indicates that the standard dipole can not describe the form factor shape of the Friedrich-Walcher parametrization.

dipole to the Friedrich-Walcher parametrization gives a χ^2_{red} above 3, which is expected, since the single dipole can not reproduce the bump structure nor the different fall-off of the two dipoles of this parametrization.

Table H.1 lists the mean values of the χ^2_{red} distributions for the different combinations and their widths (the expected width is 0.038).
All flexible models produce χ^2_{red} values very near to unity, as does the Friedrich-Walcher model, with slightly larger values. The single dipole cannot reproduce any of the other models. The double dipole shows surprisingly low values for most of the input models, but fails for Arr. 03 P and Friedrich-Walcher. It has to be noted that the (reduced) χ^2 is a random variable. In an experiment only one data set is available, and only one χ^2 can be calculated. A value of 1.033 (Double dipole + Arr. 03 P) for χ^2_{red} would not lead to a rejection of the model: For $N = 1422$, this corresponds to a total χ^2 of 1469, which is less than 1σ off the mean value of the χ^2_{red}-distribution. However, a value of $\chi^2_{\text{red}} = 1.162$ (double-dipole fit to Friedrich-Walcher pseudo data) is off by more than four standard deviations and leads to a rejection of the fit model.

Fit model	Input parametrization									
	Std. dipole		Arr. 03 P		Arr. 03 R		Arr. 07		F.-W.	
Single dipole	1.000	± 0.038	2.193	± 0.094	2.227	± 0.104	2.230	± 0.101	3.216	± 0.142
Double dipole	1.002	± 0.038	1.033	± 0.041	1.001	± 0.041	1.003	± 0.039	1.162	± 0.044
Polynomial	1.000	± 0.038	1.000	± 0.038	1.000	± 0.038	1.000	± 0.038	1.000	± 0.038
Poly. + dipole	1.000	± 0.038	1.000	± 0.038	1.000	± 0.038	1.000	± 0.038	1.000	± 0.038
Poly. × dipole	1.000	± 0.038	1.000	± 0.038	1.000	± 0.038	1.000	± 0.038	1.000	± 0.038
Inv. poly.	1.000	± 0.038	1.000	± 0.038	1.000	± 0.038	1.000	± 0.038	1.000	± 0.038
Spline	1.000	± 0.038	1.000	± 0.038	1.002	± 0.038	1.002	± 0.038	1.000	± 0.038
Spline × dipole	1.000	± 0.038	1.000	± 0.038	1.000	± 0.038	1.000	± 0.038	1.000	± 0.038
Friedrich-Walcher	1.005	± 0.038	1.004	± 0.039	1.004	± 0.038	1.004	± 0.038	1.002	± 0.038

Table H.1: Matrix of the achieved χ^2_{red} (average value ± width of the χ^2_{red} distribution) of the different model combinations. Columns: Input parametrizations. Rows: Models used in the fit.

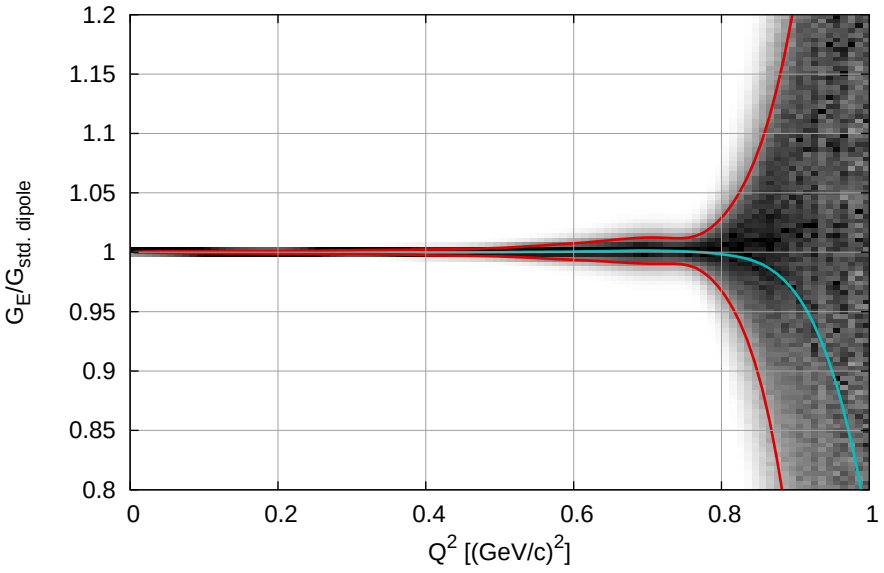

Figure H.2: Two-dimensional histogram for the electric form factor determination with the fits of the spline model to standard-dipole input data. To enhance the visibility, the one-dimensional sub-histogram at each Q^2 is rescaled so that the maximum value is 1. Superimposed are the average value (cyan) and the confidence band (red). Since the form factor results are normalized to the standard dipole, a model without bias should reproduce the horizontal line at 1. This is fulfilled here for most of the range, except for the part above 0.75 $(\mathrm{GeV}/c)^2$, where data from only one incident beam energy contribute and the form factor separation is not possible anymore.

H.2 Form factors

Histogramming the form factor at a number of given Q^2 for all generated solutions gives a distribution at each of these Q^2 values. The width of this distribution is an estimate for the error of the extracted form factor at that Q^2. Further, one can compare the average value of this distribution with the value from the input parametrization. A bias of the model would show up as deviations. Figure H.2 displays a two-dimensional map of the distribution of the electric form factor extracted by a spline-model fit to standard-dipole pseudo data. Superimposed lines represent the 68.3% pointwise confidence band (red) and the average value at a given Q^2 (cyan).

In figures H.3 to H.7, the estimated confidence band (solid lines) and the relative deviation of the fit average from the input parametrization (dashed lines) are displayed for the different input models, each one analyzed with all models used in the analysis of the data in this thesis. One can see that the single dipole and the double dipole can not reproduce the (more flexible) input models.

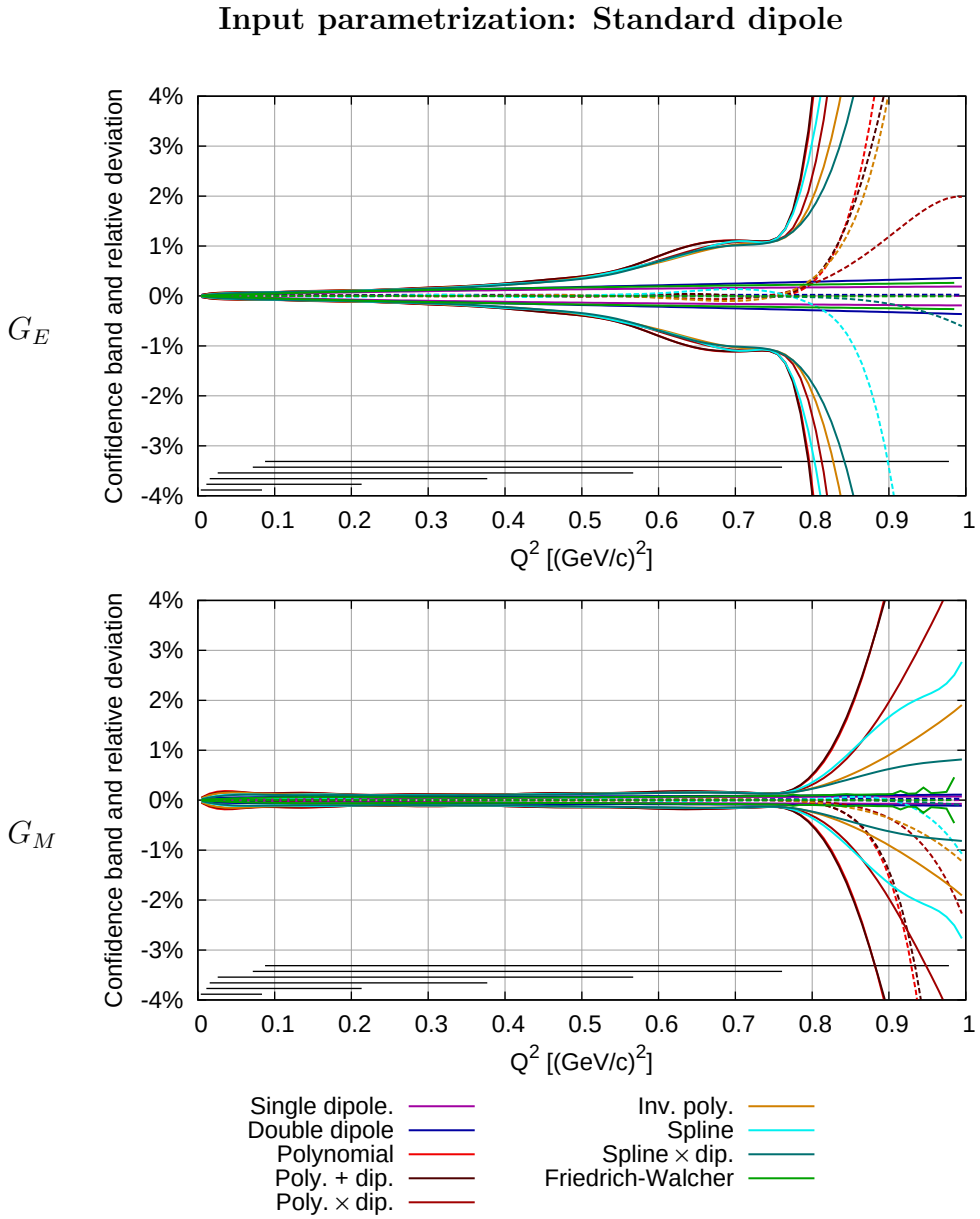

Figure H.3: Confidence band and relative deviation of the fits from the standard-dipole input data. Top: G_E. Bottom: G_M. The solid lines represent the error estimate from the fits as described in the text, the dashed lines the relative deviation of the average of the fits from the input model. For the standard dipole as input, all models can reproduce the input within the confidence band. The flexible models tend to run off to extreme values for higher Q^2.

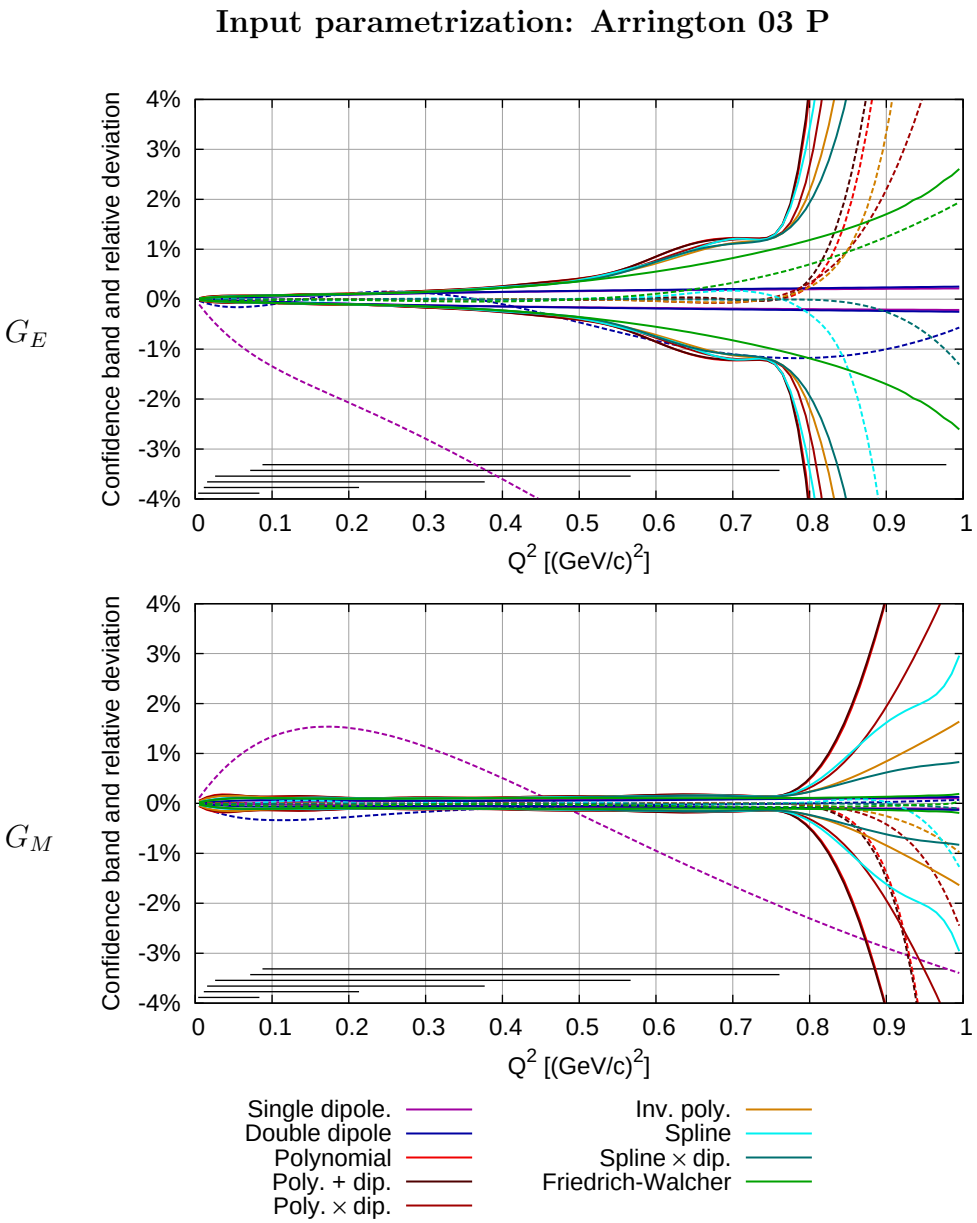

Figure H.4: As fig. H.3, but with Arrington 03 P as the input model. Solid lines: Confidence band. Dashed lines: Average of the fits. For G_E and G_M, the fits with a single and with a double dipole show large deviations, significantly outside of the confidence band.

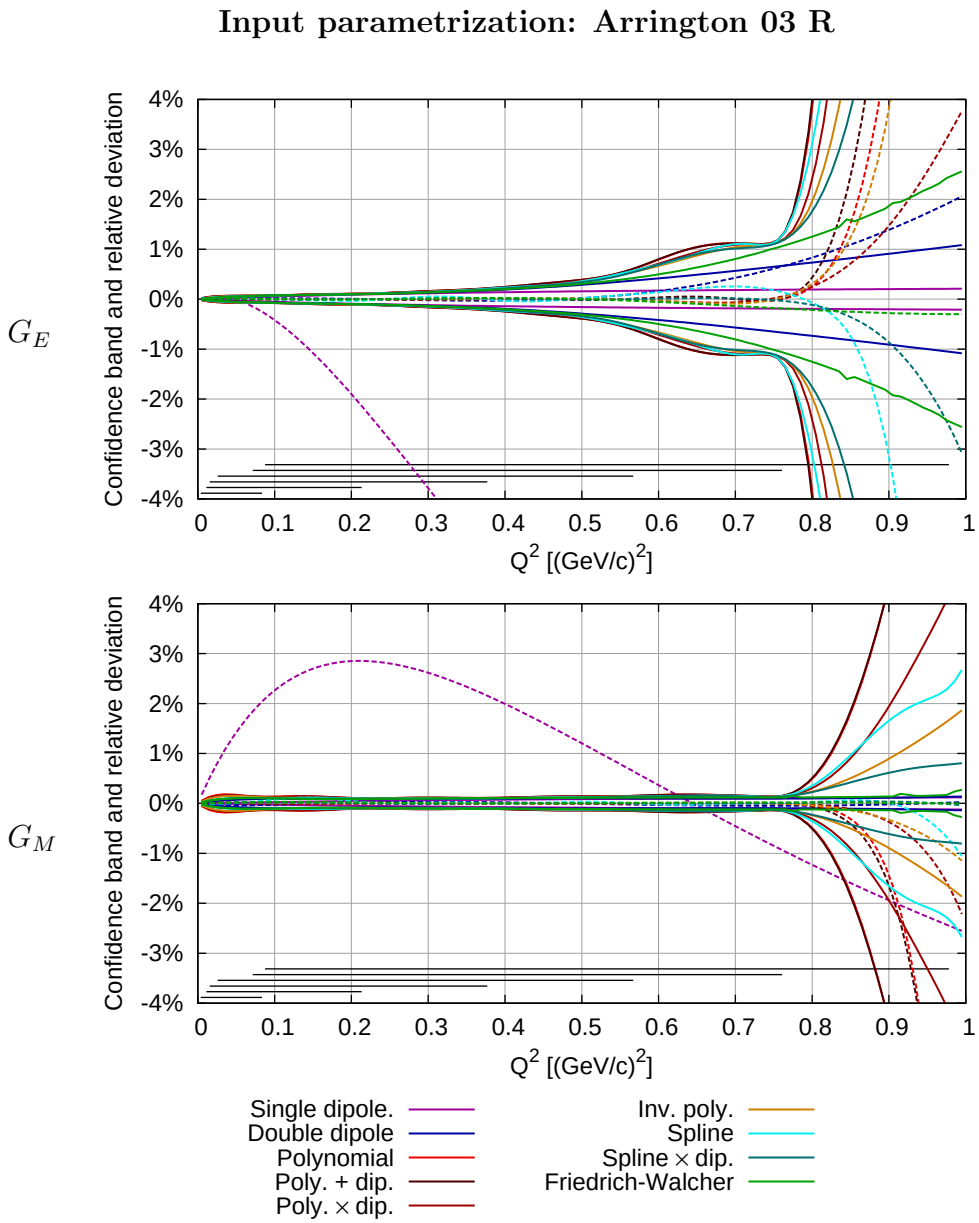

Figure H.5: As fig. H.3, but with Arrington 03 R as the input model. Solid lines: confidence band. Dashed lines: Average of the fits. Again, the fit with a single dipole shows significant deviations, while here the double-dipole model lies well within the confidence band.

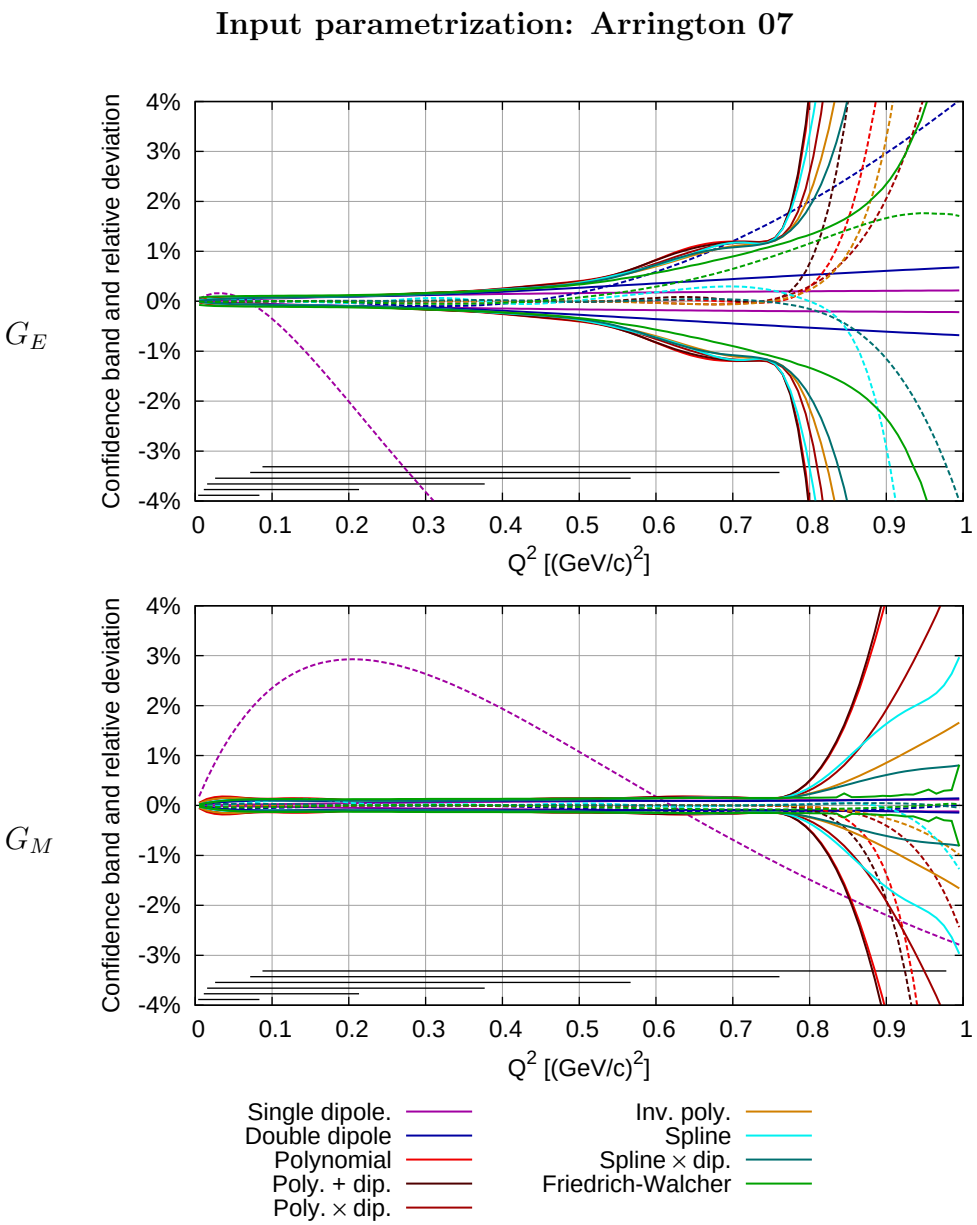

Figure H.6: As fig. H.3, but with Arrington 07 as the input model. The fits of a single dipole and of a double dipole show the same behavior as for the Arrington 03 R input data.

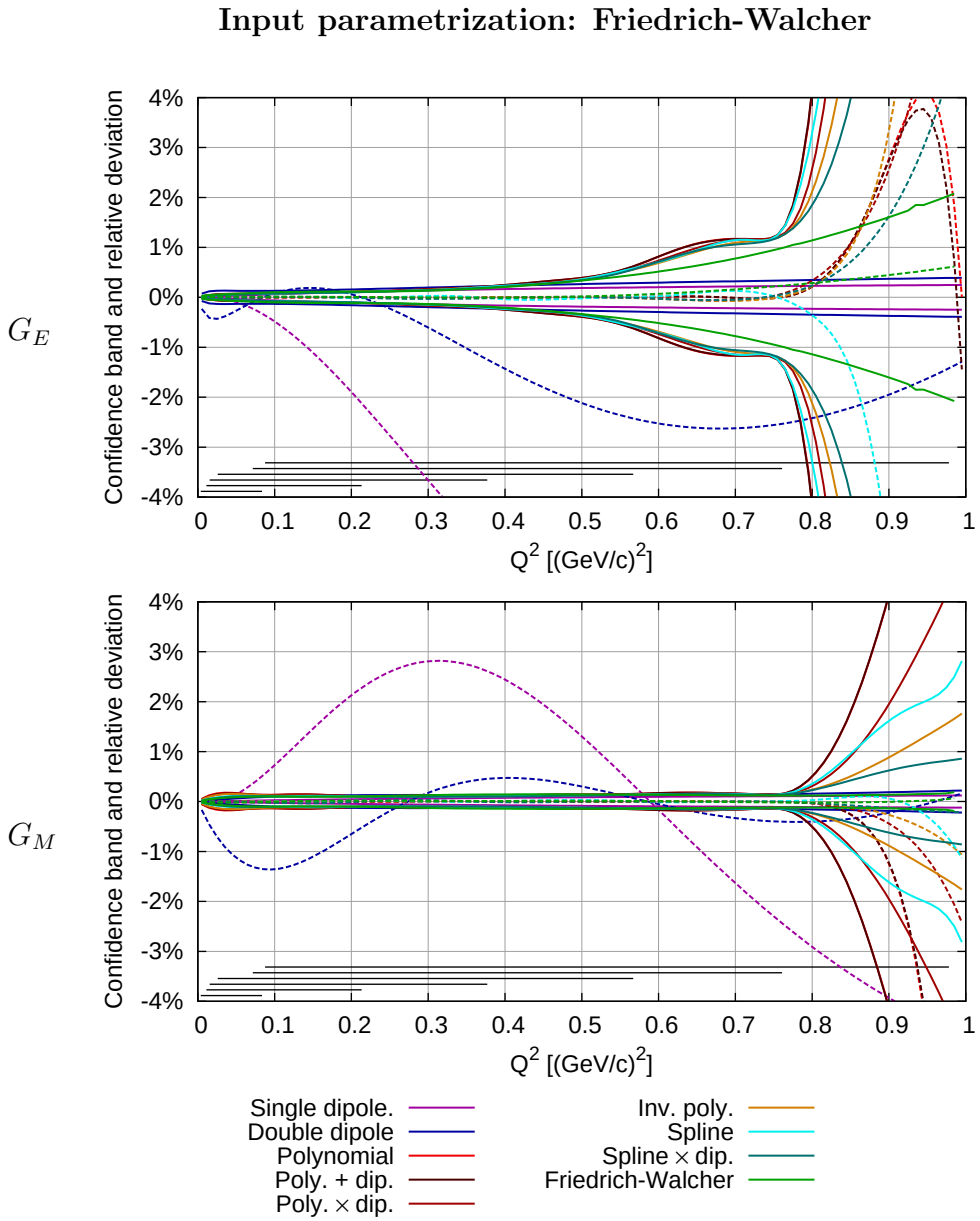

Figure H.7: As fig. H.3, but with Friedrich-Walcher as the input model. Both the fit of a single dipole and of a double dipole show large deviations.

Of more interest is the behavior of the flexible models. It is worthwhile to note that all have very similar confidence bands below 0.75 $(\mathrm{GeV}/c)^2$, independent of input parametrization and of the fit model. In that region, only the spline fit exhibits noticeable deviations from the input, in the order of 0.2% at 0.7 $(\mathrm{GeV}/c)^2$, however, they are always well inside the confidence band.
At higher Q^2, the confidence bands get wider very quickly, as does the deviation of the flexible fits from the input, especially for G_E. This means that they have very limited predictive power in the region where only (pseudo) data from one incident beam energy contribute.

For the tested input models, the Friedrich-Walcher model works fairly well both for the description of the shape in the low-Q^2 region and for the extrapolation into the higher-Q^2 region.

H.3 Radii

The extracted radii have been histogrammed for each combination of input parametrization and fit model (for an example, see fig. H.8). From these distributions, the average electric and magnetic radius and the 1σ-width are calculated. These values can be compared to the radii which are known exactly from the input parametrizations. The results are presented in table H.2. It is obvious that the single-dipole model can not be used for the radius extraction. Also, the double dipole has problems with several of the input parametrizations. The spline models exhibit a small bias to lower radii for some of the input parametrizations.

H.4 Conclusion

All flexible models and the Friedrich-Walcher parametrization are able to reproduce the whole set of studied input models. This is true with respect to the radius extraction, but also for the shape of the form factor itself. We therefore conclude that we have selected reasonably flexible models which should be able to model also the "truth" behind the experimental data.

While the single dipole simply has not enough flexibility, the double dipole does surprisingly well for some of the models, but fails in the description of the radius for others. In these cases, also χ^2_{red} is large. Still, the form factor deviations are always below 3%, what would have been missed in a less accurate measurement.

It is important to notice that the spline fit, while it reproduces the input form factor shape faithfully, exhibits a bias to lower radii for some of the input parametrizations. In these cases, the average χ^2_{red} is only raised by 0.2%, which is undetectable in a real experiment.

$\langle \mathbf{r_e} \rangle$

Fit model	Input parametrization				
	Std. dipole 811	Arr. 03 P 829	Arr. 03 R 868	Arr. 07 878	F.-W. 860
Single Dipole	0±0.7	29±1	−6±1	−15±1	−2±1
Double Dipole	0±1	10±1	0±2	3±3	81±27
Polynomial	0±7	0±7	0±6	0±6	0±6
Poly. + dipole	0±7	−1±7	0±6	−1±6	0±6
Poly. × dipole	0±5	0±5	0±4	0±4	0±5
Inv. poly.	−1±5	−1±5	0±5	−1±5	0±5
Spline	−1±3	−1±3	−3±3	−5±3	0±3
Spline × dipole	0±3	1±3	−1±3	−2±3	1±3
Friedrich-Walcher	0±1	3±2	−1±2	+2±3	−1±3

$\langle \mathbf{r_m} \rangle$

Fit model	Input parametrization				
	Std. dipole 811	Arr. 03 P 837	Arr. 03 R 863	Arr. 07 858	F.-W. 805
Single dipole	0±0.3	−32±0.4	−50±0.4	−53±0.4	5±0.4
Double dipole	0±1	12±2	2±3	3±4	49±2
Polynomial	−1±18	−1±17	−1±17	−2±17	−2±17
Poly. + dipole	0±15	−1±15	−1±14	−1±12	−1±15
Poly. × dipole	−1±14	−1±14	−1±13	−2±14	−2±14
Inv. poly.	0±13	0±13	0±13	0±12	0±13
Spline	1±7	1±7	1±6	−1±7	0±7
Spline × dipole	0±6	0±6	−1±6	−2±6	−1±6
Friedrich-Walcher	0±2	1±5	0±6	2±5	−1±6

Table H.2: The difference of the extracted radii to the input radii and the estimated errors (in atm). The numbers in the table head are the radii of the input model. The numbers in the table body are the differences of the radius between fit and input. Positive values correspond to an extracted radius larger than the input radius. Top: Charge radius. Bottom: Magnetic radius.

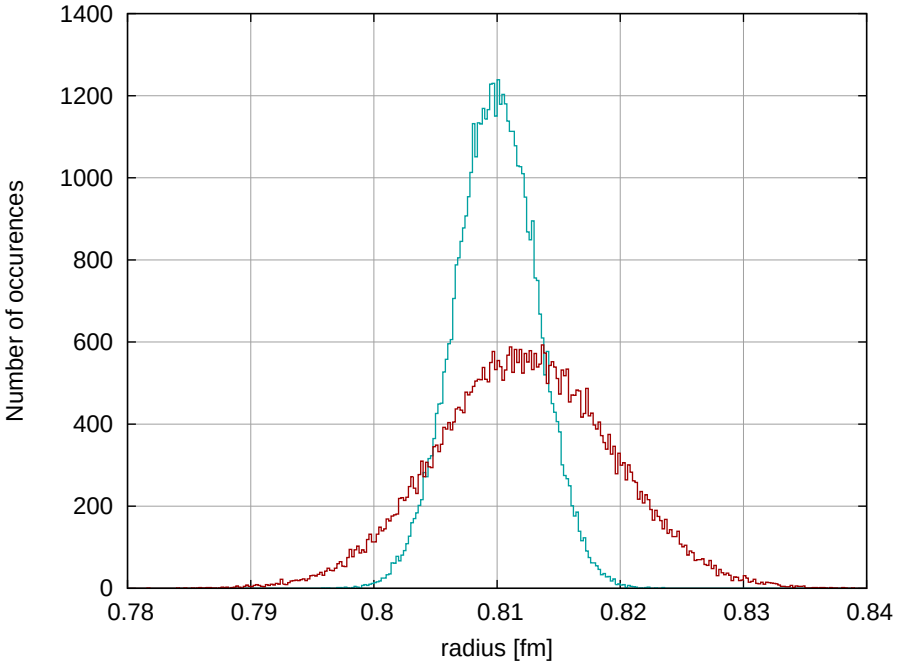

Figure H.8: The distribution of the charge (cyan, narrow) and magnetic (red, broad) radii extracted by a fit with the spline model from pseudo data generated with the standard-dipole parametrization. Since the magnetic form factor has only a small impact to the cross section at low Q^2, the magnetic radius is less well determined.

I Further details on the confidence band calculation

I.1 Linear least squares

While not directly applicable to the case at hand, it is instructive to start the discussion of the confidence band with the linear least squares problem.
A model, where the quantity y_m at x depends linearly on parameters $\vec{p}$, can be written as

$$y_m = f(x, \vec{p}) = p_1 f_1(x) + p_2 f_2(x) \dots \tag{I.1}$$

This model is to be fitted to N data points $\vec{y} = (y_1, y_2, \dots)^T$ at $\vec{x} = (x_1, x_2, \dots)^T$. The measured value y_i is a sum of the (unknown) true value $y_{\text{true},i}$ and a deviation term ϵ_i with expectation value zero and variance σ_i^2:

$$\begin{aligned} y_i &= y_{\text{true},i} + \epsilon_i & \text{(I.2)} \\ E(\epsilon_i) &= 0 & \text{(I.3)} \\ V(\epsilon_i) &= \sigma_i^2. & \text{(I.4)} \end{aligned}$$

An estimate for the truth is the parameter vector $\vec{\hat{p}}$ which minimizes the sum of the normalized deviations squared (sum of residuals squared),

$$\chi^2(\vec{p}) = \sum \frac{(y_i - f(x_i, \vec{p}))^2}{\sigma_i^2}. \tag{I.5}$$

Matrix formalism allows for a compact writing of the equations: Defining the design matrix $\mathbf{A}$, the covariance matrix of the data points $\mathbf{V}(\vec{y})$ and the weight matrix $\mathbf{W}$ as

$$\mathbf{A} = \begin{bmatrix} f_1(x_1) & f_2(x_1) & \dots \\ f_1(x_2) & f_2(x_2) & \dots \\ \dots & & \\ f_1(x_N) & f_2(x_N) & \dots \end{bmatrix}, \quad \mathbf{V}(\vec{y}) = \begin{bmatrix} \sigma_1^2 & 0 & \dots & 0 \\ 0 & \sigma_2^2 & \dots & 0 \\ \dots & & & \\ 0 & 0 & \dots & \sigma_N^2 \end{bmatrix} = \mathbf{W}^{-1}, \tag{I.6}$$

the model can be written as

$$\vec{y_m} = \mathbf{A}\vec{p}, \tag{I.7}$$

and eq. (I.5) gives

$$\chi^2(\vec{p}) = (\vec{y} - \mathbf{A}\vec{p})^T \mathbf{W} (\vec{y} - \mathbf{A}\vec{p}). \tag{I.8}$$

At the minimum, the partial derivatives of χ^2 with respect to every parameter have to vanish:

$$\vec{0} = 2\mathbf{A}^T \mathbf{W} (\vec{y} - \mathbf{A}\vec{\hat{p}}). \tag{I.9}$$

This determines the best fit parameters $\vec{\hat{p}}$:

$$\vec{\hat{p}} = (\mathbf{A}^T\mathbf{W}\mathbf{A})^{-1}\mathbf{A}^T\mathbf{W}\vec{y}. \tag{I.10}$$

By construction, $\vec{\hat{p}}$ gives the minimal sum of residuals squared:

$$\chi^2_{\min} = (\vec{y} - \mathbf{A}\vec{\hat{p}})^T\mathbf{W}(\vec{y} - \mathbf{A}\vec{\hat{p}}) = \vec{y}^T\mathbf{A}\vec{y} - \vec{\hat{p}}^T\mathbf{A}^T\mathbf{W}\vec{y}. \tag{I.11}$$

Here, eq. (I.9) has been used.

Eq. (I.10) is a linear transformation from y-space into parameter space. Therefore, the covariance matrix $\mathbf{V}(\vec{p})$ with $V_{i,j} = \mathrm{cov}(p_i, p_j) = E\left((p_i - \bar{p_i})(p_j - \bar{p_j})\right)$ can be calculated (exactly) with standard error propagation (see chapter 4 in [BL98]) from $\mathbf{V}(y)$, respectively $\mathbf{W}$:

$$\mathbf{V}(\vec{p}) = (\mathbf{A}^T\mathbf{W}\mathbf{A})^{-1}. \tag{I.12}$$

The value of the best fit, $f(x, \vec{\hat{p}})$, at any x is given by $(f_1(x), f_2(x), \dots)\vec{\hat{p}}$. Again, standard error propagation can be used to calculate the variance of $f(x, \vec{\hat{p}})$:

$$\sigma^2_{y_m} = V(f(x, \vec{\hat{p}})) = (f_1(x), f_2(x), \dots)(\mathbf{A}^T\mathbf{W}\mathbf{A})^{-1}(f_1(x), f_2(x), \dots)^T. \tag{I.13}$$

The standard deviation σ_{y_m}, the square root of the variance $V(f(x, \vec{\hat{p}}))$, defines the confidence interval at the chosen point x to the confidence level 68.3%. It should be noted already here that calculating the interval at all x gives the "pointwise confidence band", and that the probability statement is fulfilled at every point x separately, but not at all x simultaneously (see section I.3).

I.2 Covariance ellipsoids

A real symmetric positive definite matrix M allows us to define bilinear forms describing ellipsoids around $\vec{x} = \vec{0}$ [Ort86]:

$$\vec{x}^T\mathbf{M}\vec{x} = c. \tag{I.14}$$

Since the matrix $\mathbf{V}(\vec{p})^{-1}$ fulfills these conditions, one can define ellipsoids in the parameter space centered at the best fit:

$$(\vec{p} - \vec{\hat{p}})^T(\mathbf{V}(\vec{p}))^{-1}(\vec{p} - \vec{\hat{p}}) = c, \tag{I.15}$$

or, with $\Delta\vec{p} = \vec{p} - \vec{\hat{p}}$,

$$\Delta\vec{p}^T(\mathbf{V}(\hat{p}))^{-1}\Delta\vec{p} = c. \tag{I.16}$$

These ellipsoids are called parameter interval covariance ellipsoids.

One can now calculate the increase in χ^2 for a parameter variation $\vec{p} = \vec{\hat{p}} + \Delta\vec{p}$

$$\chi^2_{\min} + \Delta\chi^2 = \left(\vec{y} - \mathbf{A}\left(\vec{\hat{p}} + \Delta\vec{p}\right)\right)^T\mathbf{W}\left(\vec{y} - \mathbf{A}\left(\vec{\hat{p}} + \Delta\vec{p}\right)\right) \tag{I.17}$$

$$= \left(\vec{y} - \mathbf{A}\vec{\hat{p}}\right)^T\mathbf{W}\left(\vec{y} - \mathbf{A}\vec{\hat{p}}\right) + (\mathbf{A}\Delta\vec{p})^T\mathbf{W}(\mathbf{A}\Delta\vec{p}) \tag{I.18}$$

$$\Delta\chi^2 = \Delta\vec{p}^T\mathbf{A}^T\mathbf{W}\mathbf{A}\Delta\vec{p} \tag{I.19}$$

Eq. (I.18) follows from eq. (I.17) using eq. (I.9). From the identity of the right hand side of eq. (I.19) and the left hand side of eq. (I.16), one can see that the ellipsoids defined by (I.16) are contours of constant $\Delta\chi^2 = c$.

I.3 Pointwise confidence band

Section I.1 describes the standard error propagation. The meaning of its results is revealed by comparison with the direct construction of a "pointwise confidence band". Such a band is determined by consideration of a confidence level β, to which an appropriate region in parameter space is constructed with the help of the covariance ellipsoids defined in section I.2.

For a fixed x and given β, one wants to find a value μ, so that

$$P\left[\left|f(x,\vec{\hat{p}}) - y_{\text{true}}(x)\right| \leq \mu\right] = \beta, \tag{I.20}$$

i.e. the probability that the difference of the best fit to the true value is smaller than μ, should be β, the confidence level [Jam06]. Assuming that the model can describe the truth, one can introduce the true parameters $\vec{p}_{\text{true}}$ and eq. I.20 can be written as

$$P\left[\left|f(x,\vec{\hat{p}}) - f(x,\vec{p}_{\text{true}})\right| \leq \mu\right] = \beta. \tag{I.21}$$

In these equations, $\vec{\hat{p}}$ is a random variable. In the case at hand, $\vec{\hat{p}}$ is normal distributed around $\vec{p}_{\text{true}}$ (because the y_i are normal distributed), and the shape of the distribution, described by the covariance matrix, is independent of $\vec{\hat{p}}$. Therefore, the probability statement can be rewritten as a statement about parameter variations $\Delta\vec{p} = \vec{p} - \vec{\hat{p}}$, where we make the usual estimate $\vec{p}_{\text{true}} = \vec{\hat{p}}$ [Jam06]:

$$\begin{aligned} P\left[\left|f(x,\vec{\hat{p}} + \Delta\vec{p}) - f(x,\vec{\hat{p}})\right| \leq \mu\right] &= \beta, \\ P\left[\left|\vec{a}^T(\vec{\hat{p}} + \Delta\vec{p}) - \vec{a}^T\vec{\hat{p}}\right| \leq \mu\right] &= \beta, \\ P\left[\left|\vec{a}^T\Delta\vec{p}\right| \leq \mu\right] &= \beta, \end{aligned} \tag{I.22}$$

with $\vec{a} = (f_1(x), f_2(x), \dots)^T$ and $f(x,\vec{\hat{p}}) = \vec{a}^T\vec{\hat{p}}$. This means that, for given confidence level β, one looks for the region of parameter variations with

$$\left|\vec{a}^T\Delta\vec{p}\right| \leq \mu(\beta). \tag{I.23}$$

Eq. (I.23) defines a band in parameter space perpendicular to $\vec{a}$ (see figure I.1).

The random variable $k = \vec{a}\Delta\vec{p}$ is a linear transformation of the random variable $\Delta\vec{p}$, therefore, its probability density distribution is a Gaussian,

$$P[k = \vec{a}^T\Delta\vec{p}] = \frac{1}{\sqrt{2\pi}\sigma_k} e^{-\frac{1}{2}(\frac{k}{\sigma_k})^2}, \tag{I.24}$$

with σ_k^2 given by standard error propagation (see chapter 4 in [BL98]) as:

$$\sigma_k^2 = \vec{a}^T\mathbf{V}(\vec{p})\vec{a}. \tag{I.25}$$

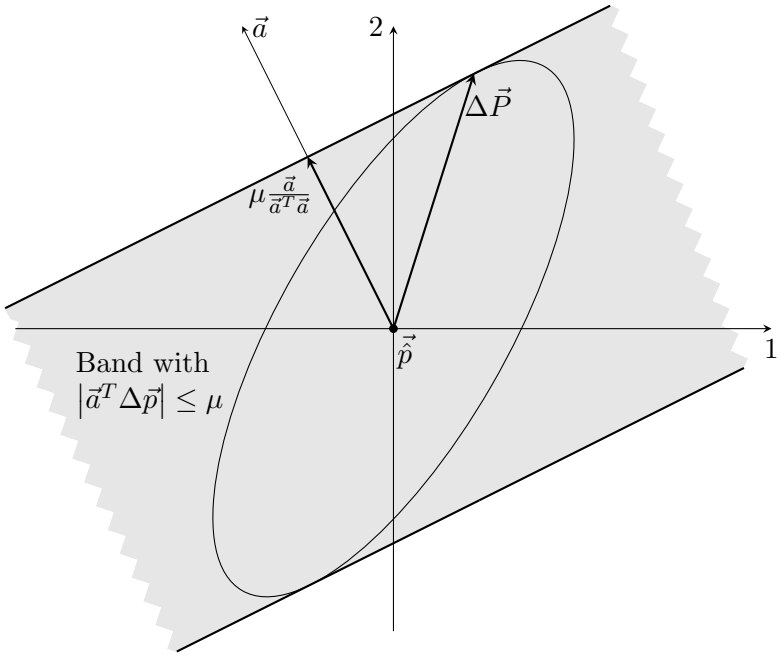

Figure I.1: Parameter band for a pointwise confidence interval at a given x in the case of two parameters. At the given x, $f(x,\vec{p})$ is a linear combination of the parameters, which is given by $\vec{a} = (f_1(x), f_2(x))^T$. The gray shaded band extends to infinity perpendicular to $\vec{a}$ and covers a probability of β. For all parameter combinations in the band, $f(x,\vec{p})$ differs from $f(x,\hat{\vec{p}})$ by at most μ. For all x, the edges of the corresponding bands are tangents of the ellipse defined by eq. (I.16) with $c = (\mu/\sigma_k)^2$.

To find the width of the band for the confidence level β, one has to find $\mu(\beta)$, so that:

$$\beta = \int_{-\mu(\beta)}^{\mu(\beta)} P[k = \vec{a}^T\Delta\vec{p}]\mathrm{d}k. \tag{I.26}$$

For β=68.3%, eq. (I.26) gives $\mu = \sigma_k$ and we find

$$\mu(\beta = 68.3\%) = \sqrt{\vec{a}^T\mathbf{V}(\vec{p})\vec{a}}, \tag{I.27}$$

which is identical to the standard error propagation eq. (9.3) (since $\frac{\partial f}{\partial p_i} = f_i$).

For all x, the parameter-band limits are tangent planes to the ellipsoid defined by eq. (I.16) with $c = (\mu/\sigma_k)^2$. To prove this, one first has to realize that any plane can be regarded as a tangent plane of an ellipsoid for an appropriately chosen c. Therefore, one only has to show that $c = (\mu/\sigma_k)^2$ for any $\vec{a}$.

A normal vector on an implicitly defined surface, $g(\vec{x}) = \text{const.}$, is given by $\vec{\nabla}g$. Therefore, a normal vector of the ellipsoid eq. (I.16) at the point $\Delta\vec{P}$ is

$$\vec{N}(\Delta\vec{P}) = \vec{\nabla}_q\left(\vec{q}^T(\mathbf{V}(\vec{p}))^{-1}\vec{q}\right)\Big|_{\vec{q}=\Delta\vec{P}} = 2(\mathbf{V}(\vec{p}))^{-1}\Delta\vec{P}. \tag{I.28}$$

Hence, the tangent plane at the point $\Delta\vec{P}$ is defined as

$$(\Delta\vec{p} - \Delta\vec{P})^T \vec{N} = 0 \tag{I.29}$$

$$(\Delta\vec{p} - \Delta\vec{P})^T (\mathbf{V}(\vec{p}))^{-1} \Delta\vec{P} = 0 \tag{I.30}$$

$$\Delta\vec{p}^T (\mathbf{V}(\vec{p}))^{-1} \Delta\vec{P} = \Delta\vec{P}^T (\mathbf{V}(\vec{p}))^{-1} \Delta\vec{P} = c. \tag{I.31}$$

On the other hand, one edge plane of the parameter band[1] is defined as

$$\Delta\vec{p}^T \vec{a} = \mu. \tag{I.32}$$

Equations (I.31) and (I.32) are equal for all $\Delta\vec{p}$ exactly when

$$c\vec{a} = \mu(\mathbf{V}(\vec{p}))^{-1} \Delta\vec{P}. \tag{I.33}$$

Multiplication of eq. (I.33) with $\vec{a}^T \mathbf{V}(\vec{p})$ from the left yields

$$\vec{a}^T \mathbf{V}(\vec{p}) c\vec{a} = \vec{a}^T \mathbf{V}(\vec{p}) \mu (\mathbf{V}(\vec{p}))^{-1} \Delta\vec{P}. \tag{I.34}$$

With eq. (I.25) follows

$$c\sigma_k^2 = \mu \vec{a}^T \Delta\vec{P}. \tag{I.35}$$

From figure I.1 and eq. I.32, the projection of $\Delta\vec{P}$ on $\vec{a}$ is μ, therefore $c = (\mu/\sigma_k)^2$, independent of the direction of $\vec{a}$ (or x). It is thus shown that for all x (leading to different directions of $\vec{a}$) the pointwise confidence interval in y-space is related to an infinite band in parameter space with limiting planes tangential to a covariance ellipsoid with constant c, which is given by the confidence level[2]. This fact will be used for the study of the simultaneous confidence band in section I.5.

I.4 Comparison of the confidence bands from linearization and Monte Carlo

The covariance matrix yields the confidence band via standard error propagation. If $f(x, \vec{p})$ depends linearly on $\vec{p}$ or if linearization, i.e. the corresponding truncation of a Taylor expansion, is a good approximation in the relevant region of the parameter space, the results found should be equal to those from the Monte Carlo approach. This has been tested in detail.

In fact, for almost all models both methods give very similar results, with significant differences only in the Q^2 range above 0.75 $(\mathrm{GeV}/c)^2$. The biggest difference is found for the Friedrich-Walcher model, where the linearization yields significantly larger errors already above 0.4 $(\mathrm{GeV}/c)^2$. This behavior can be understood by the fact that this model has a highly non-linear dependence on the parameters. Additionally, for G_E, the parameters of the two dipoles come out almost degenerate. Figure I.2 shows a comparison for $\Delta(G_E/G_{\text{std. dipole}})$ for the polynomial $\times$ dipole and the Friedrich-Walcher model. Here, Δ is half the width of the pointwise 68.3%-confidence-band around the best fit.

[1] The proof is analogous for the other edge plane, $\Delta\vec{p}^T \vec{a} = -\mu$.

[2] All these considerations are valid only if one assumes that the model, especially its smoothness, represents the truth found in nature. Only in this context, statements about the best fit value and confidence intervals at x-points between measurements have a well defined meaning.

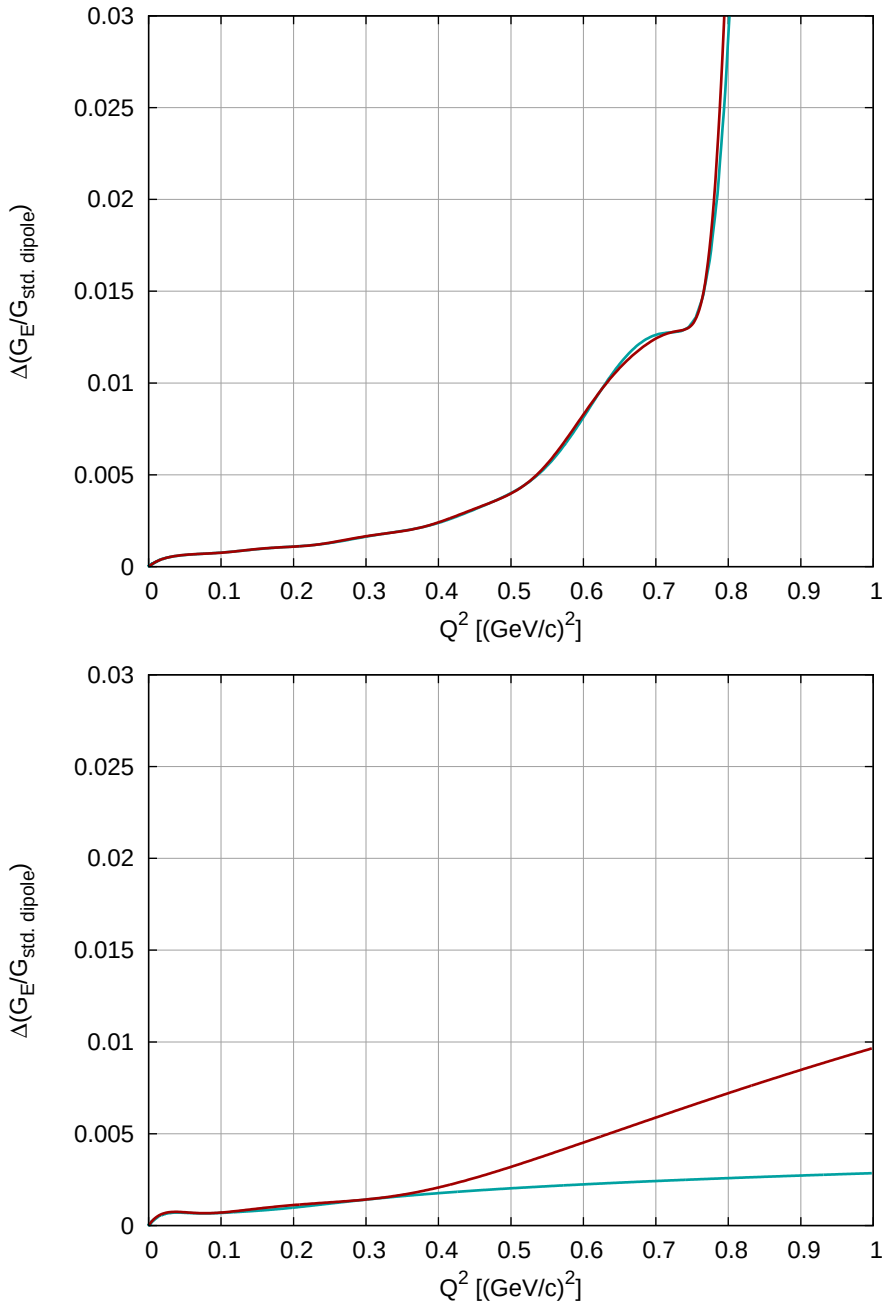

Figure I.2: Half of the width of the pointwise 68.3%-confidence-band around $G_E/G_{\text{std. dipole}}$ for the polynomial × dipole model (top) and for the Friedrich-Walcher model (bottom). Cyan curve: Monte Carlo result. Red curve: Linearization result.

I.5 Simultaneous confidence bands

The confidence bands calculated from the statistical errors of the measurements presented so far are "pointwise confidence bands", i.e. the true value of one form factor is expected to lie in the confidence band with the probability of 68.3% at a given Q^2 whatever the values at other Q^2 and whatever the value of the other form factor. While it is this "pointwise confidence band" which is usually calculated, one should be more interested in the simultaneous confidence band, i.e. in the band which contains the true curve at all points (in a region X) at the selected confidence level. In the case of symmetric bands one wants to find the curve $s(x)$, so that

$$P[f(x,\vec{\hat{p}}) - s(x) \leq y_{\text{true}}(x) \leq f(x,\vec{\hat{p}}) + s(x) \text{ for all } x \in X] = \beta. \tag{I.36}$$

The band defined by $\pm s(x)$ is the simultaneous confidence band. Since requirement eq. (I.36) is stronger, the simultaneous confidence band has to be wider than the pointwise band for the same level of confidence. The simultaneous bands are hard to construct analytically, even for simple linear models.

I.5.1 Analytical approximation

An approximation of the simultaneous confidence band can be constructed from the simultaneous confidence region for the parameters: Suppose that the N-dimensional parameter estimate $\vec{\hat{p}}$ is N-dimensional normal distributed around mean $\vec{p}_{\text{true}}$, the true parameters, with covariance $\mathbf{V}(\vec{p})$, i.e. the probability density function $pdf_{N-\text{norm}}$ is

$$pdf_{N-\text{norm}}(\vec{\hat{p}},\vec{p}_{\text{true}}) = \frac{1}{(2\pi)^{\frac{N}{2}}\,|\mathbf{V}(\vec{p})|^{\frac{1}{2}}} \exp\left[-\frac{1}{2}(\vec{\hat{p}}-\vec{p}_{\text{true}})^T\mathbf{V}^{-1}(\vec{p})(\vec{\hat{p}}-\vec{p}_{\text{true}})\right]. \tag{I.37}$$

From the Normality of $\vec{\hat{p}}$ it follows that the covariance form

$$Q(\vec{\hat{p}},\vec{p}_{\text{true}}) = (\vec{\hat{p}}-\vec{p}_{\text{true}})^T\mathbf{V}^{-1}(\vec{p})(\vec{\hat{p}}-\vec{p}_{\text{true}}) \tag{I.38}$$

has a $\chi^2(N)$ distribution. Since eq. (I.38) is symmetric in $\vec{\hat{p}}$ and $\vec{p}_{\text{true}}$, it is possible to make a statement about the probability that the parameter estimate $\vec{\hat{p}}$ lies inside an ellipsoid (see section I.2) around the true parameters, or, alternatively, that the true parameters are inside an ellipsoid around the best fit estimate. This probability β is given by

$$\beta = P[Q(\vec{\hat{p}},\vec{p}_{\text{true}}) \leq c(\beta)] = \int_0^{c(\beta)} pdf_{\chi^2(N)}(\chi^2)\mathrm{d}\chi^2. \tag{I.39}$$

The point c up to which one has to integrate depends on the confidence level β and on the number of parameters N.

To calculate the confidence band in $y(x)$, one constructs the envelope of all $f(x,\vec{p})$ with $\vec{p}$ inside the ellipsoid. The so constructed band has the same shape

No. of parameters N	1	2	3	33	37	45	47	51
c	1	2.30	3.53	36.30	40.53	48.96	51.06	55.25
$\sqrt{c}$	1	1.52	1.88	6.03	6.37	7.00	7.15	7.43

Table I.1: Values of c and $\sqrt{c}$, the scale factor between a pointwise confidence band with 68.3% confidence level and the simultaneous confidence band with the same confidence level calculated with the approximate analytical method described in subsection I.5.1.

as the pointwise confidence band, but is scaled by a factor[3] $\sqrt{c}$. From the χ^2 p.d.f., one can calculate the scaling factor for different numbers of parameters, the results for a 68.3% confidence level and the parameter numbers of the models used in this thesis are listed in the table I.1. Values for different confidence levels can be found in table of "UP" in the MINUIT reference manual [Jam94].

The construction guarantees that the true curve is inside the confidence band with at least the probability chosen via the covariance ellipsoid in parameter space. However, depending on the model, and the covered x-range X, the confidence band may contain the true curve with a larger probability, since also parameters outside the ellipsoid may lead to curves inside the confidence band. This is illustrated for the two-dimensional case by a toy model [Dis10]: From the "true" basis model $y = 2 - 3x$ a large number of pseudo data sets were generated. Each data set contains 20 data points. One can now test for each of the data sets whether its fit is inside the confidence band calculated by the method above. In fact, for this model 1% of the fits are inside the confidence band in the range of the data points, but outside of the band for infinite x. If one is interested in the simultaneous confidence band restricted to the x-range of the data, the calculated band therefore is a 69%-band instead of the aimed at 68%-band. The parameters of the curves which are inside the confidence band inside the data range, but outside further out, can be recognized from figure I.3.

For larger parameter numbers, the difference between aimed at confidence level and the confidence level of the band constructed in the described way gets bigger. E.g. for an extension of the toy model to 10 parameters, it was found that already above 98% of the curves lie inside the band instead of the aimed at 68.3%. This means that with larger numbers of parameters the factor $\sqrt{c}$ gets larger (see table I.1), but that this factor has to be reduced considerably due to the inappropriateness of this analytical approximation.

To see how this comes about, one has to revisit subsection I.3 which defines the parameter band for a pointwise confidence interval at a point x. The simultaneous band is the intersection of all pointwise parameter bands for $x \in X$, scaled to achieve the desired confidence level. The so constructed parameter space is equal to an ellipsoid if the directions of $\vec{a}(x)$ cover completely half of a

[3] The factor c is applied at the level of the variances. Thus, the confidence band is scaled with $\sqrt{c}$.

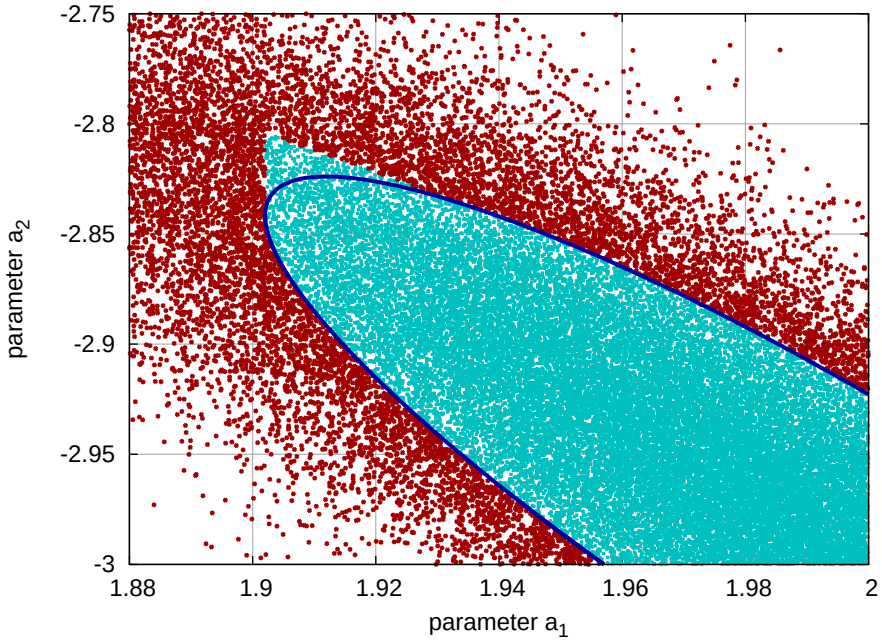

Figure I.3: One quarter of the parameter space of the toy model. The blue curve is the ellipse according to eq. (I.16) with $c = 2.3$, which encloses 68.3% of the best fit parameter combinations from the Monte Carlo data sets. Cyan points represent parameter combinations whose curves are inside of the confidence bands constructed according to subsection I.5.1 inside the data range. Red points represent parameters of curves which are partly outside of the confidence band inside the data range. Cyan points that are outside of the ellipse produce curves which cross the confidence bands outside of the range of the data points. Adapted from [Dis10].

unity sphere of dimension (N-1), i.e. a half-circle in the two-dimensional case. For a model $y = p_1 + p_2 x$, this is the case if $X = [-\infty, \infty]$. However, in the toy model, X is limited to $[0, 1]$ and not all directions are covered (see figure I.4).

For larger parameter numbers, the dimensionality of this half sphere is larger than one (the dimension of x), therefore the directions of $\vec{a}(x)$ describe a curve in the (N-1)-dimensional subspace of the directions in the parameters and can not cover the complete subspace. The resemblance of the intersection volume with the ellipsoid is then lost more and more with higher dimensionality (except for pathological cases, e.g. where the curve is a fractal). This explains the difference of the factors $\sqrt{c}$ in table I.1 and those for β=0.683 in table I.2: While the approximation via the ellipsoid ($\sqrt{c}$) severely over-predicts the scaling factors and produces values around 7 for the number of parameters at hand, the better method using Monte Carlo described in subsection I.5.2 yields factors around 2.3 (table I.2).

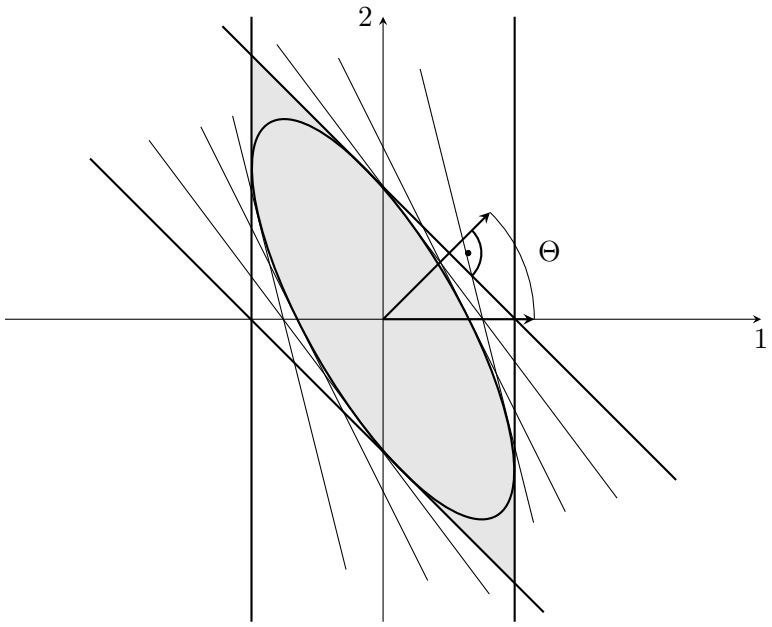

Figure I.4: Geometric construction of the simultaneous confidence band. The intersection (gray shaded area) of all parameter bands for the pointwise confidence band is almost an ellipse. However, since the directions of $\vec{a}$ only cover a range Θ, there are additional "corners".

I.5.2 Simultaneous confidence bands from Monte Carlo

With the assumption that the simultaneous confidence bands have the same shape as the pointwise bands, a Monte Carlo approach can provide a better approximation of the scaling factor and hence of the bands.

- First, the pointwise confidence band has to be constructed in the way described in subsection 9.1.1.
- Now, the width of the band is multiplied by a scaling factor. Every fit curve from the pseudo data ensemble is now tested whether it is inside the confidence band in the selected interval. The ratio R of those completely inside to the total number gives an estimate of the confidence level achieved with the selected scaling factor.
- Since R is a monotone function of the scaling factor, standard search techniques like bisection (see chapter 9 of [PTVF92]) can be used to find the appropriate scaling factor for a given confidence level.

This procedure has been performed for all models used in the analysis with the requirement that the fit curves are completely inside the confidence band for G_E, G_M and G_E/G_M (simultaneously) in the Q^2 region from 0 up to 0.75 $(\mathrm{GeV}/c)^2$. The probability statement (I.36) requires simultaneity for all $x \in X$. This is approximated with densely selected Q^2 points. Table I.2 lists the scaling factors which are to be applied to the pointwise confidence bands (with confidence level

Model	Scaling factor			
	β=68.3%	β=80%	β=90%	β=95%
Spline	2.22	2.46	2.76	3.03
Spline × dipole	2.17	2.41	2.71	3.00
Polynomial	2.34	2.57	2.86	3.12
Polynomial + dipole	2.37	2.61	2.91	3.18
Polynomial × dipole	2.28	2.51	2.81	3.08
Inverse polynomial	2.24	2.47	2.77	3.03
Double dipole	1.73	1.99	2.33	2.64
Friedrich-Walcher	2.03	2.29	2.63	2.94

Table I.2: The scaling factors which have to be applied to the 68.3% pointwise confidence bands presented in this work to construct simultaneous confidence bands within the Q^2 range of the measurement with the given confidence levels.

68.3%) to construct the simultaneous confidence bands of the chosen confidence level. It has to be noted that the small increments in the factors for higher confidence levels indicate a faster drop of the distribution than a Gaussian.

J The model parameters from the fits

The precision of the parameters shown in the tables have been chosen to assure negligible rounding errors in the form factors calculated with these parameters.

J.1 Polynomial models

For the parametrizations, see section 7.3

	Polynomial, $n = 10$		Poly. + dip., $n = 10$	
i	a_i^E	a_i^M	a_i^E	a_i^M
1	-3.3686	-2.5952	-0.5462	+0.2247
2	+14.5606	+1.0222	+8.4132	-4.9624
3	-88.1912	+23.4945	-74.1588	+34.6437
4	+453.6244	-93.0372	+412.3289	-110.4415
5	-1638.7911	+140.7984	-1511.5330	+158.4156
6	+3980.7174	-0.3656	+3680.7305	-0.6291
7	-6312.6333	-305.6759	-5842.6829	-335.5010
8	+6222.3646	+444.6251	+5767.2393	+488.0699
9	-3443.2251	-273.6688	-3197.2449	-301.1986
10	+814.4112	+64.5811	+757.7072	+71.3869

	Poly. $\times$ dip., $n = 8$		Inv. poly., $n = 7$	
i	a_i^E	a_i^M	a_i^E	a_i^M
1	-0.4980	+0.2472	+3.3615	+2.5239
2	+5.4592	-4.9123	-3.0343	+7.6694
3	-34.7281	+29.7509	+29.6677	-30.0897
4	+124.3173	-84.0430	-85.6169	+68.4884
5	-262.9808	+129.3256	+130.7053	-79.0470
6	+329.1395	-111.1068	-101.5145	+43.9206
7	-227.3306	+49.9753	+34.2926	-9.0837
8	+66.6980	-9.1659	–	–

J.2 Spline and spline $\times$ dipole model

The spline model has 8 parameters with knots at $0.2\,(\mathrm{GeV}/c)^2$ intervals from $0\,(\mathrm{GeV}/c)^2$ to $1\,(\mathrm{GeV}/c)^2$.
The spline $\times$ dipole model has 7 parameters with knots at $0.25\,(\mathrm{GeV}/c)^2$ intervals from $0\,(\mathrm{GeV}/c)^2$ to $1\,(\mathrm{GeV}/c)^2$.

Hence, the spline is defined for $0\,(\mathrm{GeV}/c)^2 \leq Q^2 \leq 1\,(\mathrm{GeV}/c)^2$. For the parametrizations, see section 7.4.

	Spline, $n = 8$		Spline × dipole, $n = 7$	
i	a_i^E	a_i^M	a_i^E	a_i^M
-1	-6.31651	-2.08450	-2.04607	+2.38427
0	-2.83182	-2.80421	-0.12746	-0.17812
1	-1.97181	-1.91391	-0.13069	-0.00069
2	-1.48803	-1.43427	-0.07138	+0.04974
3	-1.18342	-1.14666	-0.12528	+0.06191
4	-1.00683	-0.94838	-0.32693	+0.10366
5	-0.85394	-0.80697	-2.55871	+0.01874
6	-1.27114	-0.70011	–	–

J.3 Double-dipole and Friedrich-Walcher model

For the parametrizations, see sections 7.3 and 7.5

	Double dipole		Friedrich-Walcher	
Parameter	G_E	G_M	G_E	G_M
a_0	+0.98462	+0.28231	+13.13613	+0.99377
a_1	+0.68414	+1.34919	+0.67183	+0.71253
a_2	+0.01933	+0.55473	+0.67186	-2.93647
a_b	–	–	-0.18245	-0.05312
Q_b	–	–	+0.00636	-0.39067
σ_b	–	–	+0.15274	+0.11611

J.4 Extended Gari-Krümpelmann model

For the parametrization, see section 7.6.

Parameter	Value
$\frac{g_{\rho'}}{f_{\rho'}}$	-1.54007
$\kappa_{\rho'}$	-280.6672
$\frac{g_\omega}{f_\omega}$	-0.52063
κ_ω	+183.0761
$\frac{g_\phi}{f_\phi}$	-0.02544
κ_ϕ	+396.0842
μ_ϕ	+0.2052
$\frac{g_{\omega'}}{f_{\omega'}}$	+1.54644
$\kappa_{\omega'}$	-209.8490
λ_1	+0.19945
λ_D	+0.67102
λ_2	+38933.
λ_{QCD}	+0.150 (not varied)
N	+1.0 (not varied)

K Numerical results: Cross sections and form factors

The cross section data with the normalizations from all models and form factor values for a larger set of Q^2 values will be available shortly on the web. Nevertheless, the cross section data with the spline normalization and the form factor results including the error margins for a selection of Q^2 values will be given here.

K.1 Cross sections

Table K.1 lists the cross section results after all corrections. The central angle of the spectrometer is given as θ_{central}, $Q^2_{\text{avg.}}$ denotes the average Q^2 of the setting. The normalizations determined by the spline fit are applied to the data. The 6th and 11th column lists the combination of the normalization constants for this measurement (refer to table K.2 for the mapping to those defined in appendix G). With this information, a (re)fit with floating normalization, as was done in this work, can be performed.

E_{in} MeV	Spec. & θ_{central}	Q^2_{avg} $\frac{\text{GeV}^2}{c^2}$	$\frac{\sigma_{\text{exp}}}{\sigma_{\text{dip}}}$	$\Delta\frac{\sigma_{\text{exp}}}{\sigma_{\text{dip}}}$	Norm.	Spec. & θ_{central}	Q^2_{avg} $\frac{\text{GeV}^2}{c^2}$	$\frac{\sigma_{\text{exp}}}{\sigma_{\text{dip}}}$	$\Delta\frac{\sigma_{\text{exp}}}{\sigma_{\text{dip}}}$	Norm.
180	A,35.50	0.011280	0.9893	0.0031	n_3	A,35.50	0.011272	0.9929	0.0030	n_3
180	A,35.50	0.011286	0.9914	0.0031	n_3	A,35.50	0.011268	0.9923	0.0030	n_3
180	A,35.50	0.011286	0.9977	0.0038	n_3	A,35.50	0.011285	0.9904	0.0037	n_3
180	A,35.50	0.011281	0.9879	0.0037	n_3	A,35.50	0.011281	0.9923	0.0038	n_3
180	A,35.50	0.011269	0.9889	0.0038	n_3	A,35.50	0.011272	0.9945	0.0042	n_3
180	A,35.50	0.011283	0.9892	0.0042	n_3	A,38.00	0.012838	0.9992	0.0036	n_3
180	A,38.00	0.012836	0.9896	0.0035	n_3	A,38.00	0.012840	0.9907	0.0034	n_3
180	A,38.00	0.012840	0.9890	0.0034	n_3	A,38.00	0.012838	0.9985	0.0035	n_3
180	A,38.00	0.012838	0.9983	0.0036	n_3	A,40.50	0.014480	0.9915	0.0031	n_3
180	A,40.50	0.014480	0.9916	0.0031	n_3	A,40.50	0.014481	0.9935	0.0031	n_3
180	A,40.50	0.014480	0.9926	0.0031	n_3	A,43.00	0.016192	0.9920	0.0031	n_3
180	A,43.00	0.016192	0.9893	0.0031	n_3	A,43.00	0.016197	0.9852	0.0062	n_3
180	A,43.00	0.016193	0.9925	0.0030	n_3	A,43.00	0.016193	0.9931	0.0035	n_3
180	A,45.51	0.017978	0.9873	0.0056	n_3	A,45.51	0.017979	0.9823	0.0033	n_3
180	A,45.51	0.017975	0.9923	0.0029	n_3	A,48.00	0.019801	0.9894	0.0052	n_3
180	A,48.00	0.019803	0.9856	0.0031	n_3	A,48.00	0.019803	0.9829	0.0054	n_3
180	A,48.00	0.019803	0.9868	0.0036	n_3	A,48.00	0.019803	0.9868	0.0033	n_3
180	A,50.51	0.021699	0.9866	0.0039	n_3	A,50.51	0.021694	0.9839	0.0023	n_3
180	A,50.51	0.021701	0.9964	0.0054	n_3	A,50.51	0.021700	0.9816	0.0030	n_3
180	A,50.51	0.021694	0.9856	0.0032	n_3	A,53.01	0.023627	0.9814	0.0032	n_3
180	A,53.01	0.023633	0.9811	0.0038	n_3	A,53.01	0.023634	0.9862	0.0028	n_3
180	A,53.01	0.023635	0.9865	0.0028	n_3	A,55.50	0.025600	0.9779	0.0048	n_3
180	A,55.50	0.025593	0.9778	0.0029	n_3	A,55.50	0.025599	0.9781	0.0034	n_3
180	A,55.50	0.025601	0.9849	0.0050	n_3	A,55.50	0.025599	0.9811	0.0022	n_3
180	A,58.00	0.027608	0.9818	0.0047	n_3	A,58.00	0.027603	0.9814	0.0024	n_3
180	A,58.00	0.027603	0.9804	0.0025	n_3	A,58.00	0.027609	0.9776	0.0024	n_3
180	A,60.50	0.029635	0.9777	0.0021	n_3	A,63.00	0.031691	0.9805	0.0020	n_3
180	A,65.49	0.033759	0.9802	0.0021	n_3	A,65.49	0.033758	0.9758	0.0021	n_3
180	A,68.01	0.035870	0.9847	0.0021	n_3	A,68.01	0.035869	0.9844	0.0021	n_3
180	A,70.50	0.037961	0.9809	0.0021	n_3	A,70.50	0.037962	0.9783	0.0021	n_3
180	A,72.99	0.040052	0.9785	0.0019	n_3	A,75.50	0.042157	0.9822	0.0021	n_3
180	A,75.50	0.042158	0.9805	0.0021	n_3	A,78.00	0.044252	0.9832	0.0022	n_3
180	A,78.00	0.044255	0.9774	0.0021	n_3	A,80.50	0.046339	0.9768	0.0040	n_3

Table K.1: Cross section data with normalization from spline model

180	A,80.50	0.046338	0.9807	0.0025	n_3	A,80.50	0.046336	0.9801	0.0022	n_3
180	A,83.01	0.048418	0.9774	0.0045	n_3	A,83.01	0.048418	0.9821	0.0023	n_3
180	A,85.51	0.050470	0.9796	0.0046	n_3	A,85.51	0.050468	0.9809	0.0027	n_3
180	A,85.51	0.050467	0.9733	0.0023	n_3	A,85.51	0.050466	0.9736	0.0051	n_3
180	A,85.51	0.050467	0.9748	0.0035	n_3	A,85.51	0.050468	0.9792	0.0027	n_3
180	A,88.00	0.052491	0.9822	0.0051	n_3	A,88.00	0.052492	0.9821	0.0023	n_3
180	A,90.50	0.054499	0.9748	0.0030	n_3	A,90.50	0.054494	0.9804	0.0052	n_3
180	A,90.50	0.054495	0.9764	0.0021	n_3	A,93.01	0.056484	0.9744	0.0050	n_3
180	A,93.01	0.056484	0.9832	0.0031	n_3	A,93.01	0.056484	0.9791	0.0030	n_3
180	A,95.50	0.058421	0.9802	0.0053	n_3	A,95.50	0.058421	0.9799	0.0031	n_3
180	A,95.50	0.058422	0.9825	0.0027	n_3	A,97.99	0.060326	0.9799	0.0051	n_3
180	A,97.99	0.060327	0.9848	0.0030	n_3	A,97.99	0.060327	0.9786	0.0030	n_3
180	A,97.99	0.060327	0.9796	0.0031	n_3	A,97.99	0.060326	0.9819	0.0030	n_3
180	A,100.50	0.062204	0.9889	0.0046	n_3	A,100.50	0.062204	0.9774	0.0029	n_3
180	A,100.50	0.062204	0.9807	0.0025	n_3	A,103.00	0.064042	0.9818	0.0048	n_3
180	A,103.00	0.064043	0.9773	0.0035	n_3	A,103.00	0.064044	0.9807	0.0025	n_3
180	A,105.51	0.065843	0.9791	0.0051	n_3	A,105.51	0.065844	0.9819	0.0030	n_3
180	A,105.51	0.065838	0.9833	0.0026	n_3	A,90.50	0.054498	0.9860	0.0028	n_3
180	B,20.01	0.003843	0.9951	0.0045	n_1n_3	B,20.01	0.003839	0.9984	0.0045	n_1n_3
180	B,20.50	0.004031	0.9942	0.0046	n_1n_3	B,20.50	0.004028	0.9926	0.0045	n_1n_3
180	B,20.50	0.004031	1.0001	0.0047	n_1n_3	B,20.50	0.004031	0.9926	0.0046	n_1n_3
180	B,21.00	0.004227	0.9954	0.0047	n_1n_3	B,21.50	0.004426	0.9993	0.0047	n_1n_3
180	B,21.50	0.004426	0.9952	0.0047	n_1n_3	B,22.00	0.004626	0.9925	0.0052	n_1n_3
180	B,22.00	0.004626	0.9897	0.0052	n_1n_3	B,22.00	0.004626	0.9975	0.0044	n_1n_3
180	B,22.00	0.004625	0.9947	0.0043	n_1n_3	B,22.50	0.004833	0.9940	0.0043	n_1n_3
180	B,22.50	0.004838	0.9891	0.0043	n_1n_3	B,23.00	0.005051	1.0011	0.0044	n_1n_3
180	B,23.00	0.005047	1.0012	0.0044	n_1n_3	B,23.00	0.005046	0.9957	0.0038	n_1n_3
180	B,23.00	0.005046	0.9957	0.0038	n_1n_3	B,23.51	0.005271	1.0002	0.0039	n_1n_3
180	B,23.51	0.005271	0.9985	0.0039	n_1n_3	B,23.51	0.005272	0.9990	0.0039	n_1n_3
180	B,23.51	0.005266	0.9961	0.0039	n_1n_3	B,24.01	0.005487	0.9963	0.0038	n_1n_3
180	B,24.01	0.005487	0.9939	0.0044	n_1n_3	B,24.50	0.005708	0.9908	0.0072	n_1n_3
180	B,24.50	0.005707	0.9934	0.0042	n_1n_3	B,24.50	0.005707	1.0003	0.0037	n_1n_3
180	B,24.50	0.005713	0.9956	0.0066	n_1n_3	B,24.50	0.005707	0.9960	0.0040	n_1n_3
180	B,24.50	0.005708	0.9925	0.0068	n_1n_3	B,25.01	0.005940	0.9960	0.0046	n_1n_3
180	B,25.01	0.005941	0.9965	0.0042	n_1n_3	B,25.01	0.005941	1.0012	0.0049	n_1n_3
180	B,25.01	0.005941	0.9994	0.0030	n_1n_3	B,25.50	0.006168	1.0021	0.0068	n_1n_3
180	B,25.50	0.006174	0.9922	0.0038	n_1n_3	B,25.50	0.006174	0.9939	0.0041	n_1n_3
180	B,25.50	0.006174	0.9919	0.0040	n_1n_3	B,25.50	0.006168	0.9902	0.0048	n_1n_3
180	B,26.01	0.006415	0.9906	0.0036	n_1n_3	B,26.01	0.006415	0.9913	0.0036	n_1n_3
180	B,26.01	0.006415	0.9939	0.0061	n_1n_3	B,26.01	0.006413	0.9967	0.0036	n_1n_3
180	B,26.01	0.006415	0.9921	0.0043	n_1n_3	B,26.51	0.006646	0.9941	0.0063	n_1n_3
180	B,26.51	0.006646	0.9963	0.0029	n_1n_3	B,26.51	0.006646	0.9984	0.0058	n_1n_3
180	B,26.51	0.006646	0.9982	0.0030	n_1n_3	B,26.51	0.006646	0.9968	0.0031	n_1n_3
180	B,26.51	0.006646	0.9926	0.0030	n_1n_3	B,27.00	0.006895	0.9848	0.0057	n_1n_3
180	B,27.00	0.006895	0.9922	0.0027	n_1n_3	B,27.50	0.007144	0.9934	0.0026	n_1n_3
180	B,28.00	0.007390	0.9926	0.0027	n_1n_3	B,28.00	0.007390	0.9970	0.0027	n_1n_3
180	B,28.50	0.007652	0.9941	0.0027	n_1n_3	B,28.50	0.007652	0.9894	0.0027	n_1n_3
180	B,29.00	0.007906	0.9919	0.0026	n_1n_3	B,29.00	0.007911	0.9932	0.0026	n_1n_3
180	B,29.50	0.008175	0.9933	0.0024	n_1n_3	B,29.99	0.008431	0.9906	0.0026	n_1n_3
180	B,29.99	0.008431	0.9913	0.0026	n_1n_3	B,30.50	0.008713	0.9935	0.0026	n_1n_3
180	B,30.50	0.008712	0.9902	0.0026	n_1n_3	B,31.00	0.008981	0.9908	0.0045	n_1n_3
180	B,31.00	0.008981	0.9966	0.0030	n_1n_3	B,31.00	0.008980	0.9907	0.0026	n_1n_3
180	B,31.49	0.009259	0.9851	0.0050	n_1n_3	B,31.49	0.009259	0.9896	0.0027	n_1n_3
180	B,32.00	0.009540	0.9998	0.0051	n_1n_3	B,32.00	0.009539	0.9911	0.0031	n_1n_3
180	B,32.00	0.009539	0.9876	0.0028	n_1n_3	B,32.00	0.009545	0.9927	0.0056	n_1n_3
180	B,32.00	0.009545	0.9897	0.0039	n_1n_3	B,32.00	0.009545	0.9911	0.0030	n_1n_3
180	B,32.51	0.009836	0.9960	0.0055	n_1n_3	B,32.51	0.009836	0.9951	0.0025	n_1n_3
180	B,32.99	0.010113	0.9897	0.0032	n_1n_3	B,32.99	0.010113	0.9881	0.0055	n_1n_3
180	B,32.99	0.010113	0.9926	0.0023	n_1n_3	B,33.50	0.010410	0.9897	0.0053	n_1n_3
180	B,33.50	0.010410	0.9935	0.0032	n_1n_3	B,33.50	0.010410	0.9923	0.0033	n_1n_3
180	B,34.00	0.010705	1.0015	0.0055	n_1n_3	B,34.00	0.010705	0.9927	0.0032	n_1n_3
180	B,34.00	0.010705	0.9915	0.0028	n_1n_3	B,34.50	0.011003	0.9901	0.0052	n_1n_3
180	B,34.50	0.011003	0.9921	0.0030	n_1n_3	B,34.50	0.011003	0.9915	0.0031	n_1n_3
180	B,34.50	0.011003	0.9915	0.0031	n_1n_3	B,34.50	0.011003	0.9908	0.0031	n_1n_3
180	B,35.00	0.011305	0.9901	0.0046	n_1n_3	B,35.00	0.011305	0.9943	0.0029	n_1n_3
180	B,35.00	0.011305	0.9940	0.0025	n_1n_3	B,35.50	0.011609	0.9971	0.0048	n_1n_3
180	B,35.50	0.011609	0.9904	0.0037	n_1n_3	B,35.50	0.011609	0.9910	0.0025	n_1n_3
180	B,36.00	0.011917	0.9897	0.0049	n_1n_3	B,36.00	0.011917	0.9908	0.0029	n_1n_3
180	B,36.00	0.011917	0.9931	0.0025	n_1n_3	B,36.50	0.012228	0.9878	0.0025	n_1n_3
180	B,36.50	0.012228	0.9882	0.0025	n_1n_3	B,37.00	0.012542	0.9929	0.0025	n_1n_3
180	B,37.00	0.012542	0.9921	0.0027	n_1n_3	B,37.50	0.012859	0.9936	0.0031	n_1n_3
180	B,32.99	0.010113	0.9972	0.0033	n_1n_4	B,32.99	0.010113	0.9898	0.0058	n_1n_4
180	B,32.99	0.010113	0.9983	0.0024	n_1n_4	B,37.50	0.012859	0.9897	0.0031	n_1n_4
180	B,37.50	0.012859	0.9996	0.0033	n_1n_4	B,38.01	0.013185	0.9907	0.0036	n_1n_4
180	B,38.01	0.013185	0.9936	0.0036	n_1n_4	B,38.50	0.013502	0.9898	0.0033	n_1n_4
180	B,38.50	0.013503	0.9905	0.0033	n_1n_4	B,39.00	0.013828	0.9918	0.0030	n_1n_4
180	B,39.00	0.013828	0.9882	0.0030	n_1n_4	B,39.49	0.014151	0.9902	0.0029	n_1n_4
180	B,39.49	0.014151	0.9952	0.0029	n_1n_4	B,40.50	0.014823	0.9884	0.0057	n_1n_4
180	B,40.50	0.014823	0.9944	0.0034	n_1n_4	B,40.50	0.014823	0.9936	0.0029	n_1n_4
180	B,41.50	0.015500	0.9912	0.0024	n_1n_4	B,41.50	0.015500	0.9896	0.0024	n_1n_4
180	B,42.50	0.016187	0.9909	0.0025	n_1n_4	B,42.50	0.016188	0.9863	0.0025	n_1n_4
180	B,43.00	0.016535	0.9824	0.0048	n_1n_4	B,43.00	0.016535	0.9822	0.0028	n_1n_4
180	B,43.00	0.016535	0.9859	0.0024	n_1n_4	B,43.50	0.016885	0.9904	0.0048	n_1n_4
180	B,43.50	0.016885	0.9879	0.0028	n_1n_4	B,43.50	0.016886	0.9862	0.0024	n_1n_4
180	B,44.00	0.017238	0.9823	0.0048	n_1n_4	B,44.00	0.017238	0.9897	0.0028	n_1n_4
180	B,44.00	0.017238	0.9896	0.0024	n_1n_4	B,44.51	0.017600	0.9843	0.0049	n_1n_4
180	B,44.51	0.017600	0.9832	0.0028	n_1n_4	B,44.51	0.017600	0.9903	0.0025	n_1n_4
180	B,45.00	0.017950	0.9874	0.0049	n_1n_4	B,45.00	0.017950	0.9888	0.0029	n_1n_4

Table K.1: Cross section data with normalization from spline model

180	B,45.00	0.017950	0.9848	0.0025	n_1n_4	B,45.50	0.018310	0.9905	0.0047	n_1n_4
180	B,45.50	0.018310	0.9809	0.0028	n_1n_4	B,45.50	0.018310	0.9870	0.0024	n_1n_4
180	B,46.01	0.018679	0.9877	0.0047	n_1n_4	B,46.01	0.018679	0.9815	0.0028	n_1n_4
180	B,46.50	0.019036	0.9828	0.0048	n_1n_4	B,46.50	0.019036	0.9940	0.0028	n_1n_5
180	B,46.50	0.019036	0.9909	0.0024	n_1n_5	B,47.00	0.019402	0.9861	0.0048	n_1n_5
180	B,47.00	0.019403	0.9950	0.0029	n_1n_5	B,47.00	0.019403	0.9873	0.0022	n_1n_5
180	B,47.49	0.019764	0.9851	0.0047	n_1n_5	B,47.49	0.019764	0.9890	0.0028	n_1n_5
180	B,47.49	0.019764	0.9844	0.0023	n_1n_5	B,48.00	0.020142	0.9833	0.0025	n_1n_5
180	B,48.00	0.020142	0.9831	0.0034	n_1n_5	B,48.50	0.020514	0.9826	0.0023	n_1n_5
180	B,48.50	0.020514	0.9851	0.0023	n_1n_5	B,49.00	0.020889	0.9790	0.0023	n_1n_5
180	B,49.00	0.020889	0.9847	0.0048	n_1n_5	B,49.00	0.020889	0.9874	0.0026	n_1n_5
180	B,49.50	0.021266	0.9792	0.0023	n_1n_5	B,49.50	0.021266	0.9858	0.0033	n_1n_5
180	B,60.00	0.029547	0.9744	0.0028	n_1n_5	B,60.00	0.029547	0.9754	0.0028	n_1n_5
180	C,90.50	0.054477	0.9822	0.0038	n_2n_4	C,90.50	0.054477	0.9765	0.0066	n_2n_4
180	C,90.50	0.054479	0.9805	0.0027	n_2n_4	C,90.50	0.054479	0.9710	0.0035	n_2n_4
180	C,75.49	0.042134	0.9837	0.0030	n_2n_4	C,75.49	0.042133	0.9853	0.0030	n_2n_4
180	C,77.98	0.044216	0.9807	0.0030	n_2n_4	C,77.98	0.044217	0.9755	0.0030	n_2n_4
180	C,80.49	0.046310	0.9837	0.0036	n_2n_4	C,80.49	0.046311	0.9817	0.0029	n_2n_4
180	C,82.98	0.048370	0.9796	0.0029	n_2n_4	C,82.98	0.048369	0.9796	0.0029	n_2n_4
180	C,88.01	0.052480	0.9807	0.0061	n_2n_4	C,88.01	0.052482	0.9784	0.0035	n_2n_4
180	C,88.01	0.052481	0.9772	0.0031	n_2n_4	C,93.00	0.056455	0.9765	0.0026	n_2n_4
180	C,93.00	0.056455	0.9805	0.0026	n_2n_4	C,98.01	0.060323	0.9781	0.0027	n_2n_4
180	C,98.01	0.060322	0.9804	0.0027	n_2n_4	C,100.50	0.062190	0.9813	0.0053	n_2n_4
180	C,100.50	0.062188	0.9835	0.0027	n_2n_4	C,103.00	0.064024	0.9824	0.0054	n_2n_4
180	C,103.00	0.064026	0.9811	0.0031	n_2n_4	C,103.00	0.064025	0.9733	0.0027	n_2n_4
180	C,105.54	0.065847	0.9771	0.0055	n_2n_4	C,105.54	0.065846	0.9858	0.0032	n_2n_4
180	C,105.54	0.065846	0.9816	0.0032	n_2n_4	C,108.04	0.067596	0.9847	0.0056	n_2n_4
180	C,108.04	0.067595	0.9788	0.0032	n_2n_4	C,108.04	0.067596	0.9802	0.0028	n_2n_4
180	C,110.51	0.069275	0.9823	0.0033	n_2n_4	C,110.51	0.069275	0.9823	0.0029	n_2n_4
180	C,113.06	0.070965	0.9773	0.0058	n_2n_4	C,113.06	0.070963	0.9797	0.0034	n_2n_4
180	C,113.06	0.070962	0.9824	0.0029	n_2n_4	C,115.56	0.072567	0.9846	0.0058	n_2n_4
180	C,115.56	0.072568	0.9817	0.0035	n_2n_4	C,117.94	0.074049	0.9795	0.0060	n_2n_4
180	C,117.94	0.074049	0.9878	0.0036	n_2n_5	C,117.94	0.074049	0.9893	0.0031	n_2n_5
180	C,120.49	0.075577	0.9848	0.0062	n_2n_5	C,123.08	0.077078	0.9885	0.0061	n_2n_5
180	C,123.08	0.077077	0.9880	0.0037	n_2n_5	C,123.08	0.077078	0.9891	0.0029	n_2n_5
180	C,125.59	0.078472	0.9926	0.0033	n_2n_5	C,125.59	0.078472	0.9952	0.0045	n_2n_5
180	C,128.02	0.079770	0.9891	0.0030	n_2n_5	C,128.02	0.079768	0.9922	0.0030	n_2n_5
180	C,130.55	0.081062	0.9916	0.0031	n_2n_5	C,130.55	0.081064	0.9951	0.0065	n_2n_5
180	C,130.55	0.081062	0.9912	0.0035	n_2n_5	C,132.95	0.082233	0.9868	0.0032	n_2n_5
180	C,132.95	0.082231	0.9866	0.0045	n_2n_5	C,135.53	0.083428	0.9915	0.0032	n_2n_5
180	C,135.53	0.083428	0.9855	0.0032	n_2n_5					
315	A,43.00	0.047935	0.9789	0.0027	n_9	A,43.00	0.047930	0.9762	0.0030	n_9
315	A,43.00	0.047932	0.9728	0.0027	n_9	A,43.00	0.047940	0.9746	0.0027	n_9
315	A,43.00	0.047939	0.9757	0.0029	n_9	A,43.00	0.047929	0.9742	0.0027	n_9
315	A,43.00	0.047922	0.9698	0.0027	n_9	A,43.00	0.047933	0.9778	0.0024	n_9
315	A,43.00	0.047938	0.9765	0.0024	n_9	A,43.00	0.047925	0.9780	0.0024	n_9
315	A,43.00	0.047925	0.9758	0.0024	n_9	A,43.00	0.047927	0.9731	0.0024	n_9
315	A,43.00	0.047929	0.9783	0.0024	n_9	A,43.00	0.047915	0.9757	0.0024	n_9
315	A,48.00	0.058153	0.9777	0.0024	n_9	A,48.00	0.058160	0.9754	0.0025	n_9
315	A,48.00	0.058150	0.9739	0.0025	n_9	A,48.00	0.058152	0.9770	0.0025	n_9
315	A,48.00	0.058158	0.9708	0.0025	n_9	A,48.00	0.058154	0.9773	0.0025	n_9
315	A,53.01	0.068797	0.9726	0.0024	n_9	A,53.01	0.068790	0.9731	0.0024	n_9
315	A,53.01	0.068804	0.9707	0.0024	n_9	A,53.01	0.068808	0.9714	0.0024	n_9
315	A,58.00	0.079705	0.9671	0.0030	n_9	A,58.00	0.079719	0.9718	0.0025	n_9
315	A,58.00	0.079729	0.9711	0.0025	n_9	A,63.00	0.090777	0.9681	0.0027	n_9
315	A,63.00	0.090771	0.9725	0.0027	n_9	A,68.01	0.101850	0.9746	0.0030	n_9
315	A,73.01	0.112804	0.9689	0.0033	n_9	A,73.01	0.112786	0.9730	0.0033	n_9
315	A,78.00	0.123531	0.9765	0.0028	n_9	A,78.00	0.123529	0.9752	0.0028	n_9
315	A,83.01	0.134023	0.9709	0.0033	n_9	A,83.01	0.134023	0.9740	0.0034	n_9
315	A,82.99	0.133976	0.9721	0.0033	n_9	A,82.99	0.133994	0.9699	0.0033	n_9
315	A,88.00	0.144119	0.9749	0.0033	n_9	A,88.00	0.144115	0.9752	0.0033	n_9
315	A,40.50	0.042987	0.9720	0.0035	n_7n_9	A,40.50	0.042983	0.9780	0.0035	n_7n_9
315	A,40.50	0.042989	0.9764	0.0037	n_7n_9	A,40.50	0.042984	0.9776	0.0028	n_7n_9
315	A,40.50	0.042983	0.9787	0.0028	n_7n_9	A,40.50	0.042983	0.9778	0.0028	n_7n_9
315	A,40.50	0.042988	0.9777	0.0028	n_7n_9	A,40.50	0.042987	0.9763	0.0025	n_7n_9
315	A,40.50	0.042986	0.9785	0.0025	n_7n_9	A,45.51	0.052994	0.9796	0.0024	n_7n_9
315	A,45.51	0.052988	0.9777	0.0024	n_7n_9	A,45.51	0.052988	0.9786	0.0024	n_7n_9
315	A,45.51	0.052995	0.9778	0.0024	n_7n_9	A,45.51	0.052980	0.9731	0.0024	n_7n_9
315	A,45.51	0.052988	0.9751	0.0024	n_7n_9	A,50.50	0.063415	0.9729	0.0023	n_7n_9
315	A,50.50	0.063413	0.9732	0.0023	n_7n_9	A,50.50	0.063412	0.9752	0.0023	n_7n_9
315	A,50.50	0.063413	0.9760	0.0022	n_7n_9	A,55.50	0.074213	0.9695	0.0021	n_7n_9
315	A,55.50	0.074219	0.9712	0.0021	n_7n_9	A,55.50	0.074214	0.9707	0.0025	n_7n_9
315	A,55.50	0.074221	0.9728	0.0025	n_7n_9	A,60.50	0.085226	0.9681	0.0026	n_7n_9
315	A,60.50	0.085213	0.9732	0.0027	n_7n_9	A,60.50	0.085216	0.9702	0.0026	n_7n_9
315	A,60.50	0.085221	0.9682	0.0027	n_7n_9	A,65.51	0.096314	0.9709	0.0031	n_7n_9
315	A,70.50	0.107282	0.9710	0.0034	n_7n_9	A,70.50	0.107279	0.9704	0.0034	n_7n_9
315	A,75.50	0.118153	0.9709	0.0035	n_7n_9	A,75.50	0.118154	0.9715	0.0035	n_7n_9
315	A,80.51	0.128804	0.9738	0.0033	n_7n_9	A,85.51	0.139118	0.9714	0.0033	n_7n_9
315	A,80.50	0.128788	0.9690	0.0032	n_7n_9	A,80.50	0.128784	0.9741	0.0033	n_7n_9
315	A,85.49	0.139068	0.9742	0.0033	n_7n_9	A,85.49	0.139073	0.9724	0.0033	n_7n_9
315	B,19.50	0.011079	0.9858	0.0047	n_6n_9	B,19.99	0.011631	0.9873	0.0031	n_6n_9
315	B,19.99	0.011630	0.9881	0.0031	n_6n_9	B,20.50	0.012217	0.9905	0.0032	n_6n_9
315	B,20.50	0.012218	0.9900	0.0032	n_6n_9	B,21.00	0.012806	0.9844	0.0033	n_6n_9
315	B,21.00	0.012806	0.9927	0.0033	n_6n_9	B,21.50	0.013406	0.9890	0.0033	n_6n_9
315	B,21.50	0.013406	0.9899	0.0031	n_6n_9	B,21.50	0.013406	0.9923	0.0032	n_6n_9
315	B,22.00	0.014019	0.9850	0.0032	n_6n_9	B,22.00	0.014018	0.9890	0.0032	n_6n_9
315	B,22.50	0.014643	0.9860	0.0033	n_6n_9	B,22.50	0.014643	0.9877	0.0033	n_6n_9
315	B,22.50	0.014642	0.9903	0.0031	n_6n_9	B,22.50	0.014643	0.9902	0.0031	n_6n_9

Table K.1: Cross section data with normalization from spline model

315	B,23.00	0.015280	0.9917	0.0032	n_6n_9	B,23.00	0.015280	0.9911	0.0032	n_6n_9
315	B,23.51	0.015941	0.9897	0.0033	n_6n_9	B,23.51	0.015941	0.9908	0.0033	n_6n_9
315	B,23.51	0.015941	0.9863	0.0030	n_6n_9	B,23.51	0.015941	0.9895	0.0030	n_6n_9
315	B,24.00	0.016587	0.9870	0.0030	n_6n_9	B,24.00	0.016588	0.9899	0.0030	n_6n_9
315	B,24.00	0.016587	0.9897	0.0030	n_6n_9	B,24.00	0.016588	0.9877	0.0030	n_6n_9
315	B,24.50	0.017259	0.9821	0.0031	n_6n_9	B,24.50	0.017259	0.9846	0.0031	n_6n_9
315	B,24.50	0.017259	0.9847	0.0026	n_6n_9	B,24.50	0.017259	0.9838	0.0026	n_6n_9
315	B,25.01	0.017956	0.9834	0.0031	n_6n_9	B,25.01	0.017956	0.9871	0.0031	n_6n_9
315	B,25.01	0.017957	0.9852	0.0035	n_6n_9	B,25.50	0.018635	0.9886	0.0030	n_6n_9
315	B,25.50	0.018636	0.9873	0.0030	n_6n_9	B,25.50	0.018636	0.9868	0.0030	n_6n_9
315	B,25.50	0.018636	0.9837	0.0031	n_6n_9	B,26.00	0.019341	0.9917	0.0031	n_6n_9
315	B,26.00	0.019341	0.9858	0.0031	n_6n_9	B,26.51	0.020071	0.9861	0.0030	n_6n_9
315	B,26.51	0.020071	0.9877	0.0031	n_6n_9	B,27.00	0.020783	0.9882	0.0034	n_6n_9
315	B,27.50	0.021520	0.9872	0.0032	n_6n_9	B,28.00	0.022268	0.9870	0.0033	n_6n_9
315	B,28.00	0.022268	0.9909	0.0033	n_6n_9	B,28.50	0.023026	0.9837	0.0032	n_6n_9
315	B,28.50	0.023026	0.9878	0.0032	n_6n_9	B,29.00	0.023795	0.9922	0.0033	n_6n_9
315	B,29.00	0.023795	0.9894	0.0033	n_6n_9	B,29.50	0.024573	0.9876	0.0031	n_6n_9
315	B,29.50	0.024584	0.9899	0.0031	n_6n_9	B,30.01	0.025378	0.9887	0.0033	n_6n_9
315	B,30.50	0.026159	0.9810	0.0033	n_6n_9	B,30.50	0.026159	0.9811	0.0033	n_6n_9
315	B,31.00	0.027001	0.9758	0.0033	n_6n_9	B,30.01	0.025378	0.9731	0.0029	n_6n_9
315	B,30.01	0.025377	0.9773	0.0030	n_6n_9	B,30.50	0.026161	0.9807	0.0031	n_6n_9
315	B,30.50	0.026171	0.9846	0.0031	n_6n_9	B,31.00	0.026968	0.9831	0.0031	n_6n_9
315	B,31.00	0.026979	0.9822	0.0031	n_6n_9	B,31.51	0.027813	0.9793	0.0032	n_6n_9
315	B,31.51	0.027814	0.9832	0.0032	n_6n_9	B,32.00	0.028612	0.9806	0.0026	n_6n_9
315	B,32.00	0.028645	0.9861	0.0032	n_6n_9	B,32.00	0.028622	0.9819	0.0032	n_6n_9
315	B,32.51	0.029477	0.9810	0.0025	n_6n_9	B,33.01	0.030321	0.9827	0.0024	n_6n_9
315	B,33.50	0.031180	0.9793	0.0026	n_6n_9	B,33.50	0.031180	0.9802	0.0026	n_6n_9
315	B,34.00	0.032018	0.9804	0.0027	n_6n_9	B,34.00	0.032018	0.9826	0.0027	n_6n_9
315	B,35.00	0.033784	0.9761	0.0022	n_6n_9	B,35.00	0.033784	0.9786	0.0022	n_6n_9
315	B,35.51	0.034676	0.9806	0.0021	n_6n_9	B,35.51	0.034676	0.9759	0.0021	n_6n_9
315	B,36.00	0.035550	0.9801	0.0025	n_6n_9	B,36.00	0.035550	0.9796	0.0022	n_6n_9
315	B,36.50	0.036479	0.9739	0.0037	n_6n_9	B,37.00	0.037391	0.9780	0.0035	n_6n_9
315	B,37.00	0.037391	0.9759	0.0035	n_6n_9	B,38.01	0.039253	0.9785	0.0026	n_6n_9
315	B,34.50	0.032913	0.9751	0.0022	n_6n_9	B,38.01	0.039253	0.9798	0.0026	n_6n_9
315	B,38.50	0.040169	0.9838	0.0024	n_6n_9	B,38.50	0.040168	0.9797	0.0024	n_6n_9
315	B,39.00	0.041082	0.9758	0.0022	n_6n_9	B,39.00	0.041109	0.9762	0.0022	n_6n_9
315	B,39.51	0.042074	0.9804	0.0022	n_6n_9	B,39.51	0.042076	0.9787	0.0022	n_6n_9
315	B,40.00	0.043011	0.9811	0.0022	n_6n_9	B,40.00	0.043010	0.9779	0.0022	n_6n_9
315	B,40.50	0.043972	0.9732	0.0021	n_6n_9	B,41.01	0.044957	0.9749	0.0021	n_6n_9
315	B,41.01	0.044957	0.9760	0.0021	n_6n_9	B,41.50	0.045912	0.9749	0.0021	n_6n_9
315	B,41.50	0.045912	0.9767	0.0021	n_6n_9	B,42.00	0.046891	0.9803	0.0021	n_6n_9
315	B,42.00	0.046892	0.9768	0.0021	n_6n_9	B,42.50	0.047878	0.9734	0.0021	n_6n_9
315	B,42.50	0.047877	0.9749	0.0021	n_6n_9	B,43.00	0.048869	0.9752	0.0018	n_6n_9
315	B,43.00	0.048869	0.9790	0.0018	n_6n_9	B,43.00	0.048869	0.9769	0.0018	n_6n_9
315	C,73.01	0.112760	0.9761	0.0032	n_8n_9	C,73.01	0.112766	0.9763	0.0030	n_8n_9
315	C,73.01	0.112756	0.9773	0.0030	n_8n_9	C,90.50	0.149044	0.9727	0.0042	n_8n_9
315	C,73.01	0.112755	0.9762	0.0029	n_8n_9	C,73.01	0.112767	0.9751	0.0028	n_8n_9
315	C,90.50	0.149041	0.9726	0.0040	n_8n_9	C,90.50	0.149034	0.9651	0.0037	n_8n_9
315	C,90.50	0.149035	0.9710	0.0040	n_8n_9	C,90.50	0.149034	0.9702	0.0039	n_8n_9
315	C,90.50	0.149041	0.9711	0.0040	n_8n_9	C,90.50	0.149042	0.9757	0.0040	n_8n_9
315	C,90.50	0.149043	0.9668	0.0032	n_8n_9	C,90.50	0.149049	0.9719	0.0032	n_8n_9
315	C,90.50	0.149051	0.9697	0.0031	n_8n_9	C,90.50	0.149048	0.9710	0.0031	n_8n_9
315	C,90.50	0.149049	0.9712	0.0037	n_8n_9	C,90.50	0.149041	0.9705	0.0031	n_8n_9
315	C,74.54	0.116073	0.9705	0.0021	n_8n_9	C,75.49	0.118103	0.9722	0.0022	n_8n_9
315	C,75.49	0.118106	0.9732	0.0022	n_8n_9	C,80.49	0.128743	0.9720	0.0024	n_8n_9
315	C,90.50	0.149044	0.9669	0.0032	n_8n_9	C,80.49	0.128742	0.9694	0.0024	n_8n_9
315	C,83.02	0.134032	0.9654	0.0025	n_8n_9	C,83.02	0.134039	0.9660	0.0026	n_8n_9
315	C,85.51	0.139110	0.9684	0.0025	n_8n_9	C,85.51	0.139110	0.9676	0.0025	n_8n_9
315	C,88.01	0.144149	0.9689	0.0026	n_8n_9	C,88.01	0.144149	0.9660	0.0026	n_8n_9
315	C,90.50	0.149022	0.9731	0.0027	n_8n_9	C,90.50	0.149021	0.9684	0.0027	n_8n_9
315	C,93.00	0.153847	0.9651	0.0026	n_8n_9	C,95.49	0.158494	0.9693	0.0027	n_8n_9
315	C,98.01	0.163125	0.9670	0.0028	n_8n_9	C,98.01	0.163129	0.9686	0.0027	n_8n_9
315	C,100.50	0.167543	0.9752	0.0028	n_8n_9	C,103.00	0.171884	0.9692	0.0029	n_8n_9
315	C,103.00	0.171883	0.9703	0.0030	n_8n_9	C,105.54	0.176131	0.9727	0.0026	n_8n_9
315	C,105.54	0.176133	0.9754	0.0026	n_8n_9	C,105.54	0.176126	0.9736	0.0026	n_8n_9
315	C,108.04	0.180212	0.9726	0.0032	n_8n_9	C,108.04	0.180214	0.9731	0.0032	n_8n_9
315	C,110.53	0.184096	0.9738	0.0029	n_8n_9	C,110.53	0.184092	0.9706	0.0029	n_8n_9
315	C,113.06	0.187956	0.9711	0.0029	n_8n_9	C,113.06	0.187951	0.9728	0.0030	n_8n_9
315	C,115.56	0.191581	0.9733	0.0031	n_8n_9	C,115.56	0.191578	0.9767	0.0031	n_8n_9
315	C,117.94	0.194941	0.9733	0.0032	n_8n_9	C,117.94	0.194943	0.9733	0.0032	n_8n_9
315	C,120.49	0.198371	0.9764	0.0033	n_8n_9	C,120.49	0.198376	0.9789	0.0033	n_8n_9
315	C,123.08	0.201723	0.9765	0.0034	n_8n_9	C,123.08	0.201725	0.9766	0.0034	n_8n_9
315	C,125.59	0.204811	0.9844	0.0035	n_8n_9	C,125.59	0.204807	0.9803	0.0035	n_8n_9
315	C,130.55	0.210517	0.9805	0.0035	n_8n_9	C,130.55	0.210517	0.9813	0.0035	n_8n_9
315	C,132.95	0.213074	0.9785	0.0034	n_8n_9	C,132.95	0.213074	0.9784	0.0034	n_8n_9
450	A,33.01	0.058555	0.9648	0.0070	n_{13}	A,33.01	0.058565	0.9695	0.0066	n_{13}
450	A,33.01	0.058571	0.9780	0.0066	n_{13}	A,38.00	0.075818	0.9729	0.0076	n_{13}
450	A,38.00	0.075811	0.9764	0.0060	n_{13}	A,38.00	0.075812	0.9739	0.0060	n_{13}
450	A,38.00	0.075795	0.9754	0.0060	n_{13}	A,43.00	0.094317	0.9729	0.0045	n_{13}
450	A,43.00	0.094323	0.9757	0.0046	n_{13}	A,43.00	0.094316	0.9764	0.0046	n_{13}
450	A,43.00	0.094335	0.9730	0.0046	n_{13}	A,43.00	0.094320	0.9758	0.0035	n_{13}
450	A,43.00	0.094320	0.9737	0.0048	n_{13}	A,43.00	0.094335	0.9771	0.0061	n_{13}
450	A,43.00	0.094337	0.9728	0.0063	n_{13}	A,43.00	0.094322	0.9710	0.0057	n_{13}
450	A,43.00	0.094331	0.9739	0.0058	n_{13}	A,43.00	0.094325	0.9804	0.0053	n_{13}
450	A,43.00	0.094328	0.9750	0.0052	n_{13}	A,43.00	0.094336	0.9745	0.0052	n_{13}
450	A,43.00	0.094323	0.9747	0.0059	n_{13}	A,48.00	0.113689	0.9731	0.0045	n_{13}
450	A,48.00	0.113679	0.9727	0.0045	n_{13}	A,48.00	0.113679	0.9682	0.0045	n_{13}
450	A,48.00	0.113688	0.9650	0.0045	n_{13}	A,48.00	0.113689	0.9725	0.0035	n_{13}

Table K.1: Cross section data with normalization from spline model

450	A,53.01	0.133564	0.9613	0.0042	n_{13}	A,53.01	0.133565	0.9682	0.0042	n_{13}
450	A,53.01	0.133566	0.9639	0.0033	n_{13}	A,58.00	0.153650	0.9638	0.0045	n_{13}
450	A,58.00	0.153654	0.9660	0.0038	n_{13}	A,63.00	0.173672	0.9617	0.0047	n_{13}
450	A,63.00	0.173678	0.9633	0.0039	n_{13}	A,68.01	0.193443	0.9629	0.0031	n_{13}
450	A,73.01	0.212685	0.9629	0.0036	n_{13}	A,73.01	0.212686	0.9641	0.0036	n_{13}
450	A,78.00	0.231281	0.9662	0.0037	n_{13}	A,78.00	0.231300	0.9672	0.0037	n_{13}
450	A,83.01	0.249254	0.9690	0.0033	n_{13}	A,83.01	0.249240	0.9728	0.0047	n_{13}
450	A,88.00	0.266281	0.9754	0.0037	n_{13}	A,88.00	0.266272	0.9696	0.0037	n_{13}
450	A,90.50	0.274462	0.9698	0.0029	n_{14}	A,90.50	0.274464	0.9669	0.0028	n_{14}
450	A,35.51	0.067030	0.9724	0.0067	$n_{11}n_{13}$	A,35.51	0.067012	0.9713	0.0067	$n_{11}n_{13}$
450	A,35.51	0.067027	0.9678	0.0064	$n_{11}n_{13}$	A,35.51	0.067023	0.9762	0.0065	$n_{11}n_{13}$
450	A,40.50	0.084873	0.9738	0.0054	$n_{11}n_{13}$	A,40.50	0.084858	0.9812	0.0054	$n_{11}n_{13}$
450	A,40.50	0.084881	0.9806	0.0054	$n_{11}n_{13}$	A,40.50	0.084869	0.9806	0.0054	$n_{11}n_{13}$
450	A,40.50	0.084869	0.9755	0.0039	$n_{11}n_{13}$	A,40.50	0.084878	0.9807	0.0039	$n_{11}n_{13}$
450	A,45.51	0.103943	0.9676	0.0051	$n_{11}n_{13}$	A,45.51	0.103941	0.9729	0.0051	$n_{11}n_{13}$
450	A,45.51	0.103924	0.9724	0.0040	$n_{11}n_{13}$	A,45.51	0.103943	0.9692	0.0048	$n_{11}n_{13}$
450	A,45.51	0.103942	0.9736	0.0048	$n_{11}n_{13}$	A,50.51	0.123557	0.9710	0.0033	$n_{11}n_{13}$
450	A,50.51	0.123560	0.9628	0.0041	$n_{11}n_{13}$	A,50.51	0.123568	0.9691	0.0041	$n_{11}n_{13}$
450	A,55.50	0.143516	0.9680	0.0034	$n_{11}n_{13}$	A,55.50	0.143546	0.9652	0.0031	$n_{11}n_{13}$
450	A,55.50	0.143538	0.9638	0.0039	$n_{11}n_{13}$	A,55.50	0.143522	0.9660	0.0039	$n_{11}n_{13}$
450	A,60.50	0.163616	0.9622	0.0036	$n_{11}n_{13}$	A,60.50	0.163599	0.9630	0.0036	$n_{11}n_{13}$
450	A,65.49	0.183467	0.9630	0.0039	$n_{11}n_{13}$	A,65.49	0.183466	0.9612	0.0038	$n_{11}n_{13}$
450	A,70.50	0.202996	0.9644	0.0034	$n_{11}n_{13}$	A,70.50	0.203027	0.9605	0.0034	$n_{11}n_{13}$
450	A,75.50	0.221986	0.9649	0.0043	$n_{11}n_{13}$	A,75.50	0.221992	0.9652	0.0035	$n_{11}n_{13}$
450	A,80.50	0.240280	0.9643	0.0039	$n_{11}n_{13}$	A,80.50	0.240264	0.9690	0.0039	$n_{11}n_{13}$
450	A,85.51	0.257797	0.9695	0.0035	$n_{11}n_{13}$	A,85.51	0.257815	0.9712	0.0040	$n_{11}n_{13}$
450	A,90.50	0.274397	0.9736	0.0038	$n_{11}n_{13}$	A,90.50	0.274406	0.9741	0.0036	$n_{11}n_{13}$
450	B,16.00	0.015218	0.9791	0.0065	$n_{10}n_{13}$	B,16.00	0.015218	0.9865	0.0066	$n_{10}n_{13}$
450	B,16.00	0.015218	0.9770	0.0065	$n_{10}n_{13}$	B,16.00	0.015217	0.9770	0.0065	$n_{10}n_{13}$
450	B,16.50	0.016173	0.9732	0.0063	$n_{10}n_{13}$	B,16.50	0.016171	0.9791	0.0064	$n_{10}n_{13}$
450	B,16.50	0.016171	0.9801	0.0075	$n_{10}n_{13}$	B,16.50	0.016172	0.9810	0.0060	$n_{10}n_{13}$
450	B,17.01	0.017172	0.9765	0.0060	$n_{10}n_{13}$	B,17.01	0.017171	0.9818	0.0060	$n_{10}n_{13}$
450	B,17.01	0.017172	0.9820	0.0054	$n_{10}n_{13}$	B,17.01	0.017171	0.9848	0.0054	$n_{10}n_{13}$
450	B,17.50	0.018157	0.9848	0.0055	$n_{10}n_{13}$	B,17.50	0.018157	0.9879	0.0055	$n_{10}n_{13}$
450	B,18.00	0.019185	0.9779	0.0042	$n_{10}n_{13}$	B,18.49	0.020220	0.9786	0.0042	$n_{10}n_{13}$
450	B,18.49	0.020221	0.9785	0.0048	$n_{10}n_{13}$	B,18.49	0.020219	0.9809	0.0048	$n_{10}n_{13}$
450	B,19.00	0.021322	0.9788	0.0049	$n_{10}n_{13}$	B,19.00	0.021322	0.9813	0.0049	$n_{10}n_{13}$
450	B,19.50	0.022428	0.9804	0.0041	$n_{10}n_{13}$	B,19.50	0.022429	0.9802	0.0046	$n_{10}n_{13}$
450	B,20.01	0.023583	0.9838	0.0059	$n_{10}n_{13}$	B,20.01	0.023583	0.9789	0.0060	$n_{10}n_{13}$
450	B,20.50	0.024714	0.9768	0.0055	$n_{10}n_{13}$	B,20.50	0.024713	0.9830	0.0056	$n_{10}n_{13}$
450	B,21.00	0.025890	0.9845	0.0051	$n_{10}n_{13}$	B,21.00	0.025890	0.9808	0.0050	$n_{10}n_{13}$
450	B,21.50	0.027093	0.9757	0.0050	$n_{10}n_{13}$	B,21.50	0.027092	0.9781	0.0057	$n_{10}n_{13}$
450	B,21.50	0.027094	0.9764	0.0049	$n_{10}n_{13}$	B,21.50	0.027093	0.9768	0.0049	$n_{10}n_{13}$
450	B,22.00	0.028317	0.9780	0.0039	$n_{10}n_{13}$	B,22.50	0.029566	0.9787	0.0047	$n_{10}n_{13}$
450	B,22.50	0.029568	0.9836	0.0046	$n_{10}n_{13}$	B,22.50	0.029565	0.9819	0.0043	$n_{10}n_{13}$
450	B,22.50	0.029566	0.9824	0.0044	$n_{10}n_{13}$	B,23.00	0.030836	0.9786	0.0043	$n_{10}n_{13}$
450	B,23.00	0.030836	0.9738	0.0043	$n_{10}n_{13}$	B,23.51	0.032158	0.9828	0.0034	$n_{10}n_{13}$
450	B,23.51	0.032158	0.9803	0.0032	$n_{10}n_{13}$	B,24.00	0.033445	0.9781	0.0040	$n_{10}n_{13}$
450	B,24.00	0.033446	0.9765	0.0040	$n_{10}n_{13}$	B,24.00	0.033445	0.9779	0.0040	$n_{10}n_{13}$
450	B,24.00	0.033444	0.9812	0.0040	$n_{10}n_{13}$	B,24.50	0.034781	0.9812	0.0032	$n_{10}n_{13}$
450	B,24.50	0.034783	0.9816	0.0032	$n_{10}n_{13}$	B,24.50	0.034782	0.9776	0.0029	$n_{10}n_{13}$
450	B,25.01	0.036170	0.9786	0.0037	$n_{10}n_{13}$	B,25.01	0.036170	0.9798	0.0037	$n_{10}n_{13}$
450	B,25.50	0.037518	0.9800	0.0042	$n_{10}n_{13}$	B,25.50	0.037522	0.9814	0.0035	$n_{10}n_{13}$
450	B,26.00	0.038920	0.9795	0.0034	$n_{10}n_{13}$	B,26.00	0.038919	0.9763	0.0034	$n_{10}n_{13}$
450	B,26.49	0.040309	0.9806	0.0043	$n_{10}n_{13}$	B,26.49	0.040308	0.9811	0.0035	$n_{10}n_{13}$
450	B,27.00	0.041777	0.9815	0.0034	$n_{10}n_{13}$	B,27.00	0.041777	0.9768	0.0034	$n_{10}n_{13}$
450	B,27.50	0.043239	0.9784	0.0028	$n_{10}n_{13}$	B,28.00	0.044714	0.9795	0.0030	$n_{10}n_{13}$
450	B,28.00	0.044717	0.9755	0.0030	$n_{10}n_{13}$	B,28.50	0.046213	0.9776	0.0031	$n_{10}n_{13}$
450	B,28.50	0.046214	0.9780	0.0031	$n_{10}n_{13}$	B,29.00	0.047729	0.9773	0.0036	$n_{10}n_{13}$
450	B,29.00	0.047730	0.9781	0.0030	$n_{10}n_{13}$	B,29.50	0.049261	0.9791	0.0030	$n_{10}n_{13}$
450	B,29.50	0.049265	0.9806	0.0030	$n_{10}n_{13}$	B,29.99	0.050785	0.9756	0.0031	$n_{10}n_{13}$
450	B,29.99	0.050784	0.9748	0.0031	$n_{10}n_{13}$	B,30.50	0.052405	0.9768	0.0028	$n_{10}n_{13}$
450	B,30.50	0.052405	0.9792	0.0038	$n_{10}n_{13}$	B,31.00	0.053971	0.9741	0.0028	$n_{10}n_{13}$
450	B,31.00	0.053972	0.9769	0.0034	$n_{10}n_{13}$	B,31.51	0.055632	0.9730	0.0029	$n_{10}n_{13}$
450	B,32.00	0.057214	0.9744	0.0030	$n_{10}n_{13}$	B,31.51	0.055633	0.9754	0.0030	$n_{10}n_{13}$
450	B,32.00	0.057196	0.9766	0.0029	$n_{10}n_{13}$	B,32.50	0.058878	0.9751	0.0033	$n_{10}n_{14}$
450	B,32.50	0.058852	0.9748	0.0032	$n_{10}n_{14}$	B,33.01	0.060538	0.9741	0.0032	$n_{10}n_{14}$
450	B,33.01	0.060538	0.9711	0.0032	$n_{10}n_{14}$	B,33.50	0.062169	0.9752	0.0033	$n_{10}n_{14}$
450	B,33.50	0.062168	0.9756	0.0033	$n_{10}n_{14}$	B,34.00	0.063852	0.9708	0.0030	$n_{10}n_{14}$
450	B,34.00	0.063853	0.9711	0.0030	$n_{10}n_{14}$	B,34.50	0.065549	0.9725	0.0029	$n_{10}n_{14}$
450	B,34.50	0.065547	0.9729	0.0029	$n_{10}n_{14}$	B,35.00	0.067257	0.9742	0.0027	$n_{10}n_{14}$
450	B,35.50	0.068982	0.9753	0.0029	$n_{10}n_{14}$	B,35.50	0.069029	0.9757	0.0029	$n_{10}n_{14}$
450	B,36.00	0.070747	0.9728	0.0029	$n_{10}n_{14}$	B,36.00	0.070721	0.9763	0.0029	$n_{10}n_{14}$
450	B,40.00	0.085110	0.9693	0.0025	$n_{10}n_{14}$	B,40.00	0.085111	0.9686	0.0025	$n_{10}n_{14}$
450	B,32.00	0.057214	0.9769	0.0037	$n_{10}n_{15}$	B,32.00	0.057196	0.9786	0.0035	$n_{10}n_{15}$
450	B,32.00	0.057194	0.9806	0.0027	$n_{10}n_{15}$	B,36.50	0.072519	0.9645	0.0034	$n_{10}n_{15}$
450	B,36.50	0.072519	0.9668	0.0034	$n_{10}n_{15}$	B,37.00	0.074283	0.9662	0.0033	$n_{10}n_{15}$
450	B,37.00	0.074283	0.9650	0.0033	$n_{10}n_{15}$	B,37.50	0.076059	0.9713	0.0029	$n_{10}n_{15}$
450	B,37.50	0.076061	0.9713	0.0029	$n_{10}n_{15}$	B,37.99	0.077811	0.9678	0.0027	$n_{10}n_{15}$
450	B,37.99	0.077810	0.9710	0.0028	$n_{10}n_{15}$	B,38.50	0.079645	0.9691	0.0020	$n_{10}n_{15}$
450	B,39.00	0.081459	0.9690	0.0020	$n_{10}n_{15}$	B,39.49	0.083246	0.9720	0.0025	$n_{10}n_{15}$
450	B,39.49	0.083246	0.9653	0.0068	$n_{10}n_{15}$	B,39.49	0.083244	0.9682	0.0025	$n_{10}n_{15}$
450	B,40.00	0.085110	0.9691	0.0025	$n_{10}n_{15}$	B,40.00	0.085111	0.9714	0.0025	$n_{10}n_{15}$
450	B,40.50	0.086952	0.9725	0.0025	$n_{10}n_{15}$	B,40.50	0.086952	0.9721	0.0025	$n_{10}n_{15}$
450	B,41.01	0.088843	0.9706	0.0025	$n_{10}n_{15}$	B,41.01	0.088843	0.9701	0.0025	$n_{10}n_{15}$
450	B,41.49	0.090632	0.9710	0.0025	$n_{10}n_{15}$	B,41.49	0.090633	0.9683	0.0025	$n_{10}n_{15}$
450	B,42.00	0.092539	0.9718	0.0025	$n_{10}n_{15}$	B,42.00	0.092540	0.9707	0.0026	$n_{10}n_{15}$
450	B,42.50	0.094419	0.9710	0.0024	$n_{10}n_{15}$	B,42.50	0.094418	0.9721	0.0023	$n_{10}n_{15}$

Table K.1: Cross section data with normalization from spline model

450	B,43.00	0.096307	0.9712	0.0026	$n_{10}n_{15}$	B,43.00	0.096307	0.9693	0.0026	$n_{10}n_{15}$
450	B,43.50	0.098203	0.9688	0.0026	$n_{10}n_{15}$	B,43.50	0.098205	0.9680	0.0026	$n_{10}n_{15}$
450	B,44.00	0.100105	0.9682	0.0026	$n_{10}n_{15}$	B,44.00	0.100107	0.9714	0.0026	$n_{10}n_{15}$
450	B,44.51	0.102055	0.9683	0.0026	$n_{10}n_{15}$	B,44.51	0.102055	0.9704	0.0026	$n_{10}n_{15}$
450	B,45.00	0.103939	0.9704	0.0026	$n_{10}n_{15}$	B,45.00	0.103940	0.9731	0.0027	$n_{10}n_{15}$
450	B,45.50	0.105866	0.9702	0.0024	$n_{10}n_{15}$	B,45.50	0.105862	0.9731	0.0024	$n_{10}n_{15}$
450	B,46.01	0.107833	0.9711	0.0024	$n_{10}n_{15}$	B,46.01	0.107832	0.9716	0.0024	$n_{10}n_{15}$
450	B,46.50	0.109733	0.9713	0.0024	$n_{10}n_{15}$	B,46.50	0.109733	0.9692	0.0024	$n_{10}n_{15}$
450	B,47.00	0.111677	0.9699	0.0024	$n_{10}n_{15}$	B,47.00	0.111678	0.9685	0.0024	$n_{10}n_{15}$
450	B,47.51	0.113663	0.9667	0.0025	$n_{10}n_{15}$	B,47.51	0.113662	0.9672	0.0025	$n_{10}n_{15}$
450	B,48.00	0.115581	0.9691	0.0029	$n_{10}n_{15}$	B,48.00	0.115582	0.9659	0.0029	$n_{10}n_{15}$
450	B,48.50	0.117543	0.9656	0.0029	$n_{10}n_{15}$	B,48.50	0.117544	0.9642	0.0029	$n_{10}n_{15}$
450	C,73.01	0.212676	0.9694	0.0042	$n_{12}n_{15}$	C,73.01	0.212694	0.9689	0.0040	$n_{12}n_{15}$
450	C,75.49	0.221949	0.9638	0.0034	$n_{12}n_{15}$	C,75.49	0.221938	0.9669	0.0034	$n_{12}n_{15}$
450	C,75.49	0.221949	0.9657	0.0032	$n_{12}n_{15}$	C,75.49	0.221941	0.9614	0.0032	$n_{12}n_{15}$
450	C,77.98	0.231289	0.9648	0.0031	$n_{12}n_{15}$	C,77.98	0.231277	0.9627	0.0031	$n_{12}n_{15}$
450	C,80.49	0.240258	0.9633	0.0031	$n_{12}n_{15}$	C,80.49	0.240260	0.9689	0.0032	$n_{12}n_{15}$
450	C,83.02	0.249310	0.9640	0.0024	$n_{12}n_{15}$	C,85.51	0.257838	0.9698	0.0024	$n_{12}n_{15}$
450	C,88.01	0.266320	0.9707	0.0032	$n_{12}n_{15}$	C,88.01	0.266331	0.9676	0.0086	$n_{12}n_{15}$
450	C,88.01	0.266324	0.9655	0.0031	$n_{12}n_{15}$	C,90.50	0.274445	0.9740	0.0032	$n_{12}n_{15}$
450	C,90.50	0.274434	0.9770	0.0032	$n_{12}n_{15}$	C,93.00	0.282468	0.9746	0.0033	$n_{12}n_{15}$
450	C,95.49	0.290101	0.9779	0.0033	$n_{12}n_{15}$	C,95.49	0.290115	0.9791	0.0033	$n_{12}n_{15}$
450	C,98.01	0.297722	0.9774	0.0034	$n_{12}n_{15}$	C,98.01	0.297708	0.9792	0.0034	$n_{12}n_{15}$
450	C,100.50	0.304881	0.9829	0.0034	$n_{12}n_{15}$	C,100.50	0.304878	0.9869	0.0035	$n_{12}n_{15}$
450	C,103.00	0.311934	0.9821	0.0032	$n_{12}n_{15}$	C,103.00	0.311928	0.9884	0.0032	$n_{12}n_{15}$
450	C,105.54	0.318730	0.9926	0.0036	$n_{12}n_{15}$	C,105.54	0.318734	0.9912	0.0036	$n_{12}n_{15}$
450	C,108.04	0.325279	0.9893	0.0042	$n_{12}n_{15}$	C,108.04	0.325293	0.9906	0.0036	$n_{12}n_{15}$
450	C,110.53	0.331453	0.9922	0.0036	$n_{12}n_{15}$	C,110.53	0.331457	0.9909	0.0037	$n_{12}n_{15}$
450	C,113.06	0.337572	0.9927	0.0038	$n_{12}n_{15}$	C,113.06	0.337586	0.9919	0.0038	$n_{12}n_{15}$
450	C,115.56	0.343296	0.9987	0.0038	$n_{12}n_{15}$	C,115.56	0.343294	1.0019	0.0039	$n_{12}n_{15}$
450	C,117.94	0.348571	0.9996	0.0036	$n_{12}n_{15}$	C,117.94	0.348570	1.0012	0.0036	$n_{12}n_{15}$
450	C,120.49	0.353927	1.0013	0.0037	$n_{12}n_{15}$	C,120.49	0.353925	1.0079	0.0037	$n_{12}n_{15}$
450	C,123.08	0.359153	1.0018	0.0037	$n_{12}n_{15}$	C,123.08	0.359149	1.0057	0.0037	$n_{12}n_{15}$
450	C,125.41	0.363583	1.0088	0.0037	$n_{12}n_{15}$	C,125.41	0.363581	1.0094	0.0037	$n_{12}n_{15}$
450	C,128.02	0.368375	1.0036	0.0038	$n_{12}n_{15}$	C,128.02	0.368376	1.0050	0.0038	$n_{12}n_{15}$
450	C,130.55	0.372734	1.0140	0.0045	$n_{12}n_{15}$	C,130.55	0.372723	1.0051	0.0044	$n_{12}n_{15}$
450	C,132.95	0.376647	1.0059	0.0045	$n_{12}n_{15}$	C,132.95	0.376656	1.0055	0.0045	$n_{12}n_{15}$
585	A,25.51	0.058977	0.9844	0.0079	n_{18}	A,25.51	0.058979	0.9769	0.0073	n_{18}
585	A,25.51	0.059000	0.9777	0.0073	n_{18}	A,25.51	0.058977	0.9742	0.0064	n_{18}
585	A,25.51	0.059004	0.9655	0.0064	n_{18}	A,25.51	0.059009	0.9714	0.0059	n_{18}
585	A,25.51	0.058979	0.9737	0.0064	n_{18}	A,25.51	0.059005	0.9770	0.0072	n_{18}
585	A,25.51	0.058983	0.9762	0.0073	n_{18}	A,25.51	0.059006	0.9618	0.0069	n_{18}
585	A,25.51	0.058977	0.9691	0.0071	n_{18}	A,25.51	0.058983	0.9714	0.0072	n_{18}
585	A,28.01	0.070729	0.9686	0.0052	n_{18}	A,28.01	0.070729	0.9704	0.0052	n_{18}
585	A,28.01	0.070729	0.9722	0.0052	n_{18}	A,28.01	0.070731	0.9742	0.0052	n_{18}
585	A,28.01	0.070727	0.9669	0.0052	n_{18}	A,28.01	0.070728	0.9690	0.0052	n_{18}
585	A,28.01	0.070726	0.9698	0.0052	n_{18}	A,28.01	0.070732	0.9640	0.0052	n_{18}
585	A,28.01	0.070725	0.9592	0.0051	n_{18}	A,28.01	0.070729	0.9674	0.0052	n_{18}
585	A,30.50	0.083123	0.9717	0.0040	n_{18}	A,30.50	0.083129	0.9675	0.0040	n_{18}
585	A,30.50	0.083137	0.9722	0.0033	n_{18}	A,33.01	0.096406	0.9714	0.0030	n_{18}
585	A,33.01	0.096406	0.9712	0.0025	n_{18}	A,33.01	0.096385	0.9677	0.0045	n_{19}
585	A,33.01	0.096405	0.9693	0.0046	n_{19}	A,33.01	0.096403	0.9789	0.0046	n_{19}
585	A,33.01	0.096402	0.9668	0.0046	n_{19}	A,33.01	0.096400	0.9723	0.0046	n_{19}
585	A,33.01	0.096404	0.9753	0.0046	n_{19}	A,33.01	0.096405	0.9765	0.0046	n_{19}
585	A,33.01	0.096399	0.9740	0.0046	n_{19}	A,35.51	0.110004	0.9754	0.0037	n_{19}
585	A,35.51	0.109997	0.9696	0.0037	n_{19}	A,35.51	0.109999	0.9650	0.0037	n_{19}
585	A,38.00	0.124134	0.9718	0.0031	n_{19}	A,38.00	0.124138	0.9696	0.0030	n_{19}
585	A,40.51	0.138677	0.9719	0.0027	n_{19}	A,40.51	0.138681	0.9686	0.0026	n_{19}
585	A,42.99	0.153507	0.9678	0.0023	n_{19}	A,45.51	0.168762	0.9681	0.0021	n_{19}
585	A,48.01	0.184048	0.9636	0.0021	n_{19}	A,50.49	0.199229	0.9679	0.0022	n_{19}
585	A,53.01	0.214841	0.9632	0.0021	n_{19}	A,55.50	0.230113	0.9639	0.0022	n_{19}
585	A,58.00	0.245623	0.9648	0.0023	n_{19}	A,60.51	0.260796	0.9682	0.0023	n_{19}
585	A,63.00	0.275886	0.9683	0.0024	n_{19}	A,65.49	0.290508	0.9673	0.0024	n_{19}
585	A,68.01	0.305441	0.9707	0.0025	n_{19}	A,70.50	0.319488	0.9730	0.0026	n_{19}
585	A,73.01	0.333796	0.9776	0.0028	n_{19}	A,75.50	0.347294	0.9746	0.0028	n_{19}
585	A,78.00	0.360902	0.9809	0.0029	n_{19}	A,80.51	0.373781	0.9824	0.0030	n_{19}
585	A,80.51	0.373795	0.9811	0.0021	n_{19}	A,82.99	0.386560	0.9878	0.0022	n_{19}
585	A,85.49	0.398678	0.9859	0.0022	n_{19}	A,88.01	0.410848	0.9926	0.0023	n_{19}
585	A,90.50	0.422207	0.9987	0.0023	n_{19}	A,73.01	0.333795	0.9775	0.0015	n_{19}
585	B,16.00	0.025543	0.9893	0.0073	$n_{16}n_{18}$	B,16.51	0.027166	0.9753	0.0080	$n_{16}n_{18}$
585	B,16.51	0.027167	0.9725	0.0080	$n_{16}n_{18}$	B,17.01	0.028802	0.9857	0.0082	$n_{16}n_{18}$
585	B,17.01	0.028801	0.9887	0.0081	$n_{16}n_{18}$	B,17.50	0.030441	0.9784	0.0080	$n_{16}n_{18}$
585	B,17.50	0.030440	0.9795	0.0081	$n_{16}n_{18}$	B,18.00	0.032159	0.9858	0.0086	$n_{16}n_{18}$
585	B,18.00	0.032158	0.9785	0.0085	$n_{16}n_{18}$	B,18.00	0.032158	0.9773	0.0085	$n_{16}n_{18}$
585	B,18.51	0.033953	0.9791	0.0083	$n_{16}n_{18}$	B,18.51	0.033954	0.9824	0.0083	$n_{16}n_{18}$
585	B,18.51	0.033953	0.9763	0.0082	$n_{16}n_{18}$	B,18.51	0.033953	0.9778	0.0073	$n_{16}n_{18}$
585	B,18.51	0.033953	0.9892	0.0075	$n_{16}n_{18}$	B,18.51	0.033954	0.9815	0.0069	$n_{16}n_{18}$
585	B,18.51	0.033954	0.9841	0.0069	$n_{16}n_{18}$	B,18.51	0.033953	0.9808	0.0061	$n_{16}n_{18}$
585	B,18.99	0.035678	0.9768	0.0061	$n_{16}n_{18}$	B,18.99	0.035678	0.9780	0.0057	$n_{16}n_{18}$
585	B,19.50	0.037554	0.9799	0.0062	$n_{16}n_{18}$	B,19.99	0.039389	0.9860	0.0070	$n_{16}n_{18}$
585	B,19.99	0.039390	0.9813	0.0070	$n_{16}n_{18}$	B,19.99	0.039390	0.9695	0.0067	$n_{16}n_{18}$
585	B,19.99	0.039390	0.9742	0.0069	$n_{16}n_{18}$	B,19.99	0.039390	0.9777	0.0069	$n_{16}n_{18}$
585	B,19.99	0.039389	0.9740	0.0051	$n_{16}n_{18}$	B,19.99	0.039389	0.9828	0.0052	$n_{16}n_{18}$
585	B,19.99	0.039389	0.9772	0.0052	$n_{16}n_{18}$	B,19.99	0.039390	0.9780	0.0052	$n_{16}n_{18}$
585	B,20.49	0.041305	0.9774	0.0052	$n_{16}n_{18}$	B,20.49	0.041305	0.9752	0.0052	$n_{16}n_{18}$
585	B,21.00	0.043301	0.9763	0.0053	$n_{16}n_{18}$	B,21.00	0.043301	0.9703	0.0053	$n_{16}n_{18}$
585	B,21.00	0.043301	0.9675	0.0052	$n_{16}n_{18}$	B,21.00	0.043300	0.9752	0.0053	$n_{16}n_{18}$
585	B,21.00	0.043301	0.9831	0.0043	$n_{16}n_{18}$	B,21.00	0.043301	0.9757	0.0043	$n_{16}n_{18}$

Table K.1: Cross section data with normalization from spline model

585	B,21.00	0.043302	0.9784	0.0037	$n_{16}n_{18}$	B,21.00	0.043301	0.9802	0.0034	$n_{16}n_{18}$
585	B,21.00	0.043301	0.9793	0.0030	$n_{16}n_{18}$	B,21.00	0.043303	0.9702	0.0041	$n_{16}n_{19}$
585	B,21.50	0.045293	0.9730	0.0041	$n_{16}n_{19}$	B,22.00	0.047322	0.9801	0.0042	$n_{16}n_{19}$
585	B,22.50	0.049388	0.9651	0.0042	$n_{16}n_{19}$	B,23.01	0.051532	0.9737	0.0042	$n_{16}n_{19}$
585	B,23.51	0.053670	0.9776	0.0042	$n_{16}n_{19}$	B,23.99	0.055744	0.9772	0.0042	$n_{16}n_{19}$
585	B,23.99	0.055745	0.9738	0.0042	$n_{16}n_{19}$	B,23.99	0.055744	0.9759	0.0034	$n_{16}n_{19}$
585	B,24.50	0.057996	0.9735	0.0034	$n_{16}n_{19}$	B,24.99	0.060186	0.9706	0.0034	$n_{16}n_{19}$
585	B,24.99	0.060185	0.9766	0.0028	$n_{16}n_{19}$	B,25.50	0.062501	0.9745	0.0028	$n_{16}n_{19}$
585	B,25.50	0.062501	0.9828	0.0025	$n_{16}n_{19}$	B,25.50	0.062501	0.9749	0.0024	$n_{16}n_{19}$
585	B,26.00	0.064804	0.9765	0.0021	$n_{16}n_{19}$	B,26.00	0.064802	0.9769	0.0019	$n_{16}n_{19}$
585	B,26.51	0.067186	0.9720	0.0019	$n_{16}n_{19}$	B,27.00	0.069497	0.9736	0.0019	$n_{16}n_{19}$
585	B,27.49	0.071840	0.9718	0.0018	$n_{16}n_{19}$	B,28.00	0.074309	0.9703	0.0020	$n_{16}n_{19}$
585	B,28.50	0.076761	0.9671	0.0020	$n_{16}n_{19}$	B,29.01	0.079290	0.9706	0.0020	$n_{16}n_{19}$
585	B,29.51	0.081796	0.9720	0.0020	$n_{16}n_{19}$	B,29.99	0.084222	0.9701	0.0020	$n_{16}n_{19}$
585	B,30.50	0.086833	0.9664	0.0020	$n_{16}n_{19}$	B,31.00	0.089414	0.9684	0.0021	$n_{16}n_{19}$
585	B,31.49	0.091963	0.9676	0.0022	$n_{16}n_{19}$	B,32.00	0.094648	0.9649	0.0022	$n_{16}n_{19}$
585	B,32.51	0.097391	0.9704	0.0023	$n_{16}n_{19}$	B,32.99	0.099993	0.9693	0.0024	$n_{16}n_{19}$
585	B,33.49	0.102709	0.9671	0.0020	$n_{16}n_{19}$	B,33.99	0.105428	0.9686	0.0021	$n_{16}n_{19}$
585	B,34.51	0.108218	0.9677	0.0022	$n_{16}n_{19}$	B,35.00	0.110965	0.9667	0.0023	$n_{16}n_{19}$
585	B,35.00	0.110966	0.9701	0.0023	$n_{16}n_{19}$	B,35.00	0.111009	0.9657	0.0022	$n_{16}n_{19}$
585	B,35.00	0.110965	0.9682	0.0023	$n_{16}n_{19}$	B,35.00	0.111010	0.9645	0.0022	$n_{16}n_{19}$
585	B,35.00	0.110966	0.9688	0.0023	$n_{16}n_{19}$	B,35.00	0.110966	0.9614	0.0022	$n_{16}n_{19}$
585	B,35.00	0.110966	0.9684	0.0023	$n_{16}n_{19}$	B,35.00	0.110919	0.9662	0.0022	$n_{16}n_{19}$
585	B,35.00	0.111010	0.9637	0.0042	$n_{16}n_{19}$	B,35.00	0.111009	0.9675	0.0022	$n_{16}n_{19}$
585	B,35.00	0.111009	0.9694	0.0022	$n_{16}n_{19}$	B,35.00	0.110965	0.9680	0.0019	$n_{16}n_{19}$
585	B,31.49	0.091963	0.9643	0.0023	$n_{16}n_{20}$	B,35.00	0.110965	0.9648	0.0020	$n_{16}n_{20}$
585	B,35.50	0.113745	0.9670	0.0014	$n_{16}n_{20}$	B,36.50	0.119393	0.9648	0.0012	$n_{16}n_{20}$
585	B,37.50	0.125073	0.9686	0.0012	$n_{16}n_{20}$	B,38.50	0.130810	0.9668	0.0012	$n_{16}n_{20}$
585	B,39.51	0.136662	0.9658	0.0012	$n_{16}n_{20}$	B,40.50	0.142457	0.9681	0.0012	$n_{16}n_{20}$
585	B,41.50	0.148354	0.9664	0.0054	$n_{16}n_{20}$	B,41.50	0.148354	0.9635	0.0013	$n_{16}n_{20}$
585	B,42.00	0.151321	0.9649	0.0016	$n_{16}n_{20}$	B,42.50	0.154298	0.9656	0.0016	$n_{16}n_{20}$
585	B,43.00	0.157280	0.9659	0.0015	$n_{16}n_{20}$	B,43.50	0.160274	0.9656	0.0015	$n_{16}n_{20}$
585	B,44.01	0.163333	0.9668	0.0015	$n_{16}n_{20}$	B,44.51	0.166346	0.9650	0.0016	$n_{16}n_{20}$
585	B,45.00	0.169304	0.9612	0.0016	$n_{16}n_{20}$	B,45.50	0.172331	0.9666	0.0016	$n_{16}n_{20}$
585	B,46.01	0.175415	0.9662	0.0017	$n_{16}n_{20}$	B,46.51	0.178456	0.9657	0.0016	$n_{16}n_{20}$
585	B,47.01	0.181497	0.9610	0.0016	$n_{16}n_{20}$	C,73.01	0.334011	0.9801	0.0040	$n_{17}n_{20}$
585	C,73.01	0.334037	0.9802	0.0021	$n_{17}n_{20}$	C,77.98	0.361000	0.9853	0.0022	$n_{17}n_{20}$
585	C,83.02	0.386973	0.9853	0.0023	$n_{17}n_{20}$	C,93.00	0.433773	1.0017	0.0026	$n_{17}n_{20}$
585	C,98.01	0.454929	1.0097	0.0028	$n_{17}n_{20}$	C,103.00	0.474529	1.0151	0.0029	$n_{17}n_{20}$
585	C,108.04	0.492722	1.0236	0.0132	$n_{17}n_{20}$	C,108.04	0.492691	1.0209	0.0029	$n_{17}n_{20}$
585	C,110.51	0.500929	1.0261	0.0037	$n_{17}n_{20}$	C,112.92	0.508866	1.0267	0.0038	$n_{17}n_{20}$
585	C,115.56	0.516976	1.0356	0.0036	$n_{17}n_{20}$	C,117.94	0.524063	1.0326	0.0037	$n_{17}n_{20}$
585	C,120.49	0.531168	1.0389	0.0038	$n_{17}n_{20}$	C,123.08	0.538158	1.0351	0.0038	$n_{17}n_{20}$
585	C,125.47	0.544191	1.0419	0.0039	$n_{17}n_{20}$	C,128.02	0.550385	1.0481	0.0040	$n_{17}n_{20}$
585	C,130.55	0.556122	1.0541	0.0042	$n_{17}n_{20}$	C,132.95	0.561312	1.0515	0.0041	$n_{17}n_{20}$
585	C,135.53	0.566478	1.0491	0.0042	$n_{17}n_{20}$					
720	A,38.00	0.183535	0.9640	0.0036	n_{25}	A,38.00	0.183527	0.9578	0.0034	n_{25}
720	A,38.00	0.183534	0.9564	0.0034	n_{25}	A,40.50	0.204463	0.9537	0.0030	n_{25}
720	A,40.50	0.204456	0.9535	0.0027	n_{25}	A,40.50	0.204443	0.9584	0.0030	n_{25}
720	A,43.00	0.225760	0.9638	0.0067	n_{25}	A,43.00	0.225763	0.9587	0.0027	n_{25}
720	A,43.00	0.225763	0.9575	0.0059	n_{25}	A,43.00	0.225765	0.9616	0.0036	n_{25}
720	A,43.00	0.225760	0.9583	0.0027	n_{25}	A,45.51	0.247044	0.9626	0.0028	n_{25}
720	A,48.00	0.268566	0.9670	0.0026	n_{25}	A,50.50	0.290050	0.9702	0.0027	n_{25}
720	A,53.01	0.312024	0.9719	0.0027	n_{25}	A,55.50	0.333157	0.9758	0.0028	n_{25}
720	A,58.00	0.354269	0.9753	0.0029	n_{25}	A,60.50	0.374909	0.9738	0.0030	n_{25}
720	A,63.00	0.395409	0.9861	0.0027	n_{25}	A,65.51	0.415422	0.9879	0.0057	n_{25}
720	A,65.51	0.415428	0.9874	0.0028	n_{25}	A,68.01	0.435104	0.9977	0.0029	n_{25}
720	A,70.49	0.454010	0.9972	0.0030	n_{25}	A,73.01	0.472904	1.0036	0.0032	n_{25}
720	A,75.50	0.490801	1.0115	0.0071	n_{25}	A,75.50	0.490818	1.0060	0.0038	n_{25}
720	A,78.00	0.508461	1.0107	0.0029	n_{25}	A,80.50	0.525358	1.0130	0.0030	n_{25}
720	A,83.00	0.541891	1.0201	0.0032	n_{25}	A,88.01	0.573169	1.0297	0.0039	n_{25}
720	A,85.51	0.557785	1.0214	0.0038	n_{25}	A,90.50	0.587844	1.0283	0.0034	n_{25}
720	A,93.01	0.602181	1.0390	0.0036	n_{25}	A,95.50	0.615728	1.0347	0.0038	n_{25}
720	A,97.99	0.628831	1.0465	0.0048	n_{25}	A,97.99	0.628839	1.0473	0.0048	n_{25}
720	A,100.50	0.641440	1.0428	0.0056	n_{25}	A,100.50	0.641439	1.0435	0.0049	n_{25}
720	A,103.00	0.653555	1.0543	0.0052	n_{25}	A,103.00	0.653554	1.0567	0.0052	n_{25}
720	A,105.51	0.665077	1.0551	0.0066	n_{25}	A,105.51	0.665077	1.0510	0.0047	n_{25}
720	A,105.51	0.665075	1.0547	0.0047	n_{25}	A,108.00	0.676109	1.0571	0.0049	n_{25}
720	A,108.00	0.676105	1.0540	0.0049	n_{25}	A,73.01	0.472914	1.0038	0.0029	n_{25}
720	B,22.00	0.071131	0.9705	0.0042	$n_{21}n_{25}$	B,22.50	0.074195	0.9684	0.0040	$n_{21}n_{25}$
720	B,23.00	0.077313	0.9642	0.0040	$n_{21}n_{25}$	B,23.00	0.077316	0.9639	0.0035	$n_{21}n_{25}$
720	B,23.51	0.080545	0.9692	0.0032	$n_{21}n_{25}$	B,24.00	0.083699	0.9655	0.0035	$n_{21}n_{25}$
720	B,24.00	0.083701	0.9717	0.0077	$n_{21}n_{25}$	B,24.00	0.083699	0.9662	0.0032	$n_{21}n_{25}$
720	B,24.50	0.086960	0.9709	0.0042	$n_{21}n_{25}$	B,25.01	0.090337	0.9691	0.0032	$n_{21}n_{25}$
720	B,25.01	0.090333	0.9703	0.0032	$n_{21}n_{25}$	B,25.50	0.093616	0.9654	0.0030	$n_{21}n_{25}$
720	B,26.00	0.097015	0.9718	0.0030	$n_{21}n_{25}$	B,26.51	0.100517	0.9695	0.0030	$n_{21}n_{25}$
720	B,27.00	0.103931	0.9702	0.0030	$n_{21}n_{25}$	B,27.50	0.107449	0.9625	0.0031	$n_{21}n_{25}$
720	B,28.00	0.111012	0.9619	0.0031	$n_{21}n_{25}$	B,28.50	0.114607	0.9675	0.0028	$n_{21}n_{25}$
720	B,29.00	0.118239	0.9633	0.0055	$n_{21}n_{25}$	B,29.00	0.118240	0.9673	0.0028	$n_{21}n_{25}$
720	B,29.51	0.121933	0.9701	0.0029	$n_{21}n_{25}$	B,29.99	0.125540	0.9655	0.0029	$n_{21}n_{25}$
720	B,30.50	0.129354	0.9664	0.0030	$n_{21}n_{25}$	B,31.00	0.133128	0.9702	0.0060	$n_{21}n_{25}$
720	B,31.00	0.133125	0.9637	0.0034	$n_{21}n_{25}$	B,31.51	0.136942	0.9672	0.0027	$n_{21}n_{25}$
720	B,32.01	0.140779	0.9654	0.0027	$n_{21}n_{25}$	B,32.51	0.144645	0.9674	0.0028	$n_{21}n_{25}$
720	B,33.50	0.152375	0.9644	0.0034	$n_{21}n_{25}$	B,33.01	0.148537	0.9653	0.0033	$n_{21}n_{25}$
720	B,34.01	0.156400	0.9669	0.0032	$n_{21}n_{25}$	B,34.01	0.156397	0.9643	0.0033	$n_{21}n_{25}$
720	B,34.01	0.156397	0.9634	0.0033	$n_{21}n_{25}$	B,34.01	0.156397	0.9656	0.0040	$n_{21}n_{25}$
720	B,34.01	0.156397	0.9690	0.0040	$n_{21}n_{25}$	B,34.01	0.156397	0.9669	0.0044	$n_{21}n_{25}$
720	B,34.01	0.156397	0.9683	0.0040	$n_{21}n_{25}$	B,34.01	0.156394	0.9666	0.0040	$n_{21}n_{25}$

Table K.1: Cross section data with normalization from spline model

720	B,34.01	0.156398	0.9659	0.0040	$n_{21}n_{25}$	B,34.01	0.156400	0.9669	0.0046	$n_{21}n_{25}$
720	B,34.01	0.156396	0.9697	0.0036	$n_{21}n_{25}$	B,34.01	0.156396	0.9659	0.0036	$n_{21}n_{25}$
720	B,34.01	0.156396	0.9676	0.0037	$n_{21}n_{25}$	B,34.01	0.156396	0.9654	0.0036	$n_{21}n_{25}$
720	B,34.01	0.156402	0.9625	0.0036	$n_{21}n_{25}$	B,34.01	0.156402	0.9628	0.0036	$n_{21}n_{25}$
720	B,34.01	0.156396	0.9697	0.0037	$n_{21}n_{25}$	B,30.50	0.129354	0.9630	0.0032	$n_{21}n_{26}$
720	B,34.01	0.156396	0.9660	0.0039	$n_{21}n_{26}$	B,34.01	0.156397	0.9666	0.0035	$n_{21}n_{26}$
720	B,34.51	0.160368	0.9673	0.0031	$n_{21}n_{26}$	B,35.00	0.164283	0.9665	0.0030	$n_{21}n_{26}$
720	B,35.50	0.168290	0.9616	0.0030	$n_{21}n_{26}$	B,36.00	0.172324	0.9575	0.0025	$n_{21}n_{26}$
720	B,36.50	0.176391	0.9656	0.0025	$n_{21}n_{26}$	B,37.00	0.180473	0.9675	0.0025	$n_{21}n_{26}$
720	B,37.50	0.184570	0.9701	0.0031	$n_{21}n_{26}$	B,38.01	0.188765	0.9678	0.0032	$n_{21}n_{26}$
720	B,38.50	0.192818	0.9688	0.0032	$n_{21}n_{26}$	B,39.00	0.196987	0.9631	0.0032	$n_{21}n_{26}$
720	B,39.49	0.201067	0.9589	0.0032	$n_{21}n_{26}$	B,40.00	0.205298	0.9617	0.0027	$n_{21}n_{26}$
720	B,40.00	0.205332	0.9459	0.0088	$n_{21}n_{26}$	B,40.00	0.205303	0.9596	0.0043	$n_{21}n_{26}$
720	B,40.00	0.205333	0.9584	0.0066	$n_{21}n_{26}$	B,40.00	0.205333	0.9623	0.0047	$n_{21}n_{26}$
720	B,40.50	0.209520	0.9588	0.0034	$n_{21}n_{26}$	B,40.50	0.209521	0.9614	0.0058	$n_{21}n_{26}$
720	B,40.50	0.209521	0.9648	0.0049	$n_{21}n_{26}$	B,40.50	0.209521	0.9591	0.0066	$n_{21}n_{26}$
720	B,41.50	0.217940	0.9639	0.0034	$n_{21}n_{26}$	B,41.50	0.217937	0.9443	0.0098	$n_{21}n_{26}$
720	B,41.50	0.217940	0.9638	0.0050	$n_{21}n_{26}$	B,41.50	0.217940	0.9579	0.0048	$n_{21}n_{26}$
720	B,42.50	0.226358	0.9548	0.0031	$n_{21}n_{26}$	B,42.50	0.226388	0.9581	0.0032	$n_{21}n_{26}$
720	B,42.50	0.226391	0.9528	0.0131	$n_{21}n_{26}$	B,42.50	0.226398	0.9484	0.0097	$n_{21}n_{26}$
720	B,42.50	0.226390	0.9547	0.0040	$n_{21}n_{26}$	B,43.50	0.234889	0.9600	0.0032	$n_{21}n_{26}$
720	B,43.50	0.234888	0.9648	0.0052	$n_{21}n_{26}$	B,43.50	0.234889	0.9562	0.0041	$n_{21}n_{26}$
720	B,44.51	0.243494	0.9556	0.0031	$n_{21}n_{26}$	B,39.49	0.201109	0.9598	0.0026	$n_{23}n_{26}$
720	B,39.49	0.201113	0.9611	0.0024	$n_{23}n_{26}$	B,40.00	0.205242	0.9592	0.0026	$n_{23}n_{26}$
720	B,40.00	0.205237	0.9590	0.0046	$n_{23}n_{26}$	B,40.50	0.209429	0.9636	0.0026	$n_{23}n_{26}$
720	B,41.01	0.213721	0.9651	0.0025	$n_{23}n_{26}$	B,41.01	0.213727	0.9625	0.0025	$n_{23}n_{26}$
720	B,41.50	0.217844	0.9601	0.0026	$n_{23}n_{26}$	B,41.50	0.217836	0.9614	0.0026	$n_{23}n_{26}$
720	B,42.00	0.222191	0.9621	0.0026	$n_{23}n_{26}$	B,42.00	0.222193	0.9618	0.0034	$n_{23}n_{26}$
720	B,42.00	0.222191	0.9560	0.0037	$n_{23}n_{26}$	B,42.50	0.226427	0.9665	0.0031	$n_{23}n_{26}$
720	B,42.50	0.226422	0.9632	0.0027	$n_{23}n_{26}$	B,43.00	0.230669	0.9642	0.0032	$n_{23}n_{26}$
720	B,43.00	0.230670	0.9665	0.0042	$n_{23}n_{26}$	B,43.00	0.230666	0.9649	0.0027	$n_{23}n_{26}$
720	B,43.50	0.234784	0.9613	0.0027	$n_{23}n_{26}$	B,43.50	0.234787	0.9573	0.0027	$n_{23}n_{26}$
720	B,43.98	0.239006	0.9595	0.0027	$n_{23}n_{26}$	B,43.98	0.239009	0.9592	0.0035	$n_{23}n_{26}$
720	B,43.98	0.239010	0.9629	0.0034	$n_{23}n_{26}$	B,44.49	0.243344	0.9577	0.0025	$n_{23}n_{26}$
720	B,44.49	0.243348	0.9575	0.0025	$n_{23}n_{26}$	B,45.00	0.247693	0.9627	0.0025	$n_{23}n_{26}$
720	B,45.50	0.251967	0.9598	0.0026	$n_{23}n_{26}$	B,45.50	0.251964	0.9633	0.0026	$n_{23}n_{26}$
720	C,73.01	0.472874	1.0047	0.0024	$n_{22}n_{26}$	C,73.01	0.472876	1.0045	0.0022	$n_{22}n_{26}$
720	C,75.49	0.490760	1.0072	0.0022	$n_{22}n_{26}$	C,77.98	0.508292	1.0096	0.0023	$n_{22}n_{26}$
720	C,80.49	0.525321	1.0101	0.0023	$n_{22}n_{26}$	C,83.02	0.542028	1.0258	0.0024	$n_{22}n_{26}$
720	C,85.51	0.557861	1.0219	0.0020	$n_{22}n_{26}$	C,88.01	0.573211	1.0250	0.0021	$n_{22}n_{26}$
720	C,90.50	0.587905	1.0228	0.0141	$n_{22}n_{26}$	C,90.50	0.587898	1.0328	0.0022	$n_{22}n_{26}$
720	C,93.00	0.602155	1.0415	0.0219	$n_{22}n_{26}$	C,93.00	0.602159	1.0364	0.0028	$n_{22}n_{26}$
720	C,95.48	0.615663	1.0351	0.0029	$n_{22}n_{26}$	C,98.01	0.628986	1.0498	0.0031	$n_{22}n_{26}$
720	C,100.50	0.641508	1.0387	0.0031	$n_{22}n_{26}$	C,103.00	0.653562	1.0475	0.0033	$n_{22}n_{26}$
720	C,105.54	0.665249	1.0489	0.0028	$n_{22}n_{26}$	C,105.54	0.665238	1.0553	0.0094	$n_{22}n_{26}$
720	C,105.54	0.665258	1.0529	0.0045	$n_{22}n_{26}$	C,105.54	0.665248	1.0523	0.0070	$n_{22}n_{26}$
720	C,105.54	0.665248	1.0569	0.0049	$n_{22}n_{26}$	C,108.04	0.676303	1.0573	0.0036	$n_{22}n_{26}$
720	C,108.04	0.676298	1.0560	0.0062	$n_{22}n_{26}$	C,108.04	0.676297	1.0604	0.0052	$n_{22}n_{26}$
720	C,108.04	0.676302	1.0626	0.0072	$n_{22}n_{26}$	C,113.06	0.696913	1.0638	0.0039	$n_{22}n_{26}$
720	C,113.06	0.696937	1.0626	0.0116	$n_{22}n_{26}$	C,113.06	0.696910	1.0727	0.0058	$n_{22}n_{26}$
720	C,113.06	0.696912	1.0731	0.0056	$n_{22}n_{26}$	C,117.94	0.715149	1.0669	0.0037	$n_{22}n_{26}$
720	C,117.94	0.715149	1.0745	0.0039	$n_{22}n_{26}$	C,117.94	0.715147	1.0872	0.0122	$n_{22}n_{26}$
720	C,117.94	0.715146	1.0586	0.0048	$n_{22}n_{26}$	C,123.08	0.732478	1.0810	0.0041	$n_{22}n_{26}$
720	C,123.08	0.732479	1.0789	0.0065	$n_{22}n_{26}$	C,123.08	0.732478	1.0817	0.0051	$n_{22}n_{26}$
720	C,128.02	0.747376	1.0815	0.0040	$n_{22}n_{26}$	C,103.00	0.653623	1.0466	0.0025	$n_{24}n_{26}$
720	C,103.00	0.653605	1.0494	0.0023	$n_{24}n_{26}$	C,105.54	0.665194	1.0516	0.0026	$n_{24}n_{26}$
720	C,105.54	0.665181	1.0528	0.0046	$n_{24}n_{26}$	C,108.04	0.676367	1.0584	0.0027	$n_{24}n_{26}$
720	C,108.04	0.676359	1.0608	0.0027	$n_{24}n_{26}$	C,110.53	0.686691	1.0626	0.0026	$n_{24}n_{26}$
720	C,110.53	0.686696	1.0579	0.0026	$n_{24}n_{26}$	C,113.06	0.696973	1.0607	0.0027	$n_{24}n_{26}$
720	C,113.06	0.696971	1.0623	0.0027	$n_{24}n_{26}$	C,115.56	0.706412	1.0718	0.0027	$n_{24}n_{26}$
720	C,115.56	0.706402	1.0676	0.0036	$n_{24}n_{26}$	C,115.56	0.706395	1.0681	0.0039	$n_{24}n_{26}$
720	C,117.94	0.715171	1.0716	0.0033	$n_{24}n_{26}$	C,117.94	0.715172	1.0699	0.0028	$n_{24}n_{26}$
720	C,120.49	0.723872	1.0822	0.0035	$n_{24}n_{26}$	C,120.49	0.723864	1.0725	0.0045	$n_{24}n_{26}$
720	C,120.49	0.723854	1.0829	0.0029	$n_{24}n_{26}$	C,123.08	0.732465	1.0819	0.0030	$n_{24}n_{26}$
720	C,123.08	0.732449	1.0784	0.0030	$n_{24}n_{26}$	C,125.59	0.740162	1.0833	0.0031	$n_{24}n_{26}$
720	C,125.59	0.740162	1.0903	0.0040	$n_{24}n_{26}$	C,125.59	0.740152	1.0847	0.0039	$n_{24}n_{26}$
720	C,128.02	0.747367	1.0846	0.0028	$n_{24}n_{26}$	C,128.02	0.747354	1.0844	0.0028	$n_{24}n_{26}$
720	C,130.65	0.754572	1.0965	0.0029	$n_{24}n_{26}$	C,132.84	0.760295	1.0938	0.0030	$n_{24}n_{26}$
720	C,132.84	0.760304	1.0855	0.0029	$n_{24}n_{26}$					
855	A,43.00	0.306851	0.9584	0.0045	$n_{29}n_{30}$	A,43.00	0.306859	0.9716	0.0045	$n_{29}n_{30}$
855	A,43.00	0.306902	0.9717	0.0044	$n_{29}n_{30}$	A,43.00	0.306904	0.9740	0.0046	$n_{29}n_{30}$
855	A,43.00	0.306888	0.9630	0.0045	$n_{29}n_{30}$	A,45.51	0.335383	0.9659	0.0046	$n_{29}n_{30}$
855	A,45.51	0.335385	0.9616	0.0045	$n_{29}n_{30}$	A,45.51	0.335386	0.9667	0.0045	$n_{29}n_{30}$
855	A,45.51	0.335370	0.9690	0.0046	$n_{29}n_{30}$	A,45.51	0.335381	0.9645	0.0045	$n_{29}n_{30}$
855	A,48.00	0.363893	0.9671	0.0046	$n_{29}n_{30}$	A,48.00	0.363887	0.9747	0.0046	$n_{29}n_{30}$
855	A,48.00	0.363849	0.9772	0.0047	$n_{29}n_{30}$	A,48.00	0.363852	0.9762	0.0047	$n_{29}n_{30}$
855	A,48.00	0.363838	0.9728	0.0046	$n_{29}n_{30}$	A,50.50	0.391673	0.9765	0.0047	$n_{29}n_{30}$
855	A,50.50	0.391679	0.9743	0.0046	$n_{29}n_{30}$	A,50.50	0.391627	0.9734	0.0046	$n_{29}n_{30}$
855	A,50.50	0.391630	0.9793	0.0047	$n_{29}n_{30}$	A,50.50	0.391630	0.9805	0.0046	$n_{29}n_{30}$
855	A,53.01	0.420080	0.9847	0.0046	$n_{29}n_{30}$	A,53.01	0.420083	0.9837	0.0075	$n_{29}n_{30}$
855	A,53.01	0.420103	0.9763	0.0047	$n_{29}n_{30}$	A,53.01	0.420099	0.9856	0.0047	$n_{29}n_{30}$
855	A,53.01	0.420102	0.9910	0.0047	$n_{29}n_{30}$	A,55.50	0.447090	0.9891	0.0048	$n_{29}n_{30}$
855	A,55.50	0.447116	0.9929	0.0048	$n_{29}n_{30}$	A,55.50	0.447114	0.9864	0.0048	$n_{29}n_{30}$
855	A,55.50	0.447120	0.9869	0.0048	$n_{29}n_{30}$	A,55.50	0.447111	0.9916	0.0049	$n_{29}n_{30}$
855	A,58.00	0.474824	0.9925	0.0024	$n_{29}n_{30}$	A,60.50	0.501140	0.9997	0.0022	$n_{29}n_{30}$
855	A,63.00	0.527449	1.0010	0.0023	n_{29}	A,65.49	0.552353	1.0101	0.0023	n_{29}
855	A,68.00	0.577487	1.0217	0.0024	n_{29}	A,70.50	0.601103	1.0149	0.0024	n_{29}
855	A,73.01	0.624893	1.0248	0.0026	n_{29}	A,75.50	0.646801	1.0291	0.0035	n_{29}

Table K.1: Cross section data with normalization from spline model

855	A,78.00	0.668975	1.0329	0.0028	n_{29}	A,80.50	0.689459	1.0248	0.0066	n_{29}
855	A,83.01	0.710104	1.0447	0.0024	n_{29}	A,85.49	0.728977	1.0517	0.0025	n_{29}
855	A,88.01	0.748179	1.0574	0.0032	n_{29}	A,90.50	0.765639	1.0537	0.0028	n_{29}
855	A,85.51	0.729510	1.0489	0.0027	n_{29}	B,20.50	0.086749	0.9489	0.0067	$n_{27}n_{29}$
855	B,21.00	0.090776	0.9640	0.0068	$n_{27}n_{29}$	B,21.50	0.094880	0.9631	0.0067	$n_{27}n_{29}$
855	B,22.00	0.099046	0.9668	0.0070	$n_{27}n_{29}$	B,22.50	0.103281	0.9552	0.0069	$n_{27}n_{29}$
855	B,22.50	0.103281	0.9522	0.0069	$n_{27}n_{29}$	B,23.00	0.107588	0.9512	0.0069	$n_{27}n_{29}$
855	B,23.51	0.112043	0.9588	0.0069	$n_{27}n_{29}$	B,23.99	0.116275	0.9538	0.0069	$n_{27}n_{29}$
855	B,24.50	0.120869	0.9489	0.0068	$n_{27}n_{29}$	B,24.50	0.120863	0.9503	0.0069	$n_{27}n_{29}$
855	B,25.01	0.125517	0.9562	0.0069	$n_{27}n_{29}$	B,25.50	0.130019	0.9585	0.0070	$n_{27}n_{29}$
855	B,26.01	0.134777	0.9632	0.0071	$n_{27}n_{29}$	B,26.51	0.139501	0.9600	0.0070	$n_{27}n_{29}$
855	B,26.51	0.139498	0.9561	0.0070	$n_{27}n_{29}$	B,26.99	0.144052	0.9515	0.0068	$n_{27}n_{29}$
855	B,27.50	0.148979	0.9529	0.0069	$n_{27}n_{29}$	B,28.00	0.153845	0.9607	0.0070	$n_{27}n_{29}$
855	B,28.50	0.158758	0.9598	0.0070	$n_{27}n_{29}$	B,28.50	0.158759	0.9577	0.0069	$n_{27}n_{29}$
855	B,29.00	0.163716	0.9562	0.0112	$n_{27}n_{29}$	B,29.50	0.168723	0.9596	0.0071	$n_{27}n_{29}$
855	B,30.01	0.173879	0.9663	0.0072	$n_{27}n_{29}$	B,30.50	0.178864	0.9640	0.0071	$n_{27}n_{29}$
855	B,30.50	0.178861	0.9642	0.0072	$n_{27}n_{29}$	B,31.00	0.183980	0.9702	0.0072	$n_{27}n_{29}$
855	B,31.51	0.189255	0.9621	0.0072	$n_{27}n_{29}$	B,32.00	0.194348	0.9621	0.0073	$n_{27}n_{29}$
855	B,32.50	0.199733	0.9581	0.0073	$n_{27}n_{29}$	B,32.50	0.199740	0.9592	0.0031	$n_{27}n_{29}$
855	B,33.01	0.205114	0.9628	0.0032	$n_{27}n_{29}$	B,33.50	0.210304	0.9575	0.0031	$n_{27}n_{29}$
855	B,34.00	0.215632	0.9593	0.0032	$n_{27}n_{29}$	B,34.50	0.220998	0.9667	0.0032	$n_{27}n_{29}$
855	B,35.00	0.226369	0.9605	0.0032	$n_{27}n_{29}$	B,35.50	0.231783	0.9628	0.0032	$n_{27}n_{29}$
855	B,36.00	0.237216	0.9566	0.0043	$n_{27}n_{29}$	B,36.50	0.242666	0.9584	0.0033	$n_{27}n_{29}$
855	B,37.00	0.248141	0.9492	0.0092	$n_{27}n_{29}$	B,37.50	0.253640	0.9646	0.0028	$n_{27}n_{29}$
855	B,38.01	0.259154	0.9662	0.0028	$n_{27}n_{29}$	B,38.51	0.264689	0.9671	0.0035	$n_{27}n_{29}$
855	B,39.00	0.270221	0.9643	0.0032	$n_{27}n_{29}$	B,39.51	0.275795	0.9661	0.0035	$n_{27}n_{29}$
855	B,40.00	0.281439	0.9628	0.0035	$n_{27}n_{29}$	B,42.00	0.303812	0.9669	0.0038	$n_{27}n_{29}$
855	B,42.50	0.309426	0.9737	0.0038	$n_{27}n_{29}$	B,42.50	0.309426	0.9673	0.0038	$n_{27}n_{29}$
855	B,43.00	0.315044	0.9689	0.0039	$n_{27}n_{29}$	B,43.00	0.315047	0.9708	0.0039	$n_{27}n_{29}$
855	B,43.50	0.320659	0.9770	0.0040	$n_{27}n_{29}$	B,43.50	0.320658	0.9726	0.0040	$n_{27}n_{29}$
855	B,44.00	0.326280	0.9656	0.0035	$n_{27}n_{29}$	B,44.00	0.326280	0.9626	0.0037	$n_{27}n_{31}$
855	B,44.51	0.332017	0.9723	0.0042	$n_{27}n_{31}$	B,45.00	0.337536	0.9675	0.0037	$n_{27}n_{31}$
855	B,45.50	0.343160	0.9715	0.0037	$n_{27}n_{31}$	B,46.01	0.348887	0.9710	0.0038	$n_{27}n_{31}$
855	B,46.50	0.354414	0.9761	0.0037	$n_{27}n_{31}$	B,47.00	0.360011	0.9690	0.0037	$n_{27}n_{31}$
855	B,47.51	0.365744	0.9778	0.0038	$n_{27}n_{31}$	B,48.00	0.371228	0.9718	0.0046	$n_{27}n_{31}$
855	B,48.00	0.371229	0.9728	0.0046	$n_{27}n_{31}$	B,48.50	0.376825	0.9716	0.0045	$n_{27}n_{31}$
855	B,48.50	0.376822	0.9736	0.0044	$n_{27}n_{31}$	B,49.01	0.382527	0.9715	0.0046	$n_{27}n_{31}$
855	B,49.01	0.382528	0.9783	0.0048	$n_{27}n_{31}$	B,49.50	0.387993	0.9694	0.0072	$n_{27}n_{31}$
855	B,49.50	0.387994	0.9747	0.0043	$n_{27}n_{31}$	B,50.00	0.393568	0.9754	0.0049	$n_{27}n_{31}$
855	B,50.00	0.393570	0.9798	0.0049	$n_{27}n_{31}$	B,50.50	0.399138	0.9862	0.0050	$n_{27}n_{31}$
855	B,50.50	0.399136	0.9779	0.0099	$n_{27}n_{31}$	B,51.00	0.404683	0.9808	0.0050	$n_{27}n_{31}$
855	B,51.00	0.404678	0.9814	0.0051	$n_{27}n_{31}$	B,51.50	0.410227	0.9885	0.0066	$n_{27}n_{31}$
855	B,52.00	0.415749	0.9828	0.0052	$n_{27}n_{31}$	B,52.00	0.415753	0.9817	0.0062	$n_{27}n_{31}$
855	B,52.49	0.421156	0.9862	0.0053	$n_{27}n_{31}$	B,52.49	0.421156	0.9770	0.0053	$n_{27}n_{31}$
855	B,53.01	0.426868	0.9818	0.0054	$n_{27}n_{31}$	B,53.01	0.426862	0.9674	0.0125	$n_{27}n_{31}$
855	B,53.50	0.432252	0.9758	0.0245	$n_{27}n_{31}$	B,53.50	0.432250	0.9842	0.0055	$n_{27}n_{31}$
855	B,53.50	0.432248	0.9874	0.0055	$n_{27}n_{31}$	B,53.50	0.432249	0.9847	0.0055	$n_{27}n_{31}$
855	B,54.01	0.437820	0.9798	0.0079	$n_{27}n_{31}$	B,54.01	0.437820	0.9791	0.0084	$n_{27}n_{31}$
855	C,85.51	0.730035	1.0473	0.0028	$n_{28}n_{31}$	C,88.01	0.748648	1.0572	0.0034	$n_{28}n_{31}$
855	C,90.50	0.766140	1.0582	0.0030	$n_{28}n_{31}$	C,93.00	0.783591	1.0663	0.0032	$n_{28}n_{31}$
855	C,95.49	0.799587	1.0713	0.0033	$n_{28}n_{31}$	C,98.01	0.815697	1.0786	0.0034	$n_{28}n_{31}$
855	C,100.50	0.830341	1.0858	0.0035	$n_{28}n_{31}$	C,103.00	0.844935	1.0823	0.0037	$n_{28}n_{31}$
855	C,105.54	0.858576	1.0864	0.0046	$n_{28}n_{31}$	C,105.54	0.858572	1.1010	0.0047	$n_{28}n_{31}$
855	C,108.04	0.871801	1.0978	0.0050	$n_{28}n_{31}$	C,108.04	0.871784	1.1069	0.0046	$n_{28}n_{31}$
855	C,110.51	0.883822	1.1080	0.0049	$n_{28}n_{31}$	C,110.51	0.883818	1.1129	0.0050	$n_{28}n_{31}$
855	C,113.06	0.896041	1.1084	0.0073	$n_{28}n_{31}$	C,115.56	0.907041	1.1184	0.0048	$n_{28}n_{31}$
855	C,115.56	0.907029	1.1084	0.0048	$n_{28}n_{31}$	C,117.95	0.917352	1.1189	0.0049	$n_{28}n_{31}$
855	C,120.49	0.927436	1.1169	0.0050	$n_{28}n_{31}$	C,120.49	0.927475	1.1192	0.0051	$n_{28}n_{31}$
855	C,123.08	0.937444	1.1352	0.0067	$n_{28}n_{31}$	C,125.47	0.945952	1.1379	0.0054	$n_{28}n_{31}$
855	C,125.47	0.945946	1.1211	0.0062	$n_{28}n_{31}$	C,128.02	0.954732	1.1366	0.0054	$n_{28}n_{31}$
855	C,128.02	0.954718	1.1294	0.0054	$n_{28}n_{31}$	C,130.55	0.962743	1.1391	0.0055	$n_{28}n_{31}$
855	C,132.95	0.970050	1.1354	0.0056	$n_{28}n_{31}$	C,132.95	0.970049	1.1426	0.0056	$n_{28}n_{31}$
855	C,132.95	0.970050	1.1405	0.0056	$n_{28}n_{31}$	C,135.52	0.977245	1.1508	0.0081	$n_{28}n_{31}$
855	C,135.52	0.977231	1.1543	0.0088	$n_{28}n_{31}$					

Table K.1: Cross section data with normalization from spline model.

Energy [MeV]	Parameters
180	$n_{AB} \leftrightarrow n_1$, $n_{AC} \leftrightarrow n_2$ $n_{E,C} \leftrightarrow n_3$, $n_{E,A1} \leftrightarrow n_4$, $n_{E,A2} \leftrightarrow n_5$
315	$n_{AA} \leftrightarrow n_7$, $n_{AB} \leftrightarrow n_6$, $n_{AC} \leftrightarrow n_8$ $n_E \leftrightarrow n_9$
450	$n_{AA} \leftrightarrow n_{11}$, $n_{AB} \leftrightarrow n_{10}$, $n_{AC} \leftrightarrow n_{12}$ $n_{E,C1} \leftrightarrow n_{13}$, $n_{E,C2} \leftrightarrow n_{14}$, $n_{E,A} \leftrightarrow n_{15}$
585	$n_{AB} \leftrightarrow n_{16}$, $n_{AC} \leftrightarrow n_{17}$ $n_{E,C1} \leftrightarrow n_{18}$, $n_{E,C2} \leftrightarrow n_{19}$, $n_{E,A} \leftrightarrow n_{20}$
720	$n_{AB} \leftrightarrow n_{21}$, $n_{AC} \leftrightarrow n_{22}$, $n_{AB,2} \leftrightarrow n_{23}$, $n_{AC,2} \leftrightarrow n_{24}$ $n_{E,C} \leftrightarrow n_{25}$, $n_{E,A} \leftrightarrow n_{26}$
855	$n_{AA} \leftrightarrow n_{30}$, $n_{AB} \leftrightarrow n_{27}$, $n_{AC} \leftrightarrow n_{28}$ $n_{E,C} \leftrightarrow n_{29}$, $n_{E,A} \leftrightarrow n_{31}$

Table K.2: Mapping of the normalization constants of table K.1 to those found in appendix G.

K.2 Form factors

K.2.1 Form factors determined via Rosenbluth separation

The form factors have been extracted from the cross sections (with the normalizations from the spline fit) using the equation

$$\varepsilon\,(1+\tau)\left(\frac{\mathrm{d}\sigma}{\mathrm{d}\Omega}\right)_0 \Big/ \left(\frac{\mathrm{d}\sigma}{\mathrm{d}\Omega}\right)_{\mathrm{Mott}} = \left(\varepsilon G_E^2\left(Q^2\right) + \tau G_M^2\left(Q^2\right)\right). \tag{K.1}$$

The Rosenbluth-separation result is only given up to $Q^2 = 0.5524$ $(\mathrm{GeV}/c)^2$, up to where cross sections have been measured for at least three beam energies for fixed Q^2. The errors are the non-simultaneous 68.3% errors, that is, for a given Q^2, one expects the true value for one of the form factors inside the errors with 68.3% probability without any constraint on the other form factor.
The first four points are extracted with a forced G_M (set to $1 \cdot \mu_p G_{\text{std. dip.}}$ and $1.05 \cdot \mu_p G_{\text{std. dip.}}$ for each Q^2 value). The second group lists the results for the same points with G_M as a free parameter.

Q^2 $[(\mathrm{GeV}/c)^2]$	G_E	G_M
0.0152	$(0.9511 - 0.9530) \pm 0.0006$	forced to $(1,\ 1.05) \cdot \mu_p G_{\text{std. dip.}}$
0.0162	$(0.9483 - 0.9503) \pm 0.0004$	forced to $(1,\ 1.05) \cdot \mu_p G_{\text{std. dip.}}$
0.0172	$(0.9440 - 0.9462) \pm 0.0005$	forced to $(1,\ 1.05) \cdot \mu_p G_{\text{std. dip.}}$
0.0192	$(0.9400 - 0.9427) \pm 0.0005$	forced to $(1,\ 1.05) \cdot \mu_p G_{\text{std. dip.}}$
0.0152	0.9433 ± 0.0071	3.2859 ± 0.3955
0.0162	0.9430 ± 0.0042	3.1148 ± 0.2332
0.0172	0.9346 ± 0.0045	3.2880 ± 0.2134
0.0182	0.9434 ± 0.0037	2.6790 ± 0.2057
0.0192	0.9328 ± 0.0053	3.1029 ± 0.2263

Table K.3: Rosenbluth-separation data.

Q^2 $[(\mathrm{GeV}/c)^2]$	G_E	G_M
0.0202	0.9354 ± 0.0041	2.7368 ± 0.1861
0.0213	0.9375 ± 0.0046	2.4972 ± 0.2096
0.0236	0.9349 ± 0.0039	2.3928 ± 0.1712
0.0255	0.9250 ± 0.0029	2.4870 ± 0.1138
0.0272	0.9170 ± 0.0027	2.6058 ± 0.0894
0.0304	0.9119 ± 0.0030	2.4760 ± 0.0973
0.0322	0.9053 ± 0.0026	2.5483 ± 0.0768
0.0340	0.9021 ± 0.0017	2.4843 ± 0.0480
0.0357	0.8921 ± 0.0021	2.6470 ± 0.0460
0.0376	0.8921 ± 0.0024	2.5045 ± 0.0477
0.0394	0.8888 ± 0.0016	2.4698 ± 0.0386
0.0413	0.8800 ± 0.0014	2.5439 ± 0.0259
0.0433	0.8767 ± 0.0010	2.4878 ± 0.0201
0.0473	0.8657 ± 0.0010	2.4788 ± 0.0164
0.0494	0.8622 ± 0.0012	2.4500 ± 0.0174
0.0515	0.8579 ± 0.0013	2.4175 ± 0.0135
0.0537	0.8534 ± 0.0009	2.4014 ± 0.0111
0.0557	0.8474 ± 0.0013	2.3997 ± 0.0123
0.0580	0.8419 ± 0.0009	2.3938 ± 0.0121
0.0602	0.8364 ± 0.0012	2.3790 ± 0.0088
0.0625	0.8326 ± 0.0008	2.3574 ± 0.0076
0.0648	0.8274 ± 0.0007	2.3404 ± 0.0051
0.0672	0.8213 ± 0.0010	2.3275 ± 0.0082
0.0695	0.8162 ± 0.0008	2.3157 ± 0.0077
0.0711	0.8115 ± 0.0007	2.3072 ± 0.0055
0.0742	0.8033 ± 0.0007	2.3028 ± 0.0058
0.0773	0.7968 ± 0.0007	2.2861 ± 0.0040
0.0805	0.7909 ± 0.0005	2.2611 ± 0.0031
0.0837	0.7858 ± 0.0005	2.2327 ± 0.0039
0.0867	0.7794 ± 0.0038	2.2087 ± 0.0416
0.0908	0.7707 ± 0.0024	2.1924 ± 0.0257
0.0949	0.7625 ± 0.0031	2.1873 ± 0.0319
0.1033	0.7427 ± 0.0029	2.1669 ± 0.0260
0.1076	0.7379 ± 0.0026	2.1125 ± 0.0213
0.1120	0.7272 ± 0.0011	2.1069 ± 0.0087
0.1163	0.7212 ± 0.0017	2.0652 ± 0.0100
0.1255	0.7055 ± 0.0016	2.0243 ± 0.0110
0.1300	0.6990 ± 0.0013	1.9862 ± 0.0071
0.1348	0.6923 ± 0.0012	1.9522 ± 0.0062
0.1395	0.6857 ± 0.0015	1.9296 ± 0.0065
0.1441	0.6779 ± 0.0012	1.9096 ± 0.0059
0.1490	0.6676 ± 0.0009	1.8941 ± 0.0034
0.1538	0.6642 ± 0.0016	1.8522 ± 0.0081
0.1588	0.6551 ± 0.0012	1.8419 ± 0.0070
0.1637	0.6483 ± 0.0013	1.8164 ± 0.0053
0.1687	0.6362 ± 0.0013	1.8162 ± 0.0064
0.1739	0.6305 ± 0.0009	1.7866 ± 0.0028
0.1789	0.6247 ± 0.0011	1.7642 ± 0.0043
0.1840	0.6154 ± 0.0010	1.7447 ± 0.0036
0.1893	0.6111 ± 0.0018	1.7222 ± 0.0031

Table K.3: Rosenbluth-separation data.

Q^2 [(GeV/c)^2]	G_E	G_M
0.1943	0.6029 ± 0.0014	1.7027 ± 0.0035
0.1997	0.5931 ± 0.0008	1.6891 ± 0.0023
0.2051	0.5831 ± 0.0009	1.6746 ± 0.0030
0.2103	0.5785 ± 0.0010	1.6523 ± 0.0028
0.2156	0.5730 ± 0.0008	1.6293 ± 0.0026
0.2210	0.5687 ± 0.0021	1.6015 ± 0.0068
0.2318	0.5575 ± 0.0021	1.5609 ± 0.0067
0.2427	0.5370 ± 0.0019	1.5429 ± 0.0056
0.2481	0.5355 ± 0.0022	1.5166 ± 0.0059
0.2592	0.5257 ± 0.0023	1.4813 ± 0.0054
0.2758	0.5067 ± 0.0022	1.4351 ± 0.0040
0.2814	0.4998 ± 0.0026	1.4222 ± 0.0063
0.3069	0.4723 ± 0.0012	1.3619 ± 0.0024
0.3354	0.4447 ± 0.0012	1.2929 ± 0.0020
0.3638	0.4192 ± 0.0010	1.2310 ± 0.0015
0.3916	0.4031 ± 0.0019	1.1633 ± 0.0029
0.4201	0.3824 ± 0.0020	1.1105 ± 0.0027
0.4471	0.3609 ± 0.0027	1.0697 ± 0.0034
0.4748	0.3448 ± 0.0026	1.0214 ± 0.0029
0.5011	0.3301 ± 0.0018	0.9789 ± 0.0017
0.5274	0.3105 ± 0.0021	0.9428 ± 0.0018
0.5524	0.2972 ± 0.0021	0.9108 ± 0.0016

Table K.3: Rosenbluth-separation data.

K.2.2 Form factors determined via global fits of model parametrizations

The tables on the following pages list the form factors and the form factor ratio determined by the different models. The errors listed are the statistical error (as the pointwise confidence band with 68.3% confidence level), the experimental systematic and theoretical systematic errors (see section 9.1 and appendix I).

The Q^2 values are chosen equidistant in Q. This reflects the larger number of cross section measurements at low Q^2.

The description of the models can be found in chapter 7, the parameters for the best fits in appendix J.

K.2.2.1 Polynomial model

Q^2 [(GeV/c)^2]	$G_E \cdot 10^4$	$G_M/\mu_p \cdot 10^4$	$\mu_p \frac{G_E}{G_M} \cdot 10^4$
0.0005	$9984\pm 0\,^{+0\,+0}_{-0\,-0}$	$9988\pm 1\,^{+0\,+0}_{-0\,-0}$	$9996\pm 1\,^{+0\,+0}_{-0\,-0}$
0.0019	$9937\pm 1\,^{+1\,+1}_{-1\,-1}$	$9951\pm 2\,^{+1\,+1}_{-1\,-1}$	$9986\pm 2\,^{+1\,+0}_{-1\,-0}$
0.0043	$9859\pm 2\,^{+2\,+2}_{-2\,-2}$	$9890\pm 5\,^{+3\,+2}_{-2\,-2}$	$9969\pm 5\,^{+2\,+0}_{-2\,-0}$
0.0076	$9753\pm 3\,^{+3\,+4}_{-3\,-3}$	$9804\pm 8\,^{+5\,+3}_{-4\,-4}$	$9948\pm 8\,^{+3\,+0}_{-3\,-0}$
0.0118	$9621\pm 4\,^{+4\,+5}_{-4\,-5}$	$9695\pm 11\,^{+7\,+5}_{-6\,-5}$	$9923\pm 12\,^{+5\,+0}_{-5\,-0}$
0.0170	$9465\pm 5\,^{+6\,+7}_{-5\,-6}$	$9563\pm 14\,^{+9\,+7}_{-8\,-7}$	$9898\pm 16\,^{+7\,+1}_{-7\,-0}$
0.0232	$9288\pm 6\,^{+6\,+8}_{-6\,-8}$	$9407\pm 16\,^{+11\,+9}_{-10\,-9}$	$9874\pm 18\,^{+8\,+2}_{-8\,-1}$
0.0302	$9093\pm 6\,^{+7\,+9}_{-7\,-9}$	$9230\pm 17\,^{+14+11}_{-12-11}$	$9852\pm 20\,^{+10\,+3}_{-10\,-1}$
0.0383	$8883\pm 6\,^{+7\,+10}_{-7\,-10}$	$9033\pm 17\,^{+15+13}_{-14-13}$	$9834\pm 21\,^{+12\,+4}_{-12\,-2}$
0.0473	$8659\pm 6\,^{+7\,+11}_{-7\,-10}$	$8817\pm 16\,^{+17+14}_{-16-14}$	$9821\pm 21\,^{+13\,+4}_{-13\,-4}$
0.0572	$8425\pm 6\,^{+7\,+11}_{-7\,-11}$	$8584\pm 14\,^{+18+16}_{-17-16}$	$9814\pm 19\,^{+14\,+5}_{-14\,-5}$
0.0681	$8181\pm 6\,^{+6\,+11}_{-6\,-11}$	$8337\pm 12\,^{+19+17}_{-18-16}$	$9812\pm 18\,^{+15\,+6}_{-15\,-6}$
0.0799	$7929\pm 6\,^{+6\,+11}_{-6\,-11}$	$8079\pm 11\,^{+19+17}_{-18-17}$	$9815\pm 17\,^{+16\,+7}_{-16\,-7}$
0.0926	$7672\pm 6\,^{+5\,+11}_{-5\,-11}$	$7812\pm 11\,^{+19+18}_{-19-17}$	$9821\pm 17\,^{+17\,+8}_{-17\,-8}$
0.1063	$7410\pm 6\,^{+5\,+11}_{-5\,-11}$	$7538\pm 11\,^{+19+18}_{-18-17}$	$9830\pm 18\,^{+18\,+8}_{-18\,-9}$
0.1210	$7145\pm 6\,^{+5\,+11}_{-5\,-11}$	$7262\pm 11\,^{+18+18}_{-18-17}$	$9838\pm 19\,^{+19\,+8}_{-19\,-9}$
0.1366	$6877\pm 7\,^{+5\,+11}_{-5\,-11}$	$6986\pm 11\,^{+18+17}_{-18-16}$	$9845\pm 20\,^{+19\,+7}_{-19\,-8}$
0.1531	$6610\pm 7\,^{+5\,+11}_{-5\,-11}$	$6712\pm 10\,^{+17+17}_{-17-16}$	$9848\pm 21\,^{+20\,+7}_{-20\,-8}$
0.1706	$6343\pm 7\,^{+5\,+11}_{-5\,-11}$	$6442\pm 9\,^{+17+16}_{-16-15}$	$9846\pm 20\,^{+20\,+7}_{-21\,-7}$
0.1890	$6078\pm 7\,^{+5\,+11}_{-5\,-11}$	$6178\pm 8\,^{+16+15}_{-16-15}$	$9837\pm 18\,^{+21\,+6}_{-21\,-7}$
0.2084	$5816\pm 7\,^{+4\,+11}_{-4\,-11}$	$5922\pm 7\,^{+15+15}_{-15-15}$	$9821\pm 17\,^{+21\,+6}_{-21\,-7}$
0.2287	$5559\pm 7\,^{+3\,+10}_{-3\,-10}$	$5673\pm 6\,^{+15+15}_{-15-14}$	$9798\pm 18\,^{+22\,+7}_{-22\,-7}$
0.2500	$5306\pm 7\,^{+2\,+10}_{-2\,-10}$	$5433\pm 6\,^{+14+14}_{-14-14}$	$9766\pm 20\,^{+23\,+7}_{-23\,-7}$
0.2722	$5060\pm 8\,^{+2\,+10}_{-2\,-9}$	$5201\pm 6\,^{+14+14}_{-14-14}$	$9729\pm 23\,^{+24\,+8}_{-25\,-8}$
0.2954	$4820\pm 8\,^{+2\,+9}_{-2\,-9}$	$4977\pm 6\,^{+14+14}_{-13-13}$	$9686\pm 25\,^{+26\,+8}_{-27\,-9}$
0.3195	$4588\pm 9\,^{+3\,+9}_{-3\,-8}$	$4760\pm 6\,^{+13+13}_{-13-13}$	$9640\pm 26\,^{+29\,+9}_{-29\,-9}$
0.3445	$4365\pm 9\,^{+3\,+8}_{-3\,-8}$	$4550\pm 5\,^{+13+13}_{-12-13}$	$9593\pm 27\,^{+31\,+9}_{-31\,-9}$
0.3705	$4150\pm 10\,^{+4\,+8}_{-4\,-8}$	$4347\pm 5\,^{+12+13}_{-12-12}$	$9548\pm 29\,^{+32\,+8}_{-33\,-9}$
0.3974	$3945\pm 11\,^{+4\,+8}_{-4\,-8}$	$4150\pm 5\,^{+11+12}_{-11-12}$	$9505\pm 32\,^{+33\,+8}_{-33\,-8}$
0.4253	$3749\pm 12\,^{+5\,+8}_{-5\,-8}$	$3961\pm 5\,^{+11+11}_{-11-11}$	$9465\pm 38\,^{+34\,+7}_{-35\,-7}$
0.4542	$3562\pm 13\,^{+6\,+8}_{-6\,-8}$	$3779\pm 5\,^{+10+11}_{-10-11}$	$9426\pm 44\,^{+37\,+7}_{-37\,-6}$
0.4839	$3381\pm 14\,^{+7\,+7}_{-7\,-7}$	$3604\pm 5\,^{+10+11}_{-10-11}$	$9383\pm 49\,^{+41\,+8}_{-41\,-7}$
0.5147	$3207\pm 15\,^{+9\,+7}_{-9\,-6}$	$3436\pm 5\,^{+10+10}_{-10-10}$	$9332\pm 55\,^{+47\,+10}_{-47\,-9}$
0.5463	$3036\pm 18\,^{+11\,+6}_{-11\,-5}$	$3276\pm 5\,^{+10+10}_{-10-10}$	$9265\pm 65\,^{+55\,+13}_{-56\,-12}$
0.5789	$2867\pm 23\,^{+13\,+5}_{-13\,-4}$	$3123\pm 5\,^{+10+10}_{-10-10}$	$9178\pm 84\,^{+67\,+15}_{-68\,-15}$
0.6125	$2701\pm 28\,^{+17\,+4}_{-17\,-4}$	$2977\pm 5\,^{+10+10}_{-10-10}$	$9071\pm 107\,^{+83\,+17}_{-84\,-18}$
0.6470	$2540\pm 32\,^{+21\,+3}_{-21\,-4}$	$2838\pm 5\,^{+11+10}_{-10-9}$	$8949\pm 126\,^{+105\,+16}_{-107\,-18}$
0.6824	$2384\pm 33\,^{+28\,+3}_{-29\,-4}$	$2705\pm 4\,^{+11\,+9}_{-11\,-9}$	$8814\pm 133\,^{+139\,+14}_{-141\,-17}$
0.7188	$2233\pm 32\,^{+35\,+3}_{-36\,-4}$	$2580\pm 4\,^{+11\,+9}_{-11\,-8}$	$8656\pm 133\,^{+172\,+14}_{-175\,-16}$
0.7561	$2076\pm 33\,^{+41\,+2}_{-43\,-2}$	$2463\pm 3\,^{+11\,+8}_{-11\,-8}$	$8427\pm 143\,^{+203\,+21}_{-209\,-20}$
0.7944	$1890\pm 83\,^{+50\,+3}_{-52\,-3}$	$2356\pm 9\,^{+11\,+9}_{-11\,-8}$	$8023\pm 381\,^{+248\,+43}_{-256\,-44}$
0.8336	$1650\pm 246\,^{+59\,+13}_{-63\,-17}$	$2257\pm 23\,^{+11\,+9}_{-11\,-9}$	$7313\pm 1189\,^{+295\,+87}_{-310\,-106}$
0.8738	$1369\pm 577\,^{+72\,+31}_{-78\,-47}$	$2161\pm 45\,^{+10+10}_{-10-9}$	$6338\pm 2926\,^{+361\,+171}_{-389\,-244}$
0.9149	$1216\pm 1126\,^{+107+70}_{-120-105}$	$2058\pm 71\,^{+11+10}_{-11-9}$	$5909\pm 6071\,^{+552\,+364}_{-609\,-530}$
0.9570	$1789\pm 2082\,^{+228+169}_{-253-213}$	$1934\pm 109\,^{+15+13}_{-16-12}$	$9249\pm 12500\,^{+1255+925}_{-1364-1138}$
1.0000	$4689\pm 4328\,^{+559+422}_{-605-400}$	$1786\pm 264\,^{+33+27}_{-34-28}$	$26254\pm 28709756\,^{+3593+2788}_{-3726-2563}$

Table K.4: Form factor data determined with the polynomial model.

K.2.2.2 Polynomial + dipole model

Q^2 [(GeV/c)^2]	$G_E \cdot 10^4$	$G_M/\mu_p \cdot 10^4$	$\mu_p \frac{G_E}{G_M} \cdot 10^4$
0.0005	$9984 \pm 0^{+0}_{-0}{}^{+0}_{-0}$	$9988 \pm 0^{+0}_{-0}{}^{+0}_{-0}$	$9996 \pm 0^{+0}_{-0}{}^{+0}_{-0}$
0.0019	$9937 \pm 1^{+1}_{-1}{}^{+1}_{-1}$	$9951 \pm 1^{+1}_{-1}{}^{+1}_{-1}$	$9986 \pm 2^{+1}_{-1}{}^{+0}_{-0}$
0.0043	$9859 \pm 2^{+2}_{-2}{}^{+2}_{-2}$	$9890 \pm 3^{+3}_{-2}{}^{+2}_{-2}$	$9969 \pm 4^{+2}_{-2}{}^{+0}_{-0}$
0.0076	$9754 \pm 3^{+3}_{-3}{}^{+3}_{-3}$	$9805 \pm 5^{+5}_{-4}{}^{+4}_{-4}$	$9948 \pm 6^{+3}_{-3}{}^{+0}_{-0}$
0.0118	$9621 \pm 4^{+4}_{-4}{}^{+5}_{-5}$	$9695 \pm 7^{+7}_{-6}{}^{+6}_{-5}$	$9924 \pm 8^{+5}_{-5}{}^{+1}_{-1}$
0.0170	$9466 \pm 5^{+5}_{-5}{}^{+6}_{-6}$	$9563 \pm 10^{+9}_{-8}{}^{+8}_{-7}$	$9898 \pm 11^{+7}_{-7}{}^{+1}_{-1}$
0.0232	$9289 \pm 5^{+6}_{-6}{}^{+8}_{-7}$	$9408 \pm 11^{+11}_{-10}{}^{+10}_{-9}$	$9874 \pm 13^{+9}_{-9}{}^{+2}_{-2}$
0.0302	$9094 \pm 6^{+7}_{-7}{}^{+9}_{-9}$	$9231 \pm 13^{+13}_{-12}{}^{+12}_{-11}$	$9852 \pm 15^{+10}_{-10}{}^{+2}_{-3}$
0.0383	$8883 \pm 6^{+7}_{-7}{}^{+10}_{-10}$	$9034 \pm 13^{+15}_{-14}{}^{+13}_{-13}$	$9834 \pm 16^{+12}_{-12}{}^{+3}_{-4}$
0.0473	$8660 \pm 6^{+7}_{-7}{}^{+10}_{-10}$	$8818 \pm 13^{+17}_{-16}{}^{+15}_{-14}$	$9821 \pm 17^{+13}_{-13}{}^{+4}_{-5}$
0.0572	$8425 \pm 6^{+7}_{-7}{}^{+11}_{-11}$	$8585 \pm 13^{+18}_{-17}{}^{+16}_{-15}$	$9814 \pm 17^{+14}_{-14}{}^{+5}_{-6}$
0.0681	$8181 \pm 6^{+6}_{-6}{}^{+11}_{-11}$	$8338 \pm 12^{+19}_{-18}{}^{+17}_{-16}$	$9812 \pm 17^{+15}_{-15}{}^{+6}_{-7}$
0.0799	$7930 \pm 6^{+6}_{-6}{}^{+11}_{-11}$	$8080 \pm 11^{+19}_{-18}{}^{+17}_{-17}$	$9815 \pm 17^{+16}_{-16}{}^{+7}_{-7}$
0.0926	$7672 \pm 6^{+5}_{-5}{}^{+11}_{-11}$	$7812 \pm 11^{+19}_{-18}{}^{+17}_{-17}$	$9821 \pm 17^{+17}_{-17}{}^{+7}_{-8}$
0.1063	$7410 \pm 6^{+5}_{-5}{}^{+11}_{-11}$	$7539 \pm 10^{+19}_{-18}{}^{+17}_{-17}$	$9829 \pm 17^{+18}_{-18}{}^{+8}_{-8}$
0.1210	$7145 \pm 6^{+5}_{-5}{}^{+11}_{-11}$	$7263 \pm 10^{+18}_{-18}{}^{+17}_{-17}$	$9838 \pm 18^{+19}_{-19}{}^{+8}_{-8}$
0.1366	$6878 \pm 6^{+5}_{-5}{}^{+11}_{-11}$	$6986 \pm 10^{+18}_{-18}{}^{+17}_{-16}$	$9845 \pm 18^{+19}_{-19}{}^{+8}_{-8}$
0.1531	$6610 \pm 7^{+5}_{-5}{}^{+11}_{-11}$	$6712 \pm 9^{+17}_{-17}{}^{+16}_{-16}$	$9848 \pm 19^{+20}_{-20}{}^{+7}_{-7}$
0.1706	$6343 \pm 7^{+5}_{-5}{}^{+11}_{-11}$	$6442 \pm 8^{+17}_{-16}{}^{+16}_{-15}$	$9846 \pm 18^{+21}_{-21}{}^{+7}_{-7}$
0.1890	$6078 \pm 7^{+5}_{-5}{}^{+11}_{-11}$	$6179 \pm 7^{+16}_{-16}{}^{+15}_{-15}$	$9837 \pm 18^{+21}_{-21}{}^{+6}_{-6}$
0.2084	$5816 \pm 7^{+4}_{-4}{}^{+11}_{-11}$	$5922 \pm 6^{+15}_{-15}{}^{+15}_{-15}$	$9821 \pm 17^{+21}_{-22}{}^{+6}_{-6}$
0.2287	$5559 \pm 7^{+3}_{-3}{}^{+10}_{-10}$	$5674 \pm 6^{+15}_{-14}{}^{+15}_{-14}$	$9797 \pm 18^{+22}_{-22}{}^{+6}_{-7}$
0.2500	$5306 \pm 7^{+2}_{-2}{}^{+10}_{-10}$	$5434 \pm 6^{+14}_{-14}{}^{+14}_{-14}$	$9766 \pm 20^{+22}_{-23}{}^{+7}_{-7}$
0.2722	$5060 \pm 8^{+2}_{-2}{}^{+9}_{-9}$	$5201 \pm 6^{+14}_{-14}{}^{+14}_{-14}$	$9728 \pm 22^{+24}_{-24}{}^{+7}_{-8}$
0.2954	$4820 \pm 8^{+2}_{-2}{}^{+9}_{-9}$	$4977 \pm 6^{+13}_{-13}{}^{+14}_{-13}$	$9685 \pm 24^{+26}_{-27}{}^{+8}_{-9}$
0.3195	$4589 \pm 9^{+3}_{-3}{}^{+9}_{-9}$	$4760 \pm 6^{+13}_{-13}{}^{+13}_{-13}$	$9640 \pm 26^{+29}_{-29}{}^{+8}_{-9}$
0.3445	$4365 \pm 9^{+3}_{-3}{}^{+8}_{-8}$	$4550 \pm 5^{+13}_{-12}{}^{+13}_{-13}$	$9594 \pm 27^{+31}_{-31}{}^{+9}_{-9}$
0.3705	$4151 \pm 10^{+4}_{-4}{}^{+8}_{-8}$	$4347 \pm 5^{+12}_{-12}{}^{+12}_{-12}$	$9549 \pm 29^{+33}_{-33}{}^{+8}_{-9}$
0.3974	$3946 \pm 11^{+4}_{-4}{}^{+8}_{-8}$	$4150 \pm 5^{+11}_{-11}{}^{+12}_{-12}$	$9506 \pm 33^{+34}_{-34}{}^{+8}_{-8}$
0.4253	$3750 \pm 12^{+5}_{-5}{}^{+8}_{-8}$	$3961 \pm 5^{+11}_{-11}{}^{+11}_{-11}$	$9467 \pm 38^{+35}_{-35}{}^{+8}_{-7}$
0.4542	$3562 \pm 13^{+6}_{-6}{}^{+8}_{-7}$	$3779 \pm 5^{+10}_{-10}{}^{+11}_{-11}$	$9427 \pm 44^{+37}_{-37}{}^{+8}_{-7}$
0.4839	$3382 \pm 14^{+7}_{-7}{}^{+7}_{-7}$	$3604 \pm 5^{+10}_{-10}{}^{+11}_{-11}$	$9384 \pm 49^{+41}_{-41}{}^{+9}_{-8}$
0.5147	$3207 \pm 15^{+8}_{-9}{}^{+6}_{-6}$	$3436 \pm 5^{+10}_{-10}{}^{+10}_{-10}$	$9331 \pm 54^{+46}_{-47}{}^{+10}_{-10}$
0.5463	$3035 \pm 18^{+10}_{-11}{}^{+5}_{-5}$	$3276 \pm 5^{+10}_{-9}{}^{+10}_{-10}$	$9263 \pm 65^{+55}_{-55}{}^{+12}_{-12}$
0.5789	$2866 \pm 23^{+13}_{-13}{}^{+5}_{-5}$	$3124 \pm 5^{+10}_{-10}{}^{+10}_{-10}$	$9176 \pm 85^{+67}_{-68}{}^{+14}_{-15}$
0.6125	$2701 \pm 28^{+17}_{-17}{}^{+4}_{-4}$	$2978 \pm 5^{+10}_{-10}{}^{+10}_{-10}$	$9070 \pm 108^{+83}_{-84}{}^{+15}_{-17}$
0.6470	$2540 \pm 31^{+21}_{-22}{}^{+4}_{-4}$	$2838 \pm 5^{+11}_{-10}{}^{+9}_{-9}$	$8949 \pm 124^{+105}_{-106}{}^{+15}_{-17}$
0.6824	$2385 \pm 32^{+28}_{-29}{}^{+4}_{-4}$	$2705 \pm 4^{+11}_{-11}{}^{+9}_{-9}$	$8815 \pm 131^{+139}_{-140}{}^{+14}_{-16}$
0.7188	$2234 \pm 32^{+35}_{-36}{}^{+4}_{-4}$	$2580 \pm 4^{+11}_{-11}{}^{+9}_{-8}$	$8657 \pm 134^{+172}_{-175}{}^{+14}_{-15}$
0.7561	$2075 \pm 34^{+41}_{-43}{}^{+2}_{-2}$	$2464 \pm 3^{+11}_{-11}{}^{+8}_{-8}$	$8423 \pm 144^{+203}_{-209}{}^{+21}_{-20}$
0.7944	$1887 \pm 92^{+50}_{-53}{}^{+2}_{-3}$	$2356 \pm 10^{+11}_{-11}{}^{+9}_{-8}$	$8006 \pm 424^{+247}_{-259}{}^{+37}_{-40}$
0.8336	$1641 \pm 278^{+61}_{-66}{}^{+9}_{-13}$	$2258 \pm 26^{+10}_{-10}{}^{+9}_{-9}$	$7269 \pm 1345^{+301}_{-323}{}^{+69}_{-86}$
0.8738	$1347 \pm 651^{+76}_{-85}{}^{+22}_{-34}$	$2162 \pm 53^{+10}_{-10}{}^{+9}_{-9}$	$6229 \pm 3330^{+377}_{-420}{}^{+126}_{-182}$
0.9149	$1157 \pm 1285^{+101}_{-122}{}^{+49}_{-76}$	$2060 \pm 87^{+10}_{-10}{}^{+9}_{-9}$	$5614 \pm 7104^{+515}_{-618}{}^{+261}_{-390}$
0.9570	$1628 \pm 2400^{+178}_{-234}{}^{+123}_{-164}$	$1940 \pm 143^{+14}_{-13}{}^{+12}_{-11}$	$8389 \pm 16700^{+974}_{-1254}{}^{+682}_{-885}$
1.0000	$4257 \pm 4794^{+420}_{-551}{}^{+323}_{-344}$	$1806 \pm 338^{+29}_{-26}{}^{+24}_{-23}$	$23573 \pm 1278287^{+2650}_{-3337}{}^{+2158}_{-2228}$

Table K.5: Form factor data determined with the polynomial + dipole model.

K.2.2.3 Polynomial × dipole model

Q^2 [(GeV/c)^2]	$G_E \cdot 10^4$	$G_M/\mu_p \cdot 10^4$	$\mu_p \frac{G_E}{G_M} \cdot 10^4$
0.0005	$9984\pm 0\,^{+0}_{-0}\,^{+0}_{-0}$	$9988\pm 0\,^{+0}_{-0}\,^{+0}_{-0}$	$9997\pm 0\,^{+0}_{-0}\,^{+0}_{-0}$
0.0019	$9938\pm 1\,^{+1}_{-1}\,^{+1}_{-1}$	$9951\pm 2\,^{+1}_{-1}\,^{+1}_{-1}$	$9986\pm 2\,^{+1}_{-1}\,^{+0}_{-0}$
0.0043	$9861\pm 1\,^{+1}_{-1}\,^{+2}_{-2}$	$9891\pm 4\,^{+2}_{-3}\,^{+3}_{-3}$	$9970\pm 4\,^{+3}_{-2}\,^{+1}_{-1}$
0.0076	$9756\pm 2\,^{+2}_{-2}\,^{+3}_{-3}$	$9806\pm 6\,^{+4}_{-5}\,^{+4}_{-4}$	$9949\pm 6\,^{+4}_{-4}\,^{+1}_{-1}$
0.0118	$9625\pm 3\,^{+3}_{-3}\,^{+4}_{-4}$	$9697\pm 8\,^{+6}_{-7}\,^{+6}_{-6}$	$9926\pm 9\,^{+6}_{-5}\,^{+2}_{-2}$
0.0170	$9470\pm 4\,^{+4}_{-4}\,^{+6}_{-6}$	$9565\pm 11\,^{+8}_{-9}\,^{+8}_{-8}$	$9901\pm 12\,^{+8}_{-7}\,^{+3}_{-3}$
0.0232	$9294\pm 4\,^{+5}_{-5}\,^{+7}_{-7}$	$9411\pm 13\,^{+10}_{-12}\,^{+11}_{-10}$	$9876\pm 14\,^{+10}_{-8}\,^{+3}_{-4}$
0.0302	$9099\pm 5\,^{+5}_{-6}\,^{+8}_{-8}$	$9234\pm 14\,^{+12}_{-14}\,^{+12}_{-12}$	$9854\pm 16\,^{+12}_{-9}\,^{+4}_{-4}$
0.0383	$8888\pm 5\,^{+6}_{-6}\,^{+9}_{-9}$	$9037\pm 14\,^{+14}_{-15}\,^{+14}_{-14}$	$9835\pm 18\,^{+13}_{-10}\,^{+5}_{-5}$
0.0473	$8664\pm 5\,^{+6}_{-6}\,^{+10}_{-10}$	$8821\pm 14\,^{+15}_{-16}\,^{+15}_{-15}$	$9822\pm 18\,^{+14}_{-11}\,^{+6}_{-6}$
0.0572	$8428\pm 6\,^{+6}_{-6}\,^{+10}_{-10}$	$8589\pm 13\,^{+16}_{-17}\,^{+16}_{-16}$	$9813\pm 18\,^{+15}_{-12}\,^{+6}_{-6}$
0.0681	$8184\pm 6\,^{+6}_{-6}\,^{+11}_{-11}$	$8342\pm 12\,^{+17}_{-18}\,^{+17}_{-16}$	$9810\pm 17\,^{+15}_{-13}\,^{+7}_{-7}$
0.0799	$7932\pm 6\,^{+6}_{-5}\,^{+11}_{-11}$	$8084\pm 11\,^{+18}_{-18}\,^{+17}_{-17}$	$9811\pm 17\,^{+16}_{-15}\,^{+7}_{-7}$
0.0926	$7674\pm 6\,^{+5}_{-5}\,^{+11}_{-11}$	$7817\pm 10\,^{+18}_{-18}\,^{+17}_{-17}$	$9816\pm 16\,^{+17}_{-16}\,^{+7}_{-7}$
0.1063	$7412\pm 6\,^{+5}_{-5}\,^{+11}_{-11}$	$7545\pm 9\,^{+18}_{-18}\,^{+16}_{-16}$	$9824\pm 17\,^{+19}_{-17}\,^{+7}_{-7}$
0.1210	$7146\pm 6\,^{+5}_{-4}\,^{+11}_{-11}$	$7269\pm 9\,^{+18}_{-18}\,^{+16}_{-16}$	$9831\pm 17\,^{+21}_{-18}\,^{+7}_{-7}$
0.1366	$6879\pm 6\,^{+5}_{-4}\,^{+11}_{-11}$	$6993\pm 9\,^{+17}_{-18}\,^{+16}_{-15}$	$9838\pm 18\,^{+23}_{-19}\,^{+6}_{-6}$
0.1531	$6612\pm 7\,^{+6}_{-4}\,^{+11}_{-11}$	$6718\pm 8\,^{+17}_{-17}\,^{+15}_{-15}$	$9841\pm 18\,^{+24}_{-20}\,^{+6}_{-6}$
0.1706	$6345\pm 7\,^{+5}_{-4}\,^{+11}_{-11}$	$6448\pm 8\,^{+16}_{-17}\,^{+15}_{-15}$	$9840\pm 18\,^{+24}_{-21}\,^{+6}_{-6}$
0.1890	$6079\pm 7\,^{+5}_{-4}\,^{+11}_{-11}$	$6183\pm 7\,^{+15}_{-16}\,^{+15}_{-14}$	$9832\pm 18\,^{+23}_{-21}\,^{+6}_{-6}$
0.2084	$5818\pm 7\,^{+4}_{-3}\,^{+11}_{-11}$	$5926\pm 6\,^{+15}_{-15}\,^{+14}_{-14}$	$9818\pm 17\,^{+23}_{-21}\,^{+6}_{-6}$
0.2287	$5560\pm 7\,^{+3}_{-3}\,^{+10}_{-10}$	$5676\pm 6\,^{+14}_{-14}\,^{+14}_{-14}$	$9796\pm 18\,^{+22}_{-21}\,^{+6}_{-6}$
0.2500	$5308\pm 7\,^{+2}_{-2}\,^{+10}_{-10}$	$5434\pm 6\,^{+14}_{-14}\,^{+14}_{-14}$	$9768\pm 19\,^{+22}_{-22}\,^{+7}_{-7}$
0.2722	$5062\pm 7\,^{+1}_{-1}\,^{+9}_{-9}$	$5201\pm 6\,^{+13}_{-13}\,^{+14}_{-14}$	$9733\pm 21\,^{+23}_{-23}\,^{+8}_{-8}$
0.2954	$4823\pm 8\,^{+1}_{-0}\,^{+9}_{-9}$	$4976\pm 6\,^{+13}_{-13}\,^{+14}_{-13}$	$9694\pm 23\,^{+25}_{-25}\,^{+9}_{-9}$
0.3195	$4592\pm 8\,^{+2}_{-1}\,^{+8}_{-8}$	$4759\pm 5\,^{+13}_{-13}\,^{+13}_{-13}$	$9651\pm 25\,^{+28}_{-27}\,^{+9}_{-10}$
0.3445	$4370\pm 9\,^{+3}_{-2}\,^{+8}_{-8}$	$4549\pm 5\,^{+12}_{-12}\,^{+13}_{-13}$	$9605\pm 26\,^{+30}_{-29}\,^{+10}_{-10}$
0.3705	$4155\pm 9\,^{+3}_{-2}\,^{+8}_{-8}$	$4347\pm 5\,^{+12}_{-12}\,^{+12}_{-12}$	$9558\pm 28\,^{+32}_{-31}\,^{+10}_{-10}$
0.3974	$3949\pm 10\,^{+4}_{-3}\,^{+7}_{-7}$	$4152\pm 5\,^{+11}_{-11}\,^{+12}_{-12}$	$9511\pm 31\,^{+34}_{-34}\,^{+9}_{-9}$
0.4253	$3751\pm 11\,^{+5}_{-4}\,^{+7}_{-7}$	$3964\pm 5\,^{+11}_{-11}\,^{+11}_{-11}$	$9463\pm 35\,^{+37}_{-36}\,^{+8}_{-8}$
0.4542	$3561\pm 12\,^{+6}_{-4}\,^{+7}_{-7}$	$3782\pm 5\,^{+10}_{-10}\,^{+11}_{-11}$	$9414\pm 40\,^{+40}_{-37}\,^{+7}_{-8}$
0.4839	$3378\pm 13\,^{+7}_{-5}\,^{+7}_{-7}$	$3607\pm 5\,^{+10}_{-10}\,^{+11}_{-10}$	$9363\pm 45\,^{+42}_{-39}\,^{+7}_{-7}$
0.5147	$3201\pm 15\,^{+7}_{-5}\,^{+7}_{-7}$	$3439\pm 5\,^{+10}_{-10}\,^{+10}_{-10}$	$9308\pm 52\,^{+43}_{-41}\,^{+8}_{-8}$
0.5463	$3030\pm 17\,^{+7}_{-6}\,^{+6}_{-6}$	$3278\pm 5\,^{+9}_{-9}\,^{+10}_{-10}$	$9245\pm 62\,^{+46}_{-45}\,^{+9}_{-9}$
0.5789	$2864\pm 21\,^{+9}_{-8}\,^{+5}_{-5}$	$3124\pm 5\,^{+9}_{-9}\,^{+10}_{-10}$	$9169\pm 78\,^{+55}_{-51}\,^{+13}_{-13}$
0.6125	$2702\pm 26\,^{+13}_{-11}\,^{+4}_{-4}$	$2977\pm 5\,^{+10}_{-10}\,^{+10}_{-10}$	$9076\pm 98\,^{+72}_{-65}\,^{+17}_{-16}$
0.6470	$2543\pm 30\,^{+19}_{-16}\,^{+3}_{-3}$	$2838\pm 5\,^{+10}_{-10}\,^{+9}_{-9}$	$8958\pm 117\,^{+97}_{-88}\,^{+21}_{-20}$
0.6824	$2385\pm 32\,^{+26}_{-23}\,^{+2}_{-2}$	$2707\pm 4\,^{+11}_{-11}\,^{+9}_{-9}$	$8810\pm 129\,^{+128}_{-118}\,^{+22}_{-21}$
0.7188	$2228\pm 31\,^{+33}_{-30}\,^{+3}_{-2}$	$2582\pm 4\,^{+11}_{-11}\,^{+9}_{-9}$	$8627\pm 131\,^{+163}_{-154}\,^{+19}_{-19}$
0.7561	$2072\pm 32\,^{+39}_{-38}\,^{+4}_{-4}$	$2464\pm 3\,^{+11}_{-11}\,^{+8}_{-8}$	$8407\pm 137\,^{+195}_{-191}\,^{+12}_{-13}$
0.7944	$1920\pm 56\,^{+43}_{-44}\,^{+4}_{-4}$	$2352\pm 6\,^{+11}_{-10}\,^{+8}_{-8}$	$8164\pm 254\,^{+217}_{-222}\,^{+8}_{-10}$
0.8336	$1779\pm 142\,^{+40}_{-45}\,^{+0}_{-1}$	$2244\pm 13\,^{+10}_{-10}\,^{+8}_{-8}$	$7929\pm 679\,^{+214}_{-231}\,^{+25}_{-28}$
0.8738	$1665\pm 344\,^{+27}_{-37}\,^{+16}_{-17}$	$2140\pm 25\,^{+8}_{-8}\,^{+9}_{-9}$	$7780\pm 1710\,^{+157}_{-193}\,^{+107}_{-109}$
0.9149	$1605\pm 759\,^{+8}_{-54}\,^{+61}_{-61}$	$2040\pm 42\,^{+7}_{-6}\,^{+10}_{-10}$	$7866\pm 3950\,^{+14}_{-253}\,^{+341}_{-337}$
0.9570	$1643\pm 1546\,^{+88}_{-159}\,^{+162}_{-160}$	$1942\pm 66\,^{+5}_{-5}\,^{+12}_{-13}$	$8462\pm 8594\,^{+437}_{-803}\,^{+892}_{-870}$
1.0000	$1856\pm 2852\,^{+229}_{-365}\,^{+348}_{-343}$	$1846\pm 95\,^{+4}_{-4}\,^{+13}_{-15}$	$10051\pm 17537\,^{+1219}_{-1957}\,^{+1978}_{-1911}$

Table K.6: Form factor data determined with the polynomial × dipole model.

K.2.2.4 Inverse polynomial model

Q^2 $[(\mathrm{GeV}/c)^2]$	$G_E \cdot 10^4$	$G_M/\mu_p \cdot 10^4$	$\mu_p \frac{G_E}{G_M} \cdot 10^4$
0.0005	$9984\pm 0\,^{+0\ +0}_{-0\ -0}$	$9988\pm 0\,^{+0\ +0}_{-0\ -0}$	$9996\pm 0\,^{+0\ +0}_{-0\ -0}$
0.0019	$9937\pm 1\,^{+1\ +1}_{-1\ -1}$	$9952\pm 2\,^{+2\ +1}_{-2\ -1}$	$9985\pm 1\,^{+1\ +0}_{-1\ -0}$
0.0043	$9860\pm 1\,^{+1\ +2}_{-2\ -2}$	$9892\pm 3\,^{+3\ +2}_{-4\ -2}$	$9967\pm 3\,^{+3\ +0}_{-3\ -0}$
0.0076	$9754\pm 2\,^{+2\ +3}_{-3\ -3}$	$9809\pm 5\,^{+5\ +4}_{-6\ -4}$	$9944\pm 5\,^{+5\ +1}_{-5\ -1}$
0.0118	$9621\pm 3\,^{+3\ +5}_{-4\ -5}$	$9701\pm 8\,^{+8\ +6}_{-9\ -6}$	$9918\pm 8\,^{+7\ +1}_{-7\ -1}$
0.0170	$9466\pm 4\,^{+4\ +6}_{-5\ -6}$	$9569\pm 10^{+10\ +8}_{-11\ -8}$	$9892\pm 10\,^{+10\ +2}_{-9\ -2}$
0.0232	$9289\pm 5\,^{+5\ +7}_{-6\ -7}$	$9414\pm 12^{+13+10}_{-14-10}$	$9867\pm 13\,^{+12\ +3}_{-10\ -3}$
0.0302	$9094\pm 5\,^{+5\ +9}_{-7\ -8}$	$9237\pm 13^{+15+12}_{-16-12}$	$9845\pm 15\,^{+14\ +4}_{-12\ -4}$
0.0383	$8883\pm 5\,^{+6\ +9}_{-7\ -9}$	$9039\pm 14^{+16+14}_{-17-14}$	$9828\pm 16\,^{+15\ +4}_{-13\ -4}$
0.0473	$8659\pm 5\,^{+6\ +10}_{-7\ -10}$	$8822\pm 13^{+17+15}_{-18-15}$	$9816\pm 17\,^{+16\ +5}_{-14\ -5}$
0.0572	$8425\pm 6\,^{+6\ +11}_{-6\ -10}$	$8588\pm 13^{+18+16}_{-19-16}$	$9810\pm 17\,^{+16\ +6}_{-14\ -6}$
0.0681	$8181\pm 6\,^{+6\ +11}_{-6\ -11}$	$8339\pm 12^{+18+17}_{-19-16}$	$9810\pm 17\,^{+17\ +6}_{-15\ -7}$
0.0799	$7929\pm 6\,^{+5\ +11}_{-6\ -11}$	$8079\pm 11^{+18+17}_{-19-17}$	$9814\pm 17\,^{+17\ +7}_{-15\ -7}$
0.0926	$7672\pm 6\,^{+5\ +11}_{-5\ -11}$	$7811\pm 9\,^{+17+17}_{-19-17}$	$9822\pm 16\,^{+18\ +7}_{-15\ -7}$
0.1063	$7410\pm 6\,^{+5\ +11}_{-5\ -11}$	$7538\pm 9\,^{+17+17}_{-19-17}$	$9831\pm 16\,^{+19\ +7}_{-16\ -7}$
0.1210	$7145\pm 6\,^{+5\ +11}_{-5\ -11}$	$7262\pm 8\,^{+16+16}_{-19-16}$	$9839\pm 16\,^{+21\ +7}_{-16\ -7}$
0.1366	$6878\pm 6\,^{+5\ +11}_{-5\ -11}$	$6986\pm 8\,^{+16+16}_{-18-16}$	$9846\pm 16\,^{+22\ +7}_{-17\ -7}$
0.1531	$6610\pm 6\,^{+5\ +11}_{-5\ -11}$	$6712\pm 7\,^{+15+16}_{-17-16}$	$9848\pm 17\,^{+22\ +7}_{-17\ -7}$
0.1706	$6343\pm 7\,^{+5\ +11}_{-5\ -11}$	$6443\pm 7\,^{+15+15}_{-17-15}$	$9845\pm 17\,^{+23\ +6}_{-18\ -6}$
0.1890	$6078\pm 7\,^{+5\ +11}_{-4\ -11}$	$6180\pm 7\,^{+15+15}_{-16-15}$	$9835\pm 17\,^{+22\ +6}_{-19\ -6}$
0.2084	$5816\pm 7\,^{+4\ +11}_{-4\ -11}$	$5923\pm 6\,^{+15+15}_{-15-14}$	$9819\pm 17\,^{+22\ +6}_{-20\ -6}$
0.2287	$5558\pm 7\,^{+3\ +10}_{-3\ -10}$	$5674\pm 6\,^{+14+14}_{-15-14}$	$9795\pm 17\,^{+23\ +6}_{-22\ -6}$
0.2500	$5306\pm 7\,^{+2\ +10}_{-2\ -10}$	$5433\pm 6\,^{+14+14}_{-14-14}$	$9766\pm 18\,^{+23\ +6}_{-23\ -7}$
0.2722	$5060\pm 7\,^{+1\ +10}_{-1\ -10}$	$5200\pm 5\,^{+14+14}_{-14-14}$	$9731\pm 19\,^{+25\ +7}_{-25\ -7}$
0.2954	$4821\pm 7\,^{+1\ +9}_{-1\ -9}$	$4975\pm 5\,^{+13+14}_{-13-13}$	$9691\pm 21\,^{+26\ +8}_{-27\ -8}$
0.3195	$4591\pm 8\,^{+2\ +9}_{-1\ -9}$	$4758\pm 5\,^{+13+13}_{-13-13}$	$9649\pm 23\,^{+29\ +9}_{-29\ -9}$
0.3445	$4368\pm 8\,^{+3\ +8}_{-2\ -8}$	$4548\pm 5\,^{+12+13}_{-12-13}$	$9605\pm 25\,^{+30\ +9}_{-30\ -9}$
0.3705	$4154\pm 9\,^{+3\ +8}_{-3\ -8}$	$4346\pm 5\,^{+12+12}_{-12-12}$	$9559\pm 27\,^{+32\ +10}_{-31\ -10}$
0.3974	$3948\pm 9\,^{+4\ +7}_{-3\ -7}$	$4150\pm 5\,^{+11+12}_{-11-12}$	$9513\pm 29\,^{+33\ +10}_{-32\ -10}$
0.4253	$3750\pm 10\,^{+4\ +7}_{-3\ -7}$	$3962\pm 4\,^{+10+12}_{-11-12}$	$9466\pm 32\,^{+34\ +10}_{-33\ -10}$
0.4542	$3560\pm 11\,^{+5\ +7}_{-4\ -7}$	$3781\pm 4\,^{+10+11}_{-10-11}$	$9417\pm 37\,^{+36\ +10}_{-34\ -10}$
0.4839	$3377\pm 12\,^{+5\ +7}_{-4\ -7}$	$3606\pm 4\,^{+9\ +11}_{-10-11}$	$9366\pm 43\,^{+39\ +9}_{-35\ -9}$
0.5147	$3200\pm 14\,^{+6\ +7}_{-5\ -7}$	$3438\pm 4\,^{+9\ +10}_{-10-10}$	$9308\pm 50\,^{+42\ +8}_{-38\ -8}$
0.5463	$3029\pm 17\,^{+7\ +7}_{-6\ -7}$	$3277\pm 4\,^{+9\ +10}_{-10-10}$	$9242\pm 60\,^{+48\ +8}_{-44\ -8}$
0.5789	$2862\pm 20\,^{+10\ +6}_{-8\ -6}$	$3123\pm 4\,^{+9\ +10}_{-10-10}$	$9164\pm 73\,^{+60\ +8}_{-53\ -8}$
0.6125	$2700\pm 23\,^{+14\ +6}_{-11\ -6}$	$2977\pm 4\,^{+10\ +9}_{-10\ -9}$	$9069\pm 89\,^{+78\ +9}_{-68\ -9}$
0.6470	$2540\pm 27\,^{+20\ +5}_{-16\ -5}$	$2838\pm 4\,^{+10\ +9}_{-10\ -9}$	$8952\pm 107\,^{+102\ +11}_{-90\ -11}$
0.6824	$2383\pm 30\,^{+26\ +4}_{-23\ -4}$	$2706\pm 4\,^{+11\ +9}_{-11\ -9}$	$8807\pm 120\,^{+131\ +13}_{-119\ -14}$
0.7188	$2227\pm 30\,^{+33\ +3}_{-31\ -3}$	$2581\pm 4\,^{+11\ +9}_{-11\ -9}$	$8629\pm 125\,^{+163\ +15}_{-156\ -16}$
0.7561	$2072\pm 32\,^{+37\ +3}_{-40\ -3}$	$2463\pm 3\,^{+11\ +8}_{-11\ -8}$	$8413\pm 136\,^{+190\ +16}_{-197\ -16}$
0.7944	$1917\pm 48\,^{+40\ +4}_{-48\ -4}$	$2352\pm 4\,^{+10\ +8}_{-11\ -8}$	$8152\pm 217\,^{+206\ +11}_{-240\ -12}$
0.8336	$1761\pm 91\,^{+37\ +6}_{-56\ -6}$	$2246\pm 7\,^{+10\ +7}_{-10\ -7}$	$7842\pm 427\,^{+202\ +1}_{-282\ -1}$
0.8738	$1604\pm 163^{+31+11}_{-63-11}$	$2144\pm 11^{+9\ +7}_{-10\ -7}$	$7478\pm 797\,^{+178\ +27}_{-323\ -26}$
0.9149	$1445\pm 276^{+22+19}_{-71-18}$	$2047\pm 14^{+9\ +6}_{-10\ -6}$	$7061\pm 1407^{+144\ +70}_{-376\ -67}$
0.9570	$1286\pm 475^{+28+30}_{-83-28}$	$1952\pm 17^{+9\ +6}_{-10\ -6}$	$6590\pm 2526^{+169+132}_{-451-124}$
1.0000	$1128\pm 961^{+48+43}_{-97-39}$	$1858\pm 18^{+10\ +6}_{-9\ -6}$	$6073\pm 5356^{+278+210}_{-545-191}$

Table K.7: Form factor data determined with the inverse polynomial model.

K.2.2.5 Spline model

Q^2 [(GeV/c)^2]	$G_E \cdot 10^4$	$G_M/\mu_p \cdot 10^4$	$\mu_p \frac{G_E}{G_M} \cdot 10^4$
0.0005	$9985 \pm 0^{+0\,+0}_{-0\,-0}$	$9988 \pm 0^{+0\,+0}_{-0\,-0}$	$9997 \pm 0^{+0\,+0}_{-0\,-0}$
0.0019	$9939 \pm 0^{+0\,+1}_{-0\,-1}$	$9952 \pm 1^{+1\,+1}_{-1\,-1}$	$9986 \pm 1^{+1\,+0}_{-1\,-0}$
0.0043	$9863 \pm 1^{+1\,+1}_{-1\,-1}$	$9892 \pm 2^{+2\,+1}_{-2\,-1}$	$9970 \pm 2^{+2\,+0}_{-2\,-0}$
0.0076	$9759 \pm 1^{+2\,+2}_{-2\,-2}$	$9809 \pm 3^{+3\,+2}_{-4\,-2}$	$9949 \pm 4^{+3\,+0}_{-3\,-0}$
0.0118	$9628 \pm 2^{+2\,+3}_{-3\,-3}$	$9701 \pm 5^{+5\,+4}_{-5\,-4}$	$9925 \pm 6^{+5\,+0}_{-4\,-0}$
0.0170	$9474 \pm 3^{+3\,+5}_{-3\,-5}$	$9571 \pm 6^{+7\,+5}_{-7\,-5}$	$9899 \pm 8^{+7\,+0}_{-5\,-0}$
0.0232	$9297 \pm 4^{+4\,+6}_{-4\,-6}$	$9417 \pm 7^{+8\,+7}_{-9\,-7}$	$9872 \pm 10^{+8\,+1}_{-6\,-1}$
0.0302	$9102 \pm 4^{+5\,+7}_{-5\,-7}$	$9242 \pm 9^{+10\,+8}_{-11\,-8}$	$9848 \pm 12^{+10\,+1}_{-7\,-1}$
0.0383	$8890 \pm 5^{+5\,+8}_{-5\,-8}$	$9046 \pm 9^{+12+10}_{-12-10}$	$9828 \pm 13^{+11\,+1}_{-8\,-1}$
0.0473	$8665 \pm 5^{+6\,+9}_{-6\,-9}$	$8830 \pm 10^{+13+11}_{-14-11}$	$9813 \pm 14^{+12\,+2}_{-9\,-2}$
0.0572	$8429 \pm 5^{+6\,+10}_{-6\,-10}$	$8597 \pm 10^{+14+12}_{-15-12}$	$9805 \pm 15^{+12\,+2}_{-10\,-2}$
0.0681	$8185 \pm 6^{+6\,+11}_{-6\,-10}$	$8348 \pm 9^{+15+13}_{-15-13}$	$9804 \pm 15^{+12\,+3}_{-11\,-3}$
0.0799	$7934 \pm 6^{+5\,+11}_{-6\,-11}$	$8087 \pm 9^{+16+14}_{-16-14}$	$9810 \pm 15^{+13\,+4}_{-12\,-4}$
0.0926	$7677 \pm 6^{+5\,+11}_{-5\,-11}$	$7817 \pm 8^{+16+15}_{-16-14}$	$9822 \pm 15^{+14\,+4}_{-14\,-4}$
0.1063	$7417 \pm 6^{+5\,+11}_{-5\,-11}$	$7540 \pm 8^{+16+15}_{-16-15}$	$9837 \pm 15^{+17\,+5}_{-15\,-5}$
0.1210	$7154 \pm 6^{+5\,+11}_{-5\,-11}$	$7261 \pm 8^{+16+15}_{-17-15}$	$9853 \pm 16^{+19\,+6}_{-16\,-6}$
0.1366	$6888 \pm 6^{+6\,+10}_{-4\,-10}$	$6982 \pm 8^{+16+15}_{-17-15}$	$9865 \pm 16^{+21\,+6}_{-17\,-6}$
0.1531	$6620 \pm 6^{+6\,+10}_{-4\,-10}$	$6708 \pm 8^{+16+15}_{-16-15}$	$9869 \pm 17^{+23\,+7}_{-19\,-7}$
0.1706	$6352 \pm 6^{+5\,+10}_{-4\,-10}$	$6441 \pm 7^{+15+15}_{-16-15}$	$9862 \pm 17^{+23\,+7}_{-20\,-7}$
0.1890	$6083 \pm 6^{+5\,+10}_{-3\,-10}$	$6181 \pm 7^{+15+15}_{-15-14}$	$9842 \pm 17^{+23\,+7}_{-20\,-7}$
0.2084	$5818 \pm 6^{+4\,+10}_{-3\,-10}$	$5928 \pm 6^{+15+14}_{-15-14}$	$9815 \pm 17^{+23\,+7}_{-21\,-7}$
0.2287	$5559 \pm 7^{+3\,+10}_{-2\,-10}$	$5681 \pm 6^{+14+14}_{-14-14}$	$9784 \pm 17^{+23\,+6}_{-21\,-6}$
0.2500	$5306 \pm 7^{+2\,+10}_{-1\,-10}$	$5442 \pm 5^{+14+14}_{-14-13}$	$9750 \pm 18^{+23\,+6}_{-22\,-6}$
0.2722	$5060 \pm 7^{+2\,+10}_{-1\,-9}$	$5209 \pm 5^{+13+13}_{-13-13}$	$9714 \pm 20^{+24\,+6}_{-24\,-6}$
0.2954	$4821 \pm 7^{+1\,+9}_{-0\,-9}$	$4983 \pm 5^{+13+13}_{-13-13}$	$9675 \pm 21^{+25\,+6}_{-25\,-6}$
0.3195	$4590 \pm 8^{+1\,+9}_{-1\,-9}$	$4765 \pm 5^{+12+12}_{-12-12}$	$9634 \pm 23^{+26\,+6}_{-27\,-7}$
0.3445	$4368 \pm 8^{+2\,+8}_{-2\,-8}$	$4554 \pm 5^{+12+12}_{-12-12}$	$9592 \pm 25^{+27\,+7}_{-28\,-7}$
0.3705	$4153 \pm 9^{+3\,+8}_{-2\,-8}$	$4350 \pm 5^{+11+12}_{-11-12}$	$9548 \pm 28^{+28\,+8}_{-30\,-8}$
0.3974	$3947 \pm 10^{+3\,+7}_{-3\,-7}$	$4153 \pm 5^{+11+12}_{-11-12}$	$9505 \pm 31^{+30\,+9}_{-33\,-9}$
0.4253	$3750 \pm 11^{+4\,+7}_{-4\,-7}$	$3964 \pm 5^{+11+11}_{-10-11}$	$9461 \pm 34^{+33\,+10}_{-35\,-10}$
0.4542	$3562 \pm 11^{+5\,+6}_{-4\,-6}$	$3782 \pm 5^{+10+11}_{-10-11}$	$9418 \pm 37^{+37\,+11}_{-37\,-11}$
0.4839	$3382 \pm 12^{+7\,+6}_{-5\,-6}$	$3608 \pm 5^{+10+11}_{-10-11}$	$9374 \pm 42^{+43\,+12}_{-39\,-12}$
0.5147	$3208 \pm 14^{+8\,+5}_{-6\,-5}$	$3440 \pm 4^{+10+10}_{-10-10}$	$9326 \pm 50^{+49\,+12}_{-42\,-13}$
0.5463	$3039 \pm 17^{+10\,+5}_{-7\,-5}$	$3279 \pm 4^{+9\,+10}_{-10-10}$	$9270 \pm 61^{+56\,+13}_{-48\,-13}$
0.5789	$2874 \pm 20^{+12\,+5}_{-9\,-5}$	$3124 \pm 4^{+9\,+10}_{-10-10}$	$9200 \pm 74^{+66\,+13}_{-57\,-14}$
0.6125	$2712 \pm 23^{+14\,+4}_{-13\,-4}$	$2978 \pm 4^{+10\,+9}_{-10\,-9}$	$9107 \pm 89^{+79\,+13}_{-72\,-14}$
0.6470	$2550 \pm 27^{+18\,+4}_{-18\,-4}$	$2839 \pm 4^{+10\,+9}_{-10\,-9}$	$8982 \pm 107^{+96\,+13}_{-96\,-13}$
0.6824	$2389 \pm 31^{+23\,+4}_{-25\,-4}$	$2707 \pm 4^{+11\,+9}_{-10\,-9}$	$8825 \pm 125^{+119\,+13}_{-126\,-13}$
0.7188	$2231 \pm 31^{+30\,+4}_{-31\,-4}$	$2583 \pm 4^{+11\,+8}_{-10\,-8}$	$8639 \pm 129^{+151\,+14}_{-157\,-14}$
0.7561	$2078 \pm 33^{+39\,+3}_{-35\,-3}$	$2465 \pm 3^{+11\,+8}_{-11\,-8}$	$8432 \pm 142^{+197\,+16}_{-179\,-17}$
0.7944	$1934 \pm 69^{+53\,+1}_{-36\,-1}$	$2353 \pm 7^{+9\,+8}_{-12\,-8}$	$8218 \pm 315^{+270\,+22}_{-185\,-23}$
0.8336	$1798 \pm 161^{+80\,+1}_{-31\,-2}$	$2246 \pm 15^{+7\,+8}_{-15\,-8}$	$8005 \pm 766^{+411\,+34}_{-164\,-35}$
0.8738	$1645 \pm 346^{+143\,+6}_{-10\,-6}$	$2146 \pm 24^{+5\,+8}_{-19\,-8}$	$7666 \pm 1699^{+738\,+54}_{-59\,-55}$
0.9149	$1424 \pm 706^{+269+12}_{-19\,-13}$	$2050 \pm 29^{+3\,+8}_{-22\,-8}$	$6948 \pm 3555^{+1399\,+87}_{-105\,-88}$
0.9570	$1073 \pm 1354^{+494+23}_{-17\,-23}$	$1959 \pm 33^{+3\,+7}_{-22\,-7}$	$5478 \pm 7141^{+2607+136}_{-97\,-137}$
1.0000	$510 \pm 2363^{+844+36}_{-0\,-37}$	$1873 \pm 55^{+4\,+7}_{-16\,-7}$	$2726 \pm 13624^{+4551+205}_{-0\,-207}$

Table K.8: Form factor data determined with the spline model.

K.2.2.6 Spline × dipole model

Q^2 [(GeV/c)^2]	$G_E \cdot 10^4$	$G_M/\mu_p \cdot 10^4$	$\mu_p \frac{G_E}{G_M} \cdot 10^4$
0.0005	$9985 \pm 0^{+0\,+0}_{-0\,-0}$	$9988 \pm 0^{+0\,+0}_{-0\,-0}$	$9997 \pm 0^{+0\,+0}_{-0\,-0}$
0.0019	$9939 \pm 0^{+0\,+1}_{-0\,-1}$	$9952 \pm 1^{+1\,+1}_{-1\,-1}$	$9987 \pm 1^{+1\,+0}_{-1\,-0}$
0.0043	$9863 \pm 1^{+1\,+1}_{-1\,-1}$	$9892 \pm 2^{+2\,+1}_{-2\,-1}$	$9971 \pm 2^{+2\,+0}_{-1\,-0}$
0.0076	$9759 \pm 1^{+2\,+2}_{-2\,-2}$	$9808 \pm 3^{+3\,+2}_{-3\,-2}$	$9950 \pm 3^{+3\,+0}_{-2\,-0}$
0.0118	$9629 \pm 2^{+2\,+4}_{-2\,-3}$	$9701 \pm 4^{+4\,+4}_{-5\,-4}$	$9926 \pm 5^{+4\,+0}_{-3\,-0}$
0.0170	$9475 \pm 3^{+3\,+5}_{-3\,-5}$	$9570 \pm 5^{+6\,+5}_{-7\,-5}$	$9900 \pm 7^{+5\,+0}_{-4\,-0}$
0.0232	$9299 \pm 3^{+4\,+6}_{-4\,-6}$	$9417 \pm 7^{+8\,+7}_{-8\,-6}$	$9874 \pm 9^{+7\,+0}_{-5\,-0}$
0.0302	$9103 \pm 4^{+5\,+7}_{-5\,-7}$	$9242 \pm 8^{+9\,+8}_{-10\,-8}$	$9850 \pm 10^{+8\,+1}_{-6\,-1}$
0.0383	$8892 \pm 4^{+5\,+8}_{-5\,-8}$	$9047 \pm 9^{+11\,+9}_{-12\,-9}$	$9829 \pm 12^{+9\,+1}_{-7\,-1}$
0.0473	$8667 \pm 5^{+6\,+9}_{-6\,-9}$	$8832 \pm 9^{+13+11}_{-13-11}$	$9813 \pm 13^{+11\,+1}_{-8\,-2}$
0.0572	$8430 \pm 5^{+6\,+10}_{-6\,-10}$	$8600 \pm 9^{+14+12}_{-15-12}$	$9803 \pm 14^{+11\,+2}_{-9\,-2}$
0.0681	$8185 \pm 5^{+6\,+11}_{-6\,-11}$	$8353 \pm 9^{+15+13}_{-15-13}$	$9798 \pm 15^{+12\,+3}_{-11\,-3}$
0.0799	$7932 \pm 6^{+6\,+11}_{-6\,-11}$	$8094 \pm 9^{+16+14}_{-16-14}$	$9800 \pm 15^{+13\,+3}_{-12\,-4}$
0.0926	$7674 \pm 6^{+5\,+11}_{-5\,-11}$	$7825 \pm 8^{+16+15}_{-16-14}$	$9807 \pm 15^{+14\,+4}_{-13\,-4}$
0.1063	$7413 \pm 6^{+5\,+11}_{-5\,-11}$	$7550 \pm 8^{+16+15}_{-17-15}$	$9818 \pm 15^{+16\,+5}_{-15\,-5}$
0.1210	$7148 \pm 6^{+5\,+11}_{-4\,-11}$	$7272 \pm 7^{+17+15}_{-17-15}$	$9830 \pm 15^{+18\,+6}_{-16\,-6}$
0.1366	$6882 \pm 6^{+5\,+10}_{-4\,-10}$	$6993 \pm 7^{+16+15}_{-17-15}$	$9841 \pm 15^{+20\,+7}_{-18\,-7}$
0.1531	$6616 \pm 6^{+5\,+10}_{-4\,-10}$	$6717 \pm 7^{+16+15}_{-16-15}$	$9849 \pm 15^{+21\,+7}_{-19\,-7}$
0.1706	$6349 \pm 6^{+5\,+10}_{-3\,-10}$	$6446 \pm 7^{+16+15}_{-16-15}$	$9850 \pm 16^{+23\,+8}_{-20\,-8}$
0.1890	$6083 \pm 6^{+4\,+10}_{-3\,-10}$	$6182 \pm 6^{+15+15}_{-16-15}$	$9841 \pm 16^{+24\,+8}_{-21\,-8}$
0.2084	$5820 \pm 6^{+4\,+10}_{-2\,-10}$	$5926 \pm 6^{+15+15}_{-15-14}$	$9821 \pm 16^{+24\,+8}_{-22\,-8}$
0.2287	$5560 \pm 6^{+3\,+10}_{-2\,-10}$	$5679 \pm 6^{+15+14}_{-15-14}$	$9791 \pm 17^{+24\,+8}_{-23\,-8}$
0.2500	$5305 \pm 7^{+3\,+10}_{-1\,-9}$	$5440 \pm 5^{+14+14}_{-14-14}$	$9753 \pm 18^{+24\,+7}_{-24\,-7}$
0.2722	$5058 \pm 7^{+2\,+9}_{-1\,-9}$	$5208 \pm 5^{+14+13}_{-13-13}$	$9712 \pm 19^{+24\,+7}_{-24\,-7}$
0.2954	$4819 \pm 7^{+2\,+9}_{-0\,-9}$	$4983 \pm 5^{+13+13}_{-13-13}$	$9671 \pm 20^{+25\,+7}_{-25\,-7}$
0.3195	$4588 \pm 8^{+2\,+9}_{-1\,-9}$	$4764 \pm 5^{+12+13}_{-12-12}$	$9630 \pm 22^{+26\,+7}_{-26\,-7}$
0.3445	$4366 \pm 8^{+2\,+8}_{-1\,-8}$	$4553 \pm 5^{+12+12}_{-12-12}$	$9589 \pm 23^{+27\,+7}_{-27\,-7}$
0.3705	$4153 \pm 9^{+2\,+8}_{-2\,-8}$	$4350 \pm 4^{+11+12}_{-11-12}$	$9549 \pm 26^{+29\,+7}_{-29\,-7}$
0.3974	$3949 \pm 9^{+3\,+8}_{-2\,-7}$	$4153 \pm 4^{+11+12}_{-11-11}$	$9508 \pm 29^{+31\,+8}_{-30\,-8}$
0.4253	$3752 \pm 10^{+4\,+7}_{-3\,-7}$	$3964 \pm 4^{+10+11}_{-10-11}$	$9466 \pm 32^{+34\,+9}_{-33\,-9}$
0.4542	$3563 \pm 11^{+5\,+6}_{-4\,-6}$	$3782 \pm 4^{+10+11}_{-10-11}$	$9422 \pm 36^{+38\,+10}_{-36\,-10}$
0.4839	$3381 \pm 12^{+7\,+6}_{-5\,-6}$	$3607 \pm 4^{+10+11}_{-10-11}$	$9374 \pm 41^{+43\,+11}_{-39\,-11}$
0.5147	$3205 \pm 13^{+8\,+5}_{-6\,-5}$	$3439 \pm 4^{+10+10}_{-10-10}$	$9319 \pm 47^{+49\,+12}_{-44\,-12}$
0.5463	$3034 \pm 16^{+10\,+5}_{-8\,-5}$	$3279 \pm 4^{+10+10}_{-10-10}$	$9253 \pm 58^{+56\,+13}_{-51\,-13}$
0.5789	$2867 \pm 20^{+12\,+5}_{-10\,-5}$	$3125 \pm 4^{+10+10}_{-10-10}$	$9174 \pm 73^{+66\,+13}_{-59\,-14}$
0.6125	$2704 \pm 24^{+15\,+4}_{-12\,-4}$	$2979 \pm 4^{+10\,+9}_{-10\,-9}$	$9078 \pm 90^{+79\,+14}_{-71\,-14}$
0.6470	$2544 \pm 27^{+18\,+4}_{-16\,-4}$	$2839 \pm 4^{+10\,+9}_{-10\,-9}$	$8959 \pm 106^{+96\,+14}_{-89\,-14}$
0.6824	$2386 \pm 29^{+23\,+4}_{-22\,-4}$	$2707 \pm 4^{+10\,+9}_{-10\,-9}$	$8813 \pm 117^{+119\,+14}_{-114\,-15}$
0.7188	$2229 \pm 29^{+30\,+3}_{-29\,-3}$	$2582 \pm 3^{+11\,+8}_{-11\,-8}$	$8634 \pm 122^{+150\,+15}_{-147\,-15}$
0.7561	$2074 \pm 32^{+38\,+3}_{-38\,-3}$	$2465 \pm 3^{+11\,+8}_{-11\,-8}$	$8413 \pm 135^{+190\,+16}_{-192\,-17}$
0.7944	$1915 \pm 43^{+48\,+2}_{-52\,-2}$	$2355 \pm 5^{+11\,+8}_{-11\,-8}$	$8131 \pm 195^{+240\,+19}_{-257\,-19}$
0.8336	$1740 \pm 75^{+57\,+0}_{-74\,-0}$	$2251 \pm 7^{+11\,+8}_{-11\,-8}$	$7734 \pm 353^{+291\,+26}_{-366\,-26}$
0.8738	$1536 \pm 141^{+65\,+4}_{-112\,-3}$	$2151 \pm 10^{+11\,+8}_{-11\,-8}$	$7142 \pm 687^{+335\,+42}_{-555\,-41}$
0.9149	$1287 \pm 262^{+73\,+10}_{-173\,-10}$	$2055 \pm 11^{+11\,+7}_{-10\,-7}$	$6260 \pm 1305^{+375\,+71}_{-869\,-69}$
0.9570	$973 \pm 455^{+87\,+20}_{-265\,-19}$	$1961 \pm 10^{+11\,+7}_{-9\,-7}$	$4963 \pm 2349^{+445\,+121}_{-1366\,-117}$
1.0000	$577 \pm 724^{+115+34}_{-388-33}$	$1866 \pm 9^{+11\,+7}_{-8\,-7}$	$3092 \pm 3902^{+611\,+195}_{-2078-189}$

Table K.9: Form factor data determined with the spline × dipole model.

K.2.2.7 Double-dipole model

Q^2 [(GeV/c)^2]	$G_E \cdot 10^4$	$G_M/\mu_p \cdot 10^4$	$\mu_p \frac{G_E}{G_M} \cdot 10^4$
0.0005	$9979\pm 1\,^{+1\ +0}_{-1\ -0}$	$9986\pm 0\,^{+0\ +0}_{-0\ -0}$	$9993\pm 1\,^{+1\ +0}_{-1\ -0}$
0.0019	$9920\pm 3\,^{+3\ +0}_{-4\ -1}$	$9943\pm 0\,^{+1\ +0}_{-1\ -1}$	$9976\pm 3\,^{+3\ +1}_{-3\ -1}$
0.0043	$9828\pm 7\,^{+6\ +0}_{-6\ -1}$	$9873\pm 1\,^{+2\ +1}_{-2\ -1}$	$9954\pm 7\,^{+5\ +0}_{-6\ -2}$
0.0076	$9712\pm 10\,^{+7\ +1}_{-8\ -2}$	$9777\pm 1\,^{+3\ +2}_{-4\ -2}$	$9933\pm 9\,^{+7\ +0}_{-7\ -1}$
0.0118	$9574\pm 11\,^{+8\ +2}_{-10\ -4}$	$9655\pm 2\,^{+4\ +3}_{-5\ -3}$	$9916\pm 10\,^{+8\ +0}_{-7\ -1}$
0.0170	$9418\pm 13\,^{+9\ +4}_{-10\ -5}$	$9509\pm 3\,^{+5\ +4}_{-7\ -4}$	$9904\pm 11\,^{+8\ +0}_{-7\ -1}$
0.0232	$9244\pm 13\,^{+9\ +6}_{-11\ -7}$	$9342\pm 4\,^{+7\ +5}_{-9\ -5}$	$9895\pm 11\,^{+8\ +1}_{-6\ -2}$
0.0302	$9054\pm 13\,^{+10\ +7}_{-11\ -8}$	$9155\pm 5\,^{+9\ +6}_{-12\ -7}$	$9890\pm 10\,^{+8\ +1}_{-5\ -2}$
0.0383	$8848\pm 12\,^{+9\ +8}_{-11\ -9}$	$8950\pm 6\,^{+10\ +7}_{-14\ -8}$	$9886\pm 10\,^{+8\ +1}_{-6\ -2}$
0.0473	$8628\pm 12\,^{+9\ +9}_{-10-10}$	$8730\pm 7\,^{+12\ +8}_{-16\ -9}$	$9884\pm 9\,^{+9\ +1}_{-7\ -1}$
0.0572	$8396\pm 12\,^{+9\ +9}_{-10-11}$	$8496\pm 7\,^{+13+10}_{-17-10}$	$9881\pm 9\,^{+10\ +0}_{-9\ -0}$
0.0681	$8153\pm 11\,^{+8\ +10}_{-9\ -11}$	$8253\pm 8\,^{+14+11}_{-19-11}$	$9879\pm 9\,^{+12\ +0}_{-11\ -1}$
0.0799	$7901\pm 11\,^{+8\ +10}_{-8\ -11}$	$8000\pm 9\,^{+15+11}_{-20-12}$	$9876\pm 10\,^{+15\ +1}_{-13\ -2}$
0.0926	$7643\pm 11\,^{+7\ +10}_{-7\ -11}$	$7742\pm 9\,^{+16+12}_{-21-13}$	$9872\pm 10\,^{+17\ +2}_{-15\ -3}$
0.1063	$7379\pm 10\,^{+6\ +10}_{-7\ -11}$	$7479\pm 9\,^{+17+13}_{-21-14}$	$9866\pm 10\,^{+19\ +3}_{-17\ -4}$
0.1210	$7112\pm 10\,^{+6\ +10}_{-6\ -11}$	$7215\pm 9\,^{+17+13}_{-21-14}$	$9858\pm 11\,^{+21\ +4}_{-18\ -4}$
0.1366	$6844\pm 10\,^{+5\ +10}_{-5\ -11}$	$6949\pm 9\,^{+17+14}_{-21-15}$	$9849\pm 12\,^{+23\ +5}_{-20\ -5}$
0.1531	$6576\pm 10\,^{+5\ +10}_{-4\ -11}$	$6685\pm 9\,^{+17+14}_{-21-15}$	$9837\pm 12\,^{+25\ +6}_{-21\ -6}$
0.1706	$6310\pm 10\,^{+4\ +10}_{-3\ -10}$	$6423\pm 9\,^{+17+14}_{-20-15}$	$9824\pm 13\,^{+26\ +6}_{-22\ -7}$
0.1890	$6046\pm 10\,^{+4\ +9}_{-3\ -10}$	$6164\pm 9\,^{+17+14}_{-19-15}$	$9808\pm 14\,^{+27\ +7}_{-23\ -7}$
0.2084	$5786\pm 9\,^{+3\ +9}_{-2\ -10}$	$5910\pm 9\,^{+16+14}_{-18-15}$	$9790\pm 14\,^{+28\ +7}_{-24\ -7}$
0.2287	$5531\pm 9\,^{+3\ +9}_{-1\ -10}$	$5662\pm 8\,^{+15+14}_{-17-14}$	$9769\pm 15\,^{+28\ +8}_{-25\ -8}$
0.2500	$5282\pm 9\,^{+3\ +9}_{-1\ -9}$	$5420\pm 8\,^{+15+13}_{-16-14}$	$9746\pm 15\,^{+28\ +8}_{-26\ -8}$
0.2722	$5039\pm 9\,^{+2\ +8}_{-1\ -9}$	$5184\pm 8\,^{+14+13}_{-15-14}$	$9720\pm 16\,^{+29\ +8}_{-26\ -8}$
0.2954	$4804\pm 9\,^{+2\ +8}_{-1\ -9}$	$4956\pm 7\,^{+13+13}_{-14-13}$	$9693\pm 16\,^{+29\ +8}_{-26\ -8}$
0.3195	$4576\pm 9\,^{+2\ +8}_{-1\ -9}$	$4735\pm 7\,^{+12+12}_{-13-13}$	$9663\pm 17\,^{+29\ +8}_{-27\ -8}$
0.3445	$4356\pm 9\,^{+2\ +8}_{-2\ -8}$	$4523\pm 7\,^{+12+12}_{-12-12}$	$9631\pm 17\,^{+29\ +8}_{-27\ -8}$
0.3705	$4144\pm 9\,^{+2\ +7}_{-2\ -8}$	$4317\pm 6\,^{+11+11}_{-12-12}$	$9597\pm 17\,^{+29\ +8}_{-27\ -8}$
0.3974	$3940\pm 8\,^{+2\ +7}_{-2\ -8}$	$4120\pm 6\,^{+10+11}_{-11-12}$	$9562\pm 18\,^{+29\ +8}_{-27\ -8}$
0.4253	$3744\pm 8\,^{+2\ +7}_{-2\ -7}$	$3931\pm 5\,^{+10+11}_{-10-11}$	$9524\pm 18\,^{+30\ +8}_{-28\ -8}$
0.4542	$3557\pm 8\,^{+3\ +7}_{-2\ -7}$	$3750\pm 5\,^{+9\ +10}_{-10-11}$	$9485\pm 18\,^{+30\ +8}_{-28\ -8}$
0.4839	$3378\pm 8\,^{+3\ +6}_{-2\ -7}$	$3576\pm 5\,^{+9\ +10}_{-9\ -10}$	$9445\pm 19\,^{+31\ +8}_{-29\ -8}$
0.5147	$3207\pm 8\,^{+3\ +6}_{-2\ -7}$	$3411\pm 5\,^{+8\ +9}_{-9\ -10}$	$9403\pm 19\,^{+32\ +8}_{-29\ -8}$
0.5463	$3044\pm 8\,^{+3\ +6}_{-3\ -6}$	$3252\pm 4\,^{+8\ +9}_{-9\ -10}$	$9360\pm 19\,^{+33\ +8}_{-30\ -8}$
0.5789	$2889\pm 7\,^{+3\ +6}_{-3\ -6}$	$3101\pm 4\,^{+8\ +9}_{-8\ -9}$	$9317\pm 19\,^{+34\ +8}_{-31\ -8}$
0.6125	$2741\pm 7\,^{+3\ +5}_{-3\ -6}$	$2957\pm 4\,^{+8\ +9}_{-8\ -9}$	$9272\pm 19\,^{+35\ +8}_{-33\ -8}$
0.6470	$2601\pm 7\,^{+3\ +5}_{-3\ -6}$	$2819\pm 4\,^{+8\ +8}_{-8\ -9}$	$9227\pm 20\,^{+37\ +9}_{-34\ -8}$
0.6824	$2468\pm 7\,^{+3\ +5}_{-3\ -5}$	$2688\pm 4\,^{+8\ +8}_{-8\ -8}$	$9181\pm 20\,^{+39\ +9}_{-36\ -9}$
0.7188	$2341\pm 7\,^{+3\ +5}_{-3\ -5}$	$2563\pm 4\,^{+8\ +8}_{-8\ -8}$	$9135\pm 20\,^{+41\ +9}_{-37\ -9}$
0.7561	$2222\pm 6\,^{+3\ +5}_{-3\ -5}$	$2445\pm 4\,^{+8\ +8}_{-9\ -8}$	$9088\pm 20\,^{+44+10}_{-39-9}$
0.7944	$2108\pm 6\,^{+3\ +4}_{-3\ -5}$	$2332\pm 4\,^{+8\ +7}_{-9\ -8}$	$9041\pm 20\,^{+47+10}_{-42-10}$
0.8336	$2001\pm 6\,^{+3\ +4}_{-3\ -4}$	$2224\pm 4\,^{+8\ +7}_{-9\ -8}$	$8994\pm 21\,^{+49+11}_{-44-10}$
0.8738	$1899\pm 6\,^{+3\ +4}_{-3\ -4}$	$2122\pm 4\,^{+8\ +7}_{-9\ -7}$	$8947\pm 21\,^{+53+11}_{-47-11}$
0.9149	$1802\pm 6\,^{+3\ +4}_{-3\ -4}$	$2025\pm 4\,^{+9\ +7}_{-9\ -7}$	$8901\pm 22\,^{+56+12}_{-50-12}$
0.9570	$1711\pm 5\,^{+3\ +4}_{-3\ -4}$	$1933\pm 4\,^{+9\ +7}_{-10\ -7}$	$8854\pm 22\,^{+59+13}_{-53-12}$
1.0000	$1625\pm 5\,^{+3\ +4}_{-2\ -4}$	$1845\pm 4\,^{+9\ +7}_{-10\ -7}$	$8808\pm 23\,^{+63+13}_{-56-13}$

Table K.10: Form factor data determined with the double-dipole model.

K.2.2.8 Friedrich-Walcher model

Q^2 [(GeV/c)^2]	$G_E \cdot 10^4$	$G_M/\mu_p \cdot 10^4$	$\mu_p \frac{G_E}{G_M} \cdot 10^4$
0.0005	$9984\pm0^{+0\ +0}_{-0\ -0}$	$9987\pm0^{+0\ +0}_{-0\ -0}$	$9997\pm0^{+0\ +0}_{-0\ -0}$
0.0019	$9937\pm1^{+1\ +1}_{-1\ -1}$	$9948\pm0^{+0\ +0}_{-0\ -0}$	$9990\pm1^{+1\ +1}_{-1\ -1}$
0.0043	$9860\pm2^{+1\ +2}_{-2\ -2}$	$9883\pm0^{+0\ +0}_{-1\ -0}$	$9978\pm2^{+1\ +1}_{-1\ -1}$
0.0076	$9755\pm3^{+2\ +3}_{-3\ -3}$	$9793\pm1^{+1\ +1}_{-2\ -1}$	$9962\pm3^{+2\ +2}_{-2\ -2}$
0.0118	$9624\pm4^{+3\ +4}_{-4\ -5}$	$9679\pm1^{+1\ +1}_{-3\ -1}$	$9943\pm4^{+2\ +3}_{-2\ -4}$
0.0170	$9469\pm5^{+4\ +6}_{-5\ -6}$	$9542\pm2^{+2\ +2}_{-4\ -2}$	$9923\pm5^{+3\ +4}_{-3\ -5}$
0.0232	$9293\pm6^{+5\ +7}_{-6\ -8}$	$9384\pm2^{+2\ +3}_{-5\ -3}$	$9903\pm6^{+3\ +5}_{-3\ -5}$
0.0302	$9099\pm6^{+6\ +9}_{-7\ -9}$	$9206\pm3^{+3\ +4}_{-6\ -4}$	$9884\pm6^{+3\ +6}_{-3\ -6}$
0.0383	$8889\pm6^{+6+10}_{-7-10}$	$9009\pm3^{+4\ +5}_{-7\ -5}$	$9866\pm6^{+3\ +6}_{-3\ -6}$
0.0473	$8665\pm6^{+7+11}_{-8-11}$	$8796\pm4^{+6\ +6}_{-9\ -7}$	$9852\pm6^{+5\ +6}_{-2\ -5}$
0.0572	$8431\pm6^{+7+12}_{-8-12}$	$8568\pm6^{+7\ +8}_{-10\ -8}$	$9840\pm7^{+6\ +5}_{-1\ -4}$
0.0681	$8186\pm6^{+7+12}_{-8-12}$	$8326\pm7^{+9\ +9}_{-12-10}$	$9832\pm9^{+8\ +4}_{-2\ -3}$
0.0799	$7934\pm5^{+7+13}_{-7-13}$	$8074\pm8^{+10+11}_{-14-12}$	$9827\pm11^{+11+2}_{-5\ -1}$
0.0926	$7676\pm5^{+7+13}_{-7-12}$	$7812\pm9^{+12+13}_{-15-14}$	$9826\pm13^{+13+1}_{-7\ 0}$
0.1063	$7413\pm5^{+6+12}_{-6-12}$	$7543\pm10^{+14+14}_{-17-15}$	$9827\pm15^{+16+4}_{-10-2}$
0.1210	$7147\pm5^{+6+12}_{-6-12}$	$7270\pm10^{+15+15}_{-18-16}$	$9830\pm16^{+19+6}_{-13-4}$
0.1366	$6878\pm5^{+5+12}_{-5-12}$	$6995\pm10^{+16+16}_{-18-17}$	$9833\pm17^{+21+7}_{-16-6}$
0.1531	$6610\pm6^{+4+11}_{-4-11}$	$6721\pm9^{+16+16}_{-18-17}$	$9835\pm16^{+23+9}_{-19-7}$
0.1706	$6342\pm6^{+4+11}_{-3-11}$	$6450\pm8^{+17+16}_{-18-17}$	$9833\pm16^{+25+9}_{-21-8}$
0.1890	$6077\pm6^{+3+10}_{-2-10}$	$6185\pm7^{+16+16}_{-18-17}$	$9825\pm16^{+26+9}_{-23-9}$
0.2084	$5815\pm6^{+2+10}_{-1-10}$	$5927\pm6^{+16+16}_{-17-16}$	$9811\pm15^{+26+9}_{-25-9}$
0.2287	$5558\pm6^{+2+10}_{-1-10}$	$5677\pm6^{+15+15}_{-16-15}$	$9790\pm16^{+27+9}_{-26-9}$
0.2500	$5306\pm7^{+2+10}_{-0-10}$	$5435\pm5^{+15+15}_{-15-15}$	$9762\pm17^{+27+8}_{-27-9}$
0.2722	$5060\pm7^{+1\ +9}_{-1\ -9}$	$5202\pm5^{+14+14}_{-14-14}$	$9727\pm17^{+27+8}_{-28-8}$
0.2954	$4821\pm7^{+1\ +9}_{-1\ -9}$	$4978\pm5^{+13+14}_{-14-14}$	$9686\pm18^{+28+8}_{-28-8}$
0.3195	$4590\pm7^{+2\ +9}_{-1\ -9}$	$4761\pm4^{+13+13}_{-13-13}$	$9641\pm19^{+28+7}_{-28-8}$
0.3445	$4367\pm7^{+2\ +9}_{-1\ -9}$	$4552\pm4^{+12+13}_{-12-13}$	$9595\pm19^{+28+7}_{-28-7}$
0.3705	$4152\pm7^{+2\ +9}_{-2\ -9}$	$4349\pm4^{+11+12}_{-12-12}$	$9547\pm19^{+28+6}_{-28-7}$
0.3974	$3946\pm7^{+2\ +9}_{-2\ -9}$	$4153\pm3^{+11+12}_{-11-12}$	$9500\pm19^{+28+6}_{-28-6}$
0.4253	$3748\pm7^{+2\ +9}_{-2\ -9}$	$3964\pm3^{+10+12}_{-10-11}$	$9454\pm19^{+27+5}_{-28-6}$
0.4542	$3558\pm7^{+2\ +8}_{-2\ -9}$	$3782\pm3^{+9\ +11}_{-10-11}$	$9410\pm19^{+27+5}_{-28-5}$
0.4839	$3377\pm7^{+2\ +8}_{-2\ -9}$	$3606\pm3^{+9\ +11}_{-9\ -11}$	$9367\pm20^{+27+4}_{-28-5}$
0.5147	$3205\pm7^{+2\ +8}_{-2\ -8}$	$3437\pm3^{+9\ +10}_{-9\ -10}$	$9325\pm20^{+27+3}_{-28-4}$
0.5463	$3040\pm7^{+2\ +8}_{-2\ -8}$	$3275\pm3^{+8\ +10}_{-8\ -10}$	$9284\pm20^{+28+3}_{-29-4}$
0.5789	$2884\pm7^{+2\ +8}_{-2\ -8}$	$3120\pm2^{+8\ +10}_{-8\ -10}$	$9243\pm20^{+29+2}_{-29-3}$
0.6125	$2735\pm7^{+2\ +8}_{-2\ -8}$	$2972\pm2^{+8\ +9}_{-8\ -9}$	$9202\pm20^{+30+2}_{-30-3}$
0.6470	$2594\pm6^{+2\ +7}_{-2\ -8}$	$2832\pm2^{+8\ +9}_{-8\ -9}$	$9160\pm20^{+31+2}_{-31-2}$
0.6824	$2460\pm6^{+2\ +7}_{-1\ -7}$	$2698\pm2^{+8\ +9}_{-8\ -9}$	$9116\pm21^{+33+2}_{-32-2}$
0.7188	$2333\pm6^{+2\ +7}_{-1\ -7}$	$2572\pm2^{+8\ +8}_{-8\ -8}$	$9070\pm21^{+35+1}_{-34-2}$
0.7561	$2212\pm6^{+2\ +7}_{-1\ -7}$	$2452\pm2^{+8\ +8}_{-9\ -8}$	$9022\pm21^{+37+1}_{-35-2}$
0.7944	$2098\pm6^{+2\ +7}_{-1\ -7}$	$2339\pm2^{+8\ +8}_{-9\ -8}$	$8971\pm21^{+39+1}_{-37-2}$
0.8336	$1990\pm6^{+2\ +6}_{-1\ -7}$	$2232\pm3^{+8\ +8}_{-9\ -8}$	$8917\pm21^{+41+1}_{-39-2}$
0.8738	$1888\pm5^{+2\ +6}_{-1\ -6}$	$2131\pm3^{+8\ +8}_{-9\ -8}$	$8859\pm21^{+43+1}_{-41-2}$
0.9149	$1792\pm5^{+2\ +6}_{-1\ -6}$	$2036\pm3^{+9\ +7}_{-10\ -7}$	$8797\pm22^{+47+1}_{-43-2}$
0.9570	$1700\pm5^{+2\ +6}_{-1\ -6}$	$1947\pm3^{+9\ +7}_{-11\ -7}$	$8731\pm23^{+53+1}_{-46-2}$
1.0000	$1614\pm5^{+2\ +6}_{-1\ -6}$	$1864\pm3^{+10\ +7}_{-12\ -7}$	$8659\pm24^{+63+1}_{-49-2}$

Table K.11: Form factor data determined with the Friedrich-Walcher model.

List of Figures

List of Tables

Bibliography

[A+72] Akimov, Yu. K. *et al.*: Small angle scattering of electrons by protons. Sov. Phys. **JETP35**:651, 1972.

[A+94] Andivahis, L. *et al.*: Measurements of the electric and magnetic form-factors of the proton from $Q^2 = 1.75$ (GeV/c)^2 to 8.83 $((GeV)/c)^2$. Phys. Rev. **D50**:5491–5517, 1994.

[Ach04] Achenbach, Patrick: Kaon electroproduction with KaoS at MAMI-C 2004. Prepared for 32nd International Workshop on Gross Properties of Nuclei and Nuclear Excitation: Probing Nuclei and Nucleons with Electrons and Photons (Hirschegg 2004), Hirschegg, Austria, 11-17 Jan 2004.

[Ams09] Amsler, C. *at al.* (Particle Data Group): Review of Particle Physics. Phys. Lett. **B667**:1+, 2008 and 2009 partial update for the 2010 edition.

[AMT07] Arrington, J.; Melnitchouk, W., and Tjon, J. A.: Global analysis of proton elastic form factor data with two-photon exchange corrections. Phys. Rev. **C76**:035205, 2007.

[Arr04] Arrington, J.: Implications of the discrepancy between proton form factor measurements. Phys. Rev. **C69**:022201, 2004.

[B+71] Berger, C. *et al.*: Electromagnetic form-factors of the proton at squared four momentum transfers between 10 fm^{-2} and 50 fm^{-2}. Phys. Lett. **B35**:87, 1971.

[B+73] Bartel, W. *et al.*: Measurement of proton and neutron electromagnetic form-factors at squared four momentum transfers up to 3 (GeV/c)^2. Nucl. Phys. **B58**:429–475, 1973.

[B+90] Bosted, P. E. *et al.*: Measurements of the deuteron and proton magnetic form factors at large momentum transfers. Phys. Rev. C **42**(1):38–64, 1990.

[B+98] Blomqvist, K. I. *et al.*: The three-spectrometer facility at the Mainz microtron MAMI. Nucl. Instrum. Meth. A **403**:263–301, 1998.

[Ber04] Bernauer, Jan C.: *Vorbereitung zur hochpräzisen Messung des elektrischen und magnetischen Formfaktors von Protonen.* Master's thesis, Institut für Kernphysik der Universität Mainz, 2004.

[BHM07] Belushkin, M. A.; Hammer, H. W., and Meissner, U. G.: Dispersion analysis of the nucleon form factors including meson continua. Phys. Rev. **C75**:035202, 2007.

[BKLH02] Brash, E. J.; Kozlov, A.; Li, S., and Huber, G. M.: New empirical fits to the proton electromagnetic form factors. Phys. Rev. **C65**:051001, 2002.

[BL98] Blobel, Volker and Lohrman, Erich. *Statistische und numerische Methoden der Datenanalyse*. B. G. Teubner, Stuttgart, Leipzig, 1998.

[ble] blender, a 3D content creation suite. `http://www.blender.org`.

[BN37] Bloch, F. and Nordsieck, A.: Note on the Radiation Field of the electron. Phys. Rev. **52**:54–59, 1937.

[boo] boost C++ libraries. `http://www.boost.org`.

[BPS+75] Borkowski, F.; Peuser, P.; Simon, G. G.; Walther, V. H., and Wendling, R. D.: Electromagnetic Form-Factors of the Proton at Low Four-Momentum Transfer. Nucl. Phys. **B93**:461, 1975.

[BS05] Blunden, Peter G. and Sick, Ingo: Proton radii and two-photon exchange. Phys. Rev. C **72**(5):057601, 2005.

[C+04] Christy, M. E. *et al.*: Measurements of electron-proton elastic cross sections for $0.4 < Q^2 < 5.5$ $(\mathrm{GeV}/c)^2$. Phys. Rev. **C70**(1):015206, 2004.

[C+07] Crawford, C. B. *et al.*: Measurement of the Proton's Electric to Magnetic Form Factor Ratio from $^1\vec{H}(\vec{e}, e'p)$. Phys. Rev. Lett. **98**(5):052301, 2007.

[CH56] Chambers, E. E. and Hofstadter, R.: Structure of the Proton. Phys. Rev. **103**(5):1454–1463, 1956.

[Cha32] Chadwick, James: Possible existance of a neutron. Nature **129**:312, 1932.

[D+01] Dieterich, S. *et al.*: Polarization transfer in the $^4He(\vec{e}, e'\vec{p})H$ reaction. Phys. Lett. **B500**(1-2):47 – 52, 2001.

[de Fo83] de Forest, Taber: Off-shell electron-nucleon cross sections : The impulse approximation. Nuclear Physics **A392**(2-3):232 – 248, 1983.

[Deh10] Dehn, Marco: A1 beam position stabilization. private communication, 2010.

[DG89] Drechsel, D. and Giannini, M. M.: Electron scattering off nuclei. Rep. Prog. Phys. **52**:1083–1163, 1989.

[Dis90] Distler, Michael O.: *Aufbau und Test einer vertikalen Driftkammer*. Master's thesis, Institut für Kernphysik der Universität Mainz, 1990.

[Dis10] Distler, Michael O.: Toy model for simultaneous confidence bands. private communication, 2010.

[DMW01] Distler, Michael O.; Merkel, Harald, and Weis, Markus. Data acquisition and analysis for the 3-spectrometer-setup at MAMI. In *Proceedings of the 12th IEEE Real Time Congress on Nuclear and Plasma Sciences*, 2001.

[EGS01] Eides, Michael I.; Grotch, Howard, and Shelyuto, Valery A.: Theory of light hydrogenlike atoms. Physics Reports **342**(2-3):63 – 261, 2001.

[ES33] Estermann, I. and Stern, Otto: Über die magnetische Ablenkung von Wasserstoffmolekülen und das magnetische Moment des Protons. II. Z.Phys. **A85**:17–24, 1933.

[ESW60] Ernst, F. J.; Sachs, R. G., and Wali, K. C.: Electromagnetic form factors of the nucleon. Phys. Rev. **119**:1105–1114, 1960.

[F+99] Florizone, Richard. E. J. *et al.*: High-precision Studies of the ^{3}He(e,e′p) Reaction at the Quasielastic Peak. Phys. Rev. Lett. **83**:2308, 1999.

[FBD66] Frerejacque, Daniel; Benaksas, David, and Drickey, Darrell James: Proton Form Factors from Proton Observation. Phys. Rev. **141**:1308–1312, 1966.

[Flo98] Florizone, Richard E. J.: *The Longitudinal and Transverse Response of the $(e, e'p)$ Reaction in Helium-3 and Helium-4 in the Quasielastic Region.* PhD thesis, Massachusetts Institute of Technology, 1998.

[Fos95] Foster, Ian. *Designing and Building Parallel Programs.* Addison-Wesley, 1995.

[Fri00] Friedrich, Jan M.: *Messung der Virtuellen Comptonstreuung an MAMI zur Bestimmung Generalisierter Polarisierbarkeiten des Protons.* PhD thesis, Institut für Kernphysik der Universität Mainz, 2000.

[FS33] Frisch, R. and Stern, Otto: Über die magnetische Ablenkung von Wasserstoffmolekülen und das magnetische Moment des Protons. I. Z.Phys. **A85**:4–16, 1933.

[FW03] Friedrich, J. and Walcher, Th.: A coherent interpretation of the form factors of the nucleon in terms of a pion cloud and constituent quarks. Eur. Phys. J. **A17**:607–623, 2003.

[G+01] Gayou, O. *et al.*: Measurements of the elastic electromagnetic form factor ratio $\mu_p G_{Ep}/G_{Mp}$ via polarization transfer. Phys. Rev. C **64**(3):038202, 2001.

[GE+01] Gough Eschrich, Ivo M. *et al.*: Measurement of the Σ^- charge radius by Σ^- electron elastic scattering. Phys. Lett. **B522**:233–239, 2001.

[GHK+07] Gabrielse, G.; Hanneke, D.; Kinoshita, T.; Nio, M., and Odom, B.: Erratum: New Determination of the Fine Structure Constant from

the Electron g Value and QED. Phys. Rev. Lett. **99**(3):039902, 2007.

[GK92] Gari, M. F. and Krümpelmann, W.: The Electric neutron form-factor and the strange quark content of the nucleon. Phys. Lett. **B274**:159–162, 1992. Erratum-ibid.**B282**:483,1992.

[GM09] Geiger, Hand and Marsden, Ernest: On a diffuse reflection of the α-particles. Proceedings of the Royal Society **A82**:495–500, 1909.

[GV03] Guichon, Pierre A. M. and Vanderhaeghen, M.: How to reconcile the Rosenbluth and the polarization transfer method in the measurement of the proton form factors. Phys. Rev. Lett. **91**:142303, 2003.

[H+73] Hanson, K. M. *et al.*: Large angle quasielastic electron-deuteron scattering. Phys. Rev. **D8**:753–778, 1973.

[H+76] Höhler, G. *et al.*: Analysis of electromagnetic nucleon form factors. Nuclear Physics **B114**(3):505–534, 1976.

[HFK+76] Herminghaus, H.; Feder, A.; Kaiser, K. H.; Manz, W., and Von Der Schmitt, H.: The Design of a Cascaded 800-MeV Normal Conducting CW Racetrack Microtron. Nucl. Instrum. Meth. **138**:1–12, 1976.

[Hig10] Higinbotham, Douglas W.: Precision Measurements of the Proton Elastic Form Factor Ratio 2010. `http://arxiv.org/abs/1001.3341v2`.

[HM55] Hofstadter, Robert and McAllister, Robert W.: Electron scattering from the proton. Phys. Rev. **98**(1):217–218, 1955.

[HMW63] Hand, L. N.; Miller, D. G., and Wilson, Richard: Electric and Magnetic Form Factors of the Nucleon. Rev. Mod. Phys. **35**(2):335–349, 1963.

[Hof56] Hofstadter, Robert: Electron Scattering and Nuclear Structure. Rev. Mod. Phys. **28**(3):214–254, 1956.

[ink] Inkscape. `http://www.inkscape.org`.

[J+] Jones, Eric *et al.*: SciPy: Open source scientific tools for Python, 2001–.

[J+00] Jones, M. K. *et al.*: G_{Ep}/G_{Mp} Ratio by Polarization Transfer in $\vec{e}p \to e\vec{p}$. Phys. Rev. Lett. **84**(7):1398–1402, 2000.

[Jam94] James, F.: MINUIT - Function Minimization and Error Analysis - Reference Manual - Version 94.1. `http://wwwasdoc.web.cern.ch/wwwasdoc/minuit/minmain.html`, 1994.

[Jam06] James, Frederick. *Statistical Methods in Experimental Physics*. World Scientific, Singapore, second edition, 2006.

[Jan06] Jankowiak, A.: The Mainz Microtron MAMI: Past and future. Eur. Phys. J. **A28S1**:149–160, 2006.

[JHHY66] Janssens, T.; Hofstadter, R.; Hughes, E. B., and Yearian, M. R.: Proton form factors from elastic electron-proton scattering. Phys. Rev. **142**:922–931, 1966.

[Jov03] Jover Mañas, Gabriel V.: *Simulation of Double Polarization Variables in Virtual Compton Scattering.* Master's thesis, Institut für Kernphysik der Universität Mainz, 2003.

[JR54] Jauch, J. M. and Rohrlich, F.: The infrared divergence. Helvetica Physica Acta **27**:613, 1954.

[K+08] Kaiser, K. H. *et al.*: The 1.5-GeV harmonic double-sided microtron at Mainz University. Nucl. Instrum. Meth. **A593**:159–170, 2008.

[Kar99] Karshenboim, Savely G.: What do we actually know about the proton radius? Can. J. Phys. **77**:241–266, 1999.

[KN06] Kinoshita, Toichiro and Nio, Makiko: Improved α^4 term of the electron anomalous magnetic moment. Phys. Rev. D **73**(1):013003, 2006.

[Kor94] Korn, Manfred: *Entwicklung des Bahnrückverfolgungsverfahrens für die Drei-Spektrometer-Anlage und experimentelle Bestimmung der Abbildungseigenschaften der Spektrometer A und B mit elastischer Elektronenstreuung.* PhD thesis, Institut für Kernphysik der Universität Mainz, 1994.

[Lat] LaTeX - A document preparation system. `http://www.latex-project.org`.

[Lom01] Lomon, Earle L.: Extended Gari-Krümpelmann model fits to nucleon electromagnetic form factors. Phys. Rev. **C64**:035204, 2001.

[Lom02] Lomon, Earle L.: Effect of recent R(p) and R(n) measurements on extended Gari-Krümpelmann model fits to nucleon electromagnetic form factors. Phys. Rev. **C66**:045501, 2002.

[Lom06] Lomon, Earle L.: Effect of revised R(n) measurements on extended Gari-Krümpelmann model fits to nucleon electromagnetic form factors 2006.

[M+91] McCord, M. *et al.*: Preliminary results of a new determination of the rms charge radius of the proton. Nucl. Instrum. Meth. **B56/57**:496–499, 1991.

[M+98] Milbrath, B. D. *et al.*: Comparison of Polarization Observables in Electron Scattering from the Proton and Deuteron. Phys. Rev. Lett. **80**(3):452–455, 1998.

[MGH80] Moré, J. J.; Garbow, B. S., and Hillstrom, K. E.: User Guide for MINPACK-1. ANL-80-74, Argonne National Laboratory 1980.

[MMD96] Mergell, P.; Meissner, Ulf G., and Drechsel, Dieter: Dispersion-Theoretical Analysis of the Nucleon Electromagnetic Formfactors. Nucl. Phys. **A596**:367–396, 1996.

[MSS74] Murphy, J. J.; Shin, Y. M., and Skopik, D. M.: Proton form factor from 0.15 to 0.79 fm^{-2}. Phys. Rev. **C9**(6):2125–2129, 1974.

[MT00] Maximon, L. C. and Tjon, J. A.: Radiative corrections to electron proton scattering. Phys. Rev. **C62**:054320, 2000.

[MT05] Mohr, Peter J. and Taylor, Barry N.: CODATA recommended values of the fundamental physical constants: 2002. Rev. Mod. Phys. **77**:1–107, 2005.

[MTN08] Mohr, Peter J.; Taylor, Barry N., and Newell, David B.: CODATA Recommended Values of the Fundamental Physical Constants: 2006. Rev. Mod. Phys. **80**:633–730, 2008.

[Mv00] Melnikov, Kirill and van Ritbergen, Timo: Three-Loop Slope of the Dirac Form Factor and the 1S Lamb Shift in Hydrogen. Phys. Rev. Lett. **84**(8):1673–1676, 2000.

[N+00] Niering, M. *et al.*: Measurement of the Hydrogen 1S-2S Transition Frequency by Phase Coherent Comparison with a Microwave Cesium Fountain Clock. Phys. Rev. Lett. **84**(24):5496–5499, 2000.

[OHDG06] Odom, B.; Hanneke, D.; D'Urso, B., and Gabrielse, G.: New Measurement of the Electron Magnetic Moment Using a One-Electron Quantum Cyclotron. Phys. Rev. Lett. **97**(3):030801, 2006.

[Ort86] Ortega, J M. *Matrix theory: a second course*. Plenum Press, New York, NY, USA, 1986.

[P+71] Price, L. E. *et al.*: Backward-angle electron-proton elastic scattering and proton electromagnetic form-factors. Phys. Rev. **D4**:45–53, 1971.

[P+01] Pospischil, Thomas *et al.*: Measurement of G_{Ep}/G_{Mp} via polarization transfer at $Q^2 = 0.4$ (GeV/c)^2. Eur. Phys. J. **A12**:125–127, 2001.

[P+02] Pospischil, Thomas *et al.*: The focal plane proton polarimeter for the 3-spectrometer setup at MAMI. Nucl. Instrum. Meth. **A483**:713–725, 2002.

[P+05] Punjabi, V. *et al.*: Proton elastic form factor ratios to $Q^2 = 3.5$ GeV^2 by polarization transfer. Phys. Rev. C **71**(5):055202, 2005.

[PFS+89] Pieroth, M.; Friedrich, J.; Semmel, P.; Voegler, N.; Lerose, John, and Zimmerman, Peter D.: Radiation tail in electron scattering: Approximations in the calculation and comparison to measurements. Nuclear Instruments and Methods in Physics Research Section B: Beam Interactions with Materials and Atoms **36**(3):263 – 275, 1989.

[Pos] PostgreSQL Global Development Group: PostgreSQL. `http://www.postgresql.org`.

[Pos00] Pospischil, Thomas: *Aufbau und Inbetriebnahme eines Protonen-Polarimeters an MAMI und Messung der Proton-Polarisation in der Reaktion $p(\vec{e},e'\vec{p})\pi^0$.* PhD thesis, Institut für Kernphysik der Universität Mainz, 2000.

[PRSZ04] Povh, Bogdan; Rith, Klaus; Scholz, Christoph, and Zetsche, Frank. *Teilchen und Kerne. Eine Einführung in die physikalischen Konzepte.* Springer-Verlag GmbH, sixth edition, 2004.

[PTVF92] Press, William; Teukolsky, Saul; Vetterling, William, and Flannery, Brian. *Numerical Recipes in C.* Cambridge University Press, Cambridge, UK, 2nd edition, 1992.

[Q+05] Qattan, I. A. *et al.*: Precision Rosenbluth Measurement of the Proton Elastic Form Factors. Phys. Rev. Lett. **94**(14):142301, 2005.

[R+07] Ron, G. *et al.*: The Proton Elastic Form Factor Ratio at Low Momentum Transfer. Phys. Rev. Lett. **99**:202002, 2007.

[Ros50] Rosenbluth, M. N.: High Energy Elastic Scattering of Electrons on Protons. Phys. Rev. **79**(4):615–619, 1950.

[Ros00] Rosenfelder, R.: Coulomb Corrections to Elastic Electron-Proton Scattering and the Proton Charge Radius. Phys. Lett. **B479**:381–386, 2000.

[Rut11] Rutherford, Ernest: The scattering of α and β particles by matter and the structure of the atom. Phil. Mag. **21**:669–688, 1911.

[Rut19] Rutherford, Ernest: Collision of alpha Particles with Light Atoms; An Anomalous Effect in Nitrogen. Phil. Mag. **37**(222):537–587, 1919.

[Sac62] Sachs, R. G.: High-Energy Behavior of Nucleon Electromagnetic Form Factors. Phys. Rev. **126**(6):2256–2260, 1962.

[Sch94] Schardt, Stefan: *Aufbau und Erprobung der Drei-Spektrometer-Anordnung für Koinzidenzexperimente mit Elektronen am 855 MeV-Elektronenbeschleuniger MAMI.* PhD thesis, Institut für Kernphysik der Universität Mainz, 1994.

[Sic74] Sick, Ingo: Model-independent nuclear charge densities from elastic electron scattering. Nuclear Physics A **218**(3):509 – 541, 1974.

[Sic03] Sick, Ingo: On the rms-radius of the proton. Phys. Lett. **B576**:62–67, 2003.

[SSBW80] Simon, G. G.; Schmitt, Ch.; Borkowski, F., and Walther, V. H.: Absolute electron-proton cross sections at low momentum transfer measured with a high pressure gas target system. Nucl. Phys. **A333**(3):381–391, 1980.

[Tex] TeX live distribution. `http://www.tug.org/texlive`.

[Tho97] Thomson, Joseph J.: Cathode rays. Philosophical Magazine **44**:293, 1897.

[Tsa61] Tsai, Yung-Su: Radiative corrections to electron-proton scattering. Phys. Rev. **122**(6):1898–1907, 1961.

[U+97] Udem, Th. *et al.*: Phase-Coherent Measurement of the Hydrogen $S1$-$S2$ Transition Frequency with an Optical Frequency Interval Divider Chain. Phys. Rev. Lett. **79**:2646–2649, 1997.

[V+00] Vanderhaeghen, M. *et al.*: QED radiative corrections to virtual Compton scattering. Phys. Rev. **C62**:025501, 2000.

[van Ro95] van Rossum, Guido. Python reference manual. Report CS-R9525, Centrum voor Wiskunde en Informatica, P. O. Box 4079, 1009 AB Amsterdam, The Netherlands, 1995.

[W+94] Walker, R. C. *et al.*: Measurements of the proton elastic form factors for $1 \leq Q2 \leq 3$ $(\mathrm{GeV}/c)^2$ at SLAC. Phys. Rev. D **49**(11):5671–5689, 1994.

[WK] Williams, Thomas and Kelley, Colin: gnuplot. `http://www.gnuplot.info`.

[Won94] Wong, Chun Wa: Deuteron radius and nuclear forces in free space. Int. J. Mod. Phys. **E3**:821–908, 1994.

[YFS61] Yennie, D. R.; Frautschi, S. C., and Suura, H.: The infrared divergence phenomena and high-energy processes. Ann. Phys. **13**:379–452, 1961.

[YLR57] Yennie, D. R.; Lévy, M. M., and Ravenhall, D. G.: Electromagnetic Structure of Nucleons. Rev. Mod. Phys. **29**(1):144–157, 1957.

[ZH10] Zhan, Xiaohui and Higinbotham, Douglas W.: Preliminary results for "Precision Measurements of the Proton Elastic Form Factor Ratio". private communication, 2010.

Danksagung

Aufgrund datenschutzrechlicher Bestimmungen kann die Danksagung in der elektronischen Version nicht komplett veröffentlicht werden. Ich möchte mich bei allen bedanken, die mit Rat und Tat zum Gelingen dieser Arbeit beigetragen haben.